DISSERTATION | DOCTORAL THESIS

Titel | Title

Crystallization in highly undercooled trachybasalts: an experimental petrology perspective

verfasst von | submitted by

Dott. mag. Dott. Stefano Peres

angestrebter akademischer Grad | in partial fulfilment of the requirements for the degree of

Doktor der Naturwissenschaften (Dr.rer.nat.)

Wien | Vienna, 2025

Studienkennzahl lt. Studienblatt | Degree programme code as it appears on the student record sheet:	UA 796 605 426
Dissertationsgebiet lt. Studienblatt | Field of study as it appears on the student record sheet:	Erdwissenschaften
Betreut von | Supervisor:	Univ.-Prof. Dr. Rainer Abart

Index

Kristallisation von stark unterkühlten Trachybasalten: eine Perspektive aus der experimentellen Petrologie

Abstract (German)

In dieser Dissertation habe ich einen multimethodologischen Ansatz gewählt, welcher Synchrotronstrahlungs-Mikro-Computertomographie (SR-µCT), Rückstreuelektronen-Diffraktion (EBSD) und Elektronenstrahlmikrosonden-Analysen (EPMA) einbezieht, um untekühlte, synthetische Trachybasalte zu untersuchen. Die Schmelzen wurden bei konstantem Druck von 400 MPa beginnend von 1300 °C heruntergekühlt auf die Verweiltemperaturen von 1150 °C, 1100 °C und 1050 °C, mit isothermalen Verweilzeiten zwischen 0 Minuten und 8 Stunden.

Das erste Ergebnis dieser Arbeit ist die Entwicklung neuer Kriterien zur Bestimmung von Nukleationsmechanismen. Ich verband das Vorhandensein einer geclusterten 3D-Verteilung von Titanomagnetitkörnern (Tmt) und das Vorhandensein kristallographischer Orientierungsbeziehungen (CORs) entlang der gemeinsamen Klinopyroxen (Cpx)-Titanomagnetit-Korngrenzen als Beweis für heterogene Nukleation, wohingegen die Abwesenheit beider Eigenschaften als Beweis für die homogene Nukleation von Tmt Körnern diente.

Unter Anwendung dieser Kriterien untersuchte ich, inwiefern sich die Häufigkeit heterogener Nukleationssstellen auf die endgültige Mikrostruktur magmatischer Gesteine auswirkt. Ich konnte zeigen, dass in einer Cr-dotierten, wasserfreien Versuchsreihe die hohe Verfügbarkeit der Spinellkörner eine hohe Zahl an heterogenen Nukleationsstellen für Cpx liefert. Das Ergebnis ist eine Mikrostruktur, die charakterisiert ist durch zahlreiche kleine skelettartige Cpx Körner, welche sich auf den Spinellkörnern bilden und diese einschließen. In undotierten

wasserfreien Proben führte die geringere Dichte der sich früh bildenden Spinellkörner zu weniger Nukleationsstellen, wodurch der Cpx ausgiebig ohne eine signifikante Konkurrenz benachbarter Kristalle wachsen konnte. Daraus ergeben sich große Bereiche in den Proben, die von großen, stark dendritischen Klinopyroxenkörnern dominiert werden.

Diese Ergebnisse belegen, dass Phasen, die sich früh bilden oder vererbte Kristalle als Keime für die heterogene Nukleation fungieren und mehr noch als Unterkühlung die Kristallisationsdynamiken und die finale Gesteinsmikrostruktur stark beeinflussen. Die Verfügbarkeit heterogener Nuklei in magmatischen Systemen, die thermaler oder konstitutioneller Unterkühlung ausgesetzt sind, kann zu rascher Kristallisation führen. Das kann wiederum die Viskosität des Magmas beeinflussen und bestimmen, ob das System, abhängig von der Kristallinität, stagniert oder fragmentiert.

Crystallization in highly undercooled trachybasalts: an experimental petrology perspective

Abstract

In this thesis I adopted a multimethodological approach which involves synchrotron radiation micro-computed tomography (SR-μCT), electron backscattered diffraction (EBSD), and electron probe microanalysis (EPMA) to investigate undercooled synthetic trachybasalts. The melts were held at constant pressure of 400 MPa and cooled from 1300 °C to resting temperatures of 1150 °C, 1100 °C, and 1050 °C, followed by isothermal dwells between 0 minutes and 8 hours.

The first outcome of this work is the development of new criteria to identify nucleation mechanisms. I correlated the presence of the clustered 3D distribution of titanomagnetite grains (Tmt) and the presence of crystallographic orientation relationships (CORs) across the shared clinopyroxene (Cpx)-titanomagnetite interface as evidence for heterogenous nucleation, while the lack of these two provided evidence for homogeneous nucleation of Tmt grains.

Applying these criteria, I then investigated how the abundance of heterogeneous nucleation sites impacts the final microstructure of magmatic rocks. I demonstrated that in a Cr-doped anhydrous experimental series, the high availability of spinel grains provides abundant Cpx heterogeneous nucleation sites. The result is a microstructure characterized by numerous small skeletal Cpx grains forming on and engulfing the spinel grains. In undoped anhydrous samples the lower density of early-forming spinel grains led to fewer nucleation sites, allowing Cpx to grow extensively without significant competition from neighbouring

crystals. This results in significant portions of the samples dominated by large, highly dendritic clinopyroxene grains.

These results attest that early-forming phases or inherited crystals acting as seeds for heterogeneous nucleation, more than undercooling, can deeply impact crystallization dynamics and final rock microstructure. The availability of heterogeneous nuclei can drive rapid crystallization in magmatic systems undergoing thermal or constitutional undercooling. This, in turn, may influence magma viscosity and determine whether the system stagnates or fragments, depending on its crystallinity.

Specific vocabulary used in the thesis

In this thesis I adopted the term microstructure as proposed by *Vernon (2004)* as the small-scale features of a rock, observable under a microscope, that reveal information about its history and the processes it has undergone. I chose to use microstructure instead of texture, to avoid misunderstandings with material scientists or structural geologists, who use "texture" to refer to crystallographic preferred orientation (CPO) of crystals, for example following a deformation event.

Another specific term I will use in the thesis is clustering, here referred as groups of grains that are joined by areas of grain and/or phase boundary (e.g. *Ferguson et al., 2019*).

1. INTRODUCTION

The undercooling of a magmatic system is defined as the difference between the liquidus temperature (T_{liq}) of a magma or a specific mineral phase and the effective temperature at which the mineral phase crystallizes (*Kirkpatrick, 1981*). The undercooling can be thermal or compositionally induced when the T_{liq} increases as a consequence of decompression (loss of volatile phases) in a H2O-saturated system (*Hammer and Rutherford, 2002; Mollo and Hammer, 2017, Ballhaus et al. 2023*). The major consequence of both thermal and decompression-related undercooling is to supersaturate the melt with respect to one or multiple phases and induce nucleation and crystallization. The nucleation mechanisms can be homogeneous or heterogeneous nucleation (e.g. *Holness et al., 2023 & references therein*). Heterogeneous nucleation, i.e. nucleation on a pre-existing surface, is energetically substantially more favourable than nucleation from a melt, i.e. homogeneous nucleation, in supersaturated systems. Indeed, as shown in Fig.1.1, the energy needed to create a new stable nucleus from the melt, that is, the energy to form a crystal entirely enclosed by a new crystal-melt interface (green curve in Fig.1.1), is higher than the energy required to create a new

stable nucleus on an already existing surface (red and orange curves in Fig.1.1), as part of the crystal-melt interface is replaced by a lower energy crystal-crystal interface.

Here, for comparison, I report the equations governing homogeneous (equation 1) and heterogeneous (equation 2) nucleation of a phase beta from a starting phase alpha, in the latter case on a substrate S:

$$\Delta G(r) = -\frac{4\pi r^3}{3v_l}\Delta G_{\alpha\beta} + 4\pi r^2 \gamma_{\alpha\beta} \quad (1)$$

$$\Delta G(r) = \left(-\frac{4\pi r^3}{3}\Delta G_{\alpha\beta} + 4\pi r^2 \gamma_{\alpha\beta}\right)\left(\frac{1}{2} - \frac{3\cos\theta}{4} + \frac{cos^3\theta}{4}\right) \quad (2)$$

$$\Delta G^* = \frac{16\pi {\gamma_{\alpha\beta}}^3}{3(\Delta G_{\alpha\beta})^2} \quad (3)$$

where ΔG is the overall change in Gibbs free energy upon formation of a nucleus of β with radius r, $\Delta G_{\alpha\beta}$ is the change in Gibbs free energy due to the formation of a volume of β, $\gamma_{\alpha\beta}$ is the surface energy (also known as surface tension), θ is the wetting angle between the nucleus β and the surface S and ΔG* is the critical free energy, i.e. the energetic cost to form a nucleus of the critical radius r* which can overcome the energetic barrier for the formation of a stable nucleus. Based on energetic arguments and experimental observations, heterogeneous nucleation has been argued to be the more frequent nucleation mechanism occurring in crystallizing natural systems (Fig.1.2a; *Lofgren 1983).* Understanding the initial nucleation behaviour of crystallising systems is particularly important, because early-formed phases and their abundance could significantly affect the microstructure, i.e. the features of a rock observable under the microscope that help infer deformation, metamorphism, or crystallization history (*Vernon 2004*), as well as the crystallization order and phase composition of the final solid (*Mollo et al., 2012*).

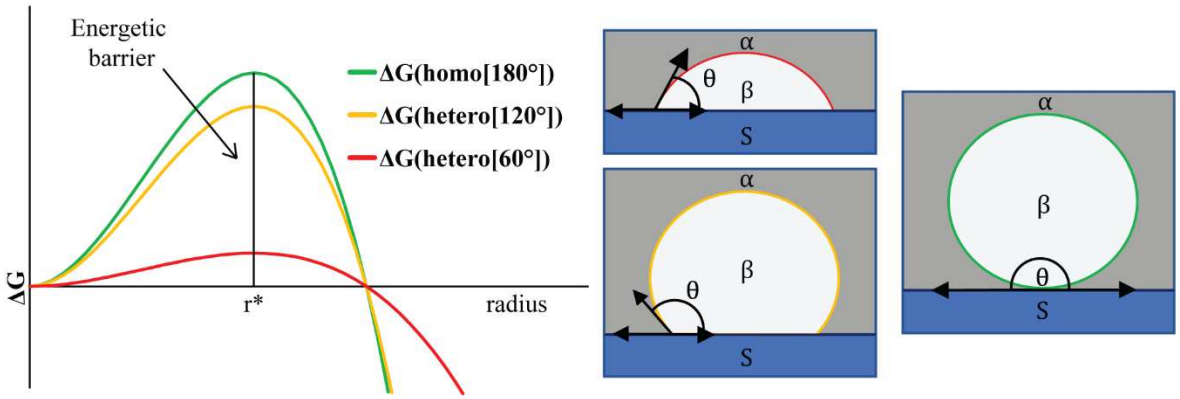

Fig. 1.1. The diagram on the left shows the change ΔG of the Gibbs energy upon formation of a spherical nucleus (crystal/bubble/droplet) on a pre-existing substrate (crystal) for different wetting angles (θ = 60° - 120° - 180°) in a heterogeneous nucleation scenario. The maximum height of the three curves are the energy barriers that need to be overcome to generate a stable nucleus (right side of the curve after the maximum). Nuclei with lower wetting angles (red and orange curve) have to create less of new crystal/melt interface (disadvantageous interface) and, instead, replace it with a lower energy crystal-crystal interface (favorable interfaces), while at the maximum wetting angle possible, i.e. 180° (green curve) the energetic barrier is the highest possible, equaling the nucleation energy barrier required for homogeneous nucleation. The right diagram shows three heterogeneously nucleated particles β from the phase α on the substrate S with different wetting angles θ. The colors of the particles match the colors of the respective curves in the diagram.

Even if heterogeneous nucleation is theoretically more energetically favoured, analytical methodologies which can prove or attest nucleation mechanisms in specific cases are rare and mostly unconclusive. In experimental petrology, heterogeneous nucleation has often been suggested based on ex-situ observations and analysis after the end of the experiment, as in-situ experiments are complicated to carry out and may be limited by the speed of 3D data acquisition acquisition and/or the spatial resolution available. In ex-situ studies, microstructural relations like the perpendicular growth of elongate crystals from an interface in the direction of the melt are one of the main features used to validate heterogeneous nucleation (Fig.1.2d; *Kirkpatrick 1977, Hammer et al. 2010, Arzilli et al. 2015, Vetere et al. 2015*).

Ex-situ, high resolution synchrotron radiation micro computed tomography (SR-μCT) is one of the best analytical methodologies to spatially characterize the 3D morphology of crystal clusters and to infer their nucleation mechanisms. Feldspar spherulites (*Arzilli et al., 2015*), clinopyroxene (Cpx) rosette-like microstructures (*Colle et al., 2023*), or, less obviously,

different populations of Titanomagnetite (Tmt) grains decorating both the internal and external edges of skeletal Cpx grains (*Peres et al., 2024*) are some examples of microstructures proposed as the consequence of heterogeneous nucleation from 3D ex-situ investigations.

Ex-situ, 2D scanning via electron backscattered diffraction (EBSD), used to study the crystallographic orientation relationships (CORs, defined as systematic relationships between the crystallographic orientations of next-neighbour crystal pairs sharing boundary segments; *Habler and Griffiths 2017*), is revealing itself to be a key analytical methodology in the quest to identify heterogeneous nucleation (*Hammer et al., 2010; Habler and Griffiths 2017; Peres et al., 2024*). This is because during heterogeneous nucleation of a crystal phase on a pre-existing surface, the factors influencing the interface energy are: a) the misorientation across the interface and b) the orientation of the interface plane relative to the two crystal lattices (*Sutton and Balluffi 1995*). When the crystallographic structures of the two crystals are similar and low surface energy planes are present, it is possible to create interfaces characterized by lower interface energy, lowering the energetic barrier to heterogeneous nucleation. CORs between the two crystal phases are thus the consequence of the prevalence of particular low energy interfaces.

1.1. Clustering mechanism and rock microstructure in the framework of the thesis

Undercooled melts are common in nature and can be found in various settings and formed through different cooling processes. Most magmatic rocks start to crystallize inside a volcanic plumbing system, i.e. a trans-crustal magmatic system composed of several communicating batches of crystal-rich magma known as crystal mushes (*Bachmann and Huber 2016; Cashman et al. 2017*). These magmatic bodies are crystal-bearing partially molten systems in which the crystals are arranged in a framework, with melt occupying the

remaining space (e.g. *Philpotts et al. 1999*, *Marsh 2002*), and represent the geologic model that in the last decades has replaced the traditional image of a volcano fed by a single melt dominated magma chamber, largely as a consequence of the failure to locate these features using geophysical methods (*Grosfils et al., 2007*) along with petrological evidence of varying pressures and temperatures of crystal formation and considerable residence times of some phases before eruption (*Dungan et al., 2004; Berlo et al., 2007; Davidson et al., 2007; Lange et al., 2013; Kilgour et al., 2014; Sides et al., 2014*). Given this recent conceptualization of the magmatic chambers as crystal mushes, it is of primary importance to understand the interaction between crystals, particularly the formation of rigid aggregates of many individual grains, i.e. crystal clusters. Crystal clustering and microstructures caused by high-undercooling events (e.g. skeletal and dendritic morphologies) deeply affect the magmatic differentiation (*Philpotts et al. 1998; 1999*) and the rheology of deep and shallow magmatic systems, influencing the possibility for a magma batch to be erupted depending on the amount of crystals, their packing and morphology (*Moitra and Gonnermann 2015; Arzilli et al., 2022*). Determining the mechanisms of crystal clustering and the variables (e.g. water content, pressure, undercooling or oxygen fugacity) influencing rapidly crystallizing rocks is therefore pivotal for assessing magmatic systems' evolution, in particular their rheology, and their eruptive style.

Clustering driving forces are supersaturation, fluid-dynamic forces and gravity. These forces result in different clustering mechanisms: heterogeneous nucleation (which I already introduced in the previous paragraph), synneusis and passive accumulation, respectively (*Jerram et al. 2003, Holness et al. 2023*). Synneusis occurs when two suspended crystals interact and join together (*Vance 1969*) under fluid-dynamic control during settling (*Schwindinger 1999, DiBenedetto et al. 2020*). This interaction tends to produce alignment of the faces of two euhedral or sub-euhedral crystals that will share a large contact surface

(Fig.1.2b; *Vance 1969, Wieser et al. 2019, Gordon & Wallis 2024*). Passive crystal accumulation is the main mechanism implied in the formation of cumulate textures (Fig.1.2c). In cumulitic rocks, crystal centres do not form statistical clusters (*Rudge et al. 2008)* unless the crystals are aligned by granular flow or compaction and fit in a shape preferred orientation (e.g. *Vukmanovic et al., 2018*). In the absence of these processes, these clusters will lack crystallographic preferred orientation (CPOs; *Wieser et al., 2019, Rudge et al. 2008*).

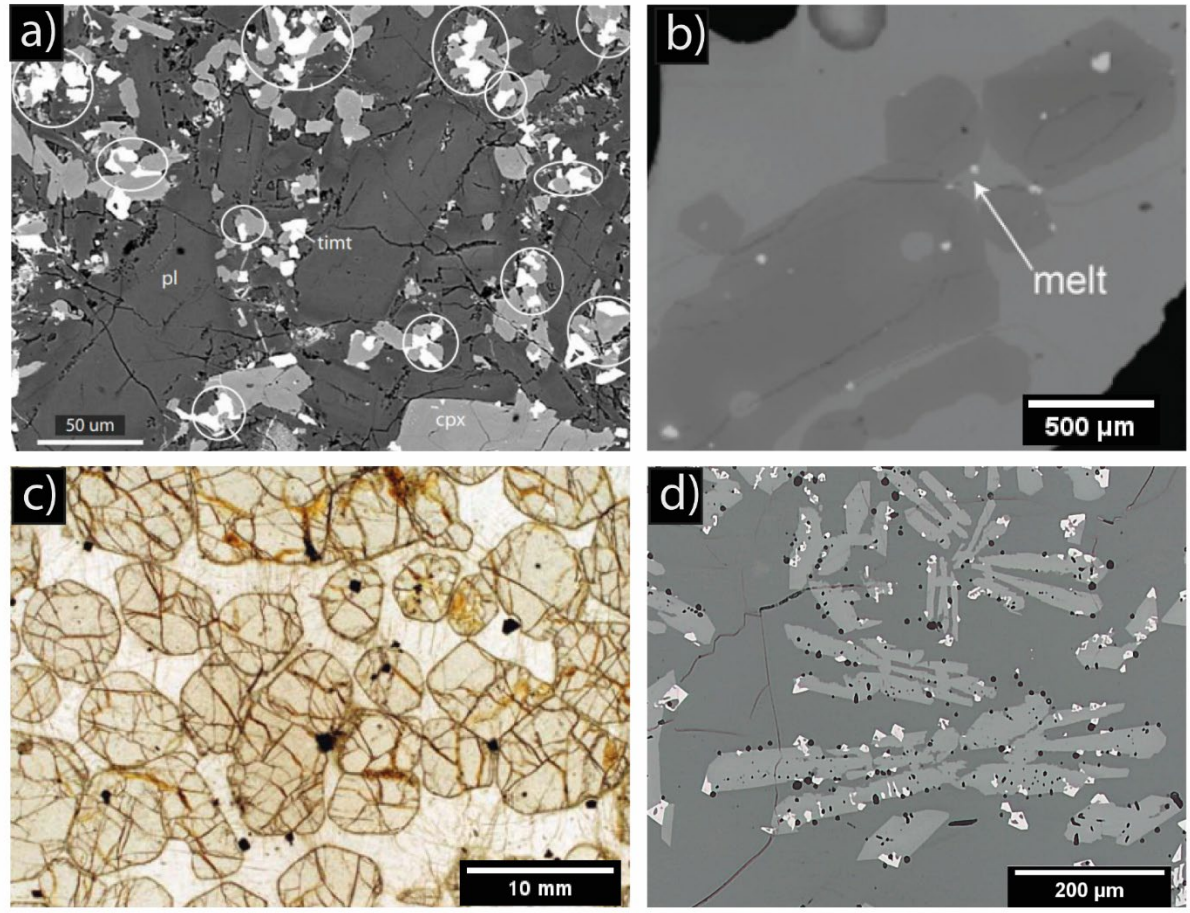

Fig.1.2) different types of clustering mechanisms a) BSE photo of an Etnean trachybasalts where [fig.1a from Hammer et al., 2010 supplementary material] the white circles highlight cpx-tmt clusters probably formed by heterogeneous nucleation (modified from fig.1a from Hammer et al., 2010 supplementary material); b) BSE photo of an Olivine clusters from Kīlauea volcano formed by synneusis [modified from fig.1a of Wieser et al., 2019]; c) photomicrograph of an olivine cumulate from the Eastern Layered Suite, Isle of Rum formed by passive accumulation [modified from fig.6a from Rudge et al., 2008]; d) microscope picture of experimental run 1100w-30min; cpx and tmt crystals are always in contact forming cluster formed by Heterogeneous nucleation (see chapter 2.4.1 in this thesis for explanation

1.2. Other examples of highly undercooled geologic terrestrial and extraterrestrial materials

Other than volcanic rocks and their experimentally simulated counterparts, the latter of which will be extensively discussed during this thesis, I will introduce in the next paragraphs some further examples of geologic materials which are formed by the rapid growth of crystals from undercooled melts. While I have not investigated them in this thesis, they are characterized by interesting microstructural features suggesting clustering by heterogeneous nucleation and fast growing from a highly undercooled melt and illustrate the broader relevance of understanding nucleation and (rapid) crystallisation processes in highly undercooled melts. The geologic examples I will briefly introduce are: a) fulgurites, b) cosmic spherules, c) chondrules.

Fulgurites (Fig.1.3b) are glasses formed by the rapid heating of rock, sand, or soil by a cloud-to-ground lightning strike (*Pasek et al., 2012*) or during an artificial high current or high voltage electrical discharges from a power line into the ground. The melting and subsequent rapid cooling of the target material can also locally generate, zones, especially at the contact with air, where the melt can crystallize at undercooling and the cooling rate compatible with the formation of dendrites (*Griffiths et al 2023*). The morphology and curvature of these dendrites was inferred to be related to spatial and/or temporal variations in undercooling/cooling rate by Griffiths et al. (2023), but no quantitative information could be extracted.

Cosmic spherules (Fig.1.3 c-e) are micrometeorites which experienced significant melting during atmospheric entry and are characterized by sub-spherical shape (*Brownlee, 1985*). Silicate-type cosmic spherules are the most common of all the micrometeorites, comprising the very vast majority of all the cosmic spherules found (*Taylor et al. 2000*). The S-type cosmic spherules are classified based on their texture, which is thought to be dependent on

the peak temperature experienced and on the cooling rate at which they recrystallize. From glass spherules which lack olivine crystals and probably experienced the highest peak temperatures and the fastest cooling rates, at decreasing peak T and cooling rate we find, in order, microstructures characterizing the Cryptocrystalline (CC) spherules, Barred olivine (BO) spherules, and Porphyritic olivine (PO) spherules (e.g. *Genge et al., 2008* and references within Fig.1.3).

Chondrules (Fig.1.3f) are igneous particles that crystallize rapidly in minutes to hours and are the most common constituent of chondrites (*Scott and Krot 2014*). These particles have been also classified based on their microstructures as porphyritic if they are composed of olivine (PO) or pyroxene (PP) grains surrounded by a fine-grained matrix or glass (*Lofgren 1989*), and non-porphyritic, which as the name suggests lacks large grains, but are composed of barred Ol (BO), or radial Px (RP), granular olivine (GO), or cryptocrystalline (CC) (*Scott and Krot 2014* and references therein). More classes of chondrule microstructures are implemented to also take the grain's size in consideration, so that the porphyritic microstructures can be crypto-porphyritic if the grain size is < 10 µm, micro- if the grain size is < 200 µm, macro- if the grain size is > 500 µm and porphyritic s.s. for sizes inside the range 200 – 500 µm (*Jones 1992*). The microstructures can vary depending on nucleation mechanism (i.e. homogeneous vs heterogeneous nucleation) and the degree of melting (partial vs complete melting) which influence the amount of crystal seeds present at the start of the crystallization process. BO, RP and CC and macro-PO are chondrule microstructures associated with complete melting and homogeneous nucleation mechanism, while GO, crypto-porphyritic and micro-porphyritic are chondrule microstructures associated with partial melting and heterogeneous nucleation on pre-existing crystal seeds (*Auxerre et al., 2022*).

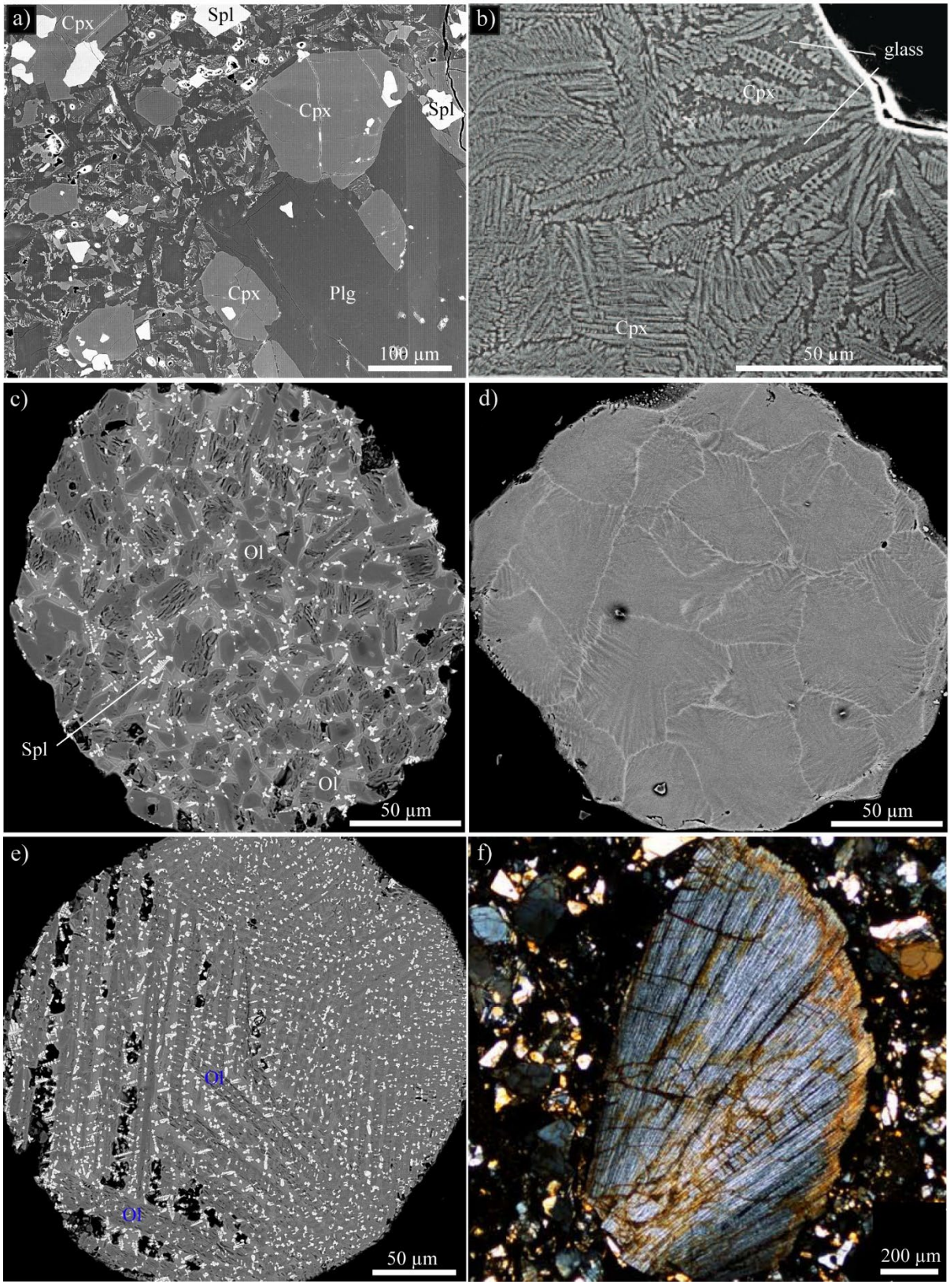

Fig.1.3. Crystal clusters and high undercooling microstructures in geologic materials; a) Secondary Emission (SE) image from a trachybasaltic samples of 1669 Mt Etna eruption; b) a rosette microstructure of dendritic Cpx originating from a point on a large vesicle in the spongy crust of a fulgurite (image modified from Griffiths et al., 2023,Fig.3e) ; c) S-type cosmic spherule with Porphyritic Olivine microstructure (PO); d) S-type cosmic spherule with Cryptocrystalline microstructure (CC); e) S-type cosmic spherule with Barred Olivine microstructure (BO); f) Chondrule with Radial Pyroxene microstructure (image modified from Watanabe et al., 2024*, Fig.2b)*

This work is aimed to focus on these two specific features occurring in undercooled melts, clustering and microstructures characterizing undercooled magmas.

1.3. Chapters summary and important scientific questions discussed

In the first part of this thesis (Chapter 2), I study and discuss the most important clustering mechanism occurring in undercooled magmas, i.e. heterogenous nucleation. More specifically, I identify the microstructural features that can reveal the nucleation mechanism occurring in a synthetic trachybasalt with hydrous starting composition (2-3 H_2O wt%). The samples, composed mainly of Cpx and Tmt grains, show ubiquitous clustering between the two phases. It was possible to distinguish 3 Tmt populations based on their morphology and spatial relationships with the Cpx they are in contact with. Through the use of SR-µCT combined with EBSD and EPMA I answer to the following scientific questions: What are the best 3D and 2D microstructural parameters that allow to distinguish heterogenous from homogenous nucleation of the crystal phases present in the experimental samples? What is the nucleation and growth history of the samples? How this can be translated to natural samples?

This chapter represent a scientific work I published as first Author in the scientific Journal "Contribution to Mineralogy and Petrology" in 2024 as *Peres et al., (2024)*. Identifying crystal nucleation mechanisms in a synthetic trachybasalt: a multimodal approach. https://doi.org/10.1007/s00410-024-02161-w

In the second part of the thesis (Chapter 3), I focus mostly on microstructures in undercooled magmas, more specifically on how heterogeneous nucleation of silicate phases on top of early formed crystals influences the overall microstructures of rocks formed during an undercooling event of moderate to high intensity. In order to guarantee the formation of early-formed crystal phases I carried out crystallization experiments for samples with

trachybasaltic starting composition (both anhydrous and hydrous) doped with 0.4% of Cr_2O_3. This minor element addition allowed the pervasive crystallization of chromium rich spinel grains that could act as heterogeneous nuclei for a high number of small skeletal Cpx grains. An undoped sample series (both anhydrous and hydrous compositions) was also created, to study the microstructures of highly undercooled melts where the nucleation of an early phase was not forced. The anhydrous samples of this series show the presence of vast portions of the samples dominated by the presence of a small number of big, highly dendritic Cpx grains. EBSD mapping of representative portions of the samples allowed me to answer to these questions: a) What is the nucleation and crystallization history of each sample? b) Is heterogenous nucleation the main nucleation mechanism of the crystal phases present? c) How does the availability of heterogenous nuclei affect the microstructures of the samples? d) How might the presence of early-forming phases affect the rheology of a magmatic system and what could be the broad consequences from a volcanological perspective?
This chapter will represent my second paper as first author related to this PhD project and will soon be submitted to a scientific journal as Peres et al., (2025/2026). " The effect of heterogeneous nuclei availability on rock microstructure: a new perspective from EBSD investigation of synthetic trachybasaltic magmas".

In the third part of the thesis (Chapter 4) I present data acquired during the PhD in the form of collaborations with other research groups but always focusing on crystallization in moderate to highly undercooled basaltic systems. More specifically in my first collaboration (*Colle et al., 2023*, Chapter 4.1) I will show 3D renderings of crystals from experimental samples with basaltic composition, carried out in order to study the effect of undercooling on clinopyroxene crystallization in magmas with Stromboli composition. 3D scans analyzed through SR-µCT are characterized by extensive clustering between Cpx and Tmt similar to the other samples presented in this work. Just from qualitative analysis of these

microstructures it is possible to infer the crystallization history of the samples quite well, and consequently suggest heterogeneous nucleation of Tmt grains and bubbles on top of Cpx grains. The collaboration resulted in the publishing of the work in the scientific journal "Lithos" titled "Effect of undercooling on clinopyroxene crystallization in a high K basalt: Implications for magma dynamics at Stromboli volcano", (2023).

Another ongoing collaboration (Chapter 4.2) is *Lanzafame et al., (under review)*, which aims to investigate the subaerial crystallization of basic lava flows, focusing on a pressure ridge formed within the pāhoehoe lava field of the 1651–1654 CE eruption at Mount Etna. My main contribution is the estimation of the growth rate of a peculiar microstructure present in the outermost layer, in direct contact with air, and consequently from a more undercooled portion of the lava flow, namely the final Na-rich rim characterizing the Plg microcrystals, which is often associated with a surrounding chemical boundary layer (CBL). Through detailed EPMA mapping of a representative CBL+ Plagioclase (Plg) grain, we established a steady-state model that links the formation of the chemical boundary layer surrounding the Na-rich Plg rim of the microlites to the microlite itself.

The penultimate part of the thesis (Chapter 5) focuses on outlining potential future developments in experimental petrology related to medium- to highly undercooled basaltic melts. A series of 4D in situ experiments were conducted at the SYRMEP beamline (Elettra Synchrotron, Trieste, Italy) in September 2024 to study the crystallization of Etnean magmas, specifically those with the composition of the 1669 eruption, at atmospheric pressure. Dynamic and single-drop undercooling experiments were performed using (a) a trachybasaltic glass as the starting material, or (b) a trachybasaltic glass with added olivine or clinopyroxene seeds, while employing an induction furnace and scanning the samples in 3D every 10 minutes. A preliminary, qualitative reconstruction and rendering of the 3D volumes from two experiments are presented in this thesis to highlight the potential of 4D in situ

seeded experiments. The preliminary images intuitively suggest general scientific questions that could be explored in future work, such as: 1) How do the seeds interact with the melt, and what chemical differences can be observed when comparing the crystal phases formed in seeded versus unseeded experiments? 2) Are there differences in the crystallization sequence, clustering mechanisms, and growth rates of crystal phases between the seeded and unseeded experiments? 3) Do the rheological properties differ between the two sets of experiments?

Finally, in Chapter 6 I outline the broader overall conclusions and significance of my PhD work, highlighting links between the individual chapters.

References

Arzilli F, Mancini L, Voltolini M, Cicconi MR, Mohammadi S, Giuli G, Mainprice D, Paris E, Barou F, Carroll MR (2015) Near-liquidus growth of feldspar spherulites in trachytic melts: 3D morphologies and implications in crystallization mechanisms. Lithos 216-217:93-105. doi: 10.1016/j.lithos.2014.12.003

Arzilli F, Polacci M, La Spina G, Le Gall N, Llewellin EW, Brooker RA, Torres-Orozco R, Di Genova D, Neave DA, Hartley ME, Mader HM, Giornado D, Awwood R, Lee PD, Heidelbach F, Burton MR (2022). Dendritic crystallization in hydrous basaltic magmas controls magma mobility within the Earth's crust. Nat Commun 13, 3354. Doi: 10.1038/s41467-022-30890-8

Auxerre M, Faure F, and Lequin D (2022), The effects of superheating and cooling rate on olivine growth in chondritic liquid. Meteorit Planet Sci, 57: 1474-1495. doi:10.1111/maps.13830

Bachmann O, Huber C (2016) Silicic magma reservoirs in the Earth's crust. Am Mineral 101:2377-2404. doi: 10.2138/am-2016-5675

Ballhaus C, Pakulla J, Wirth R, Roddatis V, Schreiber A, Münker C, Wombacher F, Kronz A, Fonseca ROC, Cieszynski H, Friedrich HH (2023). Quenching of basaltic melts by volatile exsolution. Contrib Mineral Petrol 178:57 doi: 10.1007/s00410-023-02041-9

Berlo K, Blundy J, Turner S, Hawkesworth C (2007). Textural and chemical variation in plagioclase phenocrysts from the 1980 eruptions of Mount St. Helens, USA. Contrib. Mineral. Petrol. 154, 291–308 (2007). doi: 10.1007/s00410-007-0194-8

Brownlee DE (1985). Cosmic dust: Collection and research. Annual Reviews of Earth and Planetary Sciences 13:147–173.

Cashman KV, Sparks RSJ, Blundy JD (2017) Vertically extensive and unstable magmatic systems: A unified view of igneous processes. Science 355:eaag3055. doi: 10.1126/science.aag3055

Colle F, Masotta M, Costa S, Mollo S, Landi P, Pontesilli A, Peres S, Mancini L (2023). Effect of undercooling on clinopyroxene crystallization in a high K basalt: Implications for magma dynamics at Stromboli volcano. Lithos, Volumes 456–457. 107327. Doi: 10.1016/j.lithos.2023.107327

Davidson JP, Morgan DJ, Charlier BLA, Harlou RJ, Hora M (2007). Microsampling and isotopic analysis of igneous rocks: Implications for the study of magmatic systems. Annu. Rev. Earth Planet. Sci. 35, 273–311 (2007). doi: 10.1146/annurev.earth.35.031306.140211

DiBenedetto M, Qin Z, and Suckale J (2020). Crystal aggregates record the pre-eruptive flow field in the volcanic conduit at Kīlauea, Hawaii: Science Advances, v. 6, p. eabd4850, https://doi .org/10.1126/sciadv.abd4850.

Dungan MA, Davidson J (2004). Partial assimilative recycling of the mafic plutonic roots of arc volcanoes: An example from the Chilean Andes. Geology 32, 773–776 (2004). doi: 10.1130/G20735.1

Ferguson MRM, Ehrig K, Meffre S (2019). Insights into magma histories through silicate-oxide crystal clusters: Linking the Hiltaba Suite intrusive rocks to the Gawler Range Volcanics, Gawler Craton, South Australia. Precambrian Res 321:103-122. doi: 10.1016/j.precamres.2018.11.015

Genge MJ, Engrand C, Gounelle M, Taylor S (2008). The classification of micrometeorites. Meteoritics & Planetary Science, 43: 497-515. https://doi.org/10.1111/j.1945-5100.2008.tb00668.x

Gordon C, Wallis D (2024). Resolving the “megacryst paradox”: Feldspar orientation relationships record crystal mobility in granites. *Geology*; 52 (9): 712–716. doi: https://doi.org/10.1130/G52045.1

Griffiths TA, Habler G, Ageeva O, Sutter C, Ferrière L, Abart R (2023). The Origin of Lattice Rotation during Dendritic Crystallization of Clinopyroxene, Journal of Petrology, Volume 64, Issue 1, January 2023, egac125, https://doi.org/10.1093/petrology/egac125

Grosfils EB, (2007). Magma reservoir failure on the terrestrial planets: Assessing the importance of gravitational loading in simple elastic models. J. Volcanol. Geotherm. Res. 166,47–75 (2007). doi: 10.1016/j.jvolgeores.2007.06.007

Habler G, Griffiths TA (2017) Crystallographic orientation relationships. In: Mineral reaction kinetics: Microstructures, textures, chemical and isotopic signatures. pp 541-585.

Hammer JE, Rutherford MJ (2002), An experimental study of the kinetics of decompression-induced crystallization in silicic melt, *J. Geophys. Res.*, 107(B1), doi:10.1029/2001JB000281.

Hammer JE, Sharp TG, Wessel P (2010) Heterogeneous nucleation and epitaxial crystal growth of magmatic minerals. Geology 38:367-370. doi: 10.1130/G30601.1

Holness MB, Vukmanovic Z, O’Driscoll B (2023) The Formation of Chromite Chains and Clusters in Igneous Rocks. J Petrol 64:1-24. doi: 10.1093/petrology/egac124

Jerram DA, Cheadle MJ, Philpotts AR (2003) Quantifying the Building Blocks of Igneous Rocks: Are Clustered Crystal Frameworks the Foundation? J Petrol 44:2033-2051. doi: 10.1093/petrology/egg069

Jones HR (1992). On the Relationship Between Isolated and Chondrule Olivine Grains in the Carbonaceous Chondrite ALHA77307. Geochimica et Cosmochimica Acta 56: 46782.

Kilgour GN, Saunders KE, Blundy J, Cashman KV, Scott BJ, Miller CA (2014). Timescales of magmatic processes at Ruapehu volcano from diffusion chronometry and their comparison to monitoring data. J. Volcanol. Geotherm. Res. 288,62–75 (2014). doi: 10.1016/j.jvolgeores.2014.09.010

Kirkpatrick RJ (1977). Nucleation and growth of plagioclase, Makaopuhi and Alae lava lakes, Kilauea Volcano, Hawaii. GSA Bull 88:78-84. doi: 10.1130/0016-7606(1977)88<78:NAGOPM>2.0.CO;2

Kirkpatrick RJ (1981). Kinetics of crystallization of igneous rocks. In Rev. Mineral., Vol. 8 (eds. A. C. Lasaga and R. J. Kirkpatrick), pp. 321–395

Lange AE, Nielsen RL, Tepley FJ, Kent AJR (2013). Diverse Sr isotope signatures preserved in mid-oceanic-ridge basalt plagioclase. Geology 41, 279-282

Lofgren GE (1983). Effect of Heterogeneous Nucleation on Basaltic Textures: A Dynamic Crystallization Study. J Petrol 24:229-255. doi: 10.1093/petrology/24.3.229

Lofgren GE (1989). Dynamic Crystallization of Chondrule Melts of Porphyritic Olivine Composition: Textures Experimental and Natural. Geochimica et Cosmochimica Acta 53: 461–70

Marsh BD (2002). On bimodal differentiation by solidification front instability in basaltic magmas: Part1.Basic mechanics. Geochim. Cosmochim. Acta 66:2211-2229

Moitra P, Gonnermann HM (2015). Effects of crystal shape- and size-modality on magma rheology. Geochem. Geophys. Geosyst., 16, 1–26, doi:10.1002/2014GC005554.

Mollo S, Iezzi G, Ventura G, Cavallo A, Scarlato P (2012). Heterogeneous nucleation mechanisms and formation of metastable phase assemblages induced by different crystalline seeds in a rapidly cooled andesitic melt. J Non Cryst Solids. 358: 1624-1628

Mollo S, and Hammer JE (2017) Dynamic crystallization in magmas. In Heinrich, W. and Abart, R., editors, Mineral Reaction Kinetics: Microstructures, Textures, Chemical and Isotopic Signatures, volume 16 of EMU Notes in Mineralogy, pages 146. European Mineralogical Union and the Mineralogical Society of Great Britain & Ireland, Twickenham.

Pasek M A, Block K, Pasek V (2012). Fulgurite morphology: a classification scheme and clues to formation. Contributions to Mineralogy and Petrology 164, 477–492. https://doi.org/10.1007/ s00410-012-0753-5

Peres S, Griffiths TA, Colle F, Iannini Lelarge S, Masotta M, Pontesilli A, Mancini L, Abart R (2024) Identifying crystal nucleation mechanisms in a synthetic trachybasalt: a multimodal approach. *Contrib Mineral Petrol* **179**, 84 (2024). https://doi.org/10.1007/s00410-024-02161-w

Philpotts AR, Shi J, Brustman CM (1998). Role of plagioclase crystal chains in the differentiation of partly crystallized basaltic magma. *Nature* **395**, 343–346 (1998). https://doi.org/10.1038/26404

Philpotts AR, Brustman CM, Shi J, Carlson WD, Denison C (1999). "Plagioclase-chain networks in slowly cooled basaltic magma" *American Mineralogist*, vol. 84, no. 11-12, 1999, pp. 1819-1829. https://doi.org/10.2138/am-1999-11-1209

Rudge JF, Holness MB, Smith GC (2008). Quantitative textural analysis of packings of elongate crystals. Contrib Mineral Petrol 156, 413-429. doi:10.1007/s00410-008-0293-1

Schwindinger KR (1999). Particle dynamics and aggregation of crystals in a magma chamber with application to Kilauea Iki olivines. J Volcanol Geotherm Res 88:209-238. doi: 10.1016/S03770273(99)00009-8

Scott ERD, Krot AN (2014). Chondrites and Their Components, Treatise on Geochemistry (Second Edition), Elsevier, 2014, Pages 65-137, ISBN 9780080983004, doi.org/10.1016/B978-0-08-095975-7.00104-2.

Sides IR, Edmonds M, Maclennan J, Swanson DA, Houghton BF (2014). Eruption style at Kīlauea Volcano in Hawai'i linked to primary melt composition. Nat. Geosci. 7, 464–469 (2014). doi: 10.1038/ngeo2140

Sutton AP, Balluffi RW (1995) Interfaces in crystalline materials. Clarendon Press

Taylor S, Lever JH, Harvey RP (2000). Numbers, types, and compositions of an unbiased collection of cosmic spherules. Meteoritics & Planetary Science 55:651–666.

Vance JA (1969) On synneusis. Contrib Mineral Petrol 24:7-29. doi: 10.1007/BF00398750

Vernon RH (2004). *A Practical Guide to Rock Microstructure*. Cambridge University Press; 2004.

Vetere F, Iezzi G, Behrens H, Holtz F, Ventura G, Misiti V, Cavallo A, Mollo S, Dietrich M (2015) Glass forming ability and crystallisation behaviour of sub-alkaline silicate melts. Earth-Sci Rev 150:25-44. doi: 10.1016/j.earscirev.2015.07.001

Vukmanovic Z, Holness MB, Monks K, (2018) The Skaergaard trough layering: sedimentation in a convecting magma chamber. Contrib Mineral Petrol 173, 43 (2018). https://doi.org/10.1007/s00410-018-1466-1

Watanabe K, Nakamura T, Morita T (2024). Reproduction Experiments of Radial Pyroxene Chondrules Using a Gas-jet Levitation System under Reduced Conditions The Astrophysical Journal, Volume 961, Number 1. doi: 10.3847/1538-4357/ad09e7

Wieser PE, Vukmanovic Z, Kilian R, Ringe E, Holness MB, Maclennan J, Edmonds E (2019). To sink, swim, twin, or nucleate: a critical appraisal of crystal aggregation processes. Geology 47: 948-952. doi:10.1130/G46660.1

Premise

All Chapter 2 is constituted by my first scientific paper as first author, which has been already published the 20th of August 2024 in the peer-reviewed journal "*Contribution to Mineralogy and Petrology*", Volume 179:84, Issue 9, with the title "Identifying crystal nucleation mechanisms in a synthetic trachybasalt: a multimodal approach. https://doi.org/10.1007/s00410-024-02161-w. The only modification is represented by figure referencing. In the thesis each figure is referenced by two numbers, the first corresponds to the chapter number, while the second corresponds to the figure number inside the specific chapter. For example, Fig 2.1 corresponds to the first figure of chapter 2, which in this chapter also corresponds to Fig.1 of Peres et al., (2024).

2. IDENTIFYING CRYSTAL NUCLEATION MECHANISMS IN A SYNTHETIC TRACHYBASALT: A MULTIMODAL APPROACH

Stefano Peres[1], Thomas A. Griffiths[1], Fabio Colle[2], Stefano Iannini Lelarge[3], Matteo Masotta[3,4], Alessio Pontesilli[5], Lucia Mancini[6], Rainer Abart[1]

Acknowledgements

We thank Ilka Wünsche for the sample's preparation, and operator F. Kiraly for the assistance to the FEG-EPMA measurements, carried out at the Department of Lithospheric Research, University of Vienna. EBSD measurements were carried out at the laboratory for field-emission scanning electron microscopy and focused ion beam applications at the Faculty of Geosciences, Geography and Astronomy at the University of Vienna (Austria). We would also like to thank Ralf Dohmen for his comments, suggestions and editing of the manuscript, Fabio Arzilli and an anonymous reviewer for all the precious comments and suggestions that helped improve the manuscript. This work was supported by the Austrian Science fund [P 33227-N to T.G].

ABSTRACT

To develop new criteria to distinguish different crystal nucleation mechanisms in silicate melts, we performed crystallization experiments using a synthetic hydrous (2 wt.% H_2O) trachybasalt and combined three-dimensional information from synchrotron X-ray computed microtomography with two-dimensional mapping of crystallographic orientation relationships (CORs) using electron backscatter diffraction. Crystallization experiments were performed at 400 MPa by cooling the melt from 1300°C to resting temperatures of 1150 and 1100 °C and maintaining isothermal conditions for 30 minutes and 8 hours. Three distinct titanomagnetite (Tmt) populations formed: 1) skeletal crystals, isolated or partially embedded in clinopyroxene (Cpx); 2) anhedral crystals, always attached to Cpx; 3) flattened needle-shaped crystals, embedded in Cpx. These morphologically different Tmt populations formed in response to one cooling event, with varying nucleation mechanisms and at different undercooling conditions. The clustered three-dimensional distribution of population 2 and 3 Tmt grains and the high proportion of Tmt-Cpx interfaces sharing CORs indicate that these Tmt grains heterogeneously nucleated on Cpx. The near-random three-dimensional distribution of (often isolated) population 1 Tmt grains, together with the low proportion of Tmt-Cpx interfaces sharing CORs, imply their isolated, possibly homogeneous nucleation, potentially followed by heterogeneous nucleation of Cpx on population 1 Tmt. Heterogeneous nucleation in slightly to moderately undercooled magmas should affect the sequence of crystallization as well as morphology and clustering of crystals, which may actively contribute to the variation of rheological parameters like viscosity. Finally, observed intra- and inter-sample variations in Tmt-Cpx COR frequencies indicate the potential for this parameter to record further petrological information.

2.1. INTRODUCTION

Recent geophysical and volcanological evidence suggests that magma chambers and, on a larger scale, volcanic plumbing systems, are constituted by melt-crystal mixtures known as crystal mushes (Bachmann and Huber, 2016; Cashman et al., 2017), defined as crystal-bearing partially molten systems in which the crystals are arranged in a framework, with melt occupying the remaining space (e.g. Marsh, 2002). Furthermore, even at higher melt proportions, magmas almost always bear some crystals, whose amount, grain size distribution, and grain shape influence magma rheology and can be modified by clustering processes (e.g. Holness et al. 2017). Therefore, in all magmatic systems, it is of primary importance to understand the interaction between crystals, in particular the formation of rigid aggregates of many individual grains, i.e. crystal clusters. Determining the mechanisms of crystal clustering is pivotal for assessing the evolution of magmatic systems and, via clusters' influence on rheology, their eruptive style.

Crystal clusters composed of relatively few grains have also been referred to as clumps, clots, and glomerocrysts (Garcia & Jacobson, 1979; Schwindinger & Anderson, 1989; Jerram and Cheadle 2000, Jerram et al., 2003). Here, we define crystal clusters as groups of grains that are joined by areas of grain and/or phase boundary (e.g. Ferguson et al., 2019), formed by crystallization within a magma, or by a disaggregation of a pre-existing crystal mush. Crystal clusters constitute one of the main building blocks from which igneous microstructures develop (Jerram et al., 2003, Holness et al., 2023) and can give information about cooling history (Bachmann et al., 2002), chemical and mechanical magma differentiation (Schwindinger 1999) as well as the physical conditions of crystallization (Hammer et al., 2010; Ellis et al., 2014; Holness et al., 2017; 2019).

Clustering of crystals during crystallization of a magma can occur by three main mechanisms: a) heterogeneous nucleation, b) synneusis and c) passive accumulation. Heterogeneous nucleation occurs when a new crystal nucleates and grows at the interface between the melt and a pre-existing substrate; this mechanism is increasingly favoured with increasing degree of undercooling (ΔT), defined as the difference between the liquidus temperature of a mineral phase (T_{liq}) and the effective temperature at which the mineral phase crystallises (Kirkpatrick, 1981). Compared to homogeneous nucleation, heterogeneous nucleation is favoured because the creation of a crystal-melt interface would be energetically more expensive than the creation of the same area of crystal-crystal interface. Heterogeneous nucleation is assumed to be the main clustering mechanism occurring in nature and during crystallization experiments (Walker et al., 1976; Lofgren 1983; Hammer 2008; Hammer et al., 2010; Mollo et al., 2012; Arzilli et al., 2015; Pontesilli et al., 2019; Arzilli et al, 2019; Colle et al., 2023). An important consequence of heterogeneous nucleation is that the appearance of a crystal phase can influence the timing and mechanism of nucleation of another phase, and consequently the order of crystallization in a rock/sample, especially in conditions far from thermodynamic equilibrium (Mollo et al., 2012). Synneusis occurs when two suspended crystals drift together and align during crystal settling or magma flow, typically attaching in preferred orientations that result in a lower interfacial energy (Vance 1969; Schwindinger 1999, Wieser et al., 2019; DiBenedetto et al. 2020; Dyck and Holness 2021). Finally, passive accumulation of crystals is the final result of settling, with the crystal arrangement determined by the combination of gravitational forces, crystal shape, and fluid dynamics (Rudge et al., 2008).

These clustering mechanisms are often inferred on the basis of microstructural observations. Perpendicular projection of elongate crystals from an interface in the direction of the melt has been invoked as evidence of heterogeneous nucleation (Kirkpatrick 1977; Hammer et al.

2010; Arzilli et al. 2015; Vetere et al. 2015, Colle et al., 2023). The offset of the true centres of clustered, concentrically zoned crystals from the mutual boundary has been invoked as evidence for synneusis (Vance 1969; Dowty 1980). Shape preferred orientation (SPO) in the form of magmatic foliation or lineation of minerals, and/or poikilitic and adcumulate microstructures are some of the microstructural evidence for accumulation processes (Holness et al., 2017, 2023, and references therein).

To date, only a limited number of studies have provided crystallographic evidence in support of their interpretation of clustering mechanism. Variable crystallographic orientation relationships (CORs, Habler and Griffiths, 2017) can be observed in crystal clusters formed either by heterogeneous nucleation (e.g. Hammer et al., 2010) or synneusis (e.g. Wieser et al., 2019; Dyck 2023; Gordon and Wallis 2024). These two clustering mechanisms differ in the degree of freedom allowed in the relationship between the lattices of the touching phases, and thus, in the characteristics of the CORs formed. During heterogeneous nucleation, the lattice of the pre-existing crystal should guide the nucleation and growth of the new phase in a highly restricted orientation, in order to minimize misfit with the newly formed lattice (Holness et al., 2023 and references therein). In synneusis, facets of already formed crystals come in contact, allowing small rotations of the lattices perpendicular to the interfaces and small deviations from exact parallelism of facets.

Regarding rocks formed by passive accumulation, CORs have never been studied. Indeed, if the accumulated crystals show no SPO or CPO (Wieser et al., 2019; Holness et al., 2023), certainly CORs are also absent. In contrast, strongly foliated or lineated cumulates may also be characterized by a CPO (e.g. Holness et al. 2017; Vukmanovic et al. 2018; Bertolett et al. 2019). Consequently, CORs might develop via passive crystal accumulation but should be both “statistical” (Habler & Griffiths, 2017) and weak, i.e. exhibit a large degree of freedom in the misorientation between touching crystals.

In this work, we combine synchrotron radiation computed microtomography (SR μCT) with Electron Backscatter Diffraction (EBSD) analysis to study heterogeneous nucleation mechanisms in a synthetic hydrous (2 wt.% H_2O) trachybasalt melt, crystallized experimentally at 4 kbar and 1100-1150 °C in a piston cylinder apparatus. The phase assemblage produced shows significant clustering and consists of abundant clinopyroxene (Cpx), with subordinate titanomagnetite (Tmt), amphibole (Amph), and vesicles (Ves). We focus on Cpx and Tmt crystals, for which heterogeneous nucleation and epitaxial growth of Tmt on Cpx was first inferred by the EBSD analysis of *Hammer et al. (2010)*. For the first time, we are able to determine the location of particular boundary segments characterized by the COR, and the full misorientation between the two lattices. By combining three-dimensional (3D) microstructural information with high resolution two-dimensional (2D) imaging and mapping of crystal orientation and compositional variations, we are able to constrain: i) the nucleation mechanisms of three different populations of Tmt and ii) the relative timing of Tmt formation compared to the appearance of Cpx crystals. We show that the combination of EBSD with 3D X-ray imaging by SR μCT allows multiple nucleation mechanisms to be distinguished for the same phase during the same cooling event, and furthermore, that multiple crystal morphologies may arise from a single cooling event.

2.2. METHODS

2.2.1. Crystallization experiments

Crystallization experiments were performed using as starting material a trachybasaltic glass, synthesized targeting the chemical composition of the Monte Maletto Formation of Mt. Etna (Italy) (Armienti et al., 1988; 2013). The starting mixture was prepared using analytical grade reagents (Masotta et al., 2020) mixed in stoichiometric proportions. The reagent mixture was put in a ceramic crucible and slowly heated to 1100 °C (for 12 hours) to allow complete

dehydration and decarbonation. In a second step, the mixture was loaded in a Pt crucible pre-saturated with Fe and left at 1600 °C for 1 hour to form a homogeneous melt, then quenched to a crystal-free glass by dropping the crucible into a tank of deionised water. A representative portion of the synthetic glass was analysed by using electron probe microanalysis (EPMA) to check for component loss and chemical homogeneity, as well as to confirm the absence of residual unmelted crystals. The synthetic glass produced had the following composition: SiO_2 = 47.00 ± 0.19 wt%, TiO_2 = 1.72 ± 0.03 wt%, Al_2O_3= 15.7 ± 0.19 wt%, FeO = 10.60 ± 0.09 wt%, MgO = 8.38 ± 0.10 wt%, CaO = 12.17 ± 0.13 wt%, Na_2O = 3.10 ± 0.06 wt%, K_2O = 1.30 ± 0.04 wt%.

The experiments were carried out in a non-end loaded piston cylinder (QUICKpress) installed at the HP-HT laboratory of Dipartimento di Scienze della Terra of the University of Pisa (Italy), using a standard 19-25 mm NaCl-pyrex-graphite-MgO assembly. The assembly materials impose oxygen fugacity conditions corresponding to 2 log units above the Ni-NiO buffer (Masotta et al., 2012). Pt capsules were loaded with the powdered starting glass and nominally 2 wt.% of deionised H_2O (added using a micro syringe), before being welded shut and eventually inspected for weight loss after heating at 110 °C in an oven. Pyrophyllite was used as supporting medium around the capsule in order to prevent H_2O loss (Freda et al., 2008). The length of the capsules (8 mm) and their position in the assembly were chosen in order to take advantage of the intrinsic temperature gradient of the graphite furnace (as determined by an earlier calibration of the temperature distribution in the furnace and previous experimental work done with the same apparatus; Masotta et al., 2013; Costa et al., 2020). The temperature gradient imposes at the top of the capsule a temperature that is about 50-60 °C lower than at the bottom, where temperature is measured with a factory calibrated C-type thermocouple (yielding a precision of ± 3°C). In each experiment, the assembly was cold pressurized to 400 MPa and heated at a rate of 80 °C/min to reach the temperature of

1300 °C. The experiment was maintained at this temperature for 30 minutes to ensure full melting of the starting glass powder and subsequent melt relaxation, before cooling (at the same rate of 80 °C/min) to the final resting temperatures (T_{rest}) of 1150 and 1100 °C. The T_{liq} of the trachybasalt with 2 to 3 wt.% H_2O was determined to be 1160 -1180°C based on PhasePlot simulations and previous experimental determination, e.g. Pontesilli et al., 2019; Masotta et al., 2020). Based on the measured length of the capsules after the experiment, we determined the following ΔT conditions: i) ΔT varying from 10 °C at the bottom of the capsule to ca. 60 °C at the top for experiments at 1150 °C, and ii) from 60 °C at the bottom of the capsule to ca. 110 °C at the top for experiments at 1100 °C. Experiments were terminated after 30 min or 8 hours by turning off the power supply and maintaining the pressure constant during the quench (100 °C/s). Although some experiments were also performed at shorter run durations (dwell time), we discuss the results of three experiments conducted at the following conditions: a) T_{rest} = 1150 °C and 30 minutes dwell time (abbreviated 1150w-30min), b) T_{rest} = 1100 °C and 30 minutes dwell time (abbreviated 1100w-30min), c) T_{rest} = 1100°C and 8 hours dwell time (abbreviated 1100w-8h). Sample 1150w-30min was measured by SR µCT only. Unfortunately, during sample preparation for the 2D analysis sample 1150w-30min was lost, preventing further chemical and microstructural analysis. Sample 1100w-30min was analysed through EPMA and EBSD, while sample 1100w-8h was analysed by all the techniques described in this work.

2.2.2. Synchrotron radiation computed microtomography (SR µCT) imaging

Experimental samples 1150w-30min and 1100w-8h were removed from the Pt capsule. The two resulting cylindrical samples (up to 2.5 mm in diameter and 4 mm high) were measured by SR-µCT at the SYRMEP beamline (Zandomeneghi et al., 2010) of the Elettra synchrotron facility in Basovizza (Trieste, Italy), using a filtered polychromatic X-ray beam (filters = 1.5 mm Si plus 1 mm Al corresponding to a mean X-ray beam energy of ≈ 27 keV). In order to

enhance the visualization of the Cpx phase and accurately determine the morphology of Tmt crystals, we worked in propagation-based phase contrast mode (Polacci et al., 2010). The detector used was a 16-bit, water-cooled, sCMOS macroscope camera (Hamamatsu C11440-22C) with a 2048 × 2048 pixel chip coupled, through a high numerical aperture optics, to a 17 µm-thick GGG:Eu scintillator screen. Scans were acquired setting a sample-to-detector distance of 175 mm. The scans of the whole samples were acquired in local area mode, scanning separately the upper and lower part of the sample with an effective pixel size of the camera set at 0.9 µm (corresponding to a field of view of approx. 1.8 mm x 1.8 mm). For each scan 1800 radiographs (projections) of the sample over a total rotation angle of 180° were acquired with an exposure time per projection of 1.2 s. The SYRMEP Tomo Project (STP) software suite (Brun et al., 2015) was used to reconstruct the imaged virtual volumes. In order to maximize the quality of the reconstruction and optimize the visibility of the different phases of interest, a single-distance phase retrieval algorithm (Paganin et al., 2002) was applied to projections prior to tomographic reconstruction setting the delta/beta parameter (ratio between the real and imaginary parts of the X-ray refraction index of the material) to 17. The STP software was used also for ring artefact correction.

2.2.3. EPMA

Cpx, Tmt, Amph and glass major element analyses and chemical maps were performed at the Department of Lithospheric Research of the University of Vienna, Austria, using a CAMECA SXFiveFE EPMA equipped with five wavelength dispersive spectrometers and one energy-dispersive X-ray spectrometer (EDX). All four phases were analysed at 15 kV accelerating voltage and beam current of 20 nA. A beam diameter of 1 µm was used for Cpx, Amph and Tmt spot analysis, while a diameter of 5 µm was used for the glass analysis. Peak counting times varied for each element: Na = 10 s; Si = 14 s, Al = 10 s; Fe = 22 s; K = 10 s; Ca = 20 s; Mg = 20 s; Ti = 15 s; Mn = 24 s. Detection limits were: 100-250 ppm for Al, Na, Mn, and Ti;

300-500 ppm for Si, Fe, Mg, Ca and K. Element distribution maps were acquired in beam scan mode, with a 35.5 nA beam current and 15 kV accelerating voltage. Map size varied depending on the investigated microstructure, while a fixed step size of 0.33 µm and a dwell time per pixel of 80 ms was applied. Relative Mg, Fe, Ca, Na, and Ti concentrations were mapped using five wavelength dispersive spectrometers set to the corresponding Kα emission wavelengths for each element, while Si and Al concentrations were acquired through EDX. Inside chemical maps, point analyses were acquired and the peak intensity of each element mapped calibrated with the respective quantitative concentration using the *Fiji* software (Schindelin et al., 2012).

2.2.4. Electron backscatter diffraction (EBSD) measurements

In order to determine the crystallographic orientations of the crystals in representative areas and specific spots of interest on samples, EBSD scans were collected using a FEI Quanta 3D FEG-scanning electron microscope (SEM) equipped with an EDAX Digiview 5 EBSD camera (elevation angle 5°), located at the laboratory for field-emission scanning electron microscopy and focused ion beam applications at the Faculty of Geosciences, Geography and Astronomy, University of Vienna (Austria). The OIM Data Collection v7.3.1 software was used for EBSD data acquisition, and OIM Analysis 8.0 for re-indexing. Beam conditions for all EBSD scans were 15 kV accelerating voltage and spot size 1.0 (~ 4 nA probe current), with a 1 mm SEM aperture, a working distance of 14 mm and a beam incidence angle of 20°. All scans used an EBSD camera binning of 8 x 8 pixels, a binned pattern size for Hough transforms of 140 pixels, a Hough θ step size of 1° and a 9 x 9 convolution mask. Step sizes ranged from 320 nm to 650 nm, always on a hexagonal grid. Tmt was indexed as face-centred cubic, Cpx was indexed as monoclinic (b-setting), using the lattice parameters a = 9.585 Å, b = 8.776 Å, c = 5.26 Å, and β = 106.85°, and Amph was indexed as monoclinic (b-setting) using the lattice parameters a = 9.871 Å, b = 18.028 Å, c = 5.307 Å, and β = 105.24°. After

standardizing confidence index values to the highest for each reconstructed grain using OIM Analysis 8.0, the Matlab toolbox MTEX version 5.6.1 (Bachmann et al. 2010; Hielscher et al. 2010) was used for data processing and plotting. Pixels with confidence index values below 0.1 were classified as not indexed. Grains were then calculated using a misorientation angle threshold of 15°. EBSD pixels belonging to grains less than 4 pixels in size were removed before recalculating grains with the same misorientation angle threshold to obtain the final datasets used for analysis. Finally, six iterations of smoothing were applied to the boundary traces using the smooth () function of MTEX. This does not alter the misorientation at boundary segments.

2.2.5. Image processing and analysis

The processing of 2D images acquired through optical microscopy or EPMA chemical mapping has been performed through the *Fiji* open source software (Schindelin, et al., 2012). Each image obtained was transformed to grey levels (0 is black and 255 is white) and scaled. A 2D median filter was used to remove noise.

The SR-µCT reconstructed volumes were processed with the Dragonfly software (version 2020.2 ORS, Canada; non-commercial license for academic use). A 3D median filter has been firstly applied and then the Wizard tool, which uses a combination of random forest and neural network algorithms to create trainable models capable of segmenting the Cpx, Tmt and vesicles. In the analytical work we focussed on the Tmt crystals. More specifically we separated crystals with different morphologies into three populations using a semi-automatic segmentation, as detailed in chapter "Titanomagnetite clustering parameters". A single VOI (volumes of interest) of a significant portion of the samples with size 1100x1100x1840 μm^3 and 1090x1090x1440 μm^3 for sample 1150w-30min and 1100w-8h respectively (as been shown in Fig.2.1a and Fig.2.1d) has been selected to give an overview of the general features of both samples. To increase the representativeness of different regions of each analysed

volume, we selected 4 different VOIs for sample with size of 600x600x600 μm^3 (sample 1100w-8h) and 3 different VOIs with size 500x500x500 μm^3 (sample 1150w-30min). For a meaningful description of the VOI all segmented Tmt crystal with size < 8 μm^3 have not been excluded from the quantitative analysis. We also used Dragonfly for 3D visualization of reconstructed and processed images through volume rendering procedures (see Figs. 2.1-2.3). The segmented volumes were analysed to extract the following parameters for the Tmt crystals: volume size, spatial distribution of the centroids (defined as the arithmetic mean position of all the points in the volume of a geometric figure) and Feret diameters (defined as the distance between the two parallel planes restricting the object perpendicular to that direction)

2.3. RESULTS

2.3.1. Microstructural features

We describe the microstructural features of the three experiments dividing each experiment in three regions, corresponding to the parts of the capsule at different temperature conditions: i) the bottom part, corresponding to the region at higher temperature and minimum ΔT, ii) the middle part, corresponding to the region at intermediate temperature and ΔT, and iii) the top part, corresponding to the region at lower temperature and maximum ΔT.

The (hotter) bottom part of experiment 1150w-30min, where ΔT conditions of approximately 10 °C are created, is characterized by equant and large (>100 μm) well-faceted skeletal crystals of Tmt (Fig. 2.1a and c). Moving towards the intermediate part of the capsule, the crystallinity increases, due to the appearance of relatively large (>500 μm) faceted skeletal crystals of Cpx (Fig. 2.1b). Tmt and Cpx crystals are very frequently observed in contact, with Tmt occurring preferentially at the outer surface of Cpx crystals (Fig.2.1c) but also, to a

lesser extent, internally between individual crystal branches. In the (colder) upper part of the capsule, characterized by ΔT of ca. 60 °C, the crystallinity increases further and both Cpx and Tmt crystals generally decrease in size (> 400 μm and 50 μm, respectively), although showing crystal morphologies similar to those observed in the middle part of the capsule (Fig.2.1b).

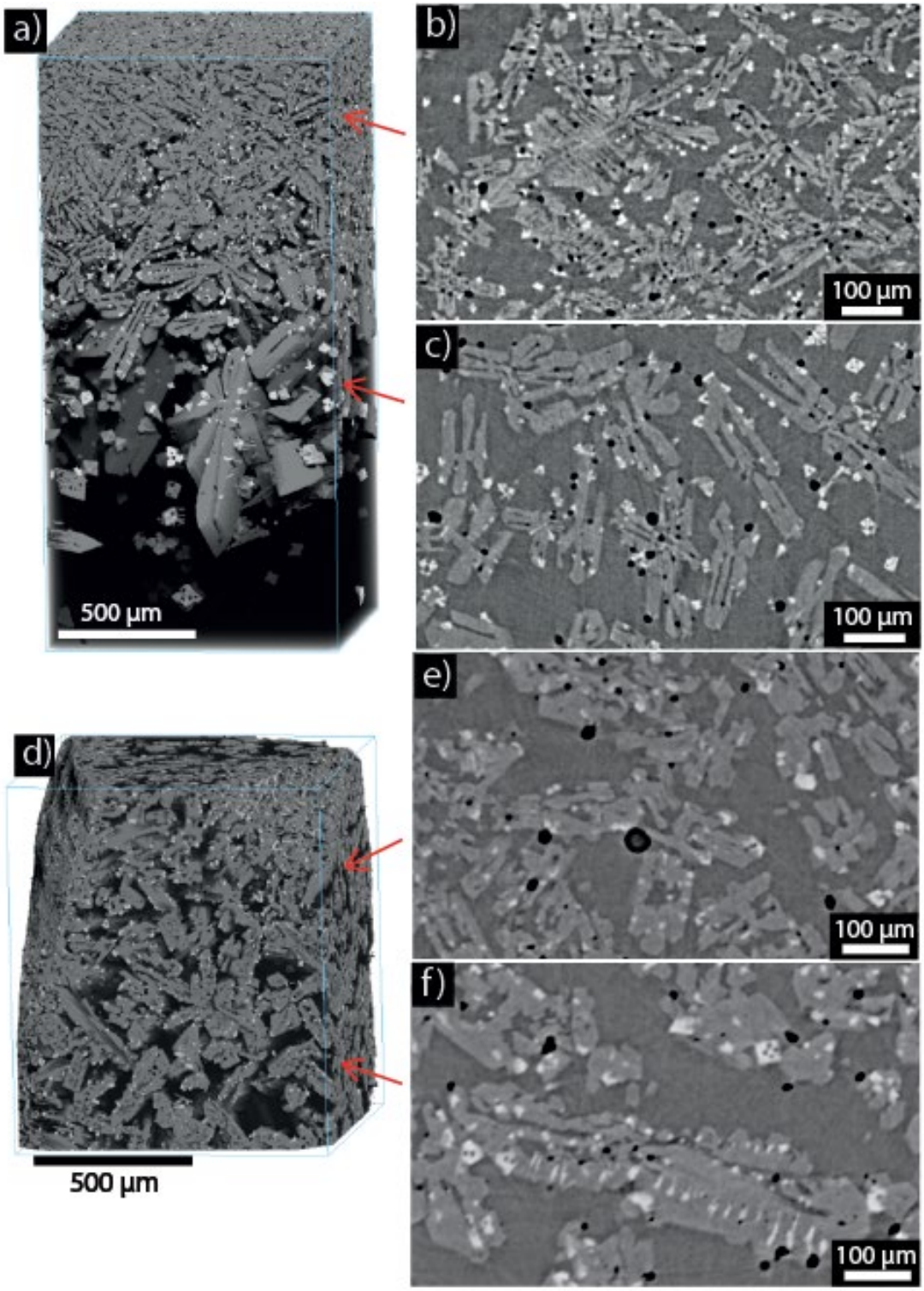

Fig. 2.1 a) and d) volume rendering of representative VOIs in the experimental samples 1150w-30min (VOI size: 1100x1100x1840 µm) and 1100w-8h (VOI size: 1090x1090x1440 µm) respectively. Voxel size is 0.9 µm. Cpx grains are grey; Tmt grains are light grey; Vesicles are dark grey; glass is translucent. Figs. 2b and c are reconstructed slices after image processing from the top and central portions of sample 1150w-30min, respectively. Figs. 2e and f are reconstructed slices after image processing from the top and bottom portions of sample 1100w-8h, respectively

The two experiments performed at 1100 °C (1100w-30min (Supplementary Figure S1) and 1100w-8h, Fig.2.1d) produced comparable microstructures: the (hotter) bottom portions of

each experiment (Fig. 1f and Supplementary Figure S1c), where ΔT = 60 °C, are characterized by large skeletal Cpx crystals up to 800 µm in size and large skeletal Tmt grains up to 285 µm. The Cpx crystals in the 8h sample are more euhedral compared to the 30 min experiments. The 1100°C samples also show a slight, but less dramatic, increase in crystallinity from the (hotter) bottom to the (colder) top portion of the sample. The (colder) top parts of these samples, where ΔT is ca. 110 °C, are characterized by higher number of smaller (100-300 µm), more dendritic Cpx and smaller anhedral Tmt (<50 µm), always in contact with Cpx grains (Fig. 1e and Supplementary Figure S1d).

2.3.2. Titanomagnetite populations

Image analysis from synchrotron radiation µCT scans allowed a precise and complete reconstruction of Tmt crystals in samples 1150w-30min and 1100w-8h in 3D. In spite of the different experimental conditions, three populations of Tmt can be distinguished in all samples, based on the dominant crystal habit and microstructural relationship with Cpx:

Population 1 (Skeletal, isolated or not completely embedded in Cpx)

Population 1 crystals have skeletal habitus with well-defined external facets, characterized by six skeletal branches disposed in an octahedral arrangement. Skeletal Tmt crystals are mostly equidimensional (Fig.2.2a-b) and can reach sizes up to 285 µm (maximum Feret diameter calculated by Dragonfly software). They are larger than the Tmt grains of the other populations at the same location in each capsule. When Tmt crystals of population 1 touch Cpx grains the complete six-branched skeletal Tmt morphology preserved even when partially or fully embedded inside a Cpx. However, in some cases the central portions of population 1 Tmt grains are in contact with a Cpx, and they show the formation of just 4 or 5

of the crystal branches, lacking the branch (or branches) that should extend in the direction of the touching Cpx crystal.

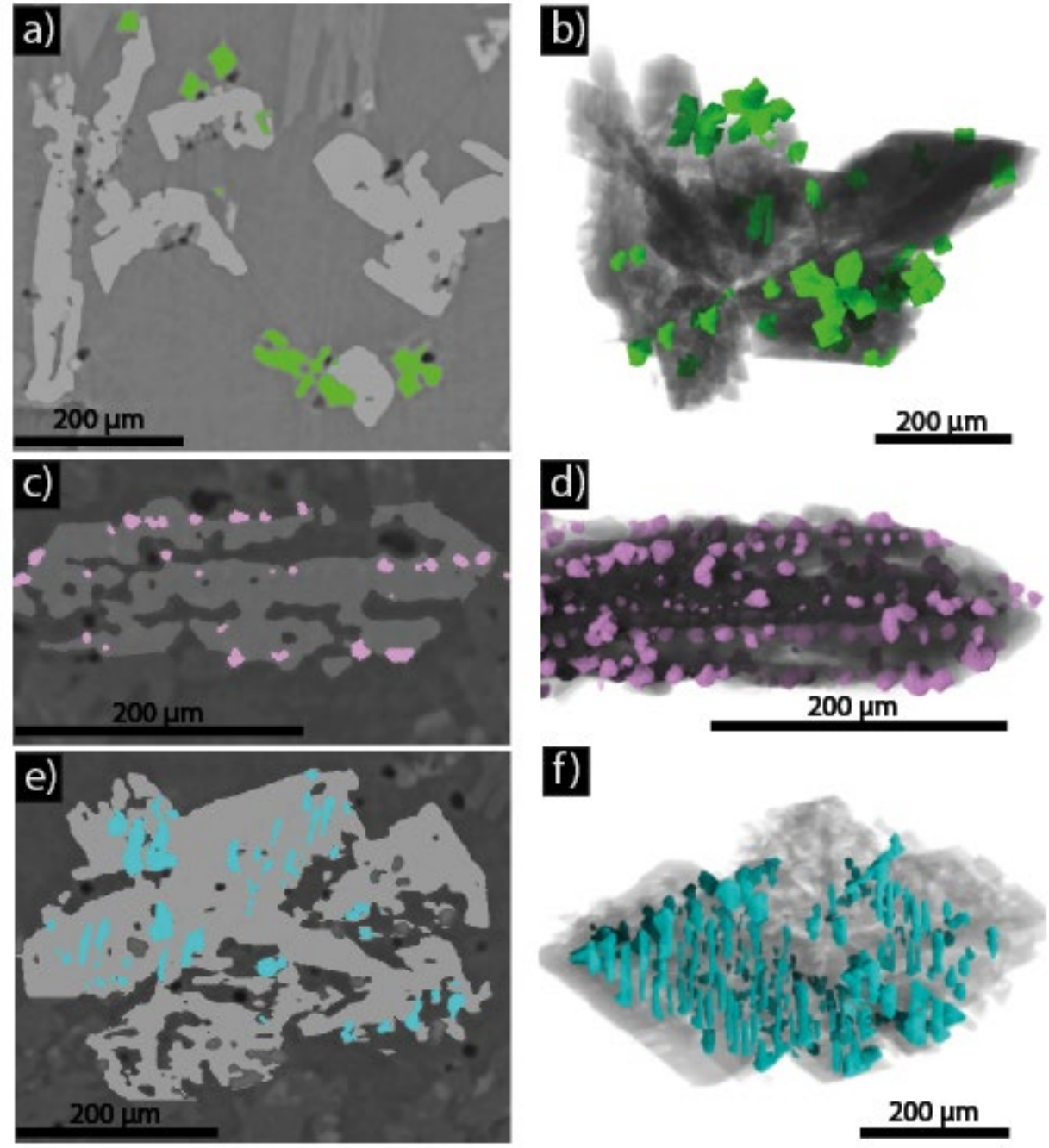

Fig.2.2 Three different Tmt populations found in all three experimental runs; in the left column are the reconstructed slices after image processing of Cpx (grey) and Tmt (coloured); in the right column are the 3D rendering pictures of the Tmt grains of the three different populations in the proximity or in contact to the nearest Cpx crystal. a-b) the green skeletal grains represent Tmt of population 1 (rendered VOI size: 600x600x315 µm); c-d) the pink anhedral grains represent Tmt of population 2 (rendered VOI size: 300x200x150 µm); e-f) the cyan elongated grains represent Tmt of population 3 (rendered VOI size: 450x700x350 µm). Voxel size is 0.9 µm

Population 2 (Anhedral, attached to Cpx)

Anhedral Tmt crystals of this population are the most abundant in terms of number and total volume, in all three samples (Fig.2.2c-d). The size of the crystals comprising this population varies between 2 μm and 100 μm, and they typically represent the smallest Tmt grains at a given position in each capsule. It is worth noting that all Tmt grains of this population are in contact with a Cpx crystal, without being completely embedded. The small, anhedral crystals usually decorate the edges and the tips of larger Cpx crystals, sharing with Cpx a planar or an irregular/rounded interface. In the less-undercooled/hotter portion of the samples, population 2 Tmt grains can also develop a skeletal, externally faceted shape in the direction of the melt outside the Cpx (Fig.2.4a-c). Regular spacing in the range between 10 μm and 30 μm is observed between neighbouring population 2 Tmt grains residing on the same Cpx crystal (Fig.2.2c-d, Fig.2.4a-c). A subtype of this population can be identified in samples 1100w-30min and 1150w-30min. These grains are characterized by an elongated shape with max size up to 100 μm, but they are not embedded in the Cpx crystal and, similar to other Tmt grains of population 2, they radiate from the edges or from the exact centre of a dendritic Cpx crystal.

Population 3 (Flattened needle-shaped crystals, embedded in Cpx)

Flattened needle-shaped Tmt crystals of population 3 are characterized by a high aspect ratio, where the longest dimension (maximum Feret diameter) can reach up to 120 μm, whereas the other two dimensions are in the range between 10 and 50 μm (mean Feret diameter) and 2 and 30 μm (minimum Feret diameter) (Fig.2.3e-f). These flattened needle-shaped crystals are almost completely embedded in Cpx, but they almost always show a melt/Tmt interface at the needle tip. Similar to Tmt population 2, Tmt population 3 also show regular spacing of neighbouring crystals in the range between 5 and 30 μm (Fig.2.2e-f, Fig.2.4d-f).

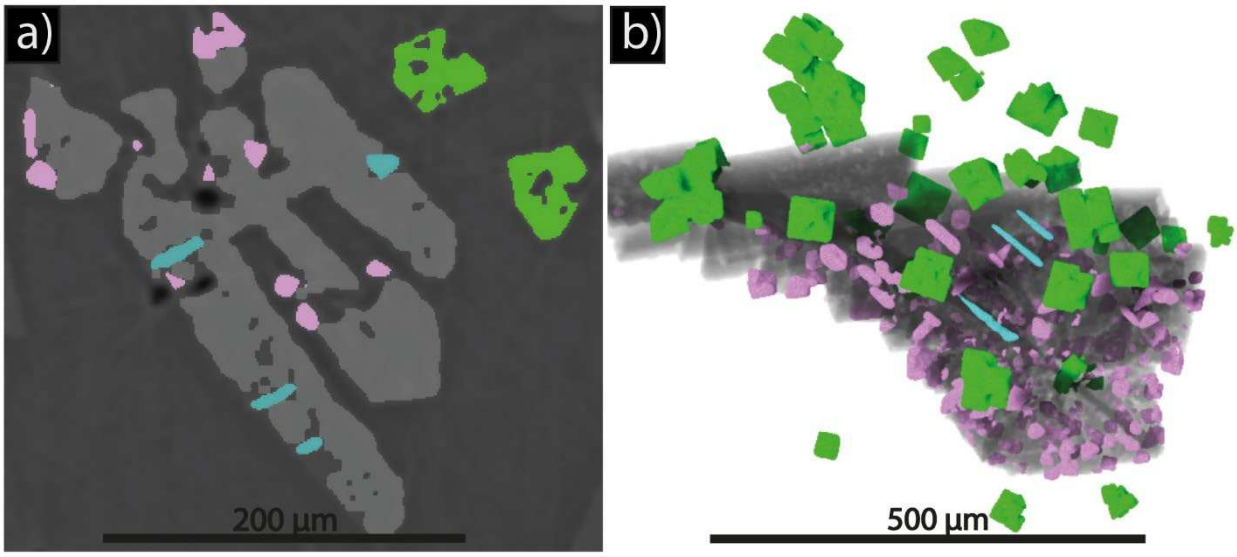

Fig.2.3 a) reconstructed slice after image processing of Cpx (grey) and Tmt (coloured); b) 3D rendering of all three different Tmt populations (coloured grains) found next or attached to a single Cpx crystal (light grey) in experimental sample 1100w-8h. (rendered VOI size: 550x540x600 µm). Voxel size is 0.9 µm

2.3.3. Clinopyroxene and Titanomagnetite chemistry

BSE images and EPMA data (Fig.2.4a,d) show that most Cpx crystals in the two samples are characterized by dendritic zoning, comprising two chemically distinct domains: 1) an Al_2O_3- and TiO_2-rich domain (brighter portions of Cpx in BSE [Fig.2.4a,d] and TiO_2 elemental maps [Fig.2.4b,e]) and 2) a SiO_2- and MgO-rich domain (darker portions of Cpx in BSE [Fig.2.4a,e], or brighter portions in the MgO elemental map [Fig.2.4c,f]). In sample 1100w-30min, the SiO_2+MgO rich zones are only a few µm thick, comprising thin infillings between bright branches or thin outer rims on Cpx. In sample 1100w-8h, the Cpx crystals are generally larger and the zoning is more pronounced, with SiO_2+MgO rich portions volumetrically more abundant and wider, reaching a few tens of µm in width. The average compositions of the different zones are reported for the different samples in table 1.

Spot analyses of single Tmt grains yields oxide compositions from 7.9 wt% to 11.6 wt% MgO, from 8.1 wt% to 12.5 wt% Al_2O_3, from 2.7 wt% to 4.4 wt% TiO_2 and from 64.5 wt% to 71.5 wt% FeO (Supplementary table, “Titanomagnetite” sheet). Cation per formula unit (cation sum = 3) and end member conversion (based on charge balance) was carried out using

the application End Member Generator_8.0 (Ferracutti et al., 2015). In all the Tmt crystals, recalculated Fe^{3+} cations per formula unit range between 1.30 and 1.45, while Fe^{2+} is between 0.50 and 0.71. In terms of mole proportions of spinel endmembers, magnetite and Mg-Ferrite endmembers each constitute (in almost equal amounts) between 28 mol% and 48 mol%, while spinel and hercynite endmembers constitute between 7 mol% and 15 mol%. The mole percentage of Ulvospinel endmember is between 1.6 and 3.0 mol%. No significant difference in composition could be determined between Tmt populations 1 and 2. EPMA chemical maps of population 3 show a clear compositional gradient of increasing TiO_2 along the crystal long axis. The TiO_2 content is lower in the portion of Tmt crystals adjacent to the central Al+Ti rich domains of Cpx, and increases towards the outer Si+Mg rich portion of the Cpx crystal. The result is a chemical gradient within Tmt with a similar orientation but opposite in direction compared to the one present in Cpx crystals. In the calibrated map from sample 1100w-8h ("EPMA Maps Calibration", Supplementary Figure S2 to S6) the inner portions of population 3 Tmt crystals record the lowest amount of TiO_2 = 2.4 wt%, reaching values of TiO_2 = 3.4 wt% in the outermost portion of the Tmt. This TiO_2 is similar to the average TiO_2 contents measured in of population 2 crystals in the sample.

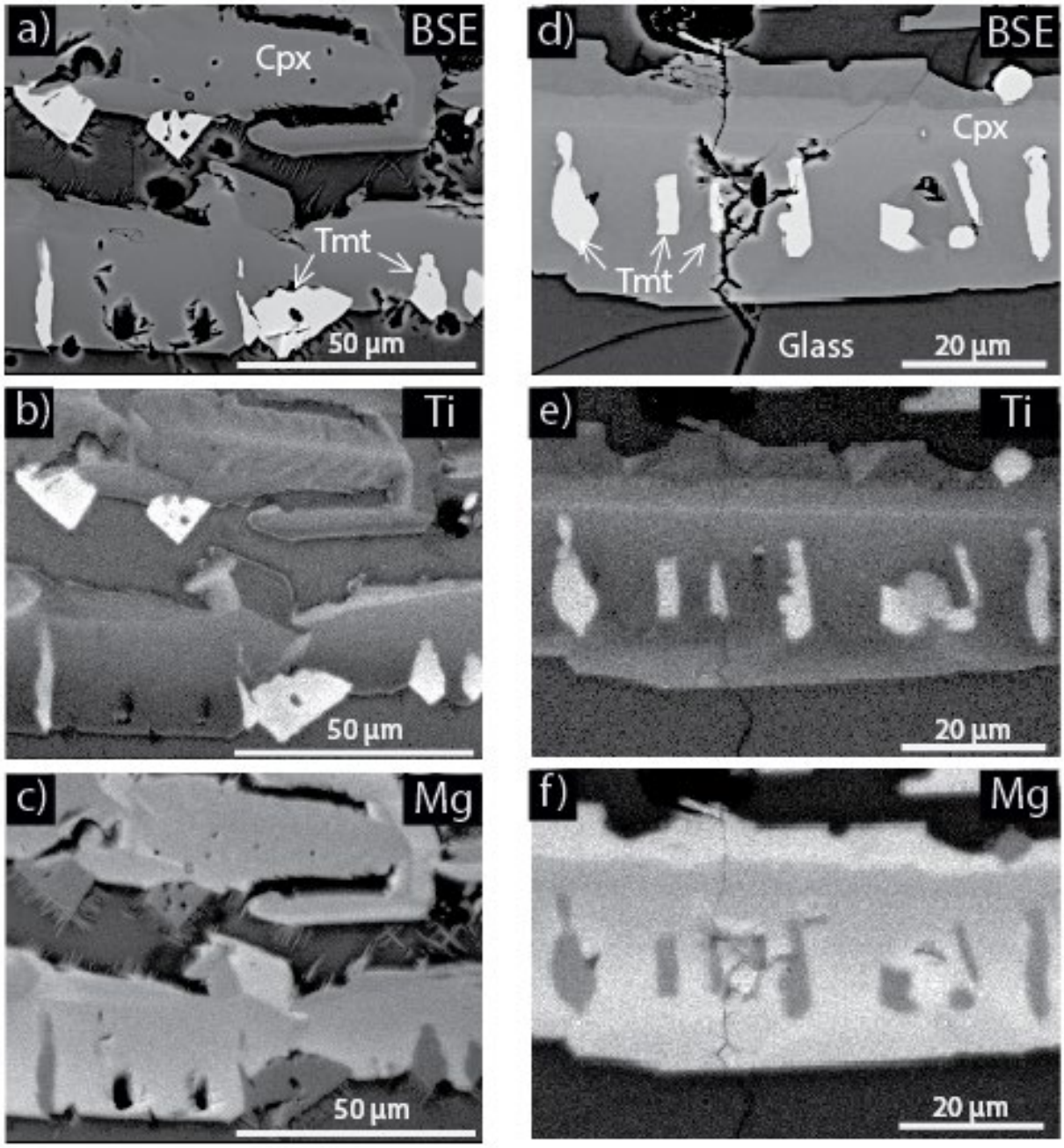

Fig.2.4 a and d) BSE image of a Cpx showing the typical dendritic sector zoning in sample 1100w-30min and 1100w-8h respectively. b-e and c-f) EPMA microchemical map of the same Cpx crystal showing the relative concentrations of Ti and Mg (c). The grey scale in the image is proportional to the Ti and Mg concentration (black = low, white = high)

2.3.4. Titanomagnetite clustering parameters

We analysed the distribution of Tmt crystal centroids in the 3D domain for samples 1150w-30min and 1100w-8h to verify the presence of periodicities in the distances between adjacent Tmt crystals. Sample 1100w-30min will not be considered since we do not have a 3D scan of the sample and the 2D analysis of the Tmt centroid distribution is not directly comparable to 3D analysis due to cutting effects. The Spatial Point Patterns of Tmt crystal centroids (i.e. the spatial position of only the centroids of the Tmt grains in a volume of interest, abbreviated SPP) in representative volumes of interest (VOIs) reveal whether this phase is statistically clustered, dispersed, or randomly distributed inside the VOI. The main clustering parameter used in this work is the pair correlation function (or radial distribution function) g(r) (abbreviated pcf from now on), defined by Ripley (1976, 1977) as

$$g(r) = \frac{1}{2\pi r}\frac{dK(r)}{dr} \qquad (1) \qquad \text{where} \quad K(r) = \frac{E}{\lambda} \qquad (2)$$

where E is the number of extra points within radius r of a randomly chosen point, λ is the intensity (points per unit volume), and r is the interpoint distance. g(r) is the probability density function for interpoint distances r, where g(r) = 1 represents complete spatial randomness of a SPP. If g(r) > 1 at a certain r, then that interpoint distance occurs more frequently than expected for a completely random distribution, indicating clustering (Rudge et al., 2008). Likewise, if g(r) < 1, that interpoint distance is less frequent than expected for a complete random distribution, indicating ordering. The greater the divergence of g(r) from 1, the stronger the divergence from a random distribution. The pair correlation function has been analysed using the "pcf" function present in the package spatstat (v1.64-1; Baddeley et al., 2015) available for *R* software (R Core Team, 2020). g(r) function have been calculated considering both translation and Ripley isotropic edge correction (Stoyan and Stoyan [1994]);

"trans" and "iso" respectively, in Sup2, "pcf" sheet). The results were similar and we decided to show in the relative graphs only g(r) calculated with Ripley isotropic edge correction.

Pcf values from sample 1150w-30min and 1100w-8h show that for the complete Tmt population, Tmt centroids are overall clustered for interpoint distances between 10 μm and 200 μm, with a peak at interpoint distances between 20 μm and 24 μm reaching a value of g(r) = 1.4. At interpoint distances greater than 100 μm the spatial disposition of centroids shows weak ordering (g(r) <1) or randomness g(r) = 1.

Tmt grains in tomographic data were sorted into three different populations, as defined above, using the Dragonfly software. From now on we use Pop1, Pop2 and Pop3 when referring to the different Tmt populations. First, all Tmt crystals completely surrounded by glass with a volume > 16.2 μm^3 (manually optimised minimum size threshold) were automatically assigned to Pop1 (100% automatic assignment). Tmt grains that touch or are embedded within Cpx but show a similar fully formed skeletal morphology to isolated Tmt crystals, were manually assigned to Pop1 as well (100% manual assignment). Subsequently, highly elongated grains almost completely embedded within Cpx, typically arranged in regular arrays were assigned to Pop3. For each Cpx in a volume, Tmt grains touching the Cpx that showed a high aspect ratio (identified by low sphericity) and specific 3D orientation (sharing a common value of the theta angle parameter that describes the elongation direction of the crystal) were initially automatically assigned to Pop3. This was followed by a visual inspection to manually remove/add specific misclassified grains from/to Pop3 (~50% of the final total of Pop3 grains were manually assigned). Finally, all grains not assigned to Pop1 or Pop3 were then automatically assigned to Pop2 (i.e. anhedral Tmt grains in touch with Cpx).

After segmentation and the sorting of Tmt into the three different populations, we extracted the shape parameters and centroid position of all Tmt grains in the two samples, to evaluate

the spatial distribution of the 3D point patterns for each population (Fig.2.5). We defined 3 VOIs of 500 x 500 x 500µm for sample 1150w-30min and 4 VOIs of 600 x 600 x 600 µm for sample 1100w-8h. Comparing the g(r) functions of the SPPs of the different populations reveals significant differences in the spatial distribution of Tmt Pop1 compared to Pop2 and Pop3. The Pop1 pcf (Fig.2.5a-b) show unclear, weakly clustered patterns in the range between 20 µm and 300 µm with peak values of $g(r) < 1.3$ in the VOIs of both samples, with the exception of the VOI sampling the colder portion of sample 1150w-30min (green line in Fig.2.5, right column). This VOI is characterized by a higher number of small Tmt crystals, completely isolated in the regions of interstitial glass between Cpx crystals, resulting in a $g(r) > 4$ at interpoint distances between 0 and 50 µm. Pop2 and Pop3 (Fig.2.5c-e) instead show clustering between 15 µm and ~ 100 µm and a peak of clustering at interpoint distances between 20 µm to 30 µm (g(r) between 1.1 and 3, and > 1.5 for all but one VOI).

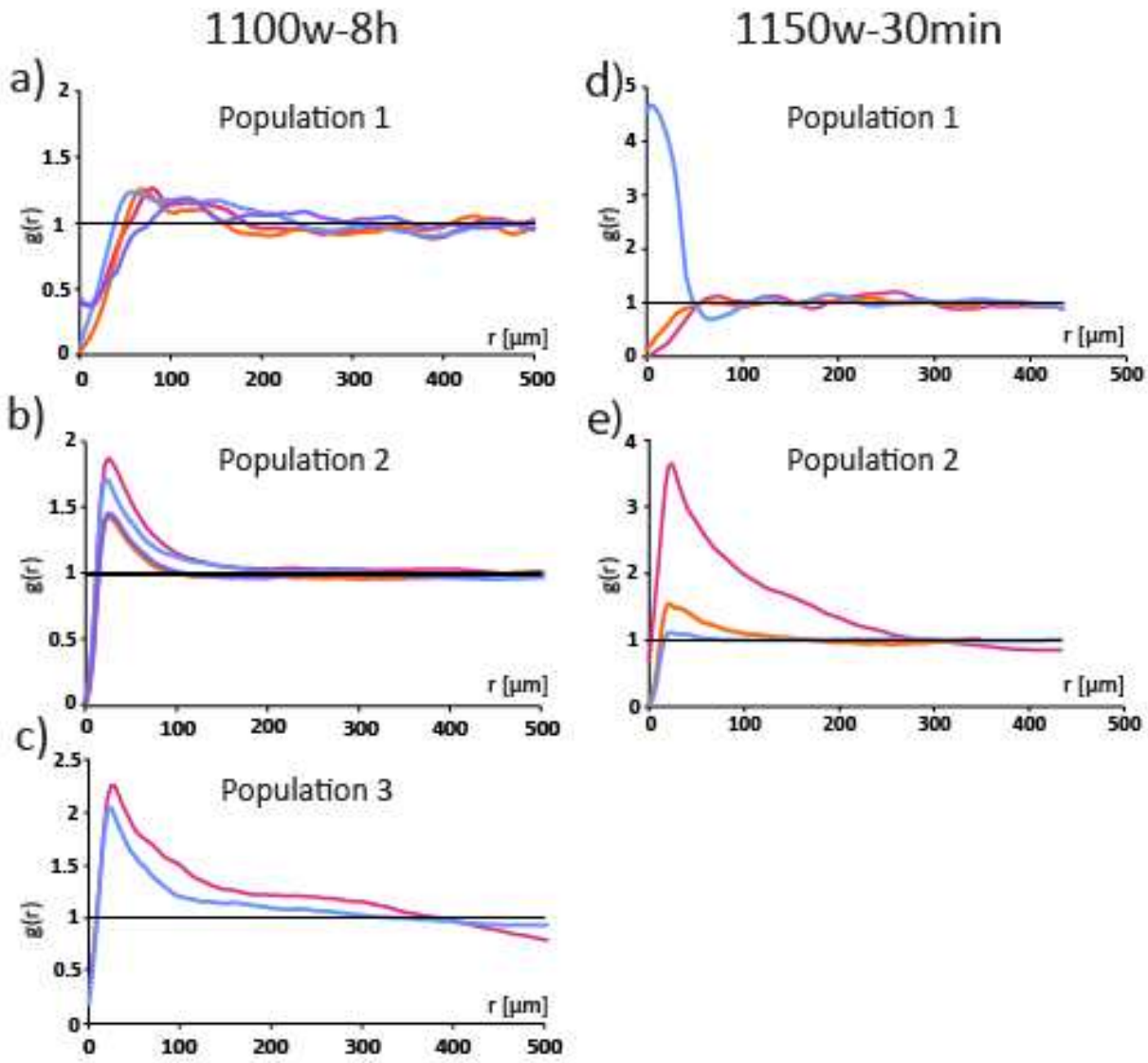

Fig.2.5 Pair correlation function (pcf) patterns for the VOIs from sample 1100w-8h (left column) and for sample 1150w-30min (right column) for the different Tmt populations. Multiple lines in each plot each display the result for a different VOI in the sample. Not all populations were present in all VOIs. In sample 1150w-30 min it was not possible to correctly measure pcf value of Tmt pop 3 because they are not frequent enough to perform the calculations. Magenta lines correspond to VOIs from the hotter (ΔT≈10°-20° and ΔT≈60°) portion of the respective samples, Orange and light blue correspond to VOI in the central (ΔT≈30°-40° and ΔT≈70°) and central-colder (ΔT≈50°-60° and ΔT≈70°-90° respectively) portions of the respective samples, purple corresponds to a VOI in the colder portion of sample 1100w-8h (ΔT≈90°-110°)

2.3.5. EBSD results

Multiple EBSD scans were acquired on samples 1100w-30min and 1100w-8h. Using MTEX, we obtained the crystallographic misorientation across each reconstructed boundary segment shared between Cpx and Tmt. CORs were visualized by plotting the distribution of Tmt orientations with respect to the Cpx lattice for all Tmt-Cpx boundary segments. The resulting pole figures (Fig.2.6) show a rotational statistical COR (Habler & Griffiths 2017). There are clear maxima corresponding to a specific COR, but also a limited degree of clockwise

rotation of Tmt about $[010]_{Cpx}$, leading to a leftward skew of the pole figure maxima that lie in the Cpx (010) plane.

Two Tmt-Cpx CORs are well-known, albeit from Tmt inclusions in Cpx crystals (Fleet et al., 1980; Feinberg et al., 2004; Ageeva et al., 2017): COR 1 ($[-110]_{Tmt} \parallel [010]_{Cpx}$, $[111]_{Tmt} \parallel (100)^*_{Cpx}$, $[-1-12]_{Tmt} \parallel [001]_{Cpx}$) and COR 2 ($[-110]_{Tmt} \parallel [010]_{Cpx}$, $[-1-11]_{Tmt} \parallel (-101)^*_{Cpx}$, $[112]_{Tmt} \parallel [101]_{Cpx}$). Like the COR observed here and the results of Hammer et al. (2010), both feature one Tmt <110> direction parallel to $[010]_{Cpx}$. COR 1 is related to COR 2 by a 4.3° clockwise rotation of Tmt about $[010]_{Cpx}$. Comparing the theoretical misorientations of CORs 1 and 2 to the misorientation distribution in our samples, we find that the misorientation peak in both samples is identical (<0.1° difference), and differs from the ideal COR 2 by 1.2° (anticlockwise rotation of Tmt about $[010]_{Cpx}$). We thus designate this commonest Tmt-Cpx boundary misorientation as COR 2*. The ideal COR 1 corresponds to the maximum extent of the clockwise-skewed orientation distribution, i.e., most Tmt-Cpx boundaries have a misorientation lying between COR 2* and COR 1 (with a maximum at COR 2*). The misorientation between COR 2* and COR 1 is 5.5°.

We classified all Tmt-Cpx boundary segments into one of four categories (Fig.2.7): 1) boundary segments with misorientations close to COR 2* (2.7° tolerance); 2) boundary segments with misorientations close to COR 1 (2.7° tolerance); 3) boundary segments not within 2.7° tolerance of COR 1 or COR 2*, but still with a misorientation < 6° from the midpoint between COR 1 and COR 2*; and 4) all remaining boundary segments. We then calculated the cumulative boundary length for each category and divided this by the total Tmt-Cpx boundary length, to obtain the boundary length fraction (BLF) belonging to each category, expressed as a percentage, abbreviated below for the four categories as BLF_{COR1}, BLF_{COR2}, $BLF_{nearCOR}$, and BLF_{noCOR}, respectively. We also calculated the total fraction of boundaries belonging to or adjacent to any COR, BLF_{anyCOR}, as 100% - BLF_{noCOR}.

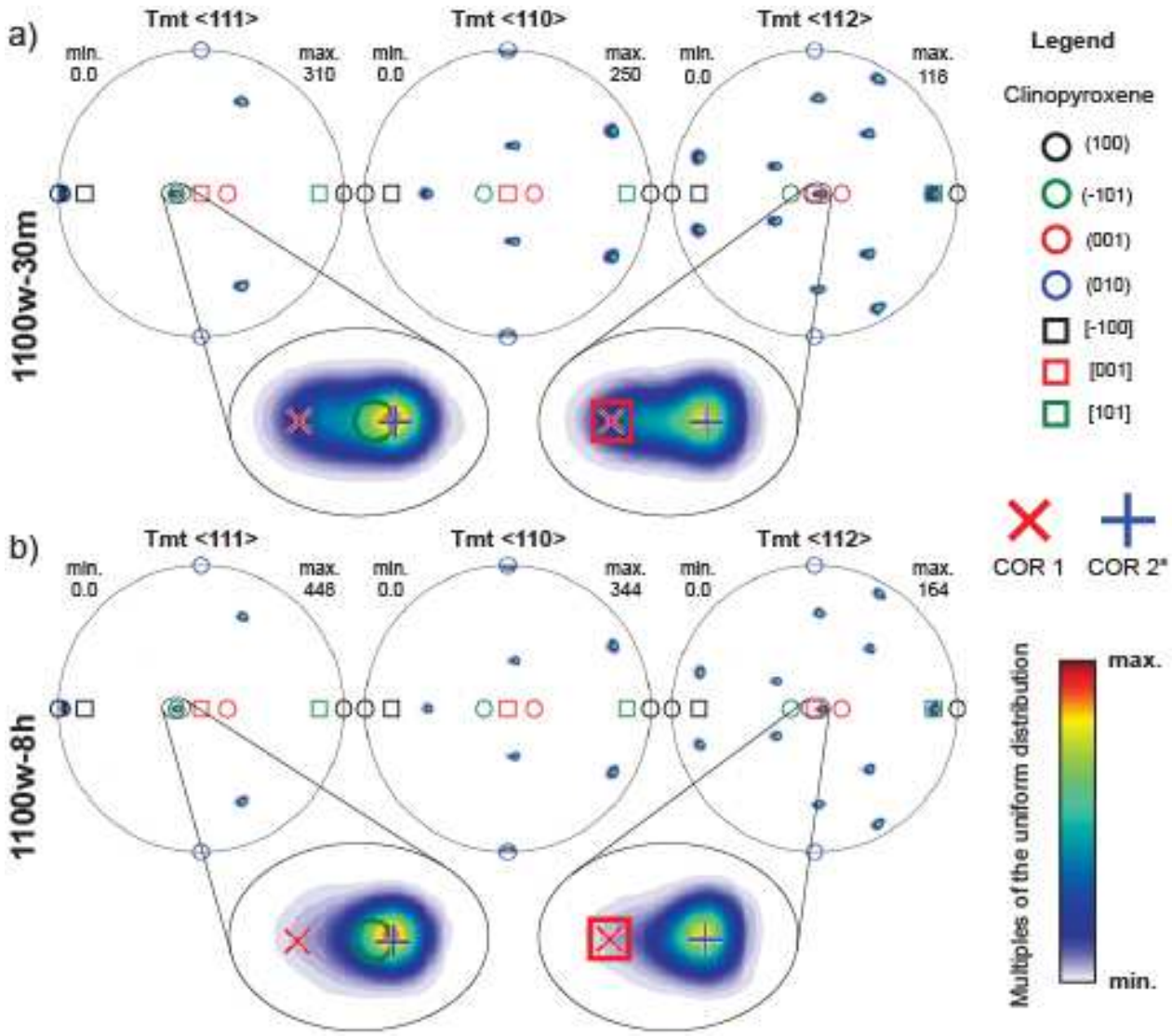

Fig.2.6 Stereographic, upper hemisphere, antipodal pole figures showing the distribution of symmetrically equivalent sets of Tmt directions with respect to the lattice of adjacent Cpx for all Tmt-Cpx boundary segments mapped in a) sample 1100w-30min and b) sample 1100w-8h. The orientation distribution functions (ODFs) used have a 1° halfwidth (MTEX de la Vallee Poussin kernel). The maximum and minimum intensity is indicated at the top left and right of each pole figure, respectively, in units of multiples of the uniform distribution. The colour map used is shown at right. Important directions (squares) and plane poles (circles) in Cpx are superimposed on all pole figures, colour coded according to the key at right. Zoomed insets of individual maxima are shown, in which the ideal positions of the relevant Tmt plane normal for COR 1 and COR 2 are marked with a red x or blue +, respectively*

A total of 2090 and 554 Tmt grains were recognized in EBSD scans of samples 1100w-30min and 1100w-8h respectively, of which 66.7% and 83.8% are in contact (i.e. share a boundary) with a Cpx grain in the 2D scans. Because of 2D cutting problems this value is a great underestimate of the true contact frequency. Image analysis of 3D volumes suggests that the actual proportion of Tmt grains in contact with Cpx is higher than 98% in both samples. Of the total length of Tmt-Cpx boundaries in EBSD scans, 91.0% and 91.1% follow or are close to a COR between Tmt and Cpx, respectively (BLF_{anyCOR}). This value varies in sample

1100w-30min from 95.3% in the hotter portion of the sample, to 91.1% in the middle and 84.7% in the colder portion of the sample. In contrast, BLF_{anyCOR} in sample 1100w-8h does not show significant variation.

COR2* is more prevalent than COR1 in both samples. Overall, BLF_{COR1} is 20.4% and 6.1% for samples 1100w-30min and 1100w-8h, respectively, while BLF_{COR2} is 51.8% and 72.1% in the same two samples. The relative preferences for the two COR types vary locally throughout both samples. BLF_{COR2} is higher in the hotter portions of samples 1100w-30min and 1100w-8h, decreasing from 80.0% and 77.4% in the hotter part down to 34.1% and 58.9% in the cooler part, respectively. BLF_{COR1}, in an opposite fashion, is at its lowest in the hotter portion, increasing from 5.7% and 1.2% up to 26.8% and 14.5% in the cooler portions of samples 1100w-30min and 1100w-8h, respectively.

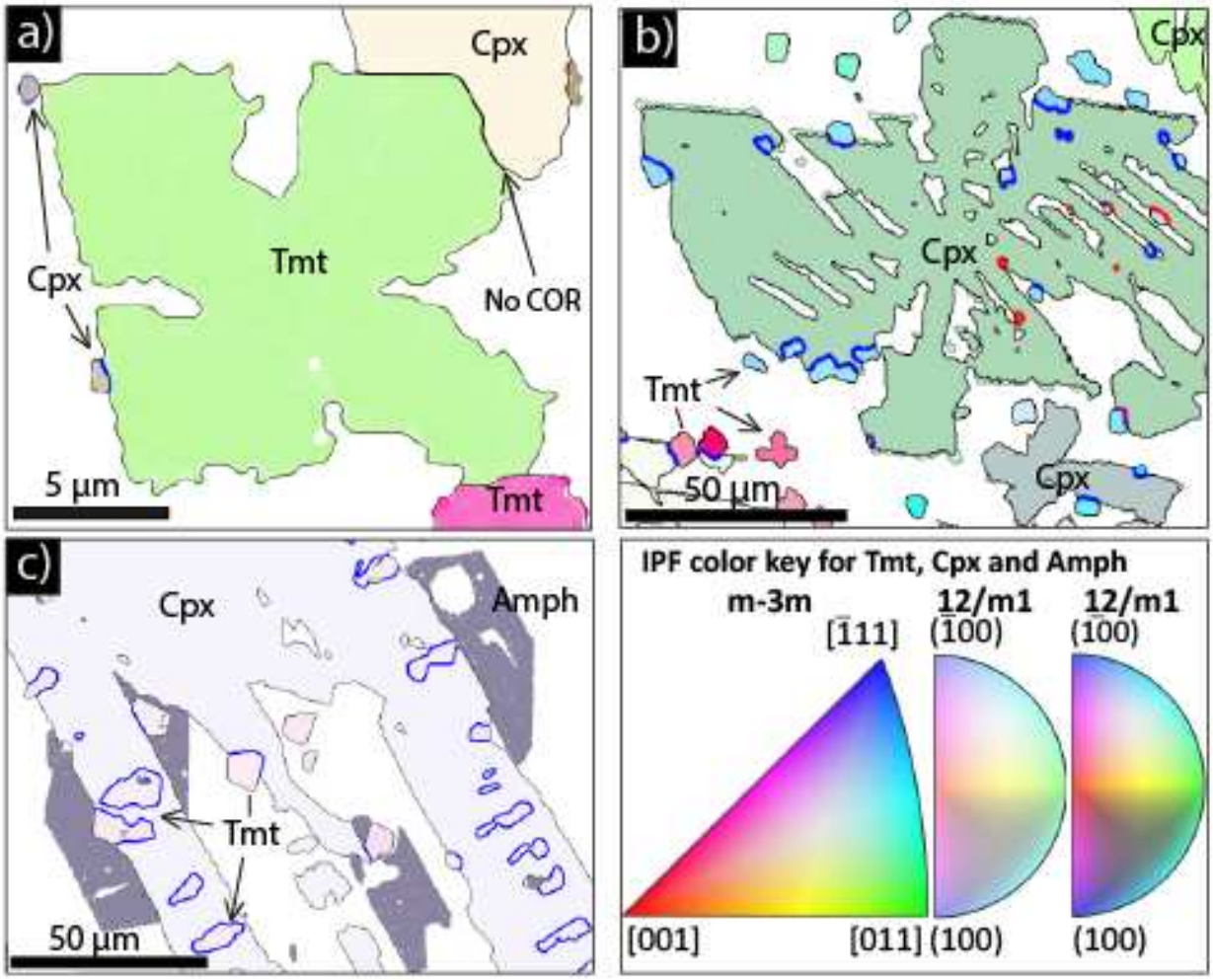

Fig.2.7 EBSD inverse pole figure (IPF) maps of Cpx-Tmt crystal clusters showing different colours for different crystallographic orientations, along with the CORs followed at different Cpx-Tmt boundary segments. a) Population 1 Tmt grain in the bottom portion of sample 1100w-30min, touching a large Cpx grain with no COR (black bold line) and 2 smaller (quench) Cpx grains top left and bottom left, following different CORs with Tmt. B) population 2 Tmt grains (all light blue coloured) touching a single Cpx grain in sample 1100w-30min. Both COR 1 and COR 2 boundaries are present; c) Population 2 (equidimensional grains) and population 3 (elongated grains) of Tmt in sample 1100w-8h all following COR 2* with the Cpx grain to which they are attached. Tmt = intense colours; cpx = lighter colours (60% transparency applied); Amph = opaque colours; Black bold lines = cpx-tmt interfaces without CORs; Red bold lines = cpx-tmt interfaces with COR type 1; Blue bold lines = cpx-tmt interfaces with COR type 2*; Purple bold lines = cpx-tmt interfaces outside of OR1 or OR2 but within a range of 6° misorientation*

In EBSD scans, Tmt populations were sorted by manual visual inspection to identify Tmt Pop1, while to distinguish Pop2 and Pop3 a circularity filter was applied: grains with circularity (defined as short axis / long axis) < 0.4 were classified as Pop3 while grains with circularity > 0.4 were sorted into Pop2. Each Tmt population shows differences in their COR frequencies (Fig.2.8). Of all populations, the boundaries of Pop1 grains in contact with a Cpx crystal are characterized by the lowest fraction of CORs, with BLF_{noCORs} at 17.9% and 33.9% in sample 1100w-30min and 1100w-8h respectively. Moreover, in sample 1100w-8h, Pop1

shows the highest $BLF_{nearCOR}$ (37.0%). Pop2 is by far the dominant population in both samples, and the Tmt-Cpx boundaries of Pop2 are mostly characterized by the presence of COR2 (BLF_{COR2} 49.9% and 71.2%, respectively) over COR1 (BLF_{COR1} 23.5% and 9.3%, respectively). Pop3 grains show the highest BLF_{COR2} (85.9% and 93.1%, respectively) and as a consequence, the lowest BLF_{COR1} (9.4% and 2.1%, respectively).

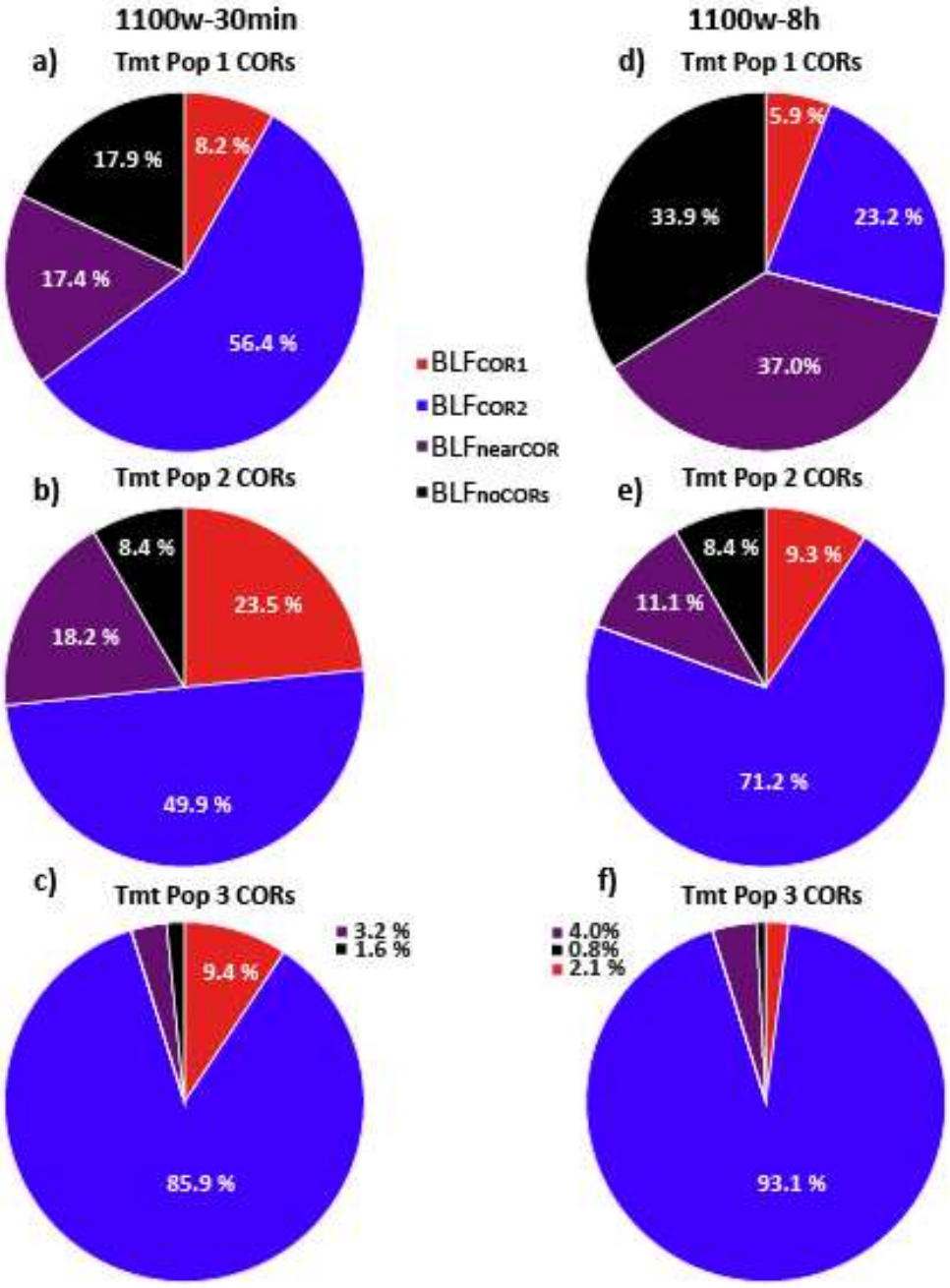

Fig.2.8 Pie charts of Tmt-Cpx boundary length fraction (in percentages) characterized by CORs in the three Tmt populations in both sample 1100w-30min (left column) and 1100w-8h (right column)

2.4. DISCUSSION

2.4.1. Nucleation mechanisms of Tmt and Cpx

The presence of three Tmt populations in each sample suggests the occurrence of different nucleation mechanisms and different relative timing of phases' appearance. The diagnostic tools we are going to employ in order to evaluate different nucleation mechanisms are: crystal morphology, spatial relationship of Tmt with the surrounding phases, Tmt clustering parameter g(x) and Tmt-Cpx CORs.

The more likely explanation for Tmt Pop1 grains totally surrounded by glass and isolated from Cpx grains is homogeneous nucleation. However, since our 3D and 2D imaging methodologies cannot resolve objects (like impurities or bubbles) at the nanoscale, it is not possible to exclude that these Tmt grains could have formed by heterogeneous nucleation on undetectable particles. Certainly, for Tmt grains assigned to Pop1 due to their similar size and/or morphology, but partially engulfed in larger Cpx crystals, the recognition of a specific nucleation mechanism requires further evaluation. In sample 1150w-30min, large, skeletal Tmt grains exhibiting 6 octahedrally arranged branches and well-developed outer facets are the only crystalline phase in the part of the sample with lower ΔT (portion of the sample approximately at 1150°C). We suggest that, due to their similarity with these isolated grains, the engulfed Tmt grains that preserve a skeletal shape and exhibit all 6 octahedral skeletal branches were also formed by the same mechanism (i.e. either homogeneous nucleation from the melt or heterogeneous nucleation on nanoparticles or bubbles), but in any case, prior to their contact with Cpx. Further support for this interpretation is provided by EBSD maps that show COR-absent boundaries for some Pop1 Tmt grains in touch with Cpx (Fig.2.7a). On the other hand, for Tmt grains of Pop1 showing well-formed skeletal shape but missing one or more branches at the contact with Cpx, we suggest that Tmt developed only some of the

octahedral branches due to Cpx blocking the extension of other branches into the melt. In EBSD maps where the 2D section is favourably oriented to reveal Tmt grains showing three branches arranged at 90° to each other, with a fourth missing, the inner portion of these Tmt crystals shows the presence of CORs with the adjacent Cpx, whereas the outer facets tend to show no COR (Fig.2.9a), suggesting that this morphology developed either due to heterogeneous nucleation of the Tmt grain on Cpx, or vice-versa. A proper distinction of what phase is nucleating on the other is not possible from 2D maps, but these "obstructed" Pop1 Tmt crystals are also observed in our 3D data. In cases where the obstructed Tmt crystal is in contact with the periphery of the Cpx grain, we suggest that heterogeneous nucleation of Tmt on Cpx is more likely. However, some Pop1 Tmt grains are in contact with the central portion of a Cpx grain, from which the Cpx branches radiate (Fig.2.9b-d). In such cases, we suggest that Cpx may have heterogeneously nucleated on a pre-existing Tmt at an early stage.

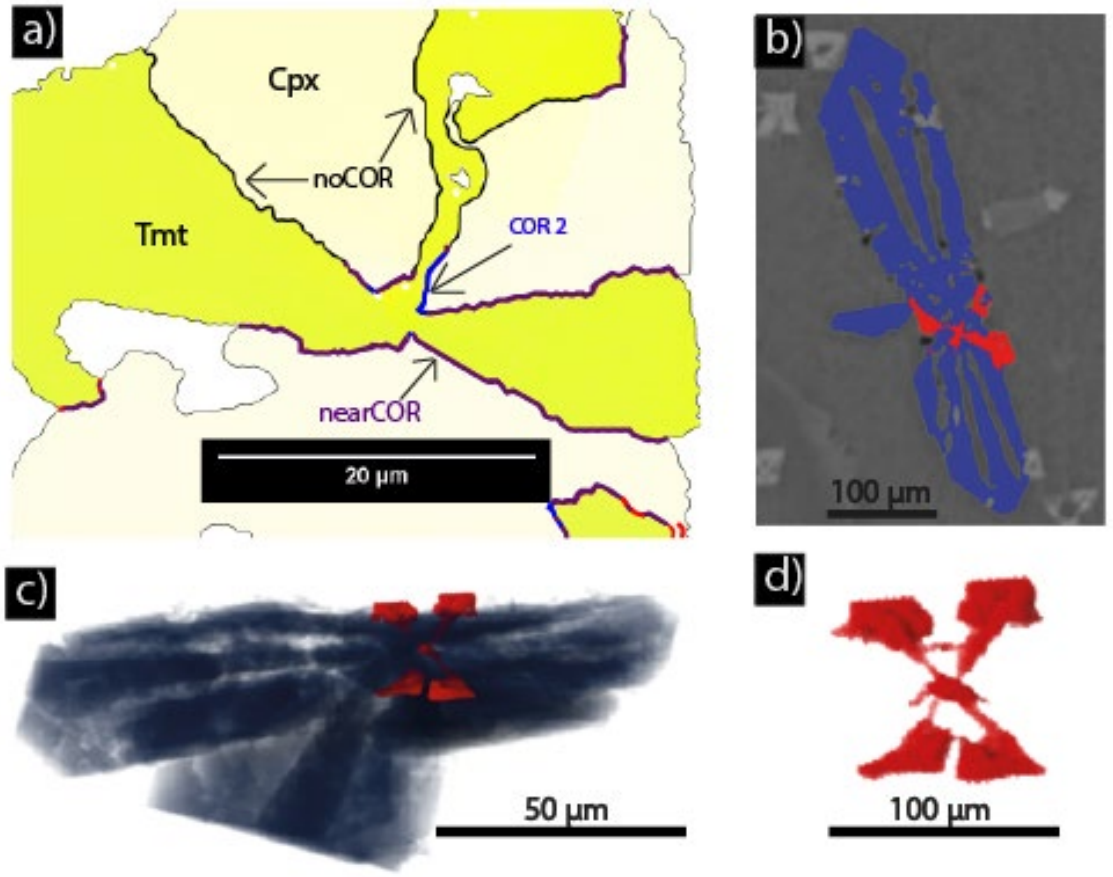

Fig.2.9 a) EBSD map of a Pop1 Tmt grain from sample 1100w-30min. IPF colour coding is identical to Fig.2.8. The grain shows a morphology similar to the one in figures a to d, including an apparent missing branch. b) reconstructed slice after image processing from sample 1150w-30min and c-d) a 3D rendering of the same crystals from b. These pictures show a cluster of Cpx (blue) and Tmt from Pop1 (red). The peculiar morphology, in which 4 developed Tmt branches out of six possible branches are almost completely engulfed in Cpx in a central position of the Cpx cluster, suggests that the Cpx may have nucleated on the Tmt grain, obstructing the development of the other 2 branches

Tmt Pop2 and Pop3 show clear evidence for heterogeneous nucleation on pre-existing Cpx crystals. EBSD scans reveal that Pop2 Tmt grains exhibit a very high length fraction of boundaries shared with Cpx that follow CORs (>90% in both samples), and Pop3 boundaries are characterized by an even higher length fraction of CORs (>95%). Heterogeneous nucleation is expected to favour CORs that represent an optimal way of arranging the lattices of crystals at shared interfaces, allowing low-energy interfaces to form, and thus minimising the height of the energetic barrier which governs the likelihood of formation of a stable nucleus. Therefore, it is interesting to know whether the observed CORs indicate the presence of low-energy interfaces. Indeed, the observed CORs represent the case in which one set of $\{110\}_{Tmt}$ planes are parallel or at a small angle (< 2.7°) to the (010) plane of Cpx, and the d-

spacings of these planes are similar in both phases (Fleet et al. 1980). In addition, Fleet et al. (1980) showed that, for exactly the two CORs observed here, there is also a correspondence between close packed oxygen planes in Tmt and the arrangement of particular layers of O atoms in Cpx, and furthermore, for the same two CORs, there also exist special (irrational) planes parallel to the $[010]_{Cpx}$ direction, along which the structures of Tmt and Cpx should match perfectly. Overall, the overwhelming preference of Tmt-Cpx boundaries for CORs 1 and 2* in our experiments supports the expectation that the interfacial energies of at least some interface planes associated with these CORs are at a local or global minimum and provides strong evidence for heterogeneous nucleation.

Despite the fact that interface free energy is dependent on both the misorientation between neighbour crystal lattices as well as on the orientation of the interface plane between them, with the interface plane orientation providing the dominant contribution (Habler and Griffiths 2017), we did not find evidence of a preferred interface plane orientation correlating with COR 1 or 2* boundaries in our EBSD maps. However, we note that the initial interface segment formed during heterogeneous nucleation of a Tmt nucleus on Cpx would be extremely small. In any case, given the frequently observed curved shape of Tmt-Cpx boundary segments with the same COR in our samples, it is clear that after nucleation, the COR did not exert complete control on interface plane orientation. This is in contrast to the observation of Fleet et al. (1980) for exsolved magnetite lamellae, where a different preferred elongation direction was found for each COR. Interestingly, Fleet et al. (1980) observed more needles oriented subparallel to the c-axis of Cpx, corresponding to a preference for COR 1, whereas here, COR 2* dominates.

In addition to the COR-based evidence for heterogeneous nucleation, we also observed specific preferential interpoint frequencies between 10 µm and 100 µm for both Tmt Pop2 and Pop3, with peaks between 20 µm and 30 µm. This distance range is a good

approximation of the average width (minimum axis) of a dendritic Cpx in the region of the sample characterized by higher degrees of ΔT (between 60 °C and 110 °C), or the average width of the single branches of a skeletal Cpx in the (hotter) region characterized by lower degrees of undercooling (between 30 °C and 60 °C). In this distance range, the diffusion rate of specific elements may play a role in the spacing of neighbour Tmt crystals nucleating along the same side of a branch, as result of diffusive boundary layers forming at the interface of fast growing Cpx (e.g., Pontesilli et al., 2019). This region is assumed to become supersaturated with respect to Tmt, with the most energetically favourable Tmt nucleation mechanism being heterogeneous nucleation on the growing Cpx crystal. During growth of a newly nucleated Tmt grain, the chemical components that are fractionated into Tmt are depleted in the surrounding melt, lowering their chemical potentials. The extent of depletion of these components in melt around a growing Tmt grain depends on the Tmt growth rate and the diffusivity of the respective components in the melt. Assuming that both the rate of Tmt growth and the component mobilities are quite similar for different Tmt grains within one sample, this produces similarly sized "depletion halos" (domains with reduced chemical potential of the components partitioning into Tmt) around each Tmt grain (Fig.2.10). The reduced or absent supersaturation of the melt with respect to Tmt within the depletion halos hinders the nucleation of new Tmt in these domains. By this mechanism, sub-regular spacing of Tmt can be produced along single Cpx facets, as observed.

2.4.2 Relative timing of nucleation of the different titanomagnetite populations

In this section we discuss the nucleation order of the different Tmt populations and the timing of their nucleation with respect to the development of Cpx crystals, using microstructural relationships and crystal morphologies. In order to interpret the nucleation and growth history of different Tmt populations, it is first important to understand the origin and temporal evolution of the observed Cpx microstructures and zoning. We infer that Cpx may have

formed by homogeneous nucleation from the melt, or by heterogeneous nucleation on extremely small particles or bubbles, and/or through heterogeneous nucleation on Pop1 Tmt grains, based on the truncated morphology of some Pop1 Tmt grains and Tmt-Cpx CORs identified near grain centres (Fig.2.9). With the exception of the portions of experiment 1150w-30m characterized by lower undercooling (close to T_{liq}), in the first minutes at the experimental temperature, right after the cooling ramp, the system is far from thermodynamic equilibrium and the melt is supersaturated with respect to Cpx and Tmt (Mollo et al., 2010; 2012; 2013; Pontesilli et al., 2019). Cpx crystallizes in a regime of diffusion-limited crystal growth, so that the growth rate is controlled by the rate at which component diffusion occurs (Sunagawa 1981; Shea and Hammer, 2013), eventually resulting in the formation of dendritic crystals characterized by high concentrations of Al + Ti (Fig.2.4b-c). As the experimental runs proceed isothermally after reaching the resting temperature, ongoing melt relaxation leads to conditions progressively closer to chemical equilibrium, characterized by progressively less supersaturated melt near the crystallizing Cpx, which favours the development of euhedral facets and results in the partial infill of the dendritic branches (Si- and Mg-rich zones; Fig.2.4c). In similar experimental samples, Pontesilli et al. (2019) showed that Cpx growth rates decreased in samples kept at experimental temperature for increasing durations between 30 minutes and 24 hours. Thus, we infer that, alongside decreasing melt supersaturation, Cpx growth rates were also decreasing during microstructural evolution of our samples, including during our 30 minutes duration experiments.

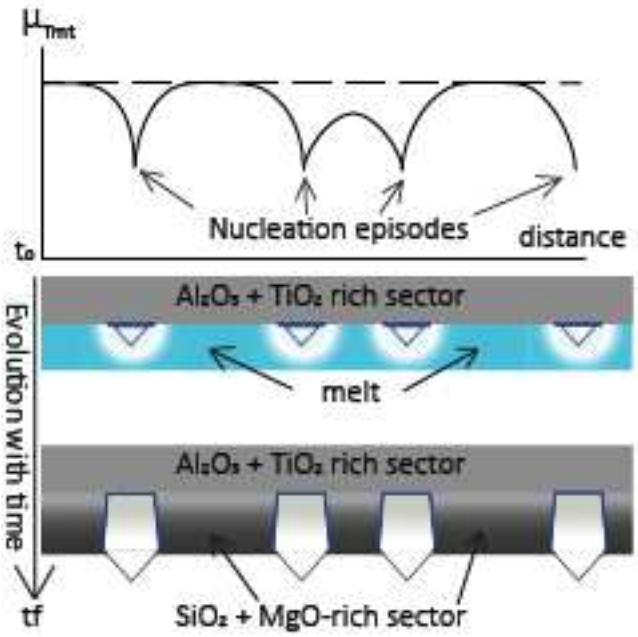

Fig.2.10 Qualitative interpretation of the Tmt chemical potential curve parallel to the Cpx branch after multiple Tmt nucleation episodes. See text for the explanation

The observation of Tmt (Pop 1) as the liquidus phase (indeed the only crystallizing phase) in the hotter domain of experiment 1150w 30m indicates that Tmt is the first phase to nucleate. The relatively large crystal size and skeletal forms are consistent with the relatively low degree of undercooling determined for this part of the experimental sample (10 °C), as also demonstrated by recent crystallization experiments performed at comparable conditions using a basalt from Stromboli (Colle et al., 2023). Under such conditions of low undercooling, lower nucleation rates and a higher growth rates are expected. In sample 1100w-30 min and 1100w-8h, based on well faceted Tmt crystal even when partially engulfed in a Cpx grain and because of the highest amount of shared boundaries between Cpx and Tmt crystals which do not show CORs (BLF_{noCORS} = 17.9% and 33.9%; Fig.2.8a-b) respectively we suggest that, also in these samples, Pop1 Tmt may be the first phase to nucleate.

We infer that Tmt Pop3 nucleated heterogeneously on Cpx in the earlier stages of Cpx growth, favoured by the chemical boundary layer developed at the melt interface. The portion of Pop3 crystals near the Al_2O_3+TiO_2-enriched zone of Cpx corresponds to the TiO_2 poor

domain of the Tmt crystals, while the TiO_2 concentration increases when the Tmt is situated in the SiO_2+MgO-rich zones of Cpx crystals. We suggest that the elongated shape is caused by co-growth of Cpx and Tmt with similar growth rates, resulting in similarity between the Tmt longest dimension and the final width of Cpx branches. Co-growth of the two phases also explains the stronger preference for COR interfaces compared to Pop2 Tmt, as the Tmt-Cpx interface is created simultaneously with the growth of both phases, which favours continued production of a low-energy interface.

Finally, we infer that Pop2 Tmt crystals formed by heterogeneous nucleation on Cpx later in its growth history, when the faceted skeletal morphology of Cpx was more developed, i.e. in conditions closer to thermodynamic equilibrium. This hypothesis is supported by the external position of most Pop2 Tmt grains with respect to touching Cpx, their greater protrusion into the melt, and the presence of frequent planar boundaries between the two crystal phases. Nonetheless, we in fact observe more or less a continuum of morphologies between the end members which we define as "typical" Pop2 and Pop3 grains (e.g. Fig.2.4, Fig.2.7b-c), and thus many Pop2 Tmt grains exhibit more curved boundaries with Cpx crystals (Fig.2.2c, Fig. 2.4a-c, Fig.2.7b). These can be explained by a slightly earlier timing of Tmt nucleation, possibly corresponding to a limited period of simultaneous growth of the two phases. This would result in a partial embedding of Tmt inside Cpx, with the geometry of the Tmt-Cpx interface controlled by the varying relative growth rates of the two phases in 3D. Despite the existence of transitional forms in between Pop3 and Pop2 morphologies, we still consider it useful to separate Pop3 from the remaining heterogeneously nucleated Tmt grains (Pop2), due to their distinctive morphological, COR, and chemical characteristics. However, the existence of a morphological continuum suggests that heterogeneous nucleation of Tmt on Cpx occurred continuously throughout Cpx growth, i.e., Pop3 and Pop2 do not correspond to separate Tmt nucleation pulses.

2.4.3. Implications

Our observations show the potential of combining spatially resolved crystallographic orientation maps with high resolution 3D information to provide detailed, spatially resolved petrological information about the conditions and mechanisms of crystal cluster formation. The newly-documented presence of multiple CORs in Cpx-Tmt clusters, whose overall abundance and relative frequency (COR1 vs COR2*) changes in relation to the degree of undercooling along the experimental sample, suggests that CORs formed by heterogeneous nucleation may represent proxies for deciphering the undercooling conditions in crystal clusters contained in natural magmas. However, it will be essential to carry out further work to understand the reason for the overall higher occurrence of Cpx-Tmt shared boundaries characterized by COR2* compared to COR1, and determine whether this preference is dependent on one or multiple physical parameters.

The second striking feature of our experimental samples is the presence of three different Tmt populations, all of them formed during a single cooling event, nucleated at the same temperature, but at different times, with the only varying condition being the extent of deviation from thermodynamic equilibrium. In the absence of combined 3D analysis and crystallographic orientation information, these different crystal populations of the same phase could have been misinterpreted as evidence of multiple temporary discrete magmatic events. Our results underline the central importance of a multimethodological analysis, not just microstructural observations, in order to explain different populations of the same crystal phase. In future, the combined application of 3D imaging, compositional mapping, and crystallographic analysis to crystal clusters offers the potential to unravel crystallization sequences with unprecedented (relative) time resolution in experimental samples and natural rocks.

From a broader volcanological point of view, our experiments reproduce magmatic conditions far from equilibrium, which can occur in the context of fast crystallization of a trachybasaltic dike (Arzilli et al., 2022) or crystallization due to a magmatic recharge of trachybasaltic composition in a crystal mush at medium to shallow (10-12 km) depths (Pontesilli et al., 2019; Masotta et al., 2020). The aforementioned works experimentally reproduce crystallization of a starting material similar to our experiments, at similar P, ΔT, H_2O content, and f_{O2}. All these cases result in the formation of skeletal-to-dendritic Cpx and minor oxides clustered together. Cpx-Tmt clustering by heterogeneous nucleation may play a fundamental role in the viscosity evolution of a magmatic system, especially in the case of the heterogeneous nucleation of Cpx on Tmt. This clustering mechanism could shorten the nucleation delay typical of magmas at low degrees of undercooling (Arzilli et al., 2019). Moreover, subsequent crystallization of fast-growing dendritic Cpx on already existing Tmt grains may suddenly increase the viscosity of a magma, leading to fragmentation (Moitra et al., 2018) and consequently, basaltic explosive eruption (Arzilli et al., 2019) if the crystallinity remains below 30%. For scenarios with higher undercooling, the result is a higher crystallinity, which can freeze the magma propagation inside dykes or lock crystal mushes in the case of future eruptions (Arzilli et al., 2022). Heterogeneous nucleation of Tmt on Cpx, triggered by rapid formation of skeletal and/or dendritic Cpx, could also have important effects on magmatic systems (Hammer et al. 2010). Cpx crystals decorated or filled with Tmt will have higher density, causing them to be more efficiently removed during settling-related fractional crystallization in melt-rich systems. Furthermore, disequilibrium crystallization of Tmt alongside Cpx should impact the major and trace element signature of coexisting melt in basaltic systems (e.g. Boudreau and Philpotts 2002), and thus also the composition of extracted melt, including in cases where crystallinity is higher and melt extraction proceeds by melt percolation or mush compaction.

2.5. CONCLUSIONS

Crystallization experiments and a multi-methodological approach including high resolution 3D SR-µCT, EPMA and EBSD mapping provide precious information about the nucleation mechanisms of Tmt and Cpx in a basaltic melt. The main findings of this work can be summarized as follows:

1) Three distinct titanomagnetite (Tmt) populations characterized by different morphologies, sizes, and spatial relations with the other phases formed in a basaltic melt cooled from superliquidus at variable degrees of undercooling (ΔT_{max}-ΔT_{min}=100°C) along a temperature gradient after applying a single cooling ramp.
2) EBSD mapping established the presence of CORs between Tmt and Cpx, which is strong evidence of heterogeneous nucleation of Tmt of populations 2 and 3. The details of the Cpx-Tmt CORs vary between the three Tmt populations, constraining differences in the timing and/or mechanism of nucleation.
3) While skeletal Tmt population 1 grains may have nucleated homogeneously from the melt, the other Tmt populations nucleated heterogeneously on Cpx, during and after Cpx crystallization.
4) The development of dendritic Cpx morphology and zoning influenced the morphology (and to a lesser extent composition) of Tmt populations 2 and 3, but not the nucleation mechanism, which remained heterogeneous.
5) We advise caution when interpreting multiple cooling events to explain differences in crystal morphologies and stress the importance of further study on the presence and proportions of different CORs in experimental and natural samples. This parameter may depend on, and thus provide information about, specific values of undercooling, which are in turn strongly related to the specific crystallisation history of the system.

Statements and Declarations

We declare we have no financial and non-financial interests that are directly or indirectly related to the work submitted for publication.

2.6. References cited

Ageeva O, Habler G, Pertsev A, Abart R (2017) Fe-Ti oxide micro-inclusions in clinopyroxene of oceanic gabbro: Phase content, orientation relations and petrogenetic implication. Lithos, 290–291: 104–115.

Armienti P, Innocenti F, Petrini R, Pompilio M, Villari L (1988) Subaphyric alkali basalt from Etna: inferences on depth and composition of the source magma. Rend. Soc. Ital. Miner. Petrol. 43, 877-891.

Armienti P, Perinelli C, Putirka K (2013) A new model to estimate deep-level magma scent rates, with applications to Mt. Etna (Sicily, Italy). J. Petrol. 45, 1-19. doi: 10.1093/petrology/egs085

Arzilli F, Mancini L, Voltolini M, Cicconi MR, Mohammadi S, Giuli G, Mainprice D, Paris E, Barou F, Carroll MR (2015) Near-liquidus growth of feldspar spherulites in trachytic melts: 3D morphologies and implications in crystallization mechanisms. Lithos 216-217:93-105. doi: 10.1016/j.lithos.2014.12.003

Arzilli F, La Spina G, Burton MR, Polacci M, Le Gall N, Hartley ME, Di Genova D, Cai B, Vo NT, Bamber EC, Nonni S, Atwood R, Llewellin EW, Brooker RA, Mader HM, Lee PD (2019) Magma fragmentation in highly explosive basaltic eruptions induced by rapid crystallization. Nature Geoscience 12, 509 1023-1028. doi: 10.1038/s41561-019-0468-6

Arzilli F, Polacci M, La Spina G, Le Gall N, Llewellin EW, Brooker RA, Torres-Orozco R, Di Genova D, Neave DA, Hartley ME, Mader HM, Giornado D, Awwood R, Lee

PD, Heidelbach F, Burton MR (2022). Dendritic crystallization in hydrous basaltic magmas controls magma mobility within the Earth's crust. Nat Commun 13, 3354. Doi: 10.1038/s41467-022-30890-8

Bachmann O, Huber C (2016) Silicic magma reservoirs in the Earth's crust. Am Mineral 101:2377-2404. doi: 10.2138/am-2016-5675

Bachmann O, Dungan MA, Lipman PW (2002) The Fish Canyon magma body, San Juan volcanic field, Colorado: Rejuvenation and eruption of an upper crustal batholith: Journal of Petrology, v. 43, p. 1469-1503, doi:10.1093/petrology/43.8.1469

Bachmann F, Hielscher R, Schaeben H (2010) Texture analysis with MTEX - free and open source software toolbox. Solid State Phenomena 160, 63–68. doi: 10.4028/www.scientific.net/SSP.160.63.

Baddeley A, Rubak E, Turner R (2015). Spatial Point Patterns: Methodology and Applications with R. Chapman and Hall/CRC Press. http://www.crcpress.com/Spatial-Point-Patterns-Methodology-and-Applications-with-R/Baddeley-Rubak-Turner/9781482210200/

Bertolett EM, Prior DJ, Gravley DM, Hampton SJ, Kennedy BM (2019) Compacted cumulates revealed by electron backscatter diffraction analysis of plutonic lithics. Geology 2019; 47 (5): 445–448. doi: https://doi.org/10.1130/G45616.1

Boudreau A, Philpotts AR (2002) Quantitative modeling of compaction in the Holyoke flood basalt flow, Hartford Basin, Connecticut. Contrib Mineral Petrol 144:176-184. doi: 10.1007/s00410-002-0391-4

Brun F, Pacilé S, Kourousias G, Dreossi D, Mancini L, Tromba G, Pugliese R (2015) . Enhanced and flexible software tools for X-ray tomography experiments at the Italian

synchrotron radiation facility Elettra, Fundamenta Informaticae 141: 233–243, doi: 10.3233/FI-2015-1273

Cashman KV, Sparks RSJ, Blundy JD (2017) Vertically extensive and unstable magmatic systems: A unified view of igneous processes. Science 355:eaag3055. doi: 10.1126/science.aag3055

Costa S, Masotta M, Gioncada A, Pistolesi M, Bosch D, Scarlato P (2020) Magma evolution at La Fossa volcano (Vulcano Island, Italy) in the last 1000 years: evidence from eruptive products and temperature gradient experiments. Contrib Mineral Petrol 175, 31 https://doi.org/10.1007/s00410-020-1669-0

Colle F, Masotta M, Costa S, Mollo S, Landi P, Pontesilli A, Peres S, Mancini L (2023). Effect of undercooling on clinopyroxene crystallization in a high K basalt: Implications for magma dynamics at Stromboli volcano. Lithos, Volumes 456–457. 107327. Doi: 10.1016/j.lithos.2023.107327

DiBenedetto M, Qin Z, and Suckale J (2020). Crystal aggregates record the pre-eruptive flow field in the volcanic conduit at Kīlauea, Hawaii: Science Advances, v. 6, p. eabd4850, https://doi .org/10.1126/sciadv.abd4850.

Dowty E (1980) Synneusis Reconsidered. Contr. Mineral. and Petrol. 74, 75–84 (1980). https://doi.org/10.1007/BF00375491

Dyck B, Holness M (2021). Microstructural evidence for convection in high-silica granite. Geology 50, 295–299. https://doi.org/10.1130/G49431.1.

Dyck B (2023) Sticking together: Mechanisms of quartz synneusis in high-silica magma. Geoscience Frontiers 14 (2023) 101512. https://doi.org/10.1016/j.gsf.2022.101512

Ellis BS, Bachmann O, Wolff JA (2014) Cumulate fragments in silicic ignimbrites: The case of the Snake River Plain. Geology 42:431-434. doi: 10.1130/G35399.1

Feinberg JM, Wenk HR, Renne PR, Scott GR (2004). Epitaxial relationships of clinopyroxene-hosted magnetite determined using electron backscatter diffraction (EBSD) technique. Am Mineral, Vol 89, pp 462-466.

Ferguson MRM, Ehrig K, Meffre S (2019) Insights into magma histories through silicate-oxide crystal clusters: Linking the Hiltaba Suite intrusive rocks to the Gawler Range Volcanics, Gawler Craton, South Australia. Precambrian Res 321:103-122. doi: 10.1016/j.precamres.2018.11.015

Ferracutti GR, Gargiulo MF, Ganuza ML (2015) Determination of the spinel group end-members based on electron microprobe analyses. Miner Petrol 109:153-160 (2015). doi:10.1007/s00710-014-0363-1

Fleet ME, Bilcox GA, Bernett RL (1980). Oriented magnetite inclusions in-pyroxenes from the Greenville Province. Canadian Mineralogist, Vol.18 pp 89-99.;

Freda C, Gaeta M, Misiti V, Mollo S, Dolfi D, Scarlato P (2008) Magma-carbonate interaction: an experimental study on ultrapotassic rocks from Alban Hills (Central Italy). Lithos 101, 397-415 doi: 10.1016/j.lithos.2007.08.008

Garcia MO, Jacobson SS (1979) Crystal clots, amphibole fractionation and the evolution of calc-alkaline magmas. Contrib Mineral Petrol 69:319-327. doi: 10.1007/BF00372257

Gordon C, Wallis D, (2024) Resolving the “megacryst paradox”: Feldspar orientation relationships record crystal mobility in granites. Geology 2024; https://doi.org/10.1130/G52045.1

Griffiths TA, Habler G, Abart R (2016) Crystallographic orientation relationships in host-inclusion systems: new insights from large EBSD datasets Am. Min. 101: 690-705. doi: 10.2138/am-2016-5442

Gualda G A R, Ghiorso MS, Lemons RV, Carley T L (2012a). Rhyolite-MELTS: a Modified Calibration of MELTS Optimized for Silica-rich, Fluid-bearing Magmatic Systems. Journal of Petrology 53, 875–890.

Habler G, Griffiths TA (2017) Crystallographic orientation relationships. In: Mineral reaction kinetics: Microstructures, textures, chemical and isotopic signatures. pp 541-585.

Hammer JE (2008) experimental Studies of the Kinetics and energetics of Magma Crystallization. Minerals, Inclusions and Volcanic Processes pp 9-59.

Hammer JE, Sharp TG, Wessel P (2010) Heterogeneous nucleation and epitaxial crystal growth of magmatic minerals. Geology 38:367-370. doi: 10.1130/G30601.1

Hielscher R, Schaeben H, Siemes H (2010) Orientation Distribution Within a Single Hematite Crystal. Math Geosci 42, 359-375. doi: 10.1007/s11004-010-9271-z

Holness MB, Farr R, Neufeld JA (2017) Crystal settling and convection in the Shiant Isles Main Sill. Contrib Mineral Petrol 172,7. doi:10.1007/ s00410-016-1325-x

Holness MB, Stock MJ, Geist D (2019) Magma chambers versus mush zones: constraining the architexture of sub-volcanic plumbing systems from microstructural analysis of crystalline enclaves. Philosophical Transactions of the Royal Society of London 377, 20180006. doi:10.1098/rsta.2018.0006

Holness MB, Vukmanovic Z, O'Driscoll B (2023) The Formation of Chromite Chains and Clusters in Igneous Rocks. J Petrol 64:1-24. doi: 10.1093/petrology/egac124

Jerram DA, Cheadle MJ (2000) On the cluster analysis of grains and crystals in rocks. Am. Min. 85(1): 47-67. doi: 10.2138/am-2000-0107

Jerram DA, Cheadle MJ, Philpotts AR (2003) Quantifying the Building Blocks of Igneous Rocks: Are Clustered Crystal Frameworks the Foundation? J Petrol 44:2033-2051. doi: 10.1093/petrology/egg069

Kirkpatrick RJ (1977) Nucleation and growth of plagioclase, Makaopuhi and Alae lava lakes, Kilauea Volcano, Hawaii. GSA Bull 88:78-84. doi: 10.1130/0016-7606(1977)88<78:NAGOPM>2.0.CO;2

Kirkpatrick RJ (1981) Kinetics of crystallization of igneous rocks. In Rev. Mineral., Vol. 8 (eds. A. C. Lasaga and R. J. Kirkpatrick), pp. 321–395

Le Maitre R (1962) Petrology of volcanic rocks, Gough Island, south Atlantic. Geol. Soc. Am. Bull. 73, 1309-1340.

Lofgren GE (1983) Effect of Heterogeneous Nucleation on Basaltic Textures: A Dynamic Crystallization Study. J Petrol 24:229-255. doi: 10.1093/petrology/24.3.229

Marsh BD (2002). On bimodal differentiation by solidification front instability in basaltic magmas: Part1.Basic mechanics. Geochim. Cosmochim. Acta 66:2211-2229

Masotta M, Freda C, Paul TA, Moore GM, Gaeta M, Scarlato P and Troll VR (2012) Low pressure experiments in piston cylinder apparatus: calibration of newly designed 25 mm furnace assemblies to P= 150 MPa. Chem. Geol. 312, 74-79. doi: 10.1016/j.chemgeo.2012.04.011

Masotta M, Pontesilli A, Mollo S, Armienti P, Ubide T, Nazzari M, Scarlato P (2020). The role of undercooling during clinopyroxene growth in trachybasaltic magmas: Insights on

magma decompression and cooling at Mt. Etna volcano. Geochim. Cosmochim. Acta . 268:258-276. doi: 10.1016/j.gca.2019.10.009

Milner S, Duncan A, Ewart A (1992). Quartz latite rheoignimbrite flows of the Etendeka Formation, north-western Namibia. Bull. Volcanol. 54, 200-219

Moitra P, Gonnermann HM, Houghton BF, Tiwary CS (2018) Fragmentation and Plinian eruption of crystallizing basaltic magma. Earth and Planetary Science Letters, v 500, 97-104, https://doi.org/10.1016/j.epsl.2018.08.003.

Mollo S, Del Gaudio P, Ventura G, Iezzi G, Scarlato P, (2010). Dependence of clinopyroxene composition on cooling rate in basaltic magmas: implications for thermobarometry. Lithos 118, 302–312.

Mollo S, Iezzi G, Ventura G, Cavallo A, Scarlato P (2012) Heterogeneous nucleation mechanisms and formation of metastable phase assemblages induced by different crystalline seeds in a rapidly cooled andesitic melt. J Non Cryst Solids. 358: 1624-1628

Mollo S, Putirka K, Iezzi G, Scarlato P (2013) The control of cooling rate on titanomagnetite composition: implications for a geospeedometry model applicable to alkaline rocks from Mt. Etna volcano. Contrib Mineral Petrol 165:457-475. doi: 10.1007/s00410-012-0817-6

Paganin D, Mayo S.C, Gureyev T.E, Miller P.R, Wilkins S.W (2002). Simultaneous phase and amplitude extraction from a single defocused image of a homogeneous object, J. Microsc 206: 33–40, doi: 10.1046/j.1365-2818.2002.01010.x.

Petrishcheva E, and Abart R (2017) Interfaces. in: Mineral Reaction Kinetics: Microstructures, Textures and Chemical Compositions. pp. 295-345

Pontesilli A, Masotta M, Nazzari M, Mollo S, Armienti P, Scarlato P, Brenna M (2019) Crystallization kinetics of clinopyroxene and titanomagnetite growing from a trachybasaltic melt: New insights from isothermal time-series experiments. Chem Geol 510:113-129. doi: 10.1016/j.chemgeo.2019.02.015

R Core Team (2020). R: A language and environment for statistical computing. R Foundation for Statistical Computing, Vienna, Austria. https://www.R-project.org/.

Rudge JF, Holness MB, Smith GC (2008) Quantitative textural analysis of packings of elongate crystals. Contrib Mineral Petrol 156, 413-429. doi:10.1007/s00410-008-0293-1

Schwindinger KR (1999) Particle dynamics and aggregation of crystals in a magma chamber with application to Kilauea Iki olivines. J Volcanol Geotherm Res 88:209-238. doi: 10.1016/S03770273(99)00009-8

Schindelin J, Arganda-Carreras I, Frise E, Kaynig V, Longair M, Pietzsch T, Preibisch S, Rueden C, Saalfeld S, Schmid B, Tinevez J.-Y, White D.J, Hartenstein V, Eliceiri K, Tomancak P, Cardona A (2012). Fiji: an open-source platform for biological-image analysis, Nat. Methods 9: 676–682,

Schwindinger KR, Anderson AT (1989) Synneusis of Kilauea Iki olivines. Contrib Mineral Petrol 103:187-198. doi: 10.1007/BF00378504

Seaman SJ (2000) Crystal Clusters, Feldspar Glomerocrysts, and Magma Envelopes in the Atascosa Lookout Lava Flow, Southern Arizona, USA: Recorders of Magmatic Events. J Petrol 41:693-716. doi: 10.1093/petrology/41.5.693

Shea T, Hammer JE (2013). Kinetics of decompression and cooling-induced crystallization of mafic-intermediate hydrous magmas. J. Volcanol. Geotherm. Res. 260, 127–145

Spry AH (1969) Metamorphic Textures. Pergamon Press, Oxford, New York, Toronto, Sydney, 358 pp.

Stoyan D, and Stoyan H (1994). Fractals, Random Shapes and Point Fields. Methods of Geometrical Statistics. XIV, 389 pp. John Wiley & Sons 1994

Sunagawa I (1981). Characteristics of crystal growth in nature as seen from the morphology of mineral crystals. Bull. Miner. 104, 81–87.

Tormey DR, Frey FA, Lopez-Escobar L (1995) Geochemistry of the active Azufre-Planchon-Peteroa volcanic complex, Chile (35 15′ S): evidence for multiple sources and processes in a cordilleran arc magmatic system. J. Petrol. 36: 265-298. doi: 10.1093/petrology/36.2.265

Vance JA (1969) On synneusis. Contrib Mineral Petrol 24:7-29. doi: 10.1007/BF00398750

Vetere F, Iezzi G, Behrens H, Holtz F, Ventura G, Misiti V, Cavallo A, Mollo S, Dietrich M (2015) Glass forming ability and crystallisation behaviour of sub-alkaline silicate melts. Earth-Sci Rev 150:25-44. doi: 10.1016/j.earscirev.2015.07.001

Vukmanovic Z, Holness MB, Monks K, (2018) The Skaergaard trough layering: sedimentation in a convecting magma chamber. Contrib Mineral Petrol 173, 43 (2018). https://doi.org/10.1007/s00410-018-1466-1

Walker D, Kirkpatrick RJ, Longhi J, Hays JF (1976) Crystallization history of lunar picritic basalt samples 12002: phase equilibria and cooling rate studies. Geol. Soc. Am. Bull. 87: 646-656

Wieser PE, Vukmanovic Z, Kilian R, Ringe E, Holness MB, Maclennan J, Edmonds E (2019). To sink, swim, twin, or nucleate: a critical appraisal of crystal aggregation processes. Geology 47: 948-952. doi:10.1130/G46660.1

Zandomeneghi D, Voltolini M. Mancini L, Brun F, Dreossi D and Polacci M (2010), Quantitative analysis of X-ray microtomography images of geomaterials: application to volcanic rocks, Geosphere, 6: 793-804, doi:10.1130/GES00561.1.

3. THE EFFECT OF HETEROGENEOUS NUCLEI AVAILABILITY ON ROCK MICROSTRUCTURE: A NEW PERSPECTIVE FROM EBSD INVESTIGATION OF SYNTHETIC TRACHYBASALTS

Premise

The following chapter will constitute the main body of a complete draft for my second paper as first author I am going to submit to a scientific journal. For this reason, I will treat it as an actual paper, constituted by all the common chapters, abstract included.

ABSTRACT

A careful examination of rock microstructures is crucial for understanding nucleation mechanisms and the crystallization history of magmatic systems. The two main factors influencing crystal morphology and the sample microstructure are undercooling and heterogeneous nucleation, the latter being the most energetically favorable nucleation mechanism in natural and synthetic rocks.

In this study, we investigate the effects of heterogeneous nuclei availability on the microstructure of moderately to highly undercooled synthetic trachybasalts. We conducted crystallization experiments on both anhydrous and hydrous (2 wt% H_2O) compositions, comparing a Cr-doped series (0.4 wt% Cr_2O_3) to an undoped series. Experiments were performed at 400 MPa by cooling melts from 1300 °C to target temperatures of 1150 °C, 1100 °C, and 1050 °C, followed by isothermal holds of 5 or 30 minutes.

In Cr-doped samples, euhedral Spinel grains nucleated first, followed by skeletal clinopyroxene crystallization via heterogeneous nucleation on Spinel surfaces. Because of the

high availability of Spinel grains acting as nuclei for heterogeneous nucleation, in Cr-doped anhydrous samples the final microstructure is composed of a high number of small skeletal clinopyroxenes forming on the Spinel grains and embedding them, independently of the undercooling conditions. In the samples with hydrous starting composition only the sample at 1050°C crystallized non-quenched clinopyroxenes grains in the first 5 minutes of the experiments. The undoped anhydrous samples exhibited two distinct microstructural domains: (a) a dendritic clinopyroxene domain, characterized by large, highly dendritic grains nucleating from the sample walls and sparse spinel grains, and (b) a skeletal clinopyroxene domain, similar to Cr-doped samples, where numerous small skeletal clinopyroxenes formed on early Spinel grains. The dendric microstructure is caused by the presence of a low amount of spinel grains or aggregates acting as heterogenous surfaces. Consequently, only a small number of clinopyroxene formed and were able to fast grow (dendritic morphology) without significant neighbors' competition like occurred in the Cr-doped anhydrous samples and in the skeletal clinopyroxenes domains of the undoped anhydrous samples.

Our findings confirm that even small compositional variations significantly impact crystallization history and final microstructure. More than undercooling, heterogeneous nuclei availability plays a dominant role in shaping microstructures. The presence of an early forming phase, or antecrysts/xenocrysts acting as seed for heterogeneous nucleation have the potential to induce fast crystallization of magmatic system that experience thermal or constitutional undercooling in response of a volatile loss potentially increasing magma viscosity and influencing its stagnation or fragmentation, depending on the crystallinity of the system. Moreover, we invoke caution when calculating crystal growth rates, as they are strongly dependent on the spatial distribution and density of early-forming phases that promote heterogeneous nucleation

3.1. INTRODUCTION

The careful examination of rock textures or microstructures is fundamental in order to extract information about the sequence, the timing, and the conditions of crystallization. In magmatic rocks with similar composition, microstructure variability depends on the balance between crystal nucleation and growth (*Vernon 2004*). Under plutonic conditions, nucleation and crystal growth are occurring close to thermodynamic equilibrium and the final rocks will be characterized by a low number of big, euhedral crystals (crystal growth over nucleation conditions). In volcanic or subvolcanic environments, more dynamic processes occur (e.g. magmatic recharges, volatile exsolution, proximity to colder wall rocks, eruptions) which favours disequilibrium thermodynamic conditions, where the final textures of the rocks are characterized a high number of smaller, chemically zoned grains with shapes ranging from highly dendritic to euhedral (*Hammer 2008; Iezzi et al., 2009; Higgins 2006; Mollo and Hammer, 2017*)

In crystallizing magmatic systems (not in thermodynamic equilibrium), undercooling (ΔT), defined as the difference between the liquidus temperature of a specific phase (T_{liq}) and the system temperature (T_{system}) (*Kirkpatrick 1981*), is one of the main driving forces influencing the early stages of crystallization (*Nabelek et al., 1978; Nabelek 2007; Hammer et Rutherford 2002; Shea and Hammer 2013*). In volcanic or shallow (subvolcanic) environments magma can experience relatively high undercooling. The surface proximity during a lava flow (*Vernon 2004*), degassing and/or decompression processes (*Ballhaus et al., 2023*), conduit dynamics (*La Spina et al., 2016, Arzilli et al., 2019*), magmatic recharges or magma mixing (*Ohashi et al., 2024*) are a few examples of environments or processes favouring high undercooling conditions. In these geologic settings, high nucleation and crystal growth rates

allow the nucleation of a high number of crystals characterized by skeletal to dendritic morphologies (*Vernon 2004*).

When a phase supersaturates the liquidus, it can crystallize directly from the melt by homogeneous nucleation or from the interface between the melt and a pre-existing substrate by heterogeneous nucleation. Heterogeneous nucleation requires a lower energetic barrier to be overcome in order to form a stable nucleus compared to homogeneous nucleation, making this nucleation mechanism the more energetically favoured in both natural and experimental samples (*Walker et al. 1976; Lofgren 1983; Hammer et al. 2010; Mollo et al. 2012; Arzilli et al., 2019; Pontesilli et al. 2019; Colle et al. 2023; Peres et al., 2024*). Pre-existing surfaces can be an already formed crystal acting as a seed overgrowing the same phase (*Lofgren 1983; Mollo et al., 2012; Holness et al., 2023*) or an already formed crystal of a different phase (*Hammer et al., 2010; Vetere et al., 2015; Peres et al., 2024*), impurities or nanoliths (*Lofgren 1983, Caceres et al., 2020*) and bubbles (*Davis and Ihinger, 1998; Pleše et al., 2019*).

The spatial relationship between clustered phases (both crystals and bubbles) in a 2D section has been one of the most basic observations used to justify a heterogenous nucleation mechanism between two phases (*Lofgren 1980; Lofgren1983; Kirkpatrick 1981; Mollo et al., 2012; Vetere et al., 2013;2015; Pontesilli et al., 2019*). More detailed 3D spatial characterization of the clustered phases by synchrotron radiation micro-Computed Tomography (SR-μCT) (*Arzilli et al., 2015; 2019; Polacci et al., 2018; Pleše et al., 2019; Colle et al., 2023*), investigations of crystallographic preferred orientation (CPO) and crystallographic orientation relationships (CORs, *Habler and Griffiths, 2017*) by electron backscatter diffraction (EBSD) (*Hammer et al., 2010; Wieser et al., 2019; Holness et al., 2023*), or the combination of both methodologies (*Arzilli et al., 2015; Peres et al., 2024*) can generate more convincing evidence that certain interfaces, particularly those exhibiting orientation relationships, should be characterized by lower energetic barrier (*Fleet et al.,*

1980), the situation preferred by heterogeneous nucleation (*Peres et al., 2024*). However, the assumption that CORs identified by EBSD can be used to determine heterogeneous nucleation, e.g. Tmt grains heterogeneously grown on Cpx grains (see *Hammer et al., 2010* and *Peres et al., 2024*) has never been directly tested by comparing the behavior of the same pair of phases for a varying and well-constrained sequence of nucleation.

In silicate melts, nucleation almost never happens contemporaneous to supersaturation, but is delayed from minutes to days, with the latency being assumed to be (generally) inversely proportional to the degree of undercooling experienced by the crystallizing system (*Gibb 1974; Fenn 1977; Swanson 1977; Nabelek et al. 1978; Donaldson 1979; Berkebile and Dowty 1982; Corrigan 1982; Polacci et al. 2018; Arzilli et al. 2019; Rusiecka et al 2020, Arzilli et al., 2022*). The presence of seeds which did not completely melt during a recharge episode, or heterogeneous sites which escaped the superheating preconditioning often applied for crystallization experiments, can shorten the nucleation delay and deeply impact the final texture of a rock/sample (*Lofgren 1983*).

In this work I will use the microstructural observations and results previously formulated and reported in Peres et al., 2024 to compare two experimental series with similar starting composition, approximating a synthetic trachybasaltic glass similar to Mt. Maletto eruption products (Mt. Etna *Armienti et al., 1988; 2013*), but differing in the amount of added Cr_2O_3 oxide. The series obtained are a) an undoped series (no Cr_2O_3 oxide added) and b) a glass doped with 0.4 wt% of Cr_2O_3 (referred to from here on as Cr-doped series/samples). Both series were carried out under constant isobaric conditions of 400 MPa, at an intrinsic fO2 of NNO+2 and dwell times between 0 and 30 minutes. The presence or absence of heterogeneous nuclei sites (in the form of Cr-Spinels) in the two sets of experiments deeply impacted the shape, size and number density of Cpx and Spl crystals, but also the final microstructure of the whole sample. A multimodal approach mainly based on EBSD but also

including, EPMA, Laser ablation, and SR-µCT analysis has been used to answer these specific questions: a) What are the nucleation mechanisms acting in the samples? b) How do the heterogeneous sites number density affect the shape and size of the crystal phases? c) Does the nucleation order of the crystallizing phases changes in the two set of experiments? d) Is it possible to discern crystals deriving from different nucleation events? e) Can EBSD and consequently CORs be effectively used to discern nucleation mechanism and crystallization order? f) Is there a nucleation delay and how this is dependent on the amount of heterogeneous sites? g) What are the implications of this experiment in a broader volcanological context?

3.2. METHODS

3.2.1 Crystallization experiments

Crystallization experiments were performed using two similar starting materials: a) a trachybasaltic glass, synthesized targeting the chemical composition of the Monte Maletto Formation of Mt. Etna (Italy) (*Armienti et al., 1988; 2013*) (see Peres al., (2024) for all the steps of the synthesis procedure). The synthetic glass produced had the following composition: SiO_2 = 47.00 ± 0.19 wt%, TiO_2 = 1.72 ± 0.03 wt%, Al_2O_3= 15.7 ± 0.19 wt%, FeO = 10.60 ± 0.09 wt%, MgO = 8.38 ± 0.10 wt%, CaO = 12.17 ± 0.13 wt%, Na_2O = 3.10 ± 0.06 wt%, K_2O = 1.30 ± 0.04 wt%. The experimental samples using this starting material will be referred to as undoped through the whole paper; b) the glass of (a) with the addition of 0.4 wt% of Cr_2O_3 will be referred as Cr-doped.

The experiments were carried out in a non-end loaded piston cylinder (QUICKpress) installed at the HP-HT laboratory of Dipartimento di Scienze della Terra of the University of Pisa (Italy), using a standard 19-25 mm NaCl-pyrex-graphite-MgO assembly. The assembly

materials impose oxygen fugacity conditions corresponding to 2 log units above the Ni-NiO buffer (*Masotta et al., 2012*). Pt capsules of different lengths were used for the different experimental series: 4-6 mm long capsules were used for Cr-doped and Undoped-5min series, while 8-10mm capsules were used for the Undoped experimental series. The capsules were loaded with the powdered starting glass for the anhydrous compositions, while to recreate hydrous conditions, nominally 2 wt.% of deionised H_2O was added using a micro syringe, before the capsules were welded shut and eventually inspected for weight loss after heating at 110 °C in an oven. Pyrophyllite was used as supporting medium around the capsule in order to prevent H_2O loss (*Freda et al., 2008*).

The capsule position in the assembly were chosen in order to take advantage of the intrinsic temperature gradient of the graphite furnace (as determined by an earlier calibration of the temperature distribution in the furnace and previous experimental work done with the same apparatus; *Masotta et al., 2013; Costa et al., 2020; Peres et al., 2024*). The temperature gradient imposes at the top of the capsule a temperature that is about 30-40 °C lower than at the bottom for the Cr-doped and the Undoped series respectively. The temperature is measured with a factory calibrated C-type thermocouple (yielding a precision of ± 3°C) near the centre of the capsules for the Cr-doped series experiments, and at the bottom of the capsule for the undoped series experiments.

In each experiment, the assembly was cold pressurized to 400 MPa and heated at a rate of 80 °C/min to reach the temperature of 1300 °C. The experiment was maintained at this temperature for 30 minutes to ensure full melting of the starting glass powder and subsequent melt relaxation, before cooling (at the same rate of 80 °C/min) to the final resting temperatures (T_{rest}) of 1150 °C, 1100 °C and 1050 °C. The T_{liq} of the trachybasalt with 2 wt.% H_2O was determined to be 1160 -1180°C based on PhasePlot simulations and previous experimental determination, (e.g. *Pontesilli et al., 2019; Masotta et al., 2020*) while the

anhydrous trachybasalt T_{liq} is around 1200-1210 °C. Table 2 (end of the file) summarizes the temperature of each sample in their bottom, center and top portions.

Cr-doped experiments were terminated after 5 min and the Undoped series experiments either after 5 or 30 min by turning off the power supply and maintaining the pressure constant during the quench (100 °C/s). The only exception is one experiment at 1100 °C, which has been quenched right after the undercooling ramp, and no dwell time was applied. The experimental runs were named as follows: each sample label comprises the resting temperature (T°C), followed by an indication of anhydrous or hydrous composition (d=dry, w=wet) and the designation Cr-doped or Undoped to represent the major element components, followed by the dwell time expressed in minutes (see table 2, Supplementary chapter, after "CONCLUSIONS"). Only Undoped samples with 30min dwell time were measured by SR μCT and analyzed through EPMA and EBSD. Samples 1100°C-undoped-0min, 1150d-Undoped-5min and 1100d-Undoped-5min were only imaged using the SEM. We carried out also repeat experiments for two samples, 1150d-Cr-doped-5min, and 1100d-Cr-doped-5min (these sample have the suffix BIS in their name).

3.2.2. Electron backscatter diffraction (EBSD) measurements

In order to determine the crystallographic orientations of the crystals in representative areas and specific spots of interest on samples, EBSD scans were collected using a FEI Quanta 3D FEG-scanning electron microscope (SEM) equipped with an EDAX Digiview 5 EBSD camera (elevation angle 5°), located at the laboratory for field-emission scanning electron microscopy and focused ion beam applications at the Faculty of Geosciences, Geography and Astronomy, University of Vienna (Austria). The OIM Data Collection v7.3.1 software was used for EBSD data acquisition, and OIM Analysis 8.0 for re-indexing. Beam conditions for all EBSD scans were 15 kV accelerating voltage and spot size 1.0 (~ 4 nA probe current), with a 1 mm SEM aperture, a working distance of 14 mm and a beam incidence angle of 20°.

All scans used an EBSD camera binning of 8 x 8 pixels, a binned pattern size for Hough transforms of 140 pixels, a Hough θ step size of 1° and a 9 x 9 convolution mask. Step sizes ranged from 320 nm to 650 nm, always on a hexagonal grid. Tmt and Spinel were indexed as face-centred cubic, Cpx was indexed as monoclinic (b-setting), using the lattice parameters a = 9.585 Å, b = 8.776 Å, c = 5.26 Å, and β = 106.85°, and amphibole (Amph) was indexed as monoclinic (b-setting) using the lattice parameters a = 9.871 Å, b = 18.028 Å, c = 5.307 Å, and β = 105.24°. After standardizing confidence index values to the highest for each reconstructed grain using OIM Analysis 8.0, the Matlab toolbox MTEX version 5.6.1 (*Bachmann et al., 2010; Hielscher et al., 2010*) was used for data processing and plotting. Pixels with confidence index values below 0.1 were classified as not indexed. Grains were then calculated using a misorientation angle threshold of 15°. EBSD pixels belonging to grains less than 4 pixels in size were removed before recalculating grains with the same misorientation angle threshold to obtain the final datasets used for analysis. Finally, six iterations of smoothing were applied to the boundary traces using the smooth () function of MTEX. This does not alter the misorientation at boundary segments.

3.2.3. EPMA

Cpx, Tmt, and glass major element analyses and chemical maps were performed at the Department of Lithospheric Research of the University of Vienna, Austria, using a CAMECA SXFiveFE EPMA equipped with five wavelength dispersive spectrometers and one energy-dispersive X-ray spectrometer (EDX). All four phases were analysed at 15 kV accelerating voltage and beam current of 20 nA. A beam diameter of 1 µm was used for Cpx, Amph Tmt and Cr-Spinel spot analysis, while a diameter of 5 µm was used for the glass analysis. Peak counting times varied for each element: Na = 10 s; Si = 14 s, Al = 10 s; Fe = 22 s; K = 10 s; Ca = 20 s; Mg = 20 s; Ti = 15 s; Mn = 24 s. Detection limits were: 100-250 ppm for Al, Na, Mn, and Ti; 300-500 ppm for Si, Fe, Mg, Ca and K. Element distribution maps were acquired

in beam scan mode, with a 35.5 nA beam current and 15 kV accelerating voltage. Map size varied depending on the investigated microstructure, while a fixed step size of 0.33 µm and a dwell time per pixel of 80 ms was applied. Relative Mg, Fe, Ca, Na, Ti and concentrations were mapped using five wavelength dispersive spectrometers set to the corresponding Kα emission wavelengths for each element, while Si and Al concentrations were acquired through EDX. In Cr-doped experiments Cr maps were also acquired, replacing the Fe chemical maps.

3.3. RESULTS

3.3.1 Sample description:

Cr-Doped series

Anhydrous doped samples (Fig.3.1a-c, e-f): These three experimental runs share similar features regardless of the ΔT applied. Skeletal Cpx crystals, with size ranging between 20 µm and 120 µm (EBSD/SEM image analysis), are the main crystal phase, comprising up to 50% of the samples. Spinel, appearing as small euhedral grains (up to 4 µm in size), composes between 4 and 6% of the samples. These grains are either scattered within glass regions or partially to completely engulfed by larger Cpx crystals. Overall, the crystallinity slightly decreases while the size of the Cpx crystals increases from the colder to the hotter portions of each sample (Table 1). In the hotter portion of the 1150d-Cr-doped-5min sample (temperature close to 1170°C), the final 500 µm of the capsules contains less than 5 vol% Cpx crystals, although euhedral Spinel grains remain present (Supplementary Figure S7).

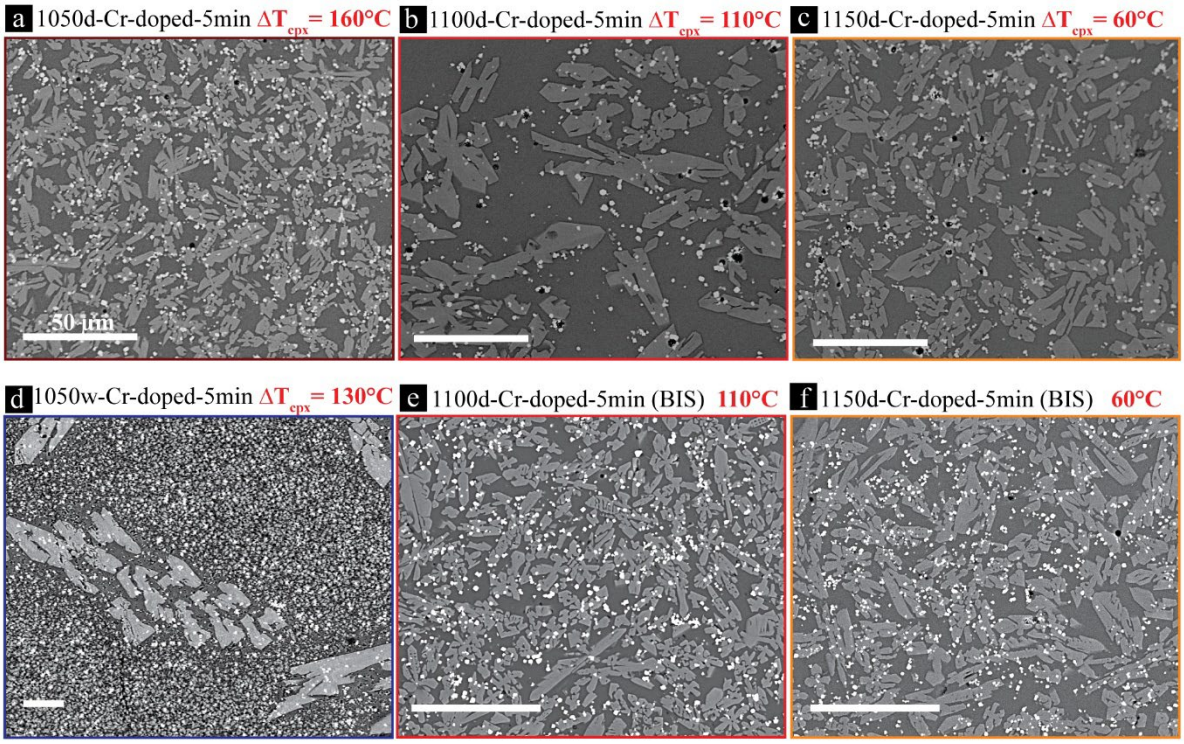

Fig.3.1. BSE images of representative areas of Cr-doped-5min samples. In white the Spl grains, in light grey are the Cpx grains; in dark grey is the remaining melt and in black are small bubbles. All scale bars are 50 µm in length.

Hydrous doped samples (Fig.3.1d): All the samples are composed of spinel grains similar in shape and size to those present in the anhydrous runs, constituting up to 5% of the samples, and distributed similarly as in anhydrous samples. Only the sample held at 1050 °C shows the presence of large (long axis up to 500 µm) skeletal Cpx crystals, which comprise less than 20% of the sample. These grains can completely engulf Spl crystals. In all samples a smaller population of Cpx grains (a few µm in size) is found arranged radially around spinel crystals.

Undoped series:

Anhydrous undoped sample 1100d-0min (Fig.3.2a): the sample is almost completely glassy (>>99%). The crystal phases observed consist of a few small BSE-bright grains in the range size between 50 nm and 200 nm (SEM measurement), probably oxides, and more likely Spl grains, surrounded by equally small dendritic crystals, which might represent a silicate phase, probably Cpx. Because of the size of the grains, I could not quantitatively measure them.

Anhydrous undoped samples held at 1150/1100/1050°C for dwell times from 5 to 30 minutes (Fig.3.2 and Fig.3.3): All five anhydrous samples are characterized by the presence of different microstructural domains as a function of the undercooling experienced and the Cpx shape in the different regions of the samples. The two main microstructural domains present in all the samples are: a) a skeletal Cpx domain characterized by small (up to 50 μm in size) skeletal shaped Cpx grains in the more undercooled portions of the samples, and b) a dendritic Cpx domain, characterized by large (up to 300 μm in size) mostly feather-shaped Cpx crystals in the less undercooled portion of the samples (Supplementary Figure S8 and S9).

The **skeletal domain** occupies the regions of the samples, which experienced higher degrees of undercooling (Fig.3.2b and d, Fig.3.3d). The size of the skeletal shaped Cpx grains range between 10 μm and 50 μm and it comprises between 45% and 50% of these regions. Spl grains comprise up to 3% of these domains and two crystals populations can be distinguished based on size and morphology: a) the first, more recognizable population, is characterized by euhedral shapes, with size up to 6 μm; b) the second population is composed by sub-micrometre anhedral crystals which decorate the edges of the Cpx crystals. The 2D sectioning we perform, in order to analyse the chemical composition and microstructural parameters of the crystal phases, observed the presence of this domain only in samples 1150d-undoped-5min, 1100d-undoped-5min and 1100d-undoped-30min. This is caused by imperfect perpendicularity of the cut with respect to the vertical dimension of the samples. Tomographic reconstruction of the whole samples (Supplementary Figure S8 and S9) reveals the presence of this domain also in sample 1150d-Undoped-30min and 1100d-Undoped-30min. In the reconstructed axial view of these samples, the lack of large dendritic Cpx crystals and the presence of recognizable euhedral Spl grains are the main evidence for the

presence of this specific domain, as segmentation of Cpx from glass is often difficult given the morphology and size of Cpx crystals.

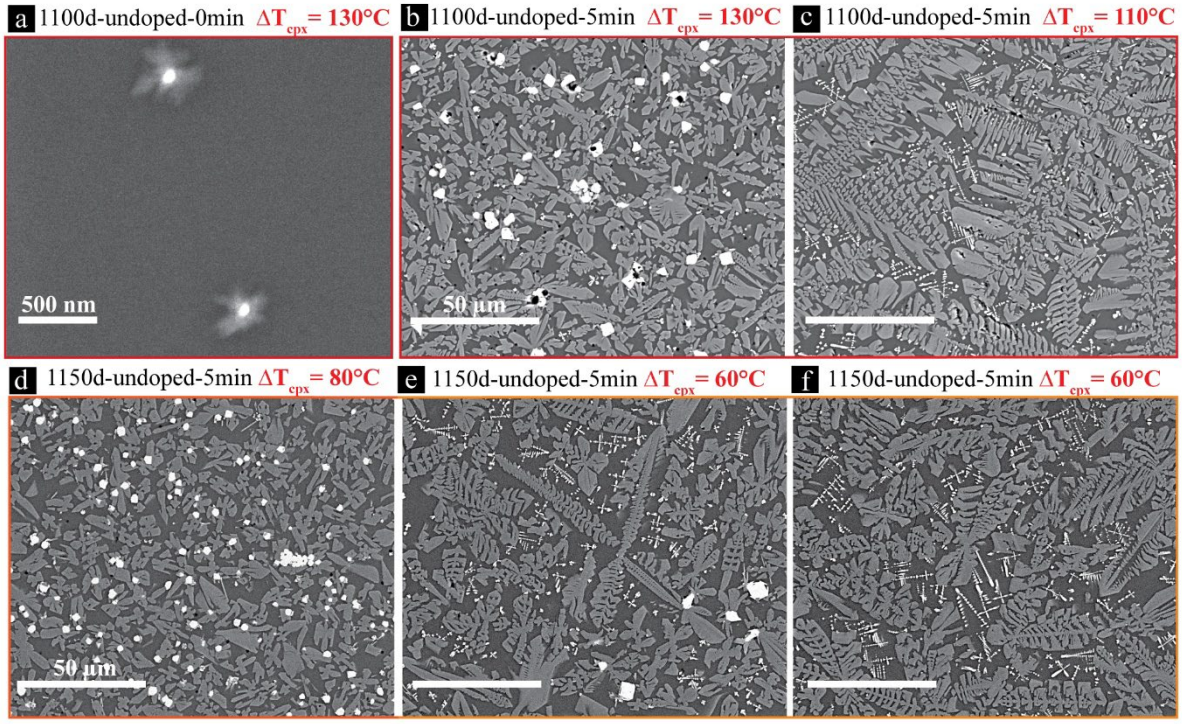

Fig.3.2. a) SE image of some of the few nanometres' size Spl and Cpx crystals present in sample 1100d-undoped-0min, the scale bars are 500 nm in length. b-f) BSE images of representative portions of undoped-5min samples; the scale bars are 50 µm long. b and d) BSE image of the skeletal cpx domain in sample hold at 1100°C and 1150°C respectively; c and f) BSE image of the dendritic (feather-like) cpx domain in sample hold at 1100°C and 1150°C respectively. e) BSE image of the transition zone between the two microstructural domains (dendritic and skeletal). In white the Spl grains, in light grey are the Cpx grains; in dark grey the remaining melt and in black are small bubbles.

The **dendritic domain** **(Fig.3.2 c and f; Fig3.3a-c)** occupies the central and bottom regions of each sample, making up between 55% and 65% of the analysed area. In the innermost/central portions of the samples the Cpx grains are characterized by a main branch, 100 µm in length, from which several orders of branches, of the same size, radially depart (Fig.3.3a-b) and that resemble, **snowflake-like shapes**. In the warmer, less undercooled portion of the samples and near the walls of the samples, Cpx dendrites assume a **feather-like shape**. The crystals showing this morphology are composed by one main branch, often curved and up to 300 µm in length and few µm in width, from which multiple shorter (10-100 µm in length) second order branches radially depart, at a space interval of a few µm from each other **(Fig.3.3c).** In the dendritic regions Cpx is the main crystal phase, comprising

between 55% and 65% of the sample. Two Spinel morphologies can be recognized in dendritic Cpx regions: i) dendritic grains characterized by a long (up to 50 µm) main branch from which shorter (a few µm in length), second-order branches radially grow from, mostly occupying glass regions at the conjunction between two or more Cpx grains; and ii) small (few µm in size) anhedral shaped Spinel grains, mostly present in the glass between Cpx crystals branches, always in contact with the Cpx .

The skeletal and dendritic domains are present in all three Undoped samples with anhydrous starting composition, in different proportions. The skeletal Cpx domain is volumetrically more abundant in 1150d_5min samples (50 to 70% of the volume) compared to other Undoped sample, like 1150d_30min samples in which this domain constitutes less than< 30% of the sample). In the experiments carried out at lower temperatures, the volume occupied by this domain is between 15 and 30%, except for sample 1050d-undoped-30min, where this domain cannot be recognized,

Along all three samples it is possible to observe Spl aggregates of the size of 100-200 µm composed by tens to hundreds of single crystals (Supplementary Figure S9). In the dendritic domain, both feathery and snowflake-like Cpx grains can radially arrange respect to single Spl grains (Fig.3.10a-c) or Spl aggregates (Supplementary Figure S11).

Hydrous undoped sample 1100w-30min, has been already described by *Peres et al., 2024*. It is composed of large (up to 500 µm in length) skeletal Cpx crystals in the portion of the sample at lower ΔT, which become shorter (between 100 and 200 µm) and more dendritic in the portion of the sample characterized by higher ΔT **(Fig.3.3e)**. Different spinel populations have been classified by their morphologies: a) large skeletal Tmt grains completely (or almost) isolated in the glass; b) smaller, anhedral to acicular Tmt grains always decorating the

internal or external branches of a Cpx crystal; c) acicular Tmt grains almost completely embedded in Cpx crystal (see chapter 2.3.2).

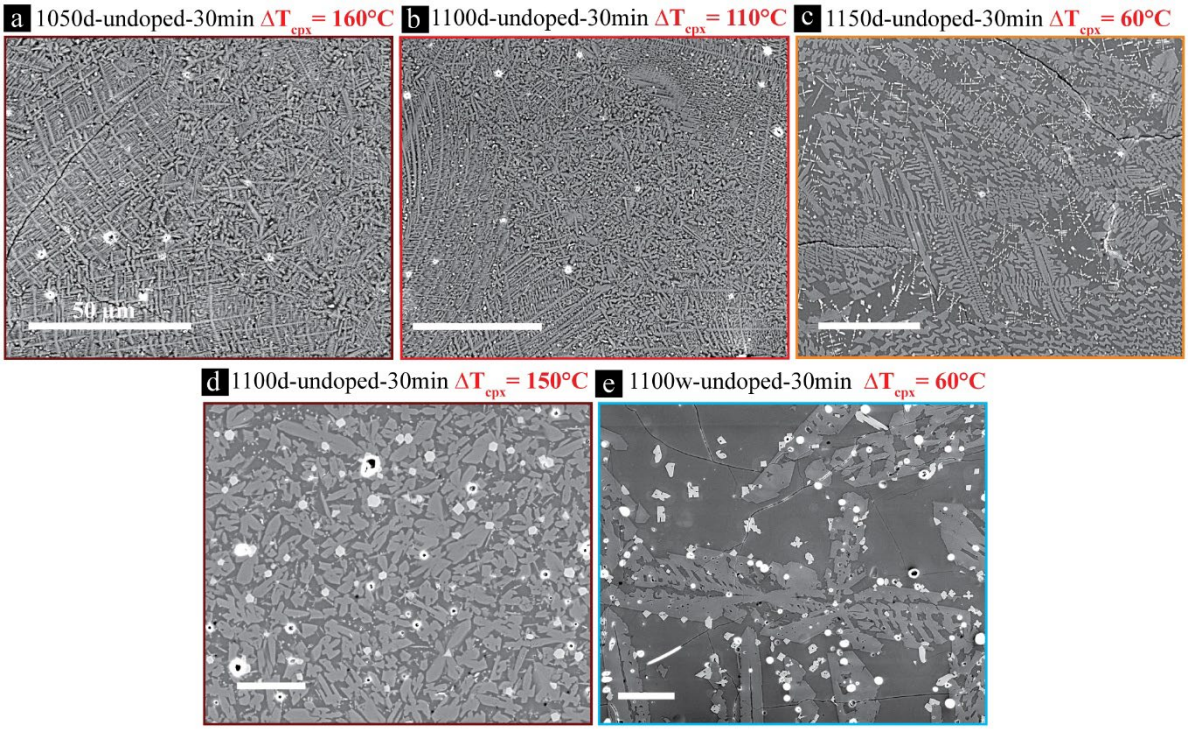

Fig.3.3. SE images of representative portions of Undoped-30min samples. a-c) dendritic domains in the anhydrous samples. Feather-like Cpx grains are more present in the left part of (a), in the side portions of (b) and the whole (c) image. Snowflake-like Cpx grains are shown in the right side of (a) and in the middle of (b). d) skeletal Cpx domain of sample 1100d-undoped-30-min. e) less undercooled portion of sample 1100w-undoped-30min. In white the Spl grains, in light grey are the Cpx grains; in dark grey is the remaining melt and in black are small bubbles. All scale bars are 50 µm in length.

3.3.2. EBSD results

Multiple EBSD scans were acquired on all dry doped samples and undoped-30min samples. The sample 1100d_undoped_0min was unsuitable for proper EBSD analysis as it comprised only nanometre-sized crystals. Samples 1150w_Cr_doped_5min and 1100w_Cr_doped_5min lacked Cpx crystals not formed during the quenching process, thus EBSD analysis was not required. Samples 1150d_undoped_5min and 1100d_undoped_5min will be analysed in the following months if necessary.

Using MTEX, we obtained statistical data/parameters like the number of Spl (Tmt) and Cpx crystals, the misorientation of each pixel to the mean orientation of the grain (mis2mean) and the mean value of all the mis2mean in a scanned area or in a sample, as well as the

crystallographic misorientation at boundary segments shared between Cpx and Spl (CORs). We will present the EBSD results organised by the aforementioned parameters:

3.3.2.1. Number of crystals, and number density

The number of crystals for each phase was calculated in order to estimate a crystal number density of each phase in representative regions of the samples (see Table 3 in Chapter 7. Tables and Supplementary Figures).

Cr-Doped anhydrous series: A total of 13,949 Spl and 3,090 Cpx grains were identified in the EBSD maps across a cumulative scanned area of 0.267 mm^2. While the number of Spl grains estimated through EBSD is reliable due to their euhedral morphology, the estimation for Cpx crystals is not valid due to the skeletal nature of Cpx grain morphologies, which inherently leads to an overestimation of the actual number of crystals present. To address this issue, a MTEX script was created to remove non-indexed points (i.e., points corresponding to glass), allowing contiguous crystals with similar orientations but separated by glass to be joined, based on the assumption they represent separate parts of the same crystal in 3D, due to the interplay between 2D cutting effects and the dendritic shape of the crystals (Supplementary Figure S10 is an example of the EBSD map where we removed the non-indexed points). After this correction, a total of 2,442 Cpx grains were counted.
The Cpx crystal number density calculated in the Cr-doped series is 9.14 x 10^3 mm^{-2}., while Spl crystal number density is 51.26 x 10^3 mm^{-2} .
Small areas (< 900 μm^2) of sample 1050w-Cr-doped-5min have been scanned to characterize the existence of CORs between oxides and Cpx, but since they are not representative of the entire sample regarding crystal number density of the two crystal phases, no results regarding this parameter will be given.

Undoped series: 13 EBSD scans were performed on samples with anhydrous starting composition, including six in the feather-like Cpx domain, three in the snowflake-like Cpx domain and four in the skeletal domain. The same filter used in the Cr-doped samples was applied to the feather-like, the snowflake-like and skeletal Cpx domains. The evaluation of Cpx numbers in the feather-like domain proved even more challenging due to the extreme dendritic morphologies. The same corrections used for the Cr-doped samples were applied, along with additional size filters to realistically assess the number of Cpx grains. We estimated based on visual inspection of morphologically distinguishable dendrite domains in EBSD maps and SEM image that the number of Cpx crystals with area greater than 500 μm^2 offers the most realistic estimation of crystal number in the scanned areas. The lower crystal number density, characteristic of the feather-like Cpx domain (dendritic region), ranged from 2.94 x 10^3 mm^{-2} to 3.64 x 10^3 mm^{-2}, while the higher density was found in the snowflake-like Cpx region, ranging from 64.35 x 10^3 mm^{-2} to 88.39 x 10^3 mm^{-2}. While this corrected range of crystal number density are reliable for the Cpx grains count, Spl grains count is not so reliable. Indeed, even if these corrected maps are good in estimating dendritic grains, if multiple Spl grains share CORs with the nearest Cpx grain, they result in having the same crystallographic orientation (different Spl grains), which here result in being considered the same grain, which introduces an underestimation in the crystal number. The range of Spl crystal number density ranges between 59.88 x 10^3 mm^{-2} and 84.56 x 10^3 mm^{-2} in the feather-like Cpx domain and between 89.40 x 10^3 mm^{-2} and 110.88 x 10^3 mm^{-2} in the snowflake-like Cpx domain, where the lower number density represents the "corrected" value, while the higher one is the value without corrections.

The skeletal regions showed Cpx crystal number density with intermediate values ranging from 34.6 x 10^3 mm^{-2} to 45.3 x 10^3 mm^{-2} , while the Spl crystal number density ranges between 34.11 x 10^3 mm^{-2} and 46.56 x10^3 mm^{-2}.

Of all samples analysed, 1100w-30min exhibited the overall lowest Cpx number densities, with values lowest in the portion of the sample with lower undercooling ($1.26x10^2/mm^2$) and higher in areas characterized by higher undercooling ($6.13x10^2/mm^2$), but still one or two orders of magnitude lower than all the anhydrous samples previously reported.

3.3.2.2. Misorientation to mean (mis2mean)

EBSD maps enable the analysis of grain lattice orientation and potential lattice misorientation. We calculated the misorientation of each EBSD pixel relative to the mean orientation of the grain to which it was assigned (**mis2mean**) and the mean value of this value over the whole map, in order to qualitatively assess the degree of bending within the grains across different scanned areas. For these samples we are going to refer to low degree of bending when the value of the "mean mis2mean" is close or lower than 1° while we refer to high degree of bending for mean mis2mean values higher than 2°.

In all the **Cr-doped experimental (Fig.3.4a) series** and the **skeletal Cpx domain of the anhydrous samples (Fig.3.4b)**, including the **hydrous sample 1100w_30min**, we observed negligible crystal bending. The mean mis2mean values ranged from 0.5° to 1° for Cpx and Spl grains, respectively while single pixel mis2mean values are up to 5° in some grains.

All 30-minute samples with an anhydrous starting composition displayed extremely bent crystals in the dendritic domain (Fig.3.4c-d). The Cpx grains in the feather-like Cpx regions (Fig.3.4c) exhibited the highest mis2mean values. Here, Cpx grains showed a whole-map mean mis2mean bending ranging from 2° to 9°, with some portions of individual grains reaching mis2mean values as high as 40° at the outermost crystal tips. For Spl grains, the whole-map mean mis2mean is slightly lower, in the range between 0.6° to 3.1, reaching the maximum in the sample 1150d-undoped-30min, with a peak of mis2mean value observed at around 15°. In the snowflake-like Cpx region in the dendritic domain (Fig.3.4d), the mean

mis2mean for Cpx is lower but Cpx is still quite bent, with the whole-map mean mis2mean ranging between 1.0° and 2.1°, where the central portions of these crystals show light bending (<2°), whereas the tips exhibited significant bending, with individual pixel mis2mean values reaching up to 15°. The skeletal Cpx domains show almost no crystallographic bending, similarly to the Cr-doped samples, with mean mis2mean values <1° for both the crystal phases.

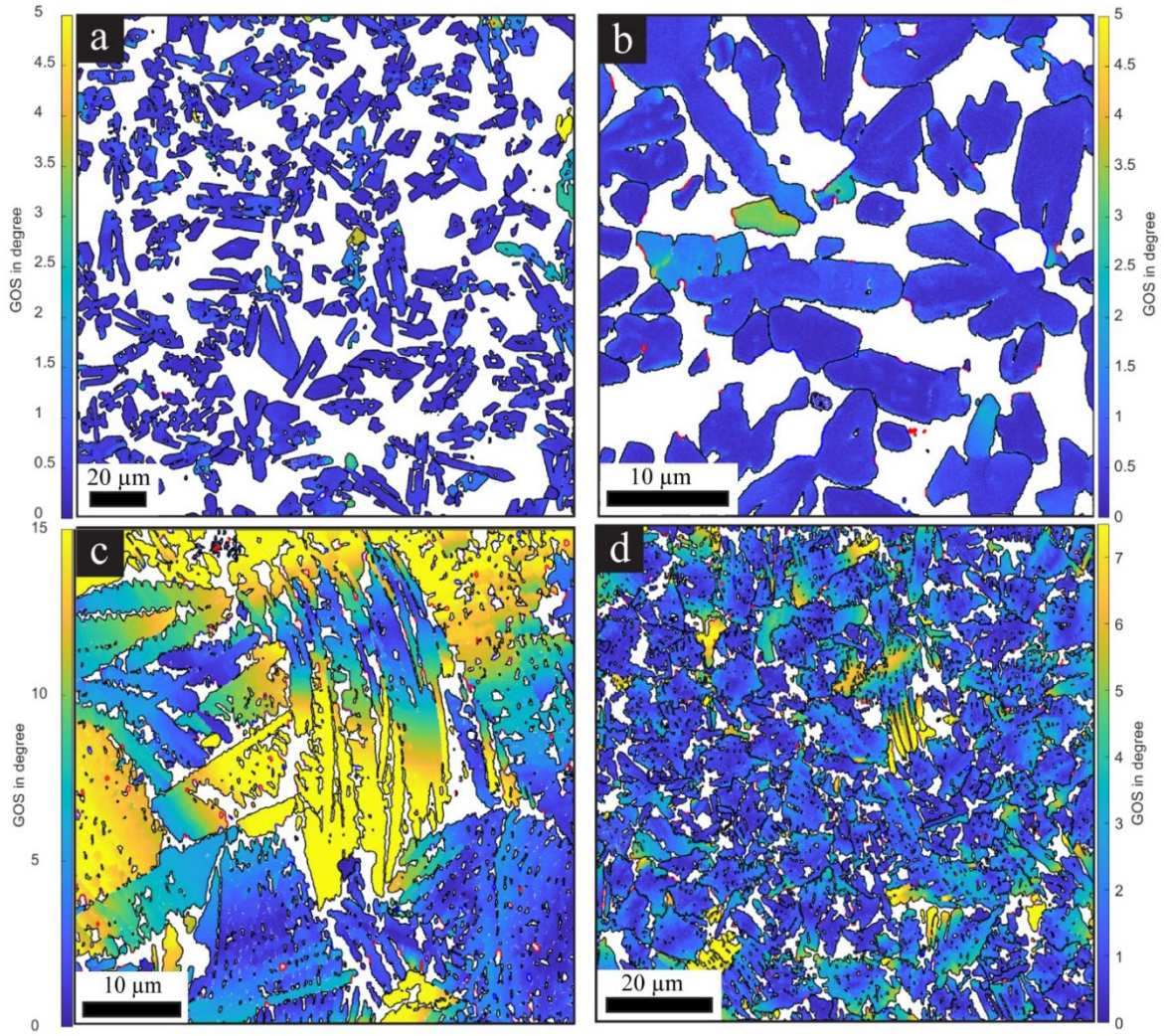

Fig.3.4. Mis2mean maps where blue colors represent low values of orientation spread, while yellow colors represent higher values of orientation spread. Blue and red borders represent the Cpx-Tmt boundaries sharing CORs. a-b) show representative portions of sample 1150d-Cr-doped-5min and 1100d-undoped-30min (skeletal cpx domain) where the Cpx grains are not deformed (blue colors). c-d) show representative portions of the dendritic Cpx domains in sample 1050d-undoped-30min characterized by feather-like Cpx grains (c) and snowflake-like Cpx (d). The Cpx grains in this sample show along the whole branches or near the tips a continuous lattice rotation resulting in high values of orientation spread (yellow colors).

3.3.2.3. COR statistics

For a complete and exhaustive understanding of the specific and rotational statistical CORs found in these scans, and the definition of COR1 and COR2, see section 2.3.5.

Also, I followed the approach of *Peres et al., (2024)* to categorize: 1) boundary segments with misorientations close to COR 2* (2.7° tolerance); 2) boundary segments with misorientations close to COR 1 (2.7° tolerance); 3) boundary segments with a misorientation < 6° from the midpoint between COR 1 and COR 2* (nearCOR); 4) all remaining boundary segments, which do not share CORs; 5) boundary length fraction (BLF) of all the four aforementioned categories, calculated as the cumulative boundary length of each category divided by the total Spl-Cpx boundary length (i.e. BLF_{COR2*}, BLF_{COR1}, $BLF_{nearCOR}$ and BLF_{noCOR}). In Figure 3.5 we show only a representative map from each experimental series.

In Cr-doped anhydrous experiments, among all Spl grains, 60.8% share a boundary with a Cpx. Of the total length of Tmt-Cpx boundaries in EBSD scans, 95.6% do not follow a COR (BLF_{noCOR}), while 4.4% are characterized by an orientation relationship (BLF_{anyCOR}). This latter value corresponds to the sum of BLF_{COR1} (0.1%), BLF_{COR2} (4.0%) and $BLF_{nearCOR}$ (0.3%) and it is similar in all the Cr-doped samples. COR2* is the most represented in all 6 samples, reaching a max of BLF_{COR2} of 6.6% in sample 1050d_Cr-doped-5min. The density of grain boundaries following or close to a COR is 2.29/mm [mm/mm^2].
In Sample 1050w_Cr_doped_5min (the only hydrous sample scanned through EBSD) (Fig.3.6 first row) only Spl and quenched Cpx boundaries show ORs, but they statistically follow the same percentages of various CORs, while the density of grain boundaries following or close to a COR is 3.94/mm [mm/mm^2].
In the undoped anhydrous experiments, among all Spl grains, 69.6% share a boundary with a Cpx grain. Although this value is similar compared to the Cr-doped series, the statistics regarding the CORs in these samples are an order of magnitude higher. Indeed, of the total

length of Tmt-Cpx boundaries in EBSD scans, 66.6% follow or are close to a COR (BLF_{anyCOR}), which can be subdivided into 22.0% of BLF_{COR1}, 31.1% of BLF_{COR2}, and 13.5% of $BLF_{nearCOR}$ (Fig.3.6 second row). The density of grain boundary length following or close to a COR is 34.85/mm [mm/mm^2].

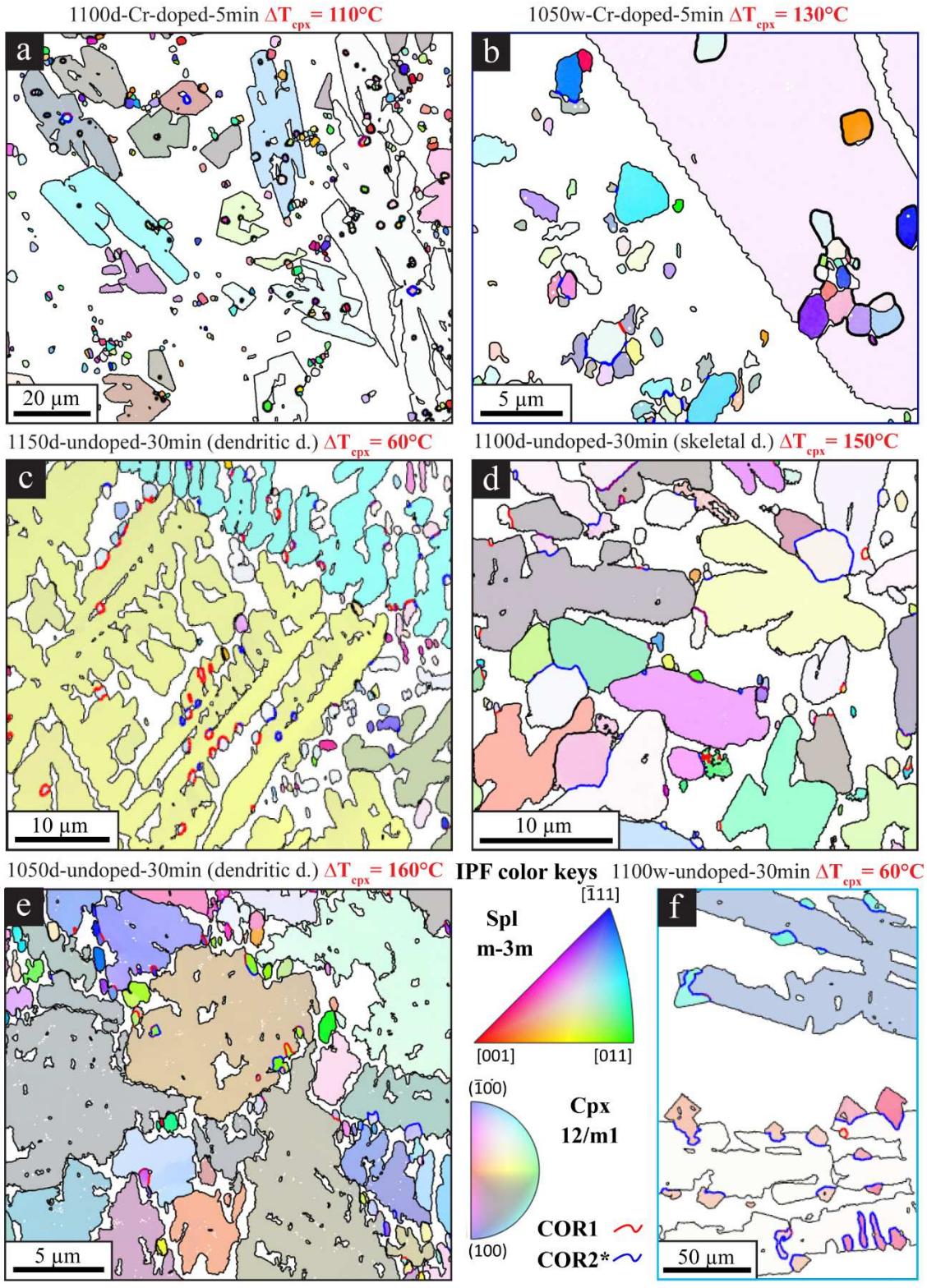

Fig.3.5 EBSD inverse pole figure (IPF) maps of Cpx-Tmt crystal clusters showing different colors for different crystallographic orientations, along with the CORs followed at different Cpx-Tmt boundary segments. a) Sample 1100d-Cr-doped-5min, almost all Spl grans in contact with a Cpx do not have no COR (black bold line). b) Sample 1050w-Cr-doped 5min. The big Cp grain embeds small Spl grains without sharing COR (black bold line); the quenched Cpx around the Spl in the surrounding glass show CORs (red and blue bold lines). c-f) sample 1150d-undoped-30min (c), 1100d-undoped-30min (d), 1050d-undoped-30min (e) and 1100w-undoped-30min (f). In all these samples most of Cpx-Spl clusters share a CORs. Spl = intense colors; cpx = lighter colors (60% transparency applied); Black bold lines = cpx-tmt interfaces without CORs; Red bold lines = cpx-tmt interfaces with COR type 1; Blue bold lines = cpx-tmt interfaces with COR type 2; Purple bold lines = cpx-tmt interfaces outside of OR1 or OR2 but within a range of 6° misorientation*

Dividing the results according to the region where the maps have been performed in the samples, i.e. feather-like, snowflake-like and skeletal Cpx domain (Fig. 3.6 third row), we see a similar amount of BLF_{anyCOR} (65.2% and 63.1% and 74.9% respectively) but a higher amount of BLF_{COR2} in the skeletal cpx domain (54.1%), compared to the feather- and snowflake-like domains (27.0% and 30.2% respectively).

In undoped hydrous sample 1100w-30min 66.7% of Spl are in contact with a Cpx crystal. 88.6% of the shared boundaries follow or are close to a COR (BLF_{anyCOR}), which can be broken down in 20.1% BLF_{COR1}, 52.5% BLF_{COR2} and 18.7% $BLF_{nearCOR}$ (Fig. 3.6 last pie chart in of the second row). The values are sensitive to the different ΔT applied in the sample. The portion of the sample with lower ΔT has a maximum of BLF_{COR2} corresponding to 80.0%, decreasing to 34.1% in the region of the sample affected by higher ΔT. BLF_{COR1} behaves in the opposite manner, increasing from 5.7% in the region with lower ΔT, to 26.8% in the region with higher ΔT *(Peres et al., 2024)*.

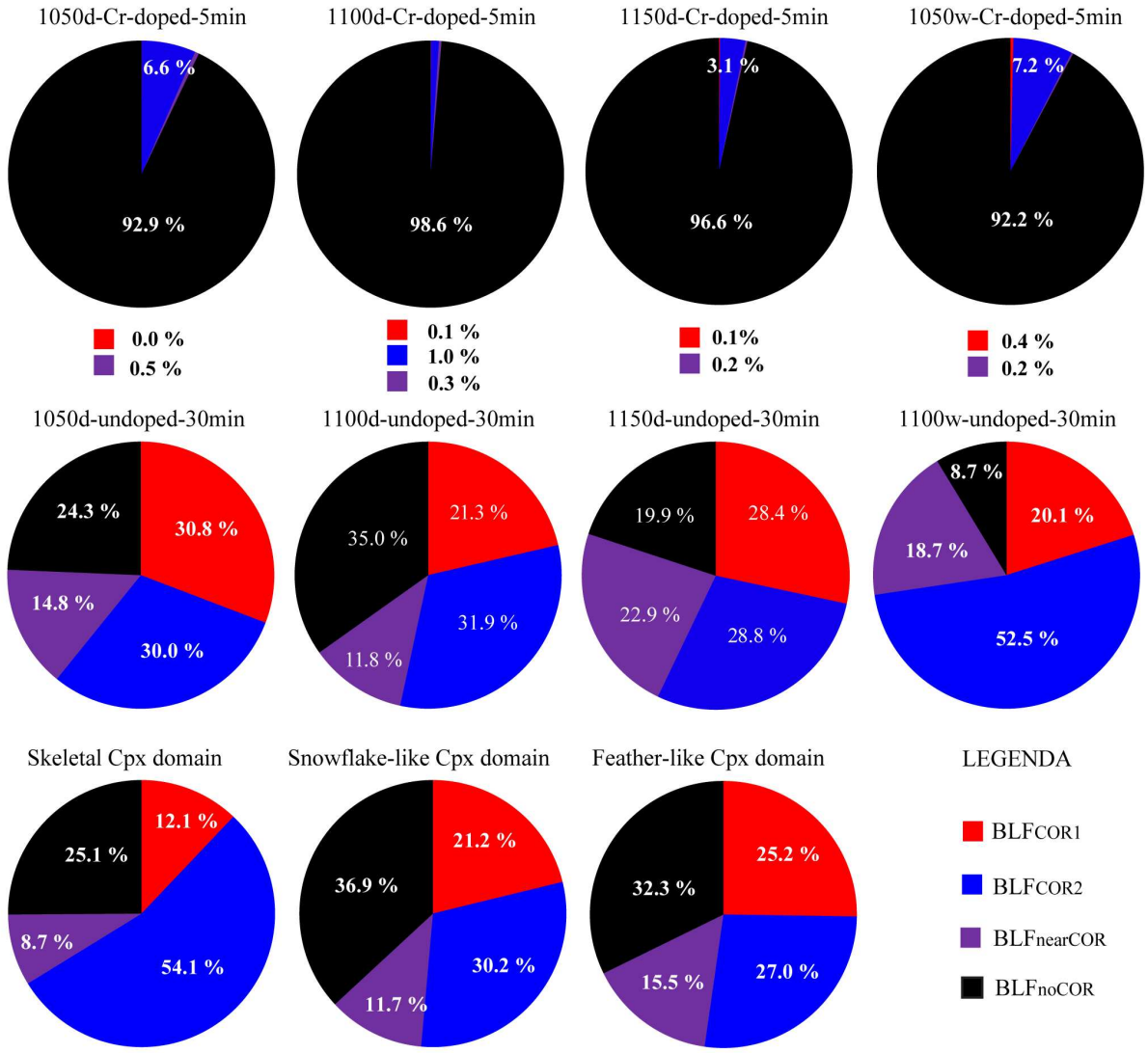

Fig.3.6. Pie charts of Tmt-Cpx boundary length fraction (in percentages) characterized by CORs in Cr-doped samples (first raw), undoped samples (second raw). Undoped samples has also been grouped Cpx domain wise (third raw).

3.3.3. EPMA chemical maps

Cr-doped experiments: EPMA chemical maps have been performed in all Cr-doped series experiments. Cr, Ti, and Mg black and white intensity maps, where whiter shades of pixels correspond to higher concentrations of the element, have been converted into red, green, and blue maps. As for the maps using grey scale values, also in the single-coloured maps the colour intensity corresponds to the concentration of the respective elements. The single-coloured maps are then combined through Fiji software to generate a multi-coloured RGB map where the colour corresponds to the amount of each element present.

All Cr-doped samples (Fig. 3.7a-b) evidence the presence of chemical zoning in both Cpx and Spl crystals. In the Cpx crystals the greener areas correspond with the Al_2O_3 + TiO_2-rich sectors, while the bluer areas correspond to the SiO_2 + MgO-rich sector. The chemical zoning in Spl grains is composed by a chromitic core (red regions in the maps) and titanomagnetite rim (green rim in the Spl grains Fig. 3.7a-b). This chemical feature is present in both the Spl crystals totally embedded in a Cpx grains and the ones surrounded by melt or quenched Cpx microlites.

Undoped series: EPMA chemical maps have been performed in sample 1100d-30min and 1100w-30min (Fig.3.7c-d). Multi-coloured maps where red, green, and blue correspond to the relative concentration of Fe, Ti and Mg have been created. The anhydrous sample 1100d-30min shows the presence of three compositionally different Spl populations. A population richer in Ti, most likely Ti-poor Titanomagnetite, which corresponds to the orange grains, often occupy interstitial regions, where the fraction of glass is higher. The second Spl population comprises grains richer in Fe and Mg. These grains correspond to the Spl coloured magenta and mostly occupy the glass between the different sub-branches of Cpx. The third Spl population is represented by the greenest grains in the undoped dry samples (Fig. 3.7c), which correspond to a higher Ti concentration. Unfortunately we have no point analysis for this Ti population so a more precise classification is not possible. This phase is also hard to index through EBSD, while Raman spectra identified the phase as an inverse spinel.
The hydrous sample 1100w-30min shows the presence of skeletal Cpx grains characterized by zoning corresponding to Al_2O_3 + TiO_2-rich inner sectors, greener in Fig. 3.7d, and SiO_2 + MgO-rich bluer sectors. Spinel grains are mostly Ti-poor Tmt grains, which correspond to the yellowish grains in the map in Fig. 3.7d.

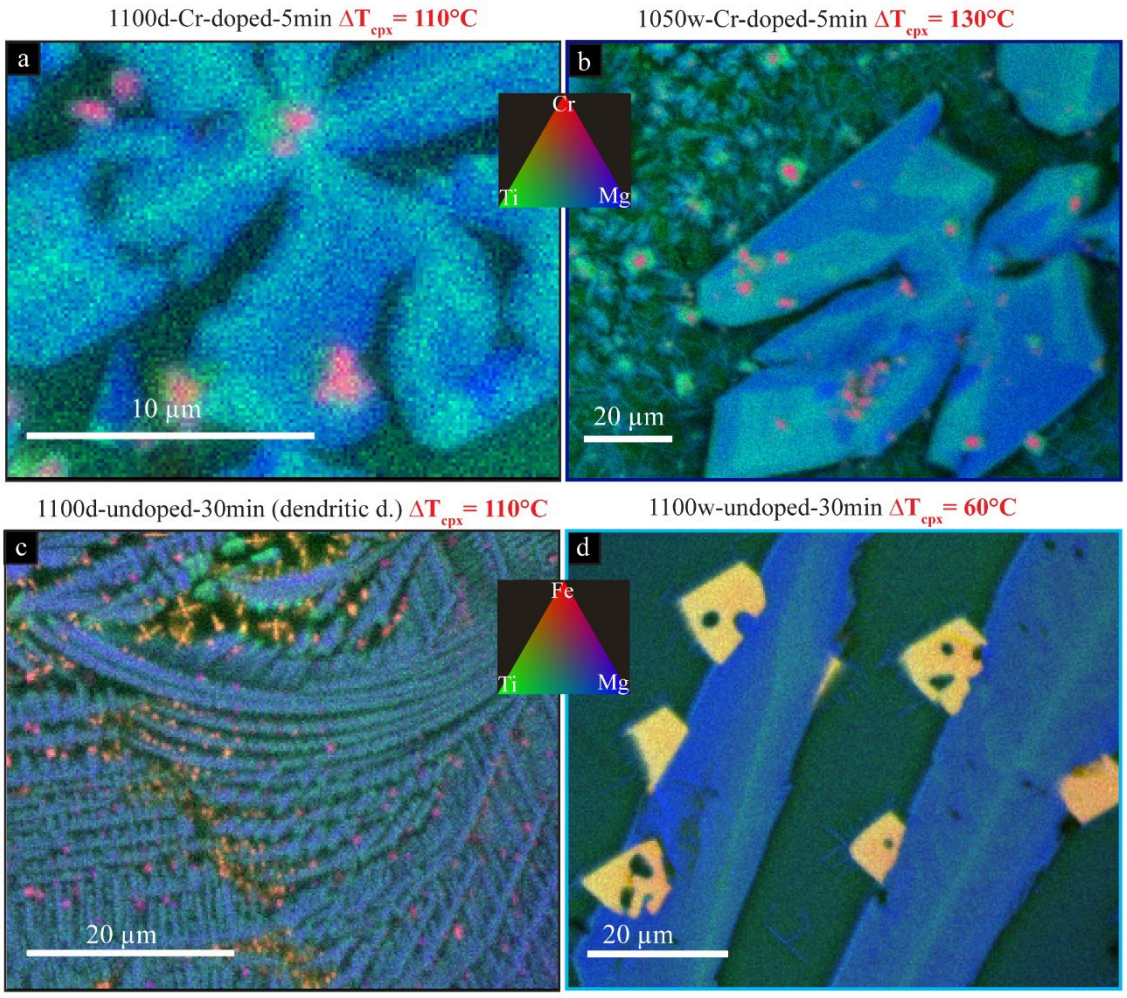

Fig.3.7. Colour-combined maps from EPMA chemical analysis. In maps (a, sample 1100d-Cr-doped-5min) and (b, sample 1050w-Cr-doped-5min), regions displaying reddish/magenta hues indicate high relative concentrations of Cr, lower concentrations of Mg, and minimal Ti. Conversely, maps (c, sample 1100d-undoped-30min) and (d, sample 1100w-undoped-30min) reddish/magenta hues indicate high relative concentrations of Fe, lower concentrations of Mg, and minimal Ti. All maps feature greenish areas in clinopyroxene (Cpx) denoting Ti-rich zonation (Al + Ti rich zones). Bluish areas in Cpx grains in these maps signify Mg-rich zonation (Si + Mg rich-zones). Yellow hues in maps (c) and (d) indicate areas with high relative Fe, lower Ti, and even lower Mg concentrations. Greenish zonation is the Spl grains denote the presence of Tmt richer zonation

3.4. DISCUSSION

3.4.1 Nucleation mechanisms in the two experimental series.

In this section, I will discuss the crystal phases or populations that form through heterogeneous and homogeneous nucleation. To discern between these two nucleation mechanisms, we will examine the microstructural relationships among the three main phases present: Spl grains, Cpx grains, and glass. This analysis will specifically focus on cross-cutting observations coupled with detailed analysis of CORs between the crystal phases. As already mentioned in chapter 2.4.1, heterogeneous nucleation is expected to favour CORs, which represent an optimal way of arranging the lattices of crystals at shared interfaces, allowing low-energy interfaces to form, and thus minimising the height of the energetic barrier which governs the likelihood of formation of a stable nucleus. The observed preference for CORs 1 and 2* at Tmt-Cpx boundaries in our experiments supports the hypothesis that the energies of these interfaces are at a local or global minimum, providing strong evidence for heterogeneous nucleation. Given that heterogeneous nucleation is considered the primary mechanism in natural settings and crystallization experiments (*Walker et al., 1976; Lofgren, 1983; Hammer et al., 2010; Mollo et al., 2012; Arzilli et al., 2019; Colle et al., 2023; Holness et al., 2023; Peres et al., 2024*), our analysis will initially focus on this mechanism within our samples. Subsequently, we will present microstructural evidence for homogeneous nucleation of the remaining phases.

3.4.2. Heterogeneous nucleation cases in the samples

3.4.2.1. Heterogeneous nucleation of Tmt on a pre-existing Cpx

This is one of the most commonly documented examples in literature (*Fleet et al., 1980; Hammer et al., 2010; Vetere et al., 2013, 2015; Peres et al., 2024*) and can be observed in all undoped samples, both anhydrous and hydrous. The microstructural features that suggest the

occurrence of this mechanism include: (i) The presence of numerous Tmt grains decorating both the internal and external surfaces of the highly dendritic or skeletal Cpx grains, as shown in Fig.3.8. These Tmt grains are considerably smaller than the Cpx grains they contact and share boundaries with the edges of the Cpx crystals. (ii) The presence of CORs between the two phases. As also illustrated in Fig.3.5c-f, in Fig.3.8 and in the pie charts for the undoped samples (left column in Fig.3.6), a high percentage (>60%) of the grain boundaries shared between Cpx and Tmt are characterized by the presence of CORs, confirming the hypothesis of heterogeneous nucleation of Tmt on Cpx.

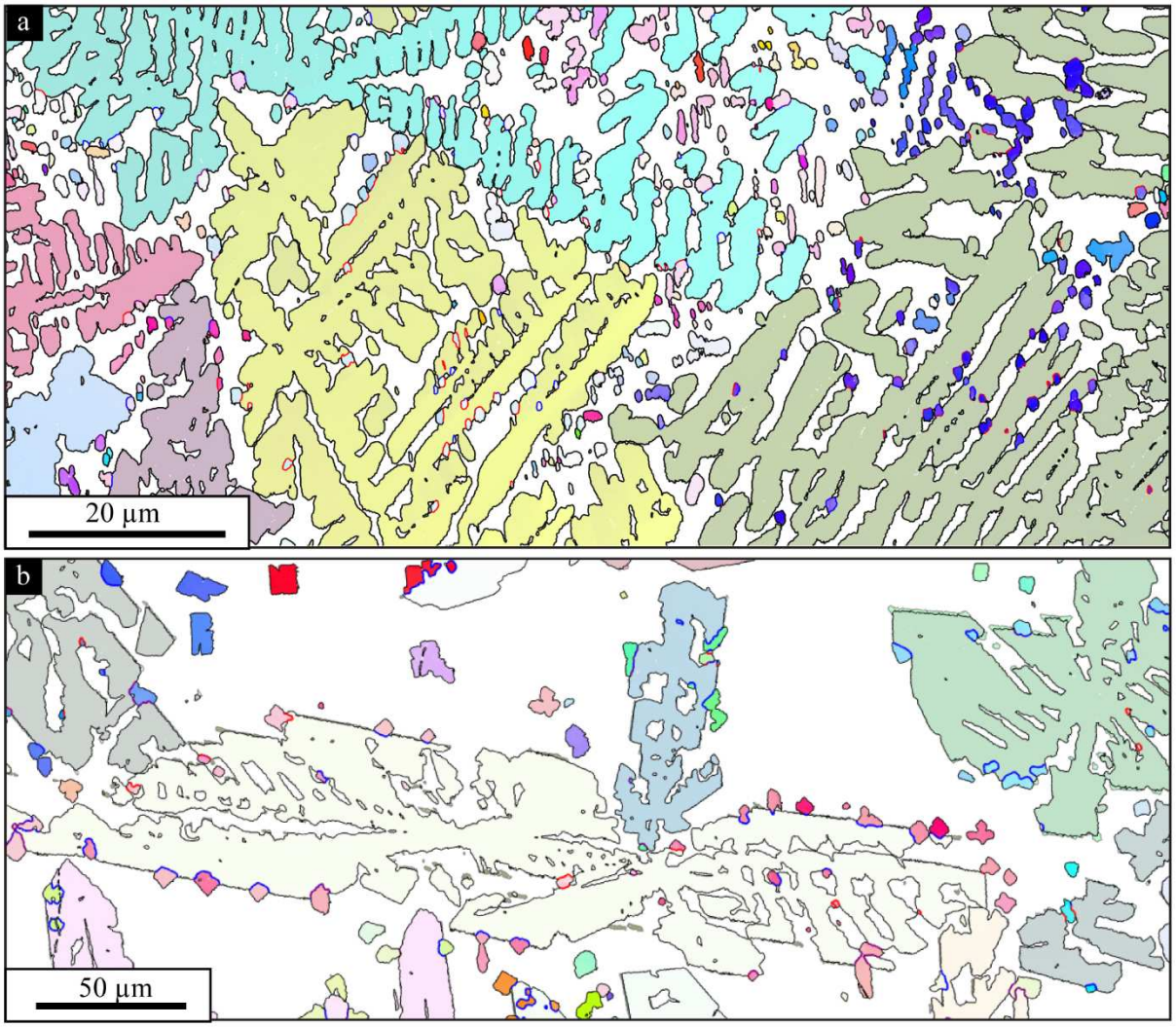

Fig.3.8. examples of Tmt heterogeneous nucleation atop of Cpx grains in sample 1050d-undoped-30min (a) and sample 1100d-undoped-30min. Noteworthy is that all the tmt grains heterogeneously grown on the same Cpx grains have similar colour, meaning that the lattice orientation of each crystal is extremely close.

3.4.2.2. Heterogeneous nucleation of Cpx on top of a pre-existing Tmt/Spl

In both Cr-doped and undoped series we found clear examples for this nucleation process but this heterogeneous nucleation case is much more cryptic compared to the one previously discussed. The main microstructural features in support of this process are the following: i) Cpx radially growing from a Spl single grain or aggregate and ii) CORs shared between the Spl grain/aggregate and the Cpx crystal.

In the Cr-doped series, sample 1050w-Cr-doped-5min provides the best case for studying this mechanism. In this sample, the Spl grains are either scattered within glass regions or completely engulfed by larger Cpx crystals, and irrespective of their location they are constituted by a Cr-rich core and a more Ti-rich rim, indicating that Spl grain grew before the big, non-quenched Cpx crystals. Moreover, the Cpx microcrystals that are in contact with Spl grains are typically smaller in size and are radially arranged (Fig.3.9a). The presence of these micro-sized grains, in contrast to the larger Cpx crystals over 300 µm also found the same sample, suggests that the smaller grain population formed during a distinct, subsequent crystallization episode, likely associated with the quenching process of the experiment. This interpretation is corroborated by the widespread presence of this microstructure in all Cr-doped samples with a hydrous composition except for the section of the 1050w-Cr-doped-5min sample where the larger Cpx crystals are found. Furthermore, the Spl grains, which consist of a chromite core crystallizing first during the cooling ramp from 1300 °C to the T_{rest}, share CORs with the radially arranged Cpx microcrystals (Fig.3.9b). This sharing of CORs combined with the microstructural evidence and well-understood crystallization order of Spl and quench Cpx is considered strong evidence for the heterogeneous nucleation of the Cpx phase atop the pre-existing Spl grains.

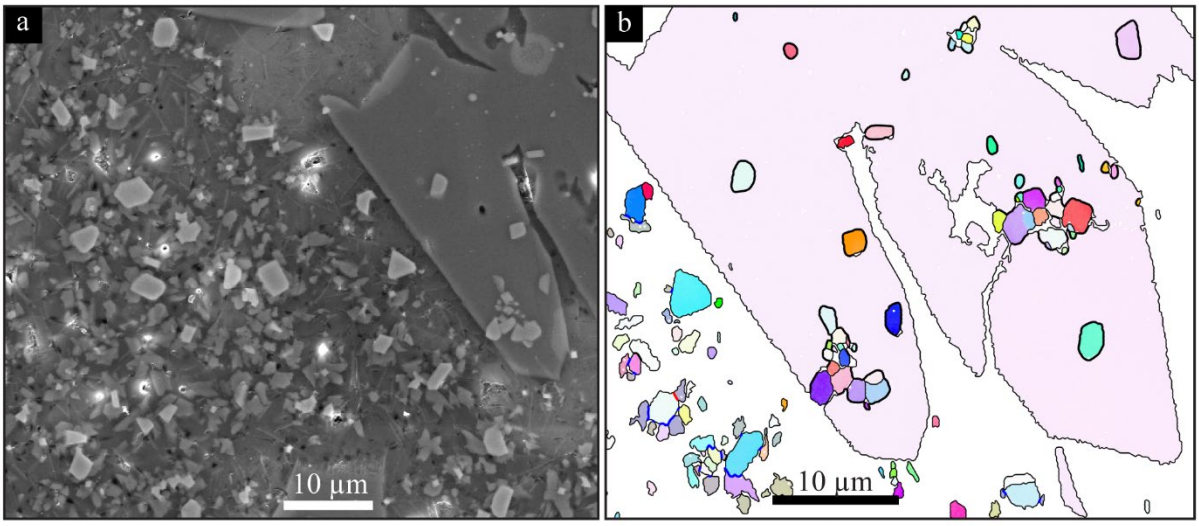

Fig.3.9 a) BSE image of sample 1050w-Cr-doped-5min. b) EBSD IPF map illustrating that the small, micron-sized quenched clinopyroxene (Cpx) grains share CORs with the adjacent spinel (Spl) grain, suggesting heterogeneous nucleation on the surface of Spl grains. Notably, the Spl grains embedded within the larger Cpx crystal do not share CORs with it, indicating that the Spl grains pre-existed and were subsequently encapsulated by the growing Cpx crystal.

Similarly, we can apply the same microstructural criteria to search for heterogeneous nucleation of Cpx on Spl among the non-quenched Cpx crystals formed in Cr-doped samples with anhydrous starting composition. All the samples are characterized by the presence of Spl grains randomly occupying glass region as well as being totally embedded inside the skeletal Cpx without a clear preference for either phase. Based on the example of the hydrous Cr-doped samples, which appear to have been free of Cpx at temperatures closer to the liquidus, we infer that the Spl grains in the anhydrous Cr-doped samples, likewise comprising a Cr-rich core and a more Ti-rich rim, also crystallized as the first phase. Even though the percentage of Spl grains that are in contact with a Cpx equals 60.1%, only less than 7% of boundary length fraction exhibit any CORs. However, the Spl grains which do share CORs with a Cpx grain are usually in a central position inside their host. Fig. 3.10 illustrates this by displaying only the Spl and Cpx grains that share CORs, along with the centroids of these particular Cpx grains. This suggests that the presence of CORs is not coincidental; rather, when present, the Spl grain is generally near the centroid of the Cpx grain. This arrangement is indicative of a heterogeneous nucleation mechanism of Cpx on pre-existing Spl grains. A possible explanation for the low amount of Spl and Cpx sharing a COR in the scanned areas may be

attributed to a 2D cutting effect. Potentially, serial sectioning would have increased the statistical area scanned in the third dimension (not investigated), revealing that a greater proportion, possibly the majority, of Cpx grains share CORs with Spl grains located near their centre. However, not all Spl grains acted as center of nucleation, otherwise there would be a much higher number density of Cpx grains and consequently a higher BLF_{anyOR}. Since the Spl grains come as the first phase, they originally occupied liquid and assumed random crystallographic orientations in the melt (all Spl grains in Fig. 3.9b have different colors). The nucleation of Cpx is likely to happen heterogeneously on any Spl grain acting as a centre of nucleation, but in these undercooling conditions, i.e. not related to quenching events, not all the Spl act as centre of nucleation. While growing, and sharing CORs with the central Spl grain from which they heterogeneously nucleated from, the Cpx crystals embed other Spl grains in their near proximity. Cpx crystals do not share CORs with these embedded Spl grains, as shown by their random orientations, demonstrated in Fig. 3.5a-b, and supported by the high percentage of BLF_{noCORs} in these experimental series. Moreover, at least at these middle to high degrees of undercooling, high crystallinity and fast kinetics, it does not seem likely that Cpx grains

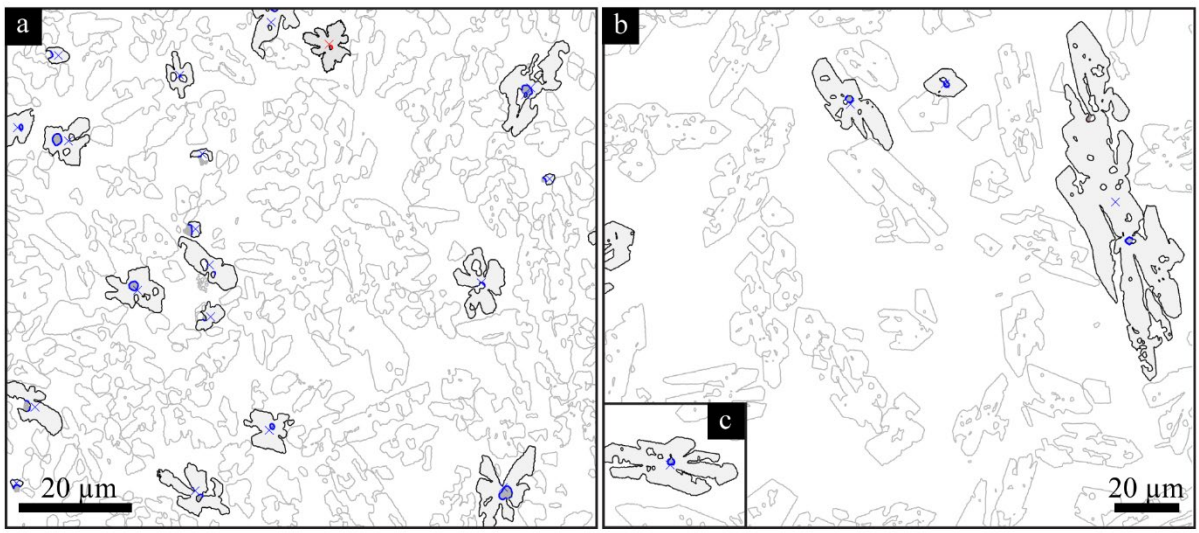

Fig.3.10. MTEX generated image from EBSD maps in which just the Cpx-Tmt clusters sharing CORs are highlighted (dark grey). The cross represents the geometric centroid of the Cpx. The proximity of the Cpx grain centroid location and the Spl

grain sharing CORs with it is evidence that the Cpx grows radially by heterogeneous nucleation from Spl grains. A) sample 1150d-Cr-doped-5min; b and inset box c) are from sample 1100d-Cr-doped-5min. the inset (c) has the same scale as (b).

engulfing the nearby Spl grains would be able to force the Spl grains to rotate so as to form post-nucleation CORs caused by a synneusis clustering mechanism, as suggested by Gordon and Wallis (2024) for their Plagioclase inclusions inside a K-feldspar megacryst in granites.

3.4.2.3. Heterogeneous nucleation of Cpx on pre-existing Spl aggregates

Spl agglomerates comprising hundreds of crystals are present in both undoped and Cr-doped series. In the case of the undoped samples they are surrounded by large, dendritic often curved feathery-like Cpx crystals which radiate from them, or smaller, snowflake-like crystals (Supplementary Figure S8 and S9). EBSD maps of these areas reveal that at least the outer layer of Spl grains composing the agglomerate share CORs with Cpx grains. The grains of Tmt sharing CORs with the Cpx crystals show limited variability in colour in figure 3.8, signifying a limited range of orientation present in the Spl agglomerate. The presence of all these microstructural features satisfies the necessary requirements to infer heterogeneous nucleation of Cpx on top of Spl for these agglomerates.

In Cr-doped samples, the Spl agglomerates scanned through EBSD do not share CORs with the poikilitic Cpx that engulf them. The Spl grains IPF colouring in the EBSD maps also show high crystallographic orientation variability, signifying that this agglomerate is composed of randomly oriented crystals (more randomly oriented compared to the Spl aggregated scanned in the undoped sample). Heterogeneous nucleation of the poikilitic Cpx on top of one single crystal included in the agglomerate is still a possibility, but we suppose that the specific Spl-Cpx couple sharing COR has not been sampled by the current 2D cut, similar to all the other Cpx crystals which do not show CORs with a Spl because the center of the crystal has not been sampled.

3.4.2.4. Heterogeneous nucleation of Cpx from the wall of the capsules

All undoped anhydrous samples show the presence of several elongated dendrites extending >500 μm in the longest dimension, which arrange perpendicular to the capsule walls. This nucleation artefact is a well-known problem for the experimental petrologists that should be always considered in the crystallization evolution of each sample. This microstructural feature can be observed mostly in our undoped anhydrous series samples. It is mostly present in the warmer and central portion of each of these samples. Several causes can be taken into consideration for this microstructure and why is not present (or not so obviously/markedly present) in the Cr-doped experimental series. The Pt-capsule walls in the warmer/ less undercooled portions of undoped samples are, together with Spl aggregates, the only surfaces possible where Cpx crystals can heterogeneously nucleate (Fig.3.11). Indeed, in contrast to the skeletal Cpx domain in the same anhydrous samples and the entire volume of Cr-doped samples, there is no ubiquitous crystallization of Spl grains as the first phase in these portions of the samples, and therefore a lack of pre-existing nucleation centers. It is likely that heterogeneous nucleation involving COR between these two phases, as is possible whenever Spl crystallises first, is energetically more favoured compared to the heterogeneous

nucleation of Cpx from the Pt-capsule walls and therefore suppresses nucleation on walls in these cases.

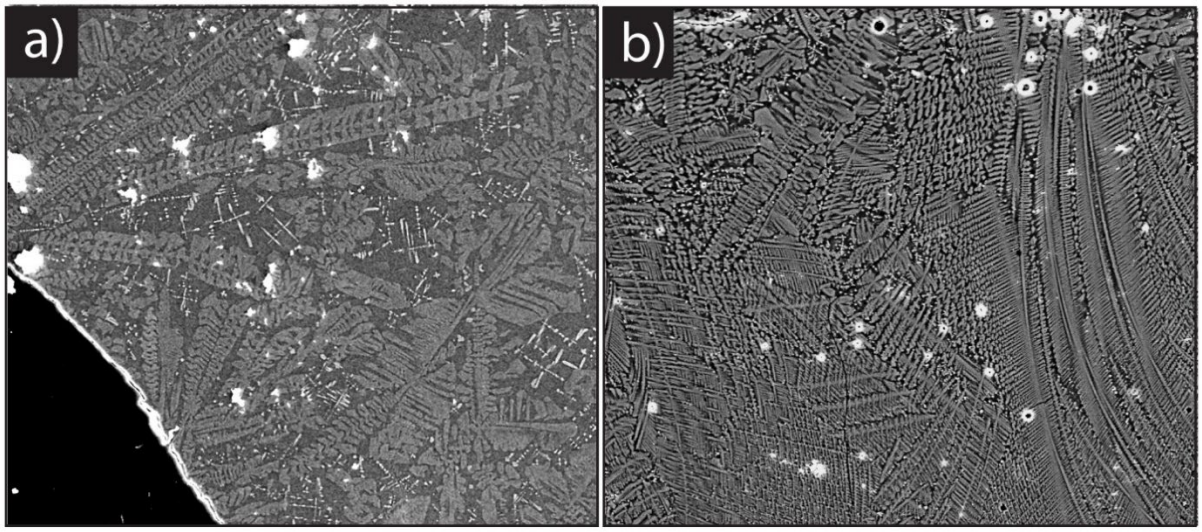

Fig. 3.11. Examples of Cpx radially growing from the Pt-capsule in samples 1150d-undoped-30min (a) and 1050d-undoped-30min (b). Bright areas with shadows at the top left of a) are artefacts caused by particles on the prepared sample surface.

3.4.3. Examples of homogeneous nucleation in the samples

In the samples with an anhydrous, undoped starting composition, larger, euhedral Tmt grains found in the skeletal Cpx domain portions of the samples may have formed through homogeneous nucleation. This region displays microstructural characteristics similar to those observed in Cr-doped experiments, such as euhedral morphology and homogeneous distribution within these specific portions of the samples (Fig. 3.12b and d). Additionally, these Tmt grains are frequently positioned near the centre of a Cpx grain, similar to the examples shown in Fig. 3.10, with shared boundaries that exhibit CORs, suggesting that these grains formed prior to Cpx crystallization. A micron-sized population of Tmt grains is also present in the skeletal domain of the anhydrous undoped sample, but these grains primarily decorate the edges and tips of Cpx crystals, which is indicative of a process of heterogeneous nucleation, occurring atop the already formed Cpx crystals.

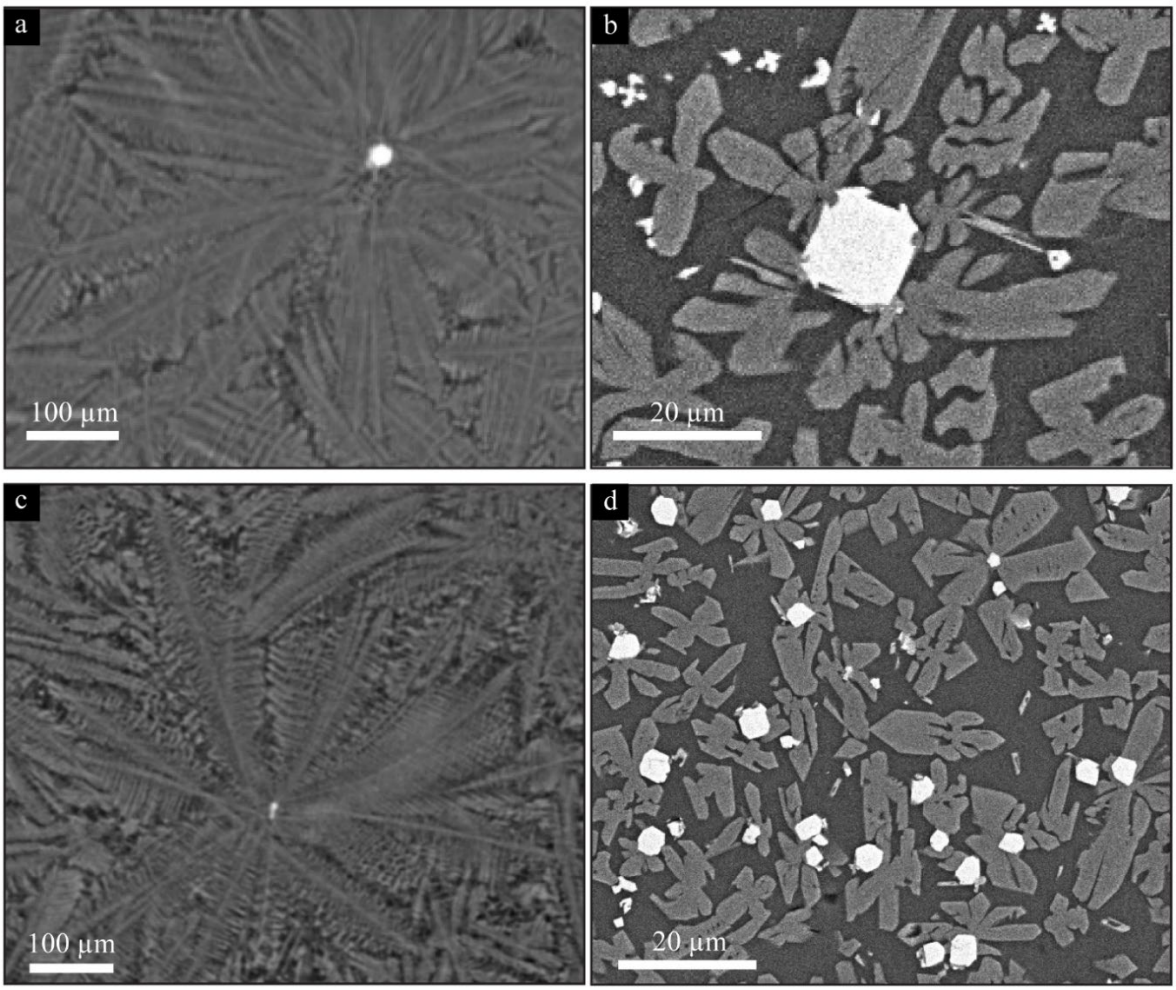

Fig.3.12. a and c) synchrotron light µCT slice of sample 1100d-undoped-30min and 1150d-undoped-30min showing Cpx grains radially arranged around a Spl grain. b and d) BSE images of sample 1150-undoped-5min showing microstructures suggesting Cpx heterogeneous nucleation on Spl grains.

The regions of the samples dominated by feather-like shape Cpx grains show a small number density of up to 500 µm size, highly dendritic Cpx. The feather-shaped Cpx grains are most likely nucleated heterogeneously from the Pt capsule walls or from Tmt aggregates, as already discussed in the previous section. On the contrary, the snowflake-like dendritic Cpx crystals may have formed by homogeneous nucleation (Fig.13b). No direct finding of Cpx grains of this kind arranged radially on Tmt single grains or aggregates are evidenced from any SEM images. Additionally, the EBSD maps allow to extrapolate that the areas with "snowflake" Cpx contain the highest crystal number density of Cpx crystals in the whole sample. The higher number density and smaller size may suggest that this Cpx population crystallized at higher nucleation rate, and that the growing Cpx grains had to compete more

with their neighbours for the same chemical components (*Mangler et al. 2022 and references therein*), the major consequence of which is the smaller size of these grains.

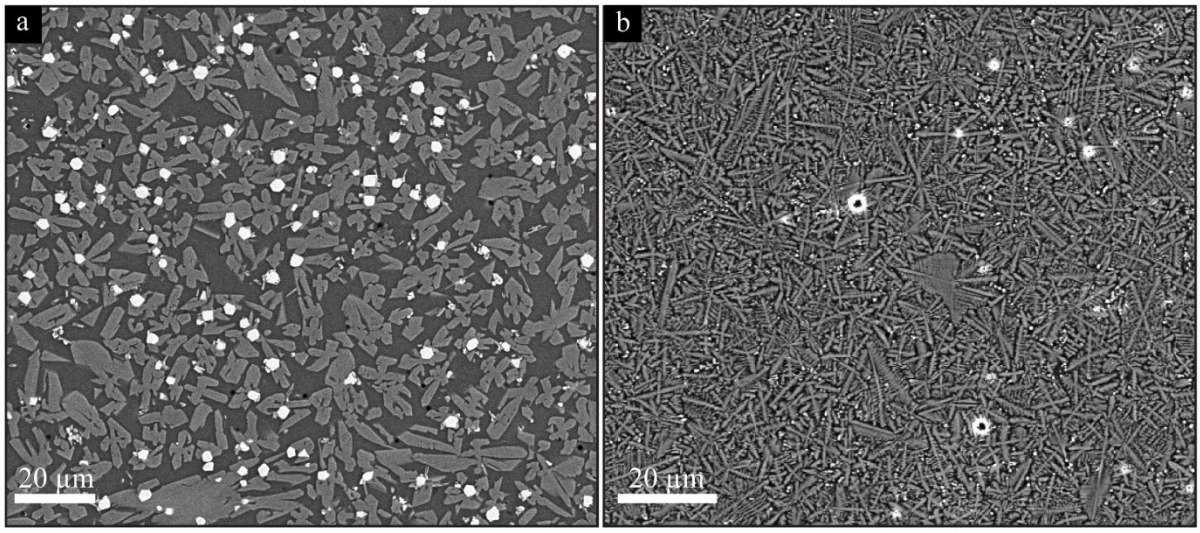

Fig.3.13. possible examples of homogeneous nucleation. a) BSE images showing homogeneous nucleation of Spl in sample 1150d-undoped-5min (skeletal Cpx domain); (b) SE image from the snowflake-like Cpx region in sample 1050d-undoped-30min.

In the sample with hydrous starting composition Cpx may form by homogeneous nucleation throughout the whole sample as reported by *Peres et al., 2024*. In this paper the authors also discuss the possibility that the early formed skeletal population of Tmt present early in the hotter, less undercooled portion of the sample may act as a surface for heterogeneous nucleation of Cpx. However, most of the microstructural features and CORs data are in accordance with the hypothesis that most of the Cpx in sample 1100w-undoped-30min formed by homogeneous nucleation.

3.4.4. Crystallization sequence in the two experimental series

The microstructural observations we collected through several imaging methodologies and microstructural investigations helped us not only to understand the nucleation mechanisms of all the phases comprising the two experimental series but also reconstruct the complete crystallization history of the various samples.

All the samples composing the C**r-doped experimental series followed similar crystallization history:** Cr2O3 was added to the original undoped starting glass to artificially

create early formed centers of nucleation to examine the effect on the Cpx heterogeneous nucleation, and avoid as much as possible any nucleation delay almost inevitably present during any magma cooling from a superliquidus temperature. By consequence, as planned, the first crystal phase to nucleate was the Chromite rich Sp grains. These grains are ubiquitously present in all the doped experiments, and probably form at T > 1250°C, and thus during the cooling ramp from 1300°C to the experimental T. Another possibility is that this added oxide did not actually completely melt and homogenize in the trachybasaltic melt. In this scenario the unmelted Cr2O3 particles could have reacted with the silicate melt to form chromite oxides. However, laser ablation measurement on the Cpx crystals and in the remaining glass evidenced the presence of Cr in both phases, suggesting that at least part of it dissolved in the melt. In either case, chromite would be the only crystalline phase present in an otherwise molten sample prior to Cpx formation. On top of the chromite grains a rim of tmt composition a few μm thick always formed, as observed in the EPMA chemical maps in Fig. 3.7. Non-quenching derived Cpx crystals follow in the crystallization order, forming through heterogenous nucleation atop the already formed Spl grains. The final crystals to form are the quenched Cpx grain population. These grains form exclusively in the samples with hydrous doped compositions in the regions of melt free from bigger Cpx crystals. In all hydrous Cr-doped samples this quenched Cpx population formed by heterogenous nucleation atop the Spl grains. This Cpx population is the only one formed across the entire length of the hydrous samples, indicating that skeletal, or dendritic bigger size Cpx grains did not have enough time to nucleate and crystallize at these temperatures after just 5 minutes of dwell time. Probably, the hydrous starting composition resulted in higher diffusivities of the components in the melt, which may have led to melt supersaturation in Cpx-components just at high undercooling, closer to the one reached in the colder portion of sample 1050d-Cr-doped -5min, i.e. $\Delta T > 130°$. In the samples at higher temperatures, a sufficiently high

undercooling, and consequently supersaturation, has been reached only during the quenching process. The existence of this quench Cpx population proves adding chromite grains as early formed heterogeneous nuclei is not enough to avoid a crystallization delay in highly undercooled but not quenched trachybasalt melts with hydrous starting composition . ΔT_{cpx} from 60° to 100° (hydrous samples) are high, but clearly not high enough for the nucleation and growth of normal, Cpx grains, while a ΔT_{cpx} near 130° (anhydrous samples) is sufficient.

Undoped experimental series: the samples with anhydrous starting compositions show a complex microstructural zonation along the z axis (the height) of the samples. All five samples are composed of two microstructural domains as we have already highlighted in chapter 3.4.4, which apparently have different crystallization histories. In the skeletal domain the microstructural observations indicate that the first crystal phase to form was probably the euhedral Tmt grains, by homogeneous nucleation from the melt (chapter 3.4.3). The skeletal Cpx grains form as the second phase atop of the already formed Tmt grains, by heterogeneous nucleation (chapters 3.4.2.2 and 3.4.2.3). The appearance of a smaller population of Spl grains, often decorating the edges and tips of the skeletal Cpx and formed by heterogeneous nucleation on top of them, conclude the sequence of crystallization of the skeletal Cpx domain.

In the dendritic Cpx domain the Tmt aggregates form as first phase. This specific microstructure may be an artefact caused by incomplete superliquidus homogenization of the glass, allowing some few nuclei to not dissolve and act as centres of nucleation, or caused by any sort of unplanned oxide contamination like gold particles entering the capsule during capsule welding, as we documented in Supplementary Figure S11. Feather-like highly dendritic Cpx grains form as the second phase, by heterogenous nucleation on the capsule walls and on the already-formed Tmt aggregates, closely followed by, if not simultaneous with, the crystallization of the snowflake-like Cpx dendrites in the inner portions of the

samples. Given that there seem to be no Tmt aggregates or other surfaces for heterogeneous nucleation in their vicinity, these Cpx snowflake-like shaped grains may have nucleated homogeneously from the melt in a short temporal range.

Elongated, skeletal Tmt grains (up to 30 μm in size), together with small (< 10 μm in size) anhedral Tmt grains are the last crystal phases to form, both by heterogeneous nucleation on Cpx, respectively from the external surfaces of the Cpx toward the interstitial glass, or in the intragranular melt trapped inside framework formed by the different dendritic branches of the Cpx (Figs. 3.7 and 3.11a).

Microstructural observations and evidence from sample 1100w-undoped-30min, which has already been discussed in chapter 2.4.2, here just summarized, show that some of the big skeletal Tmt grains of population 1 (see chapter 2.4.2) could have formed as the first phase in the sample or simultaneous to Cpx. Cpx crystallizes in a regime of diffusion-limited crystal growth, resulting in the formation of dendritic crystals characterized by high concentrations of Al + Ti (Fig. 4b-c). Tmt Pop3 nucleated heterogeneously on Cpx in the earlier stages of Cpx growth. The portion of Pop3 crystals near the Al_2O_3+TiO_2-enriched zone of Cpx corresponds to the TiO_2 poor domain of the Tmt crystals, while the TiO_2 concentration increases when the Tmt is situated in the SiO_2+MgO-rich zones of Cpx crystals. We suggest that the elongated shape is caused by co-growth of Cpx and Tmt with similar growth rates, resulting in similarity between the Tmt longest dimension and the final width of Cpx branches.

As the experimental runs proceed isothermally after reaching the resting temperature, ongoing melt relaxation leads to conditions progressively closer to chemical equilibrium, characterized by progressively less supersaturated melt near the crystallizing Cpx, which favours the development of euhedral facets and results in the partial infill of the dendritic branches (Si- and Mg-rich zones; Fig. 4c). Finally, Pop2 Tmt crystals formed by

heterogeneous nucleation on Cpx later in its growth history, when the faceted skeletal morphology of Cpx was more developed, i.e. in conditions closer to thermodynamic equilibrium. This hypothesis is supported by the external position of most Pop2 Tmt grains with respect to touching Cpx, their greater protrusion into the melt, and the presence of frequent planar boundaries between the two crystal phases

3.4.4. Why are all undoped anhydrous samples composed of two different domains?

All undoped anhydrous samples, with the exception of "1100d_undoped-0min," consist of two microstructurally distinct regions. The dendritic Cpx domain occupies the warmer (less undercooled) portion of the samples across all investigated temperatures, while the skeletal Cpx domain is found in the colder (more undercooled) areas. The volume proportions of these two domains vary with temperature. For example, in the sample "1150d-undoped-5min," the skeletal domain constitutes over 60% of the total volume, which is the highest among all experiments, but this domain becomes less prominent in experiments conducted at lower experimental temperatures (<30%).

The morphology of the Cpx is primarily influenced by the presence, and the amount of Spl (Tmt) grains that form prior to the crystallization of Cpx. In the dendritic Cpx domain, Spl aggregates or isolated euhedral grains may still be present and can serve as nuclei for heterogeneous nucleation of Cpx, but their number density is much lower compared to the euhedral Spl grains in the skeletal domain or in all Cr-doped samples. The low amount of nuclei for Cpx heterogeneous nucleation allow the formation of a small number of Cpx grains that can form and grow from the capsule walls or radiate from the Spl grains undisturbed, with low neighbour competition in an undercooled, almost crystal-free melt.

Conversely, in the skeletal domain, the abundant presence of Tmt acting as nuclei significantly increases the Cpx nucleation rate, which in turn escalates growth competition with neighbouring crystals, resulting in a higher quantity of smaller, skeletal Cpx grains.

One hypothesis explaining the formation of the different zones is that, while Tmt tends to appear first, at high undercoolings (> 70°C), Cpx growth rate is high enough that even the nucleation of few Cpx grains can cause the increase the crystallinity of the sample to more than 40-50% almost instantaneously, so that the dendritic domain dominates the overall microstructure of the sample. Another possible explanation for the formation of these zones, that is not mutually exclusive with respect to the previous explanation, relates to increased iron loss due to characteristic crimping and folding of the Pt-capsule end closest to the oven hotspot. This could result in a greater Pt-surface area at that end, altering the melt's composition locally and inhibiting substantial crystallization of euhedral Spl grains (Tmt in this case) as the initial phase, as observed in the skeletal Cpx domain. Although this iron loss is theoretically localized, it could initiate heterogeneous nucleation of Cpx grains from the capsule walls. These grains, forming in relatively open space, face less growth competition from neighboring grains. Furthermore, Electron Backscatter Diffraction (EBSD) maps indicate that the dendrites can bend their crystallographic lattice by up to 40-45° (see Fig.3.4c-d), which certainly indicates rapid crystal growth (*Griffiths et al., 2023*). Consequently, the fast crystallization of dendritic Cpx from the capsule's walls may have triggered a cascade of dendritic Cpx crystallization, rapidly occupying a significant volume in the samples processed at higher undercoolings and preventing the expected sequence of crystallization (Tmt first).

3.4.6. Implications

The most obvious insight that these two sets of experiments provide is that even extremely small changes in the starting composition may result in totally different final texture of a rock/sample. In our case of study, the addition of Cr_2O_3 (0.4 wt%) allowed to form a high number of early forming Spl grains, which acted as sites for heterogeneous nucleation of Cpx grains. In contrast, in the dendritic cpx domain of all undoped anhydrous experiments, the low amount of Spl grains acting as heterogeneous nuclei generate the condition for the crystallization of a few, extremely rapidly growing Cpx grains, which in a few minutes were able to occupy a high amount of space (crystallinity > 50%). Comparing the final texture of both anhydrous doped and undoped experimental series, we can say that the presence of early forming phases can act as effective nuclei for heterogenous nucleation, and their presence/absence and number density may have a bigger impact than the undercooling itself on the final texture of a rock.

Another important implication which can impact the experimental petrology field is that episodes of early formation of one phase can also influence experimental and natural studies of the crystal growth of a different phase. Indeed, the ubiquitous presence of any oxide as first phase (both desired and/or not considered in the case of doped experiments) acting to reduce the energetic barrier for nucleation can impose a limitation in how large individual grains of a specific phase (e.g. Cpx) can grow, if these grains must compete with other neighbour crystals that have formed by heterogeneous nucleation. This is even more emphasized in experiments carried out in disequilibrium conditions and at a high degree of undercooling, like our experimental series. Furthermore, from a qualitative comparison between sample 1100d-undoped-5min and 1100d-undoped-30min, we can say that these high undercooling experiments (in this specific case with ΔT between 110 and 100 °C) reached high crystallinities after just 5 minutes of dwell time. This fact poses questions about the

reliability of the comparison of parameters like the growth rate in time-series experiments with longer dwell time, as, in the case described, the crystal size would be a function of the spacing of heterogeneous nuclei and therefore fixed for a given starting composition, meaning that apparent growth rates would decrease with dwell time.

The process of crystallization was very effective at all the investigated temperatures in the samples with Cr-doped anhydrous composition, even after only 5 minutes of dwell time. In contrast, Cr-doped samples with hydrous composition did not crystallize Cpx during these 5 minutes at 1150°C and 1100°C, even if the melt was already filled with Spl which could have increased the possibility for Cpx heterogeneous nucleation. However, skeletal Cpx with size 2 to 10 times of the ones forming in the anhydrous samples, can form in the colder portion of the hydrous doped sample carried out at 1050°C. Moreover, in all 3 hydrous, doped samples we report the massive presence of quenched Cpx grains. The formation of this specific Cpx grain population may hint that these melts, even if almost completely crystal free (the crystallinity is lower than 5% if we are not considering the quenched Cpx in these estimations) may have been extremely close to crystallization. This crystallization event can be compared to fast crystallization events occurring in volcanic setting like eruptions or lava conduit dynamics, caused by any process where intensive (T or P) or extensive (H_2O content) parameters change, such as degassing/volatile exsolution processes or the contact with a much colder body.

The presence of Cr2O3, which is an element present in more primitive magma recharges (*Ubide and Kamber 2018*), can cause Spl crystallization, which can act as nuclei for Cpx to nucleate on. From this study we can also generalize that the presence of any kind of crystal seeds could enhance the nucleation process. The process of fast crystallization in a magmatic reservoir could lead to drastic viscosity changes and influence the eruptability of the magmatic batch. As already discussed in chapter 2.4.3, fast-growing dendritic Cpx nucleating

on already existing Tmt grains may suddenly increase the viscosity of a magma, leading to fragmentation (*Moitra et al., 2018*) and consequently enhancing the basaltic explosive eruption (*Arzilli et al., 2019*) if the crystallinity remains below 30%. For scenarios with higher undercooling, the result is a higher crystallinity, which can freeze the magma propagation inside dykes or lock crystal mushes in the case of future eruptions (*Arzilli et al., 2022*). Most of the anhydrous samples of both experimental series may be considered representative of a scenario of fast crystallization due to sudden increase of undercooling, in which the pervasive early crystallized, or inherited grains (here Cr-rich spl), can lead in only a few minutes (here 5 to 30 minutes) to a magma crystallinity higher than 50% and consequently drastically increase the viscosity of a magma batch. It is important to add a caveat, i.e. that we did not investigate or model the morphological development of the feather-like and dendritic morphology typical of our samples in experiments longer than 30 minutes. Highly dendritic, feather-like cpx have been already found in other experimental studies (*Pontesilli et al., 2019; Arzilli et al., 2019; 2022*) of magmas with extremely similar compositions. Pontesilli et al. (2019) quantified the decrease of the Cpx area % from values higher than 50% to values lower than 40% through a time series experiments with dwell times between 30 minutes and 24 hours due to textural maturation at higher dwell times. If this occurs in natural systems, we can hypothesize that even if the crystallinity of a magma batch abruptly reaches values higher than 50%, consequently locking-up the crystal mush, if the magma resides long enough, or if it experiences an episode of magma recharge from a warmer source, the crystallinity may decrease to values closer to 30%, unlocking the crystal mush.

3.5. CONCLUSIONS

The crystallization of trachybasaltic magmas, starting from similar compositions and subjected to high degrees of undercooling, can be analysed through EBSD and EPMA. These methods provide valuable insights into the different crystallization histories and textural evolutions of magma batches. The main findings of this study are:

1) In highly undercooled (here trachybasaltic) magmas, the pervasive nucleation of an early crystal phase (here Cr-Spl) facilitates the rapid and widespread heterogeneous nucleation of a second forming phase (here Cpx). In our experiments, this results in a crystallinity exceeding 50% within a time span of 5 to 30 minutes.
2) In anhydrous samples from both experimental series, the morphology of Cpx and the final texture of the samples are less influenced by the degree of undercooling than by the availability of heterogeneous nuclei. A high nuclei density (in the form of Spl grains) leads to a high number density of skeletal Cpx grains, whereas a low nuclei density results in fewer, but longer and more dendritic Cpx crystals.
3) Caution is advised when interpreting the growth rates of specific crystal phases in experimental samples. The presence and spatial distribution of an early forming phase can dictate the final length and thus the apparent growth rate of subsequent phases, particularly if they form on top of the first phase through heterogeneous nucleation.
4) Rapid and pervasive crystallization in a magmatic batch triggered by pre-existing or newly formed nuclei for subsequent heterogeneous nucleation can significantly alter its viscosity, thereby creating conditions for magma fragmentation or stagnation, depending on the level of crystallinity achieved.
5) EBSD mapping can be employed to calculate several parameters that are crucial for deriving important qualitative and/or quantitative insights into magmatic crystallization. These parameters include: a) the number density of crystal phases,

which can be linked to the nucleation rate; b) the deformation of the crystal lattice (measured as mis2mean), which can be related to the growth rate or to the degree of departure from equilibrium crystallization; c) the presence and statistics of CORs, which are essential for understanding the nucleation mechanisms.

6) Indeed, CORs are the best evidence for heterogeneous nucleation between Cpx and Spl (or vice versa) in our experimental samples. Furthermore, variations in COR frequency between and within our samples imply that COR analysis may be able provide information about the conditions under which the samples were formed, such as melt water content and degree of undercooling.

3.6. References

Armienti P, Innocenti F, Petrini R, Pompilio M, Villari L (1988) Subaphyric alkali basalt from Etna: inferences on depth and composition of the source magma. Rend. Soc. Ital. Miner. Petrol. 43, 877-891.

Armienti P, Perinelli C, Putirka K (2013) A new model to estimate deep-level magma scent rates, with applications to Mt. Etna (Sicily, Italy). J. Petrol. 45, 1-19. doi: 10.1093/petrology/egs085

Arzilli F, Mancini L, Voltolini M, Cicconi MR, Mohammadi S, Giuli G, Mainprice D, Paris E, Barou F, Carroll MR (2015) Near-liquidus growth of feldspar spherulites in trachytic melts: 3D morphologies and implications in crystallization mechanisms. Lithos 216-217:93-105. doi: 10.1016/j.lithos.2014.12.003

Arzilli F, La Spina G, Burton MR, Polacci M, Le Gall N, Hartley ME, Di Genova D, Cai B, Vo NT, Bamber EC, Nonni S, Atwood R, Llewellin EW, Brooker RA, Mader HM, Lee

PD (2019). Magma fragmentation in highly explosive basaltic eruptions induced by rapid crystallization. Nature Geoscience 12, 509 1023-1028. doi: 10.1038/s41561-019-0468-6

Arzilli F, Polacci M, La Spina G, Le Gall N, Llewellin EW, Brooker RA, Torres-Orozco R, Di Genova D, Neave DA, Hartley ME, Mader HM, Giornado D, Awwood R, Lee PD, Heidelbach F, Burton MR (2022). Dendritic crystallization in hydrous basaltic magmas controls magma mobility within the Earth's crust. Nat Commun 13, 3354. Doi: 10.1038/s41467-022-30890-8

Bachmann F, Hielscher R, Schaeben H (2010). Texture analysis with MTEX - free and open source software toolbox. Solid State Phenomena 160, 63–68. doi: 10.4028/www.scientific.net/SSP.160.63.

Ballhaus C, Pakulla J, Wirth R, Roddatis V, Schreiber A, Münker C, Wombacher F, Kronz A, Fonseca ROC, Cieszynski H, Friedrich HH (2023). Quenching of basaltic melts by volatile exsolution. Contrib Mineral Petrol 178:57 doi: 10.1007/s00410-023-02041-9

Berkebile CA, Dowty E (1982). Nucleation in laboratory charges of basaltic composition. Am Miner 67:886–899

Cáceres F, Wadsworth FB, Scheu B, Colombier M, Madonna C, Cimarelli C, Hess KH, Kaliwoda M, Ruthensteiner B, Dingwell DB (2020). Can nanolites enhance eruption explosivity? Geology, v. 48, p. 997–1001, https://doi.org/10.1130/G47317.1

Corrigan G (1982). Supercooling and the crystallization of plagioclase, olivine, and clinopyroxene from basaltic magmas. Mineral Mag 46:31–42

Colle F, Masotta M, Costa S, Mollo S, Landi P, Pontesilli A, Peres S, Mancini L (2023). Effect of undercooling on clinopyroxene crystallization in a high K basalt:

Implications for magma dynamics at Stromboli volcano. Lithos, Volumes 456–457. 107327. Doi: 10.1016/j.lithos.2023.107327

Costa S, Masotta M, Gioncada A, Pistolesi M, Bosch D, Scarlato P (2020). Magma evolution at La Fossa volcano (Vulcano Island, Italy) in the last 1000 years: evidence from eruptive products and temperature gradient experiments. Contrib Mineral Petrol 175, 31 https://doi.org/10.1007/s00410-020-1669-0

Davis MJ, Ihinger PD (1998). Heterogeneous crystal nucleation on bubbles in silicate melt: *Am Mineral*, v. 83, p. 1008-1015.

Donaldson CH (1979). An experimental investigation of the delay in nucleation of olivine in mafic magmas. Contrib Miner Petrol 69:21–32

Fenn PM (1977). The nucleation and growth of alkali feldspars from hydrous melts. Can Mineral 15:135–161

Fleet ME, Bilcox GA, Bernett RL (1980). Oriented magnetite inclusions in-pyroxenes from the Greenville Province. Canadian Mineralogist, Vol.18 pp 89-99.

Freda C, Gaeta M, Misiti V, Mollo S, Dolfi D, Scarlato P (2008). Magma-carbonate interaction: an experimental study on ultrapotassic rocks from Alban Hills (Central Italy). Lithos 101, 397-415 doi: 10.1016/j.lithos.2007.08.008

Gibb EGE (1974). Supercooling and the crystallization of plagioclase from a basaltic magma. Mineral Mag 39:641–653

Gordon C, Wallis D (2024). Resolving the “megacryst paradox”: Feldspar orientation relationships record crystal mobility in granites. *Geology*; 52 (9): 712–716. doi: https://doi.org/10.1130/G52045.1

Griffiths TA, Habler G, Ageeva O, Sutter C, Ferrière L, Abart R (2023). The Origin of Lattice Rotation during Dendritic Crystallization of Clinopyroxene, Journal of Petrology, Volume 64, Issue 1, January 2023, egac125, https://doi.org/10.1093/petrology/egac125

Habler G, Griffiths TA (2017). Crystallographic orientation relationships. In: Mineral reaction kinetics: Microstructures, textures, chemical and isotopic signatures. pp 541-585.

Hammer JE (2008). Experimental Studies of the Kinetics and energetics of Magma Crystallization. Minerals, Inclusions and Volcanic Processes pp 9-59.

Hammer, JE, Rutherford MJ (2002). An experimental study of the kinetics of decompression-induced crystallization in silicic melt, *J. Geophys. Res.*, 107(B1), doi:10.1029/2001JB000281.

Hammer JE, Sharp TG, Wessel P (2010). Heterogeneous nucleation and epitaxial crystal growth of magmatic minerals. Geology 38:367-370. doi: 10.1130/G30601.1

Hielscher R, Schaeben H, Siemes H (2010). Orientation Distribution Within a Single Hematite Crystal. Math Geosci 42, 359-375. doi: 10.1007/s11004-010-9271-z

Higgins MD (2006). Quantitative Textural Measurements in Igneous and Metamorphic Petrology. Cambridge University Press; 2006.

Holness MB, Vukmanovic Z, O'Driscoll B (2023). The Formation of Chromite Chains and Clusters in Igneous Rocks. J Petrol 64:1-24. doi: 10.1093/petrology/egac124

Iezzi G, Mollo S, Ventura G (2009) Solidification behavior of natural silicate melts and volcanological implications. In Lewis, N. and Moretti, A., editors, Volcanoes: Formation, Eruptions and Modelling, pages 127–151. Nova Publishers, New York.

Kirkpatrick RJ (1981). Kinetics of crystallization of igneous rocks. In Rev. Mineral., Vol. 8 (eds. A. C. Lasaga and R. J. Kirkpatrick), pp. 321–395

La Spina, G., Burton, M., Vitturi, M. D. M., Arzilli, F (2016). Role of syn-eruptive plagioclase disequilibrium crystallisation in basaltic magma ascent dynamics. Nat. Commun. 7, 13402

Lofgren G (1980). Experimental studies on the dynamic crystallisation of silicate melts. In Hargraves, R. B., editor, The Physics of Magmatic Processes, pag 487–551. Princeton University Press, Princeton, NJ, USA.

Lofgren GE (1983). Effect of Heterogeneous Nucleation on Basaltic Textures: A Dynamic Crystallization Study. J Petrol 24:229-255. doi: 10.1093/petrology/24.3.229

Mangler MF, Humphreys MCS, Wadsworth FB, Iveson A, Higgins MD (2022). Variation of plagioclase shape with size in intermediate magmas: a window into incipient plagioclase crystallisation. *Contrib Mineral Petrol* **177**, 64. https://doi.org/10.1007/s00410-022-01922-9

Masotta M, Freda C, Paul TA, Moore GM, Gaeta M, Scarlato P and Troll VR (2012). Low pressure experiments in piston cylinder apparatus: calibration of newly designed 25 mm furnace assemblies to P= 150 MPa. Chem. Geol. 312, 74-79. doi: 10.1016/j.chemgeo.2012.04.011

Masotta M, Mollo S, Freda C, Gaeta M, Moore G (2013). Clinopyroxene–liquid thermometers and barometers specific to alkaline differentiated magmas. Contrib. Mineral. Petrol. 166, 1545–1561.

Masotta M, Pontesilli A, Mollo S, Armienti P, Ubide T, Nazzari M, Scarlato P (2020). The role of undercooling during clinopyroxene growth in trachybasaltic magmas: Insights on magma decompression and cooling at Mt. Etna volcano. Geochim. Cosmochim. Acta. 268:258-276. doi: 10.1016/j.gca.2019.10.009

Moitra P, Gonnermann HM, Houghton BF, Tiwary CS (2018) Fragmentation and Plinian eruption of crystallizing basaltic magma. Earth and Planetary Science Letters, v 500, 97-104, https://doi.org/10.1016/j.epsl.2018.08.003.

Mollo S, and Hammer JE (2017). Dynamic crystallization in magmas. In Heinrich, W. and Abart, R., editors, Mineral Reaction Kinetics: Microstructures, Textures, Chemical and Isotopic Signatures, volume 16 of EMU Notes in Mineralogy, pages 146. European Mineralogical Union and the Mineralogical Society of Great Britain & Ireland, Twickenham.

Mollo S, Iezzi G, Ventura G, Cavallo A, Scarlato P (2012). Heterogeneous nucleation mechanisms and formation of metastable phase assemblages induced by different crystalline seeds in a rapidly cooled andesitic melt. J Non Cryst Solids. 358: 1624-1628

Nabelek PI, Taylor LA, Lofgren GE (1978) Nucleation and growth of plagioclase and the development of textures in a high-alumina basaltic melt. Proc. Lunar Planet. Sci. Conf. 9th, 715-741.

Nabelek PI (2007) Fluid evolution and kinetics of metamorphic reactions in calc-silicate contact aureoles from H2O to CO2 and back. Geology, 35, 927–930.

Ohashi M, Kennedy B, Gravley D (2024). Nucleation delay controlling the formation of mafic enclaves and banded pumice. *Contrib Mineral Petrol* 179, 102 (2024). https://doi.org/10.1007/s00410-024-02180-7

Peres S, Griffiths TA, Colle F, Iannini Lelarge S, Masotta M, Pontesilli A, Mancini L, Abart R (2024). Identifying crystal nucleation mechanisms in a synthetic trachybasalt: a multimodal approach. *Contrib Mineral Petrol* **179**, 84 (2024). https://doi.org/10.1007/s00410-024-02161-w

Pleše P, Higgins MD, Baker DR, Lanzafame G, Kudrna Prašek M, Mancini L, Rooyakkers SM (2019). Production and detachment of oxide crystal shells on bubble walls during experimental vesiculation of andesitic magmas. *Contrib Mineral Petrol* **174**, 21 https://doi.org/10.1007/s00410-019-1556-8

Polacci M, Arzilli F, La Spina G, Le Gall N, Cai B, Di Hartley ME, Genova D, Vo NT, Nonni S, Atwood RC, Llewellin EW, Lee PD, Burton MR (2018). Crystallisation in basaltic magmas revealed via in situ 4D synchrotron X-ray microtomography. Sci Rep 8:8377

Pontesilli A, Masotta M, Nazzari M, Mollo S, Armienti P, Scarlato P, Brenna M (2019). Crystallization kinetics of clinopyroxene and titanomagnetite growing from a trachybasaltic melt: New insights from isothermal time-series experiments. Chem Geol 510:113-129. doi: 10.1016/j.chemgeo.2019.02.015

Rusiecka MK, Bilodeau M, Baker DR (2020). Quantification of nucleation delay in magmatic systems: experimental and theoretical approach. *Contrib Mineral Petrol* **175**, 47. Doi: 10.1007/s00410-020-01682-4

Shea T, Hammer JE (2013). Kinetics of decompression and cooling-induced crystallization of mafic-intermediate hydrous magmas. J. Volcanol. Geotherm. Res. 260, 127–145

Swanson SE (1977). Relation of crystal-growth rate to the granitic textures. Am Miner 62:966–978

Ubide T, Kamber BS (2018). Volcanic crystals as time capsules of eruption history. *Nat Commun* **9**, 326. https://doi.org/10.1038/s41467-017-02274-w

Vernon RH (2004). *A Practical Guide to Rock Microstructure*. Cambridge University Press; 2004.

Vetere F, Sato H, Ishibashi H, De Rosa R, Donato P (2013). Viscosity changes during crystallization in shoshonitic magma: new insight on the lava flow emplacement. J. Mineral. Petrol. Sci., 108(3), 144–160.

Vetere F, Iezzi G, Behrens H, Holtz F, Ventura G, Misiti V, Cavallo A, Mollo S, Dietrich M (2015). Glass forming ability and crystallisation behaviour of sub-alkaline silicate melts. Earth-Sci Rev 150:25-44. doi: 10.1016/j.earscirev.2015.07.001

Walker D, Kirkpatrick RJ, Longhi J, Hays JF (1976). Crystallization history of lunar picritic basalt samples 12002: phase equilibria and cooling rate studies. Geol. Soc. Am. Bull. 87: 646-656

Wieser PE, Vukmanovic Z, Kilian R, Ringe E, Holness MB, Maclennan J, Edmonds E (2019). To sink, swim, twin, or nucleate: a critical appraisal of crystal aggregation processes. Geology 47: 948-952. doi:10.1130/G46660.1

4. EXAMPLES OF MICROSTRUCTURES FORMED AT HIGH UNDERCOOLING IN OTHER GEOLOGIC MATERIALS

In this chapter of the thesis, I briefly present the work I carried out during the PhD in the form of collaboration with other research groups. All the collaborations have in common the study of moderately to highly undercooled magmatic systems from an experimental and petrological perspective. Where a collaboration has already resulted in published or submitted work, I give the title, publication status, DOI (if the paper has already been published) and abstract of the publication, before focusing on the details of my contribution. All that is stated in chapters 4.1.2 (“Abstract”) and chapter 4.1.3 (“My contribution in this collaboration”, paragraph “3D reconstruction of clinopyroxene textures”) is a direct quote from the work of Colle et al., (2023)

4.1 EFFECT OF UNDERCOOLING ON CLINOPYROXENE CRYSTALLIZATION IN HIGH K BASALT: IMPLICATION FOR MAGMA DYNAMICS AT STROMBOLI VOLCANO

F. Colle, M. Masotta, S. Costa, S. Mollo, P. Landi, A. Pontesilli, **S. Peres**, L. Mancini

DOI: https://doi.org/10.1016/j.lithos.2023.107327

4.1.1. Abstract

“We present undercooling (ΔT) experiments aimed at investigating the effect of growth kinetics on the textural and compositional evolution of clinopyroxene crystals growing from a high-K basalt erupted during the 2003 paroxysm of Stromboli volcano (Italy). The experiments were performed at P = 350 MPa, T = 1050–1210 ◦C, H_2O_{melt} = 0–3 wt%, and fO_2 = Ni-NiO + 1.5 buffer. An initial stage of supersaturation was imposed to the melt under nominally anhydrous (ΔT_{anh} = 10–150 ◦C) and hydrous (ΔT_{hyd} = 25–125 ◦C) conditions. Afterwards, this supersaturation state was mitigated by melt relaxation phenomena over an annealing time of 24 h. Results show that plagioclase is the liquidus mineral phase of the

high-K basalt at ΔT_{anh} = 10 ◦C and dominates the phase assemblage as the degree of undercooling increases. Conversely, clinopyroxene and spinel co-saturate the melt at ΔT_{hyd} = 25 ◦C, followed by the subordinate formation of plagioclase. At $\Delta T_{anh/hyd} \leq 50$ ◦C, the textural maturation of clinopyroxene produces polyhedral crystals with { 111} (hourglass) and {hk0} (prism) sectors typical of a layer-by-layer growth mechanism governed by an interface-controlled crystallization regime. At $\Delta T_{anh/hyd} \geq 75$ ◦C, the attainment of dendritic and skeletal morphologies testifies to the establishment of diffusion-limited reactions at the crystal-melt interface. 3D reconstructions of synchrotron radiation X-ray microtomographic data reveal a composite growth history for clinopyroxene crystals obtained at $\Delta T_{anh/hyd} \geq 95$ ◦C. The early stage of melt supersaturation produces rosette-like structures composed of dendritic branches of clinopyroxene radiating from a common spinel grain, which acts as surface for heterogeneous nucleation. As diffusive relaxation phenomena progress over the annealing time, the elongate dendrites that constitute the inner crystal domain are partially infilled by the melt and develop skeletal overgrowths in the outer domain. With the increasing degree of undercooling, ^{T}Al and ^{M1}Ti cations are progressively incorporated in the lattice site of clinopyroxene at the expense of ^{T}Si and ^{M1}Mg cations. Because of the effect of H_2O_{melt} on the liquidus depression and melt depolymerization, crystals obtained at ΔT_{hyd} are also more enriched in ^{T}Al and ^{M1}Ti and depleted in ^{T}Si and ^{M1}Mg than those growing at ΔT_{anh}. The emerging picture is that the morphological and geochemical evolution of clinopyroxene is mutually controlled by the combined effects of melt supersaturation and relaxation phenomena. A new empirical relationship based on the cation exchange reactions in the lattice site of clinopyroxene is finally proposed to estimate the degree of undercooling governing the crystallization of augitic phenocrysts erupted during normal and violent explosions at Stromboli.”

For an exhaustive explanation of the methodological approach involved in the reconstruction of the µCT scans I suggest reading chapter 2.2 of *Colle et al., 2023*, while for the image processing refer to chapter 2.2.5 in this thesis.

4.1.2. My contribution to this collaboration

In this work I elaborated the 3D volumes of synchrotron radiation µCT scans of samples SB03-1050b and SB03-1050c. These two samples have been carried out at 350 MPa and 1050 T°C with 2-3 wt% H_2O added and 24h of dwell time. In these samples I focused on the 3D rendering of the samples in order to highlight the characteristic clustered distribution caused by heterogeneous nucleation of Tmt and vesicles on Cpx, and the possible heterogeneous nucleation of rosette-like clusters of Cpx grains on top of a single Tmt.

4.1.3. "3D reconstruction of clinopyroxene textures"

The 3D reconstructions of SR-µCT clinopyroxene data obtained at ΔT_{hyd} = 95 and 125 °C are illustrated in Fig. 2 (here Fig.4.1). Individual clinopyroxene crystals show two distinct textural domains: 1) an inner domain characterized by dendritic branches and 2) an outer domain characterized by euhedral/skeletal morphologies (here Fig.4.1a, b; in *Colle et al., 2023*, Fig. 2a, b). This textural evolution suggests that clinopyroxene growth first occurs under a high supersaturation condition, which diminishes as growth proceeds over the annealing time (*Sunagawa, 2005*). Because of progressive decrease in melt supersaturation, early formed dendritic branches with uneven faces (i.e., fast growth rate) start to assume a polyhedral form bounded by flat faces (i.e., decreasing growth rate) upon the effect of melt relaxation and infilling. According to Sunagawa (2005), outer skeleton forms and inner dendritic branches can be observed when a polyhedral clinopyroxene crystal is bisected. Furthermore, in hydrous experiments, vesicles with size (diameter) ranging from 10 to 50 µm develop in proximity of the dendritic branches, suggesting the establishment of H_2O concentration gradients at the melt interface, next to the rapidly grown dendrites (here Fig.4.1a, b; in Colle et al., 2023, Fig. 2a, b). Irrespective of anhydrous and hydrous

crystallization conditions, several clinopyroxene crystals do not grow as individual forms but rather produce rosette-like structures composed of dendritic branches and skeletal overgrowths radiating from a common spinel crystal acting as nucleation center (here Fig.4.1c, d; in Colle et al., 2023, Fig. 2c, d). Therefore, we speculate that clinopyroxene crystals may either homogeneously nucleate from the melt via a spontaneous crystallization reaction or may heterogeneously nucleate onto the spinel grain due to the presence of a catalyst surface which lowers the energetic barrier for the formation of a critical nucleus."

4.1.4. References

Colle F, Masotta M, Costa S, Mollo S, Landi P, Pontesilli A, Peres S, Mancini L (2023). Effect of undercooling on clinopyroxene crystallization in a high K basalt: Implications for magma dynamics at Stromboli volcano. Lithos, Volumes 456–457. 107327. Doi: 10.1016/j.lithos.2023.107327

Sunagawa I (2005) Crystals: Growth, Morphology and Perfection. Cambridge University Press, Cambridge, U.K., 2005, 295 + xii pages. ISBN 0–521–841–895.

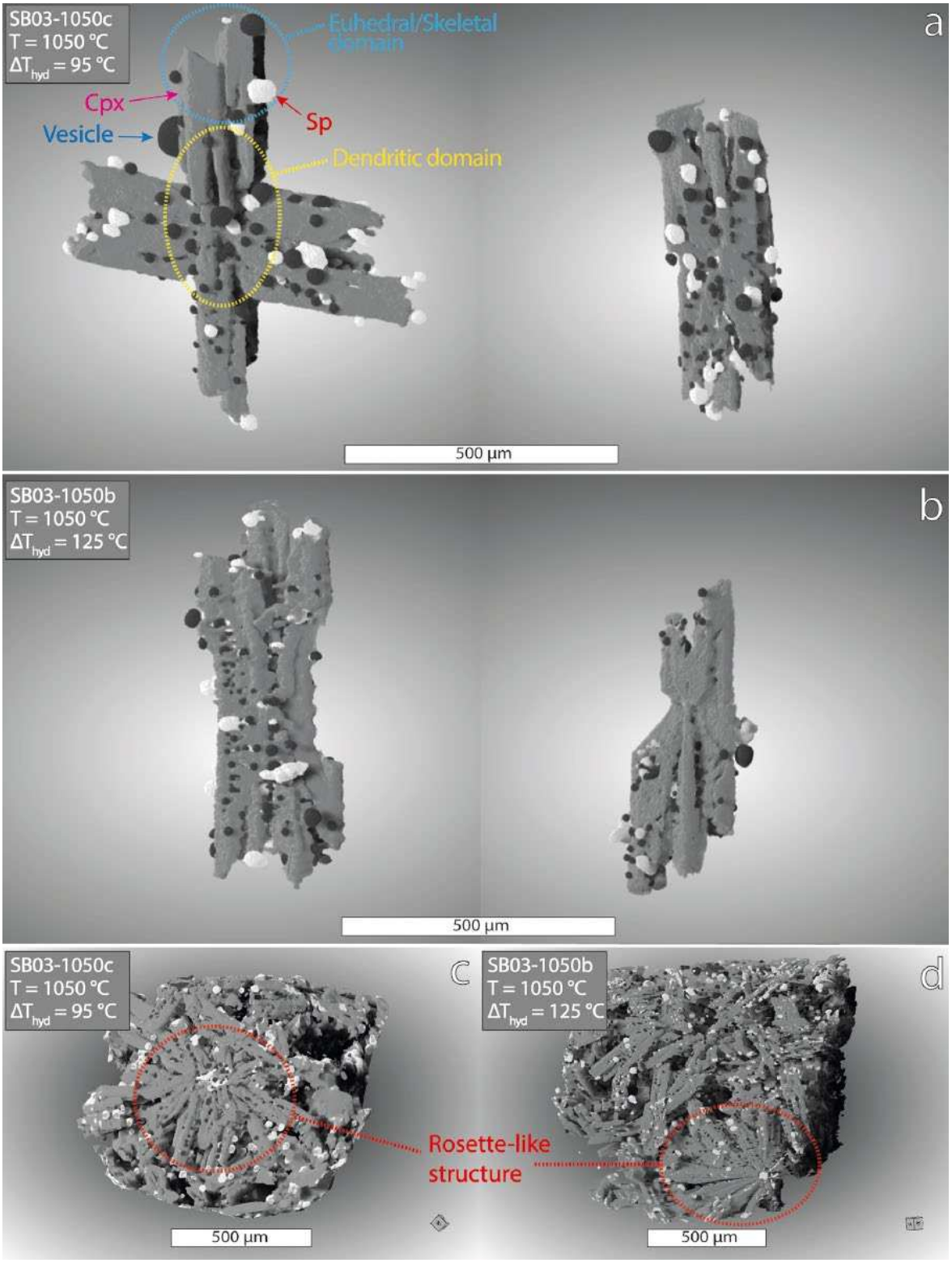

Fig.4.1.1) Volume rendering of individual crystals (a,b) and cluster (c) of clinopyroxene obtained using SR-µCT data reconstructed with an isotropic voxel size of 2.5 µm and isosurface rendering after segmentation of vesicles (coloured in dark grey) and spinel (coloured in white); yellow and blue circles indicate the inner dendritic domain and the outer euhedral/skeletal domain, respectively, whereas red circle indicate a rosette-like structure. Fig.2 of Colle et al., 2023

4.2 TRACING PRE- TO POST-ERUPTIVE CRYSTALLIZATION OF TRACHYBASALTIC MELTS: INSIGHT INTO THE 1651-1654 CE LAVAS OF MOUNT ETNA (SICILY, ITALY)

Lanzafame G.*, **Peres S.**, Casetta F., Kudrna Prašek M., Giacomoni P.P., Portale S., Abart R., Ferlito C. (under review), submitted to "Journal of Volcanology and Geothermal Research"

This collaboration has been submitted for peer review to the journal Journal of Volcanology and Geothermal Research and is currently under review. The abstract is quoted from the draft manuscript, while the following chapters provide a more comprehensive account of the methods and models used in my calculations. These chapters were written by me and may differ slightly from the version included in the paper.

4.2.1 Aim of the paper

"Understanding the crystallization of silicate melts is key to reconstructing the processes occurring from magma rising to lava emplacement, the latter representing a major hazard for human settlements during effusive eruptions. Crystal growth, along with melt H_2O degassing, strongly influences lava rheology and surface flow behaviour. This study investigates pre- to post-eruptive crystallization in trachybasaltic melts from the 1651–1654 CE eruption on Mount Etna's western flank (Sicily, Italy), one of the 17th century's most significant events due to its duration, lava field extent, and reach into inhabited areas. Investigation on different layers of a fractured pressure ridge allowed to reconstruct the crystallization history of a single flow unit, revealing significant textural differences between the inner and outer (crust) portion of the lava, allowing to quantify the extent of crystallization at subaerial conditions. By combining 2D and 3D textural analyses with chemical and mineralogical investigations, the pre-eruptive pressure-temperature (P–T) conditions of crystal formation were constrained. Phenocrysts nucleated in a vertically extended feeding system (down to 23 km below the sea level) at almost stationary condition of T = 1070-1060 °C. In the glass-rich crust, detailed chemical and textural analyses revealed chemical boundary layers around plagioclase

microlites, which was used to model a subaerial growth rate of the outermost plagioclase rim in the order of 0.2-4.5 μm/s. These findings enhance our understanding of lava behaviour during flow, offering key insights for improving hazard models, monitoring, and response during effusive volcanic events similar to the 1651–1654 CE eruption."

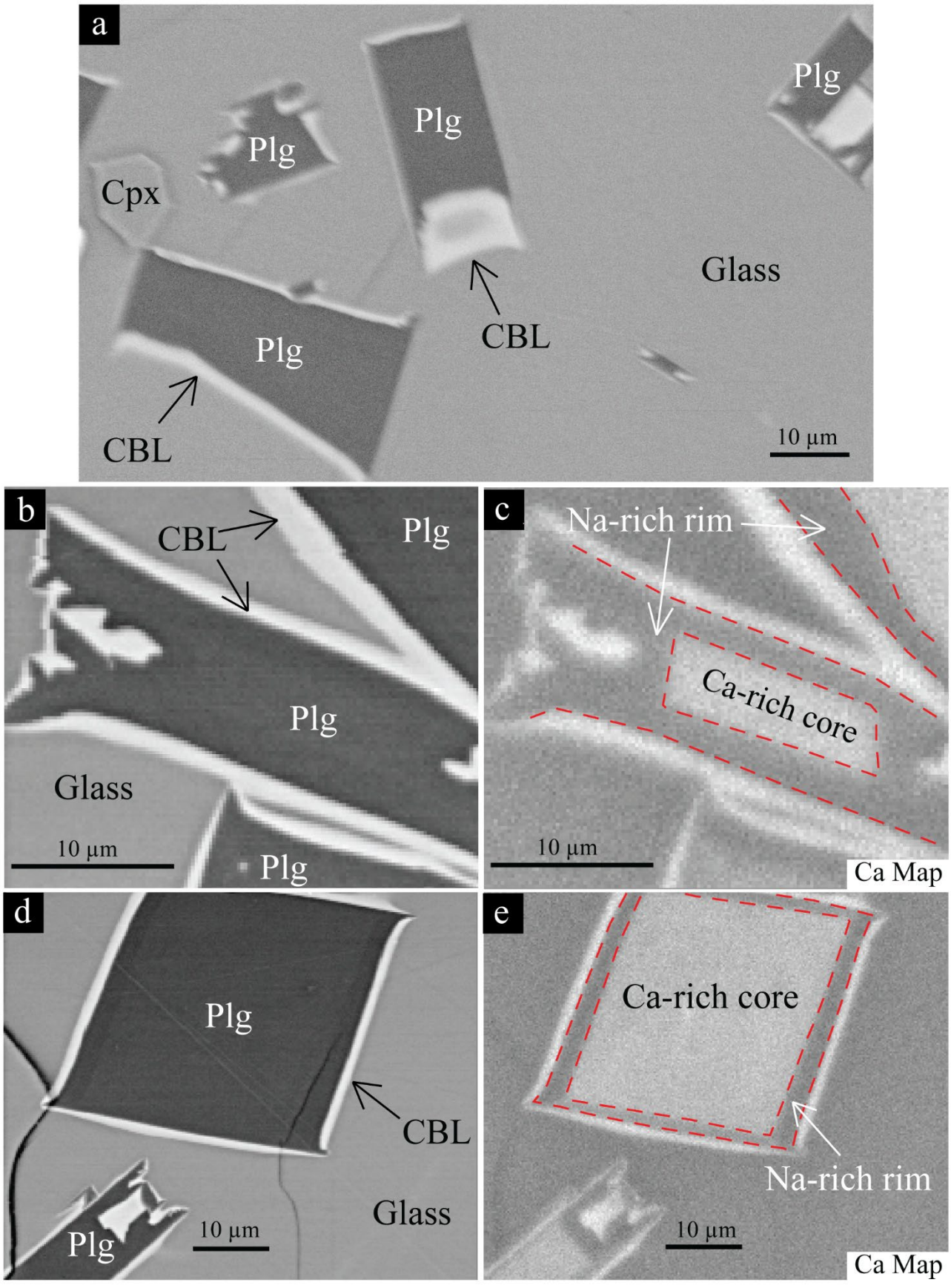

Fig.4.2.1. a) BSE image of the groundmass of a Bronte lava near the contact with air. b-d) high magnification BSE image of Pl micro-crystals (dark grey) surrounded by CBLs (white). c-e) EPMA chemical map (scanned at 15kV) showing Ca relative amount in the phases composing the scanned area.

4.2.2 My contribution to the paper

My main contribution is to model the growth rate of the final Na-rich rim characterizing the Plg microcrystals in the glass-rich crust of the lava flow (Fig.4.2.1). The same Plg grains are surrounded by a CBL which is caused by the rejection of the elements incompatible with the Na-rich Plg crystal lattice (i.e. Fe, Mg, Ti and Ca). Establishing a steady-state model, we link the formation of the CBL with the Na-rich Plg rim of the microlites in the groundmass. Given that the CBL is still visible, despite the fact that it would be expected to rapidly dissipate by fast diffusion of enriched elements into the unenriched melt at the high temperatures characteristic of melt emplacement (>1000 degrees C), we can estimate the velocity at which the Plg-melt interface has to move in order to sustain the presence of the CBL (rejecting the elements that compose it). We assume that this corresponds to the Na-rich rim growth rate. We performed accurate EPMA mapping in a representative CBL+ Plg grain and carefully model this microstructure.

In the following sections I will present the methodologies used to accomplish this work.

4.2.3 EPMA single spot analysis and chemical maps

The major element composition of mineral phases was determined by Electron Probe Micro Analysis (EPMA) using a Cameca SXFive FE electron microprobe equipped with five wavelength-dispersive (WD) and one energy-dispersive (ED) spectrometers, hosted at the Department of Lithospheric Research, University of Vienna (Austria). Routine point analyses of olivine, oxides and clinopyroxene were performed using the following operating conditions: 15 kV accelerating voltage, 20 nA beam current, 20 s counting time on peak position, 1 μm beam diameter. For feldspar and glass, the beam was defocused to 5 μm and a 10 s counting time on the peak position for Na and K were used. Detection limits were: 100-250 ppm for Al, Na, Cr, Mn, Ti and Cl; 300-500 ppm for Si, Fe, Mg, Ca, Ni and K. For all analyses, natural and synthetic standards were used for calibration, and the PAP routine was

applied for matrix correction (Pouchou and Pichoir, 1991).

Element distribution maps at the interface between plagioclase grains and glass (see discussion below) were acquired in beam scan mode using the same Cameca SXFive FE electron microprobe, with a 35.5 nA beam current and 10-15 kV accelerating voltage (e.g. Fig.4.2.2). Map size varied depending on the investigated microstructure, while a fixed step size of 0.33 μm and a dwell time per pixel of 40-80 ms was applied. Relative Fe, K, Mg, Na and Ti concentrations were mapped using five wavelength dispersive spectrometers set to the corresponding Kα emission wavelengths for each element, while Si, Al and Ca concentrations were acquired through EDS.

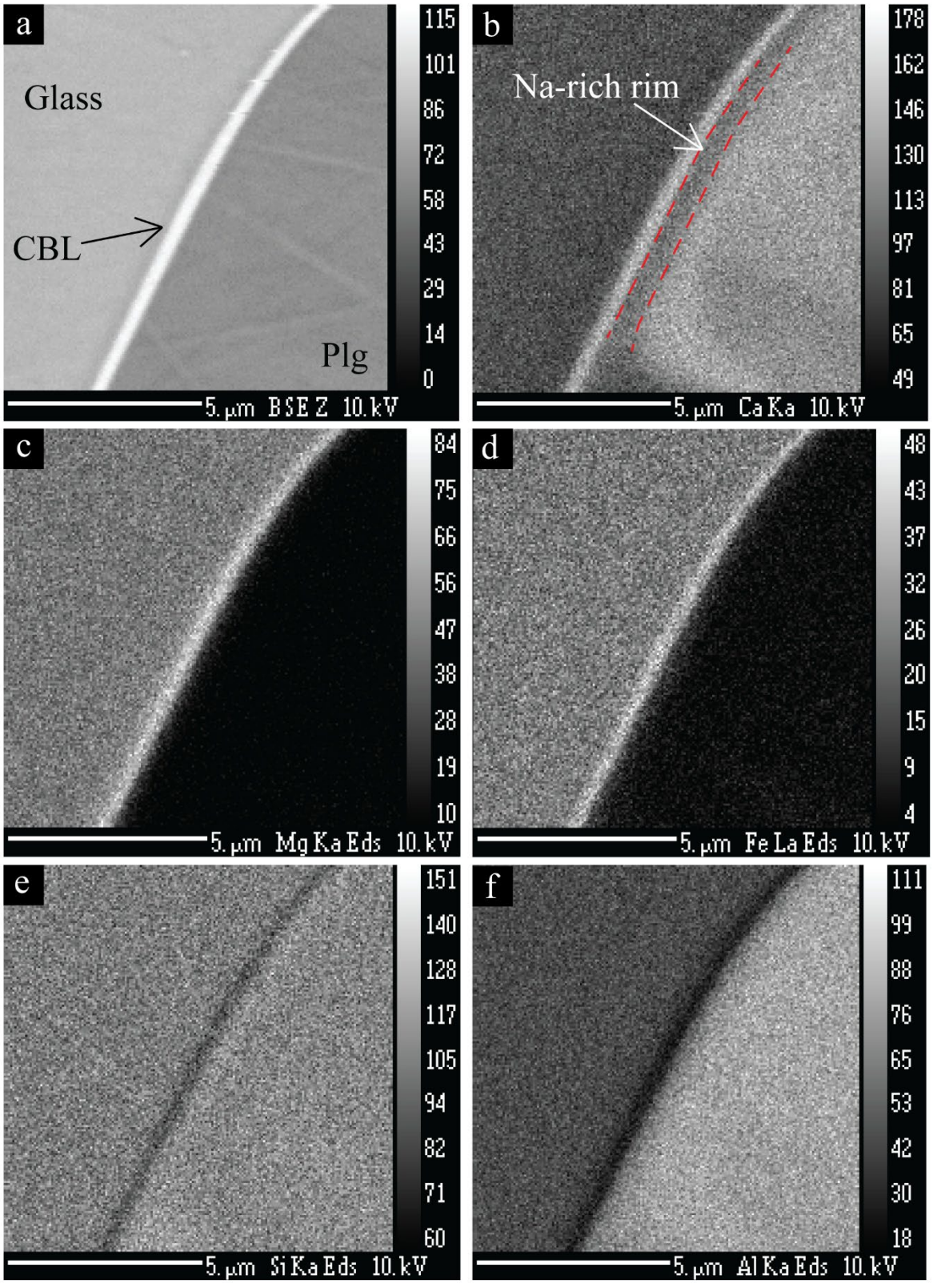

Fig.4.2.2. a) BSE image of the Pl-CBL-melt system selected for a high resolution EPMA scan (10kV). b to f) Ca, Mg, Fe, Si and Al elemental EPMA maps of the same area as (a).

4.2.4 ImageJ processing

All elemental maps and the respective BSE image have been processed by a ***"Median"*** filter of 1 pixel to remove the noise and enhance edges. Each map has been scaled through Fiji command ***"Scale"***. In order to calibrate the elemental maps, on each image, two spots 28 pixels in diameter (corresponding to 1.55 µm) at fixed locations far from the Plg-melt interface have been selected as representative of the bulk glass and the plagioclase respectively (Fig.4.2.3 left). The median grey value of pixels within these spots was calculated and correlated with a reference concentration of the respective oxide, derived from an average of 3 quantitative EPMA analyses of glass and 2 analyses of plagioclase micro-crystals. The elemental maps have been calibrated through the Fiji function ***"Calibrate"*** so that each pixel of the map corresponds to an amount of the respective oxide expressed in wt%. A chemical profile 4.44 µm long and perpendicular to the **CBL** was measured in the calibrated map using the Fiji function ***"Plot Profile"*** (Fig.4.2.3 right).

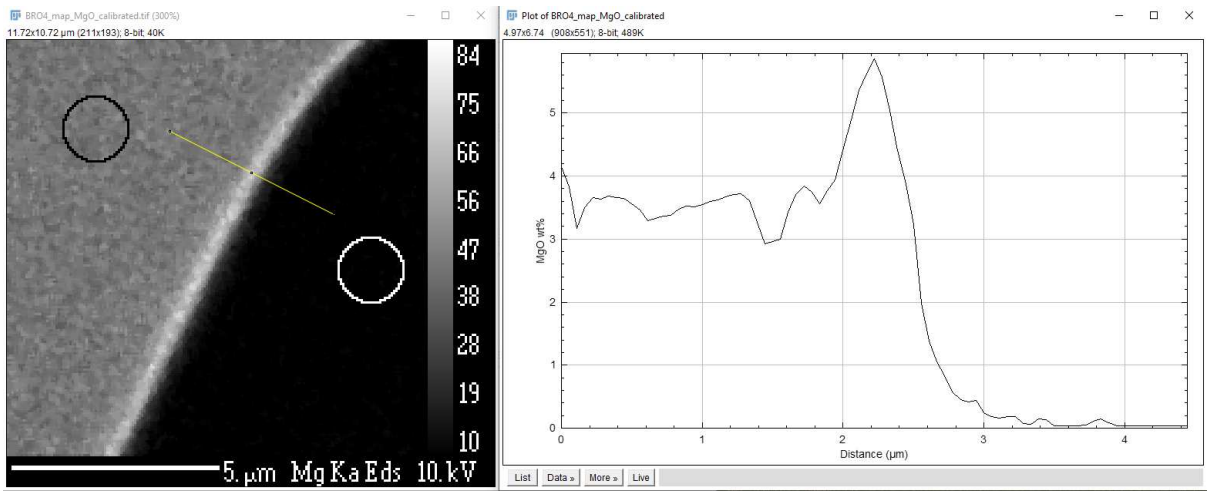

Fig. 4.2.3. After the calibration, 35 profiles (at right there is an example of them) of the same size and properly translated so that the centre of it always corresponds to the centre of the CBL, have been acquired with Fiji "plot profile" tool.

To improve representativeness and reduce data scattering, multiple profiles (35) were measured on the same chemical map. A custom Fiji macro was coded to translate the same profile line segment perpendicular to the CBL while keeping it centered on the chemical boundary layer.

4.2.5 Results: Chemical profile modelling and exponential curve fitting

The 35 new profiles have been exported to an Excel file and averaged so to obtain a more representative, less scattered chemical profile (Fig.4.2.4).

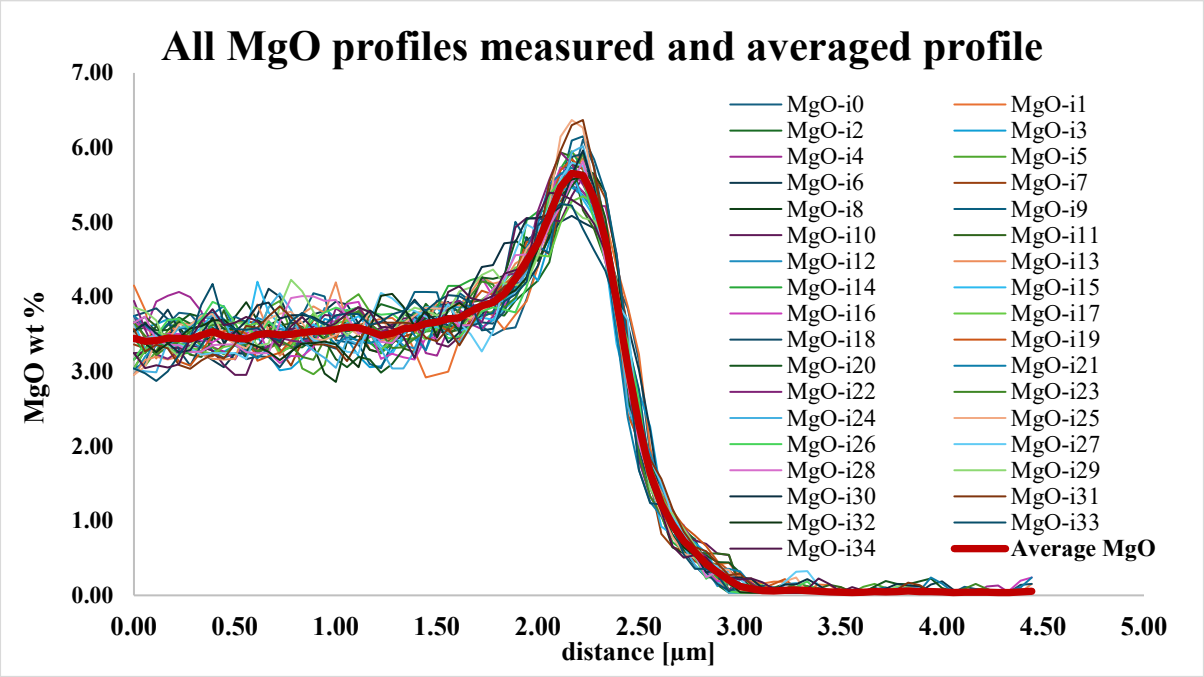

Fig. 4.2.4. Graph with all the 35 chemical profiles and the Averaged profile (thicker red line) used for the steady-state model.

Theoretically, the shape of the portion of each oxide's chemical profile extending from the crystal interface into the unaffected homogenous glass near a fast-growing crystal should approximate an exponential function due to the interplay of expulsion of incompatible components like FeO, MgO, and TiO2 from the crystal lattice (Plagioclase in this case) and their diffusion into the adjacent unaffected glass. Practical measurements face limitations due to the spatial resolution of the electron probe microanalyser (EPMA), where the diameter size of the activated volume of about 150 nm (performed at 10 kV) limits the lateral resolution of the x-ray signal. Small CBL profiles with thicknesses in the order of 0.5 - 1 µm are affected by these artefacts due to the proximity of the extremely MgO, FeO and TiO_2-poor Plagioclase in contact. As a result, the observed profiles in glass + CBL exhibit a bell-shaped curve, deviating from the theoretically expected exponential shape. When the chemical profiles are

plotted in a X-Y space, with X equal to the position of the measurement and the Y the wt% of the oxide measured, the graph shows the asymptotic portion of the curve (corresponding to the unaffected glass) near the origin, while the exponentially growing portion of the curve corresponds to the CBL, and the plagioclase measurement furthest from the origin. To focus on the formation of the CBL, we considered only the profile portions corresponding to the glass and the CBL. We achieved this by: a) identifying the Plagioclase/CBL interface through a comparison between the BSE image and the chemical maps, and disregarding the portion of the profile corresponding to the plagioclase; b) reversing the curve for plotting so that the plagioclase/CBL interface starts at the origin, with the unaffected glass further along the X-axis. This adjustment shows the peak of the bell curve near the origin while the asymptotic segment lies at higher X values.

To model the true exponential curve accurately from the experimental measurements, other assumptions are required: a) the bell-like shape of the curve, diverging from the theoretical exponential shape, is caused by the smoothing/averaging artefact as previously introduced; b) the portion of the CBL which better approximates the real exponential curve lies between the outermost edge of the CBL and a midpoint between the curve's peak and its inflection point; c) considering all measured values, including those closest to the origin which might be lower than the peak, could lead to an underestimation of the starting values after curve fitting, or the use of a curve with an overall lower R^2, less representative of the modelled data. Given the above assumptions, values near the curve's peak were excluded from consideration. Finally, a MATLAB code was developed to find the best-fitting exponential curve for the measured data based on these assumptions. The portion of the new, best fit exponential curve which includes CBL + melt (excluding the Plg segment), will be referred to in the following Equation 2 as C_{fit}

4.2.6 Discussion

All the maps revealed the presence of plagioclase grains comprising a relatively Ca-rich core always coupled with a relatively Na-rich rim between 1 and 5 µm wide (depending on the orientation in which the Pl has been cut) and a 0.5 to 2 µm wide CBL in the glass at the immediate contact with the plagioclase. The CBL is characterized by an enrichment in MgO, FeO, TiO2, and CaO and a depletion of SiO2 and Al2O3. In most of these plagioclases, it is also worth noting the presence of short tails (<1 µm) at all corners, beyond which no significant CBL is observed.

A CBL can form when chemical components that are incompatible in the growing crystal "pile up" in the glass immediately in front of the crystallization front. The extent of pile-up of a specific component depends on the difference of the equilibrium concentrations of this element in bulk, unaffected glass and in the growing crystal, and on the relation between the diffusivity of the component in the melt and the rate of crystal growth. Indeed, elements with low K_D with respect to Na-rich plagioclase, like Mg, Fe, Ti and Ca, preferentially partition into the melt and may pile-up at the moving Pl-melt interface if their diffusivities in the melt are low as compared to the velocity at which the Pl-melt interface moves during crystal growth.

The easiest scenario for modelling the chemical profile of the plagioclase-CBL-melt system is to assume that this system reaches a steady state. In this scenario, the concentration profile of a specific component ($C(x,t)$) in the CBL + melt portion of the system (we exclude Plagioclase) can be approximated by the following equation:

$$\boldsymbol{C(x,t) = C_2 + (C_1 - C_2)\exp\left(-\frac{v}{D}x\right)} \quad \textbf{(1)}$$

where $\boldsymbol{C_1}$ is the concentration of a given element at the plagioclase/CBL interface, $\mathbf{C_2}$ is the concentration of a given element at the bulk melt/glass far from the CBL, **v** is the velocity at

which the plagioclase/CBL interface moves into the melt and $\boldsymbol{D}$ is the diffusivity of the element considered. This equation describes diffusion into the half space x ≥ 0 from a source at $\boldsymbol{x} = 0$, where the strength of the source is related to the difference in element concentrations between the plagioclase and the melt/glass and the propagation velocity of the crystallization front. The modelled concentration profiles only depend on the ratio $\boldsymbol{k} = \frac{\boldsymbol{v}}{\boldsymbol{D}}$; and only this ratio can be obtained from a fit of the model curve to observed concentration data (*Lucassen et al., 2009*). Mg, Fe and Ti are the best elements to use for the intended analysis due to their very low concentrations in Plg. Since Fe can be incorporated in low amounts in the fast-growing plagioclase, as our single spot analysis and chemical profiles demonstrate (the measured plagioclases can have up to 1.0 wt% of FeO), Mg and Ti are more suited, as they show even lower concentration in the plagioclase (both <0.3 wt% of the oxide). We will focus just on Mg, since it is more abundant in the melt, and the CBL+ melt chemical profile can nicely be fitted in the exponential function modelled before (see Chapter 4.2.5). To this end, the data are linearized by rearranging Eq. 1 and taking the logarithm. Which yields:

$$\ln\left(\frac{\boldsymbol{C_2 - C_{fit}(x,t)}}{\boldsymbol{C_2 - C_1}}\right) = -\frac{\boldsymbol{v}}{\boldsymbol{D_{Mg}}}\boldsymbol{x} \quad (2)$$

D_{Mg} has been calculated through the following equation (*Zhang et al., 2010*), in a T interval between 1273K and 1373K, a T range plausible for erupted trachybasalts at the air contact, and anhydrous conditions, since we measured values of H_2O between 0.08 and 0.16 wt% still dissolved in the remaining glass of same sample through Fourier transform infrared spectroscopy (FTIR):

$$\boldsymbol{ln_{Mg}^{dry\ basalts\ to\ rhyolites}} = \boldsymbol{-5.17 - 11.37X_{SA} - 2.16X_{FM} - \frac{10993 + 17839X_{SA}}{T}} \quad (3)$$

where X is cation mole fraction, X_{FM} = Fe + Mn + Mg, and X_{SA} = Si + Al, and T is the temperature expressed in Kelvin. Equation (2) represents a straight line in $\ln\left(\frac{C_2 - C(x,t)}{C_2 - C_1}\right) - X$

space, where $\boldsymbol{k} = \frac{\boldsymbol{v}}{\boldsymbol{D}}$ represents the modulus of the angular coefficient of this line and can be calculated by a linear regression procedure. The velocity of the interface movement $\boldsymbol{v}$ can be calculated, being now the only unknown, and so also the minimum time t required for the same interface to move the distance $\boldsymbol{s}$ corresponding to the thickness of the late albitic rim in the growing plagioclase, through the equation $\boldsymbol{t = s/v}$.

All the curves modelled, the one using all measured values and the ones excluding the first measured values near the interface, can properly describe the behavior of the measured profile in the first 900 μm to 1 mm of the CBL from the Pl-melt interface. For the calculation of the rim growth time and velocity I used the modelled curve that excludes the values in the first 0.111 μm from the interface (which include the bell shape portion and so also the peak value) because these values are expected to be most strongly affected by the EPMA spot size-related artefact.

Comparing the modelled curve with the measured data profile, we observe that both the exponentially fitted curve and the measured profiles align well. More importantly, the linearized equation (2), when applied to both the fitted data $\boldsymbol{C_{fit}(x,t)}$ and the measured data $\boldsymbol{C_{measured}(x,t)}$ show that the two trends are parallel and constitute a good fit in the first 900 μm portion of the glass characterized by the presence of the CBL, which further supports the validity of the model (Fig. 4.2.5). In the glass region dominated by the unaffected glass (CBL Excluded) the measured data linearized slightly deviates from the linearized modelled curve (Fig. 4.2.5) because of the not static (meaning slightly oscillatory/non-linear) nature of the averaged profile that constitutes the measured data, which becomes evident once the actual concentration gradient has decreased to almost zero (Fig. 4.2.4).

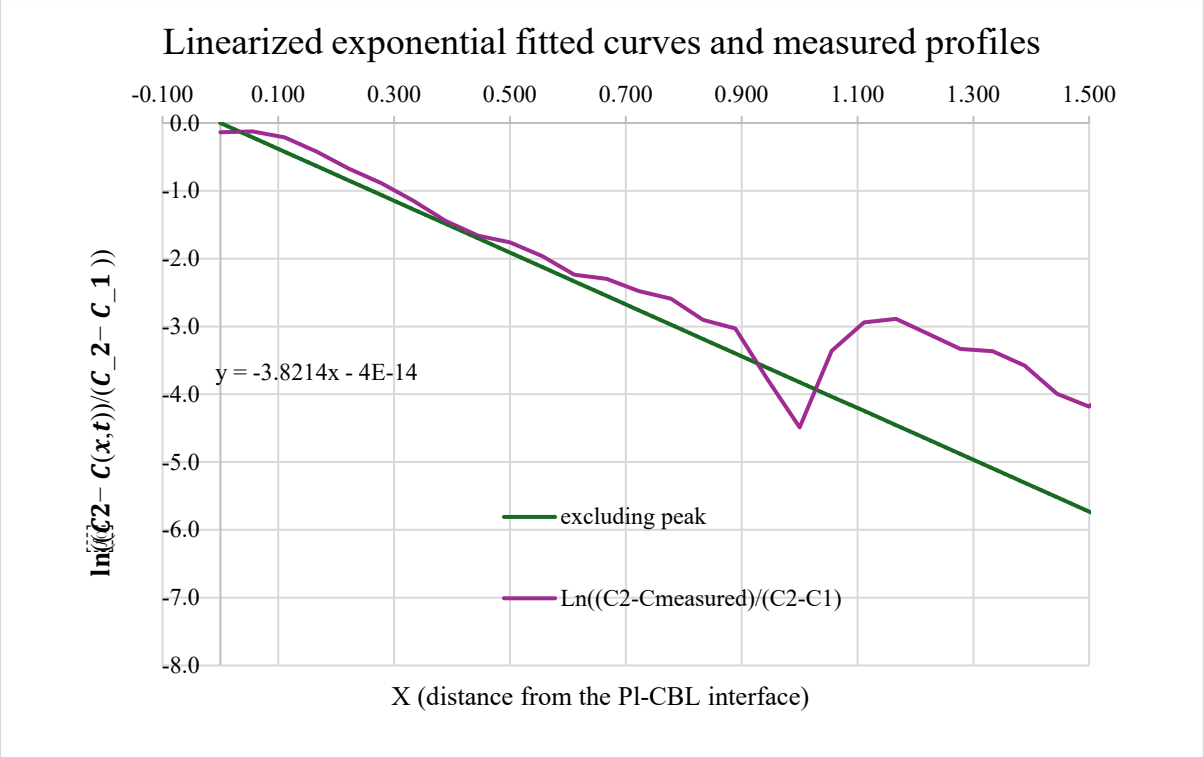

Fig.4.2.5. Linearization of Equation (2). This process allows to represent this equation as a straight line in a $\boldsymbol{ln\left(\frac{C_2 - C(x,t)}{C_2 - C_1}\right)}$ *– X space. The graph demonstrates that the modelled curve (now linearized) accurately describe the beahvour of the measured profile (also linearized) in the first 900 µm of the glass near the growing Plg grain (where glass means CBL + bulk/unaffected glass). In the graph are also included the equation that fit the linearized profiles. The angular coefficients are used to calculate* $\boldsymbol{k = \frac{v}{D}}$.

The results of the modeling suggest that these grains may have formed in the time between eruption and the final quenching of the shallowest portions of the lava flow. While we lack direct data on the growth rate of the Ca-rich core in the plagioclases, our model provides an estimate for the average growth time of the Na-rich rim. Assuming a rim thickness between 0.5 and 2 µm, measured in several BSE images, an exponentially fitted growth model, and Mg diffusivities in the melt ($\boldsymbol{D_{Mg}}$) between 0.2 and 2 µm² s^{-1}, the estimated growth time in a steady-state scenario ranges from 0.06 to 2s, which corresponds to an extremely fast growth rate in the range between 1.5 µm s^{-1} (1.5 × 10^{-4} cm s^{-1} at T = 975°C) and 7.3 µm s^{-1} (7.3 x 10^{-4} cm s^{-1} at T = 1100°C). If we arbitrarily adopt one order of magnitude lower diffusivities (consistent with a temperature of ~1123 K (850°C) from equation (3)), the estimated growth time increases to 2.9–12 seconds, corresponding to growth rate of 0.2 µm s^{-1} (2 × 10^{-5} cm

s^{-1}) which seems in the range calculated in other studies of crystal growth from undercooled melts (e.g. *Arzilli et al., 2019; Welsch et al., 2023*).

4.2.7 Further considerations and Implications

This model should be approached as a limit-case scenario and applied with caution. It is possible that a steady-state condition might not have been fully achieved (over the entire period of rim growth), or it may have been established only after some of the Na-rich rim had already crystallized, or it may have been established and then growth rate decreased. Consequently, also the growth rate estimated could be an average of all the growth stages of the Na-rich overgrowth. The listed possibilities correspond with the growth stages described by *Welsch et al., (2023)*. At the very beginning of the temperature drop, the growth rates are probably higher, and consequently CBL could have built up, i.e. the acceleration stage of Welsch et al., (2023). If a steady state was reached the Na-rich rim would be characterized by a linear growth stage (linear growth stage of Welsch et al., 2023), in which the assumptions of the model above are fully valid. The end of crystallization is characterized by a deceleration stage, which may coincide with depletion in components necessary for the crystal to grow (deceleration stages of Welsch et al., 2023)

The last stage can also be caused by the formation of a CBL itself. Indeed, a CBL near these Plg grain is characterized by an enrichment in oxides such as MgO, FeO, TiO2, and CaO, which are preferentially partitioned into the melt and “repelled” from the growing Na-rich plagioclase, and a depletion of SiO2 and Al2O3, which are preferentially partitioned into the crystal during its growth. The occurring of the depletion causes a lack of tetrahedra-forming oxides in the adjacent glass, possibly inhibiting or even halting the growth of the plagioclase crystal.

For the CBL to form, the growth rate of the crystal must exceed the diffusivities of the oxides in the surrounding melt. Simultaneously, for plagioclase growth to continue, the CBL should not be excessively depleted in SiO2 and Al2O3. At temperatures between 1050°C and 1100°C, the plagioclase growth rate might still be higher than the relevant element diffusivities, so as to sustain the formation of CBL, however, because of the relatively low diffusivities of Al and Si, a CBL depletion in Al2O3 and SiO2 would still occur, that would eventually lead to a decrease of the growth rate and possibly a halt. When the plagioclase ceases to grow, the CBL may, in this temperature range, temporarily diffuse away from the plagioclase-melt interface, allowing another episode of growth, which could potentially lead to oscillatory zoning in the Plagioclase rim. While this is a plausible scenario, we do not observe any sign on oscillatory zoning in the elements scanned through EPMA mapping with the current analytical resolution. An explanation on why we do not observe this microstructure is that the Na-rich rim of the Plg grain could have been formed at relatively low absolute temperature (< 1000 °C). The low temperature may have prevented the CBL from diffusing away in the bulk melt, halting the growth of the Na-rich rim at the end of the aforementioned deceleration stage. Quenching at contact with air is the most likely process to have formed this microstructure.

4.2.8 References

Arzilli F, La Spina G, Burton MR, Polacci M, Le Gall N, Hartley ME, Di Genova D, Cai B, Vo NT, Bamber EC, Nonni S, Atwood R, Llewellin EW, Brooker RA, Mader HM, Lee PD (2019) Magma fragmentation in highly explosive basaltic eruptions induced by rapid crystallization. Nature Geoscience 12, 509 1023-1028. doi: 10.1038/s41561-019-0468-6

Lucassen, F., Dulski, P., Abart, R., Franz, G., Dieter, R., Romer, R.L. (2010). Redistribution of HFSE elements during rutile replacement by titanite. Contrib Mineral Petrol 160, 279–295 (2010). https://doi.org/10.1007/s00410-009-0477-3

Welsch, B., Faure, F., First, E.C. (2023). Reappraising Crystallization Kinetics with Overgrowth Chronometry: an in Situ Study of Olivine Growth Velocities, Journal of Petrology, 64, 1-29. https://doi.org/10.1093/petrology/egad055

Zhang, Y., Ni, H., Chen, Y. (2010). Diffusion Data in Silicate Melts, Reviews in Mineralogy and Geochemistry 72 (1): 311- 408.

5. FUTURE DEVELOPMENTS IN EXPERIMENTAL PETROLOGY OF UNDERCOOLED MAGMAS

In situ 3D time-dependent crystallization experiments (*Polacci et al., 2018*), also known as in situ 4D crystallization experiments (*Arzilli et al., 2022*) represent a recently developed branch of experimental petrology which involves the 3D imaging of a sample as it forms using micro-Computed Tomography (μCT). The possibility of observing the microstructural relationship of crystallizing magmas and their evolution through time, under controlled laboratory conditions may represent, in my opinion, one of the most prominent directions in which the experimental petrology field should move. The two works just mentioned before, are the first to apply 4D crystallization experiments to basaltic and trachybasaltic melts. *Polacci et al., (2018)* study disequilibrium crystallization and their effect on size, shape, orientation and evolution of crystals as a function of both time and space. *Arzilli et al., (2022)* use 4D experiments to estimate the characteristic time, defined as a measure of how fast a process will approach the equilibrium (*Marsh 1998; La Spina et al., 2016*) of the crystallizing phases during disequilibrium crystallization. Both of the works brought new insight on the process of disequilibrium crystallization and its implication on volcanic and conduit dynamics characterizing explosive eruptions of mafic magmatic systems.

Inspired by these works and with the recent knowledge and results acquired during the PhD, I decided to also to write a proposal at Elettra Synchrotron in order to carry out 4D experiments.

5.1 Aim of the proposal

The aim of the proposal was to study the crystal clustering happening in crystallization experiments that had as starting composition a trachybasalt from the 1669 eruption of Mt Etna. This specific eruption has been intensely studied because the high volume of emitted

products (~ 600 × 106 m^3) and the low lava viscosity led to flows of > 16 km length, strongly impacting the local population (*Branca et al., 2013*). Moreover, syn-eruptive crystallisation in the 1669 lava flows was a key control on their rheological evolution (*Lanzafame et al 2022*). The 1669 lavas are composed of Cpx phenocrysts up to 2 cm in diameter, mm-sized Plg phenocrysts and a second Cpx population of numerous sub-millimetric crystals, clustered with Tmt set in microcrystalline groundmass.

Because of the high abundance of phenocrysts (mostly Plg, Cpx but also Ol) and the ubiquitous clustering of Cpx and Tmt in the groundmass, we wanted to investigate a) the crystallization behaviour of magmas with 1669 eruption starting composition when crystallizing after a sudden undercooling drops and b) the results of the same type of crystallization experiments on the same starting material with the addition of crystal seeds, looking at how these impact on the final microstructure of the sample.

Even if the proposal received good reviews it was unfortunately not selected as suitable for beamtime, but we were able to obtain in house time, and so we carried out the following set of experiments.

5.2 Experimental plan and Methodologies

We planned a set of 8 crystallization in-situ experiments, conducted at the SYRMEP beamline (Elettra Synchrotron) using the induction furnace developed at the same beamline (*Kudrna Prasek et al., 2018*). For all the experimental runs, the starting glass chips (+crystal seeds in the case the experiment was seeded) has been heated rapidly to 1300°C at superliquidus conditions and held at these conditions for 30 minutes to allow the release of all the bubbles formed during the melting of the starting material. Two different sets of cooling ramps were planned: a) dynamic experiments were carried out decreasing the experimental temperature in multiple intervals of 10 °C from 1210 °C to 1150 °C, with a 30 minutes dwell

time at each temperature in order to decrease the disequilibrium (Fig.5.1a); we scanned the sample at intervals of 10 minutes, starting 2 minutes after the melt reached the target T. b) single step undercooling experiments (Fig.5.1b, temperature drop experiment) to the target temperature of 1150°C and 1100°C, with consequent dwell time of 1h or until high degrees of crystallinity are reached (> 50%). Also during this experimental run we scanned the sample at intervals of 10 minutes, starting 2 minutes after the melt reached the target T. Both sets of cooling experiments have been carried using a glass composed of 1669 eruption trachybasaltic material, with the addition of crystal seeds for the seeded experiments.

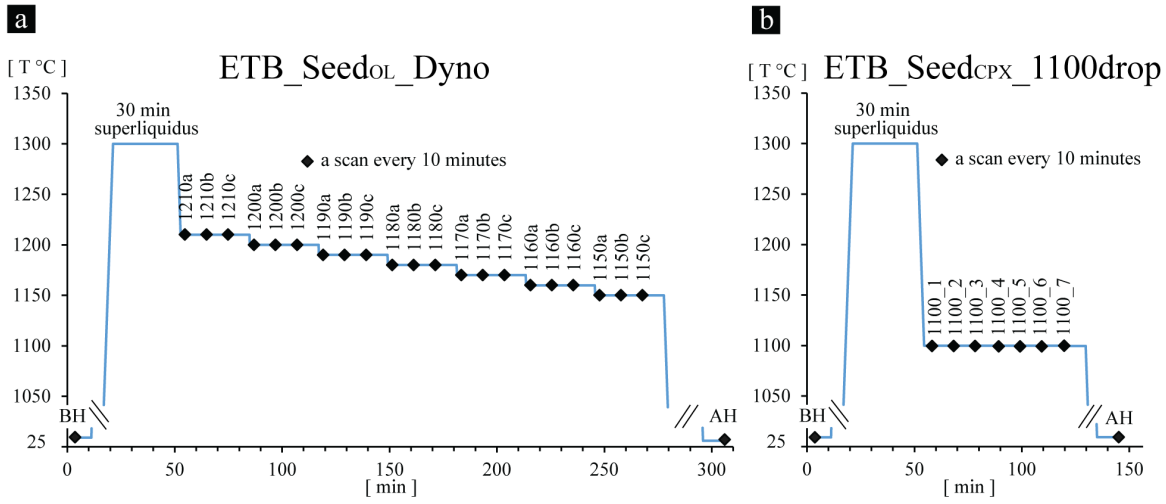

Fig.5.1. Precise schematic illustration of the thermal history of experimental samples ETB_SeedOL_Dyno and ETB_SeedCPX_1100drop. Both can be used as representative graphs for any dynamic and drop experiment samples respectively.

For the SR-µCT experiments, we used a filtered white beam in the 2.4 GeV modality of the Elettra machine, where for each scan 1800 radiographs (projections) of the sample over a total rotation angle of 180° were acquired with an exposure time per projection of 1.2 s selecting an isotropic voxel size of 1.3 microns. In order to enhance the visualization of the silicate phases, we worked in propagation-based phase contrast mode (*Polacci et al., 2010*). The detector used was a 16-bit, water-cooled, sCMOS macroscope camera (Hamamatsu C11440-22C) with a 2048 × 2048 pixel chip coupled, through a high numerical aperture optics, to a 17 µm-thick GGG:Eu scintillator screen.

A demo version of the new SYRMEP Tomo Project (STP) software suite (*Brun et al., 2015*) currently developing at the same beamline was used to reconstruct the imaged virtual volumes. The SR-µCT reconstructed volumes were processed with the Dragonfly software (version 2020.2 ORS, Canada; non-commercial license for academic use). A 3D median filter has been first applied and then each crystal phase has been extracted through a threshold process. For the preliminary analysis of these samples, I focused on qualitatively imaging and rendering the Spl, Ol and/or Cpx grains in specific portions of the sample. Plg crystals are the most common phase in all the samples, but because they are compositionally similar to the remaining glass, which translate to similar grey values in the reconstructed slices, they require a lot of time and difficult image analysis in order to be properly segmented, so I did not focus on Plg for these preliminary results.

Two experimental samples have been partially analysed: sample ETB_SeedOl_dyno and ETB_SeedCpx_drop_1100. A single VOI (volume of interest) of the bottom of each sample of size 1128 x 960 x 598 μm^3 and 2532 x 2532 x 598 μm^3 respectively has been selected to give an overview of the specific microstructures of the sample, with a focus on the crystallization at different temperatures around the crystal seeds that survived the 1300°C de-vesiculation process.

5.3 Preliminary Results

5.3.1 Brief characterization of the crystal seeds pre-heating:

In order to add seeds to the starting glass, we crushed some 1669 samples and selected olivine and Cpx grains through microscope discrimination. We added 3 Ol seeds to the glass in sample ETB_Seed$_{Ol}$_dyno and 5 Cpx grains in sample ETB_Seed$_{CPX}$_1100$_{drop}$. The 3D scan of the starting material + seeds allowed us to constrain the sizes, shapes, and the presence of any inclusions in the seeds (Fig. 5.2). Both the Ol and Cpx seeds are fragments or entire grains with sizes ranging from 300 µm to 1000 µm. Both the phases show the presence

of several Spl inclusions of sizes ranging from 10 to 250 um, and smaller number of melt and fluid inclusions.

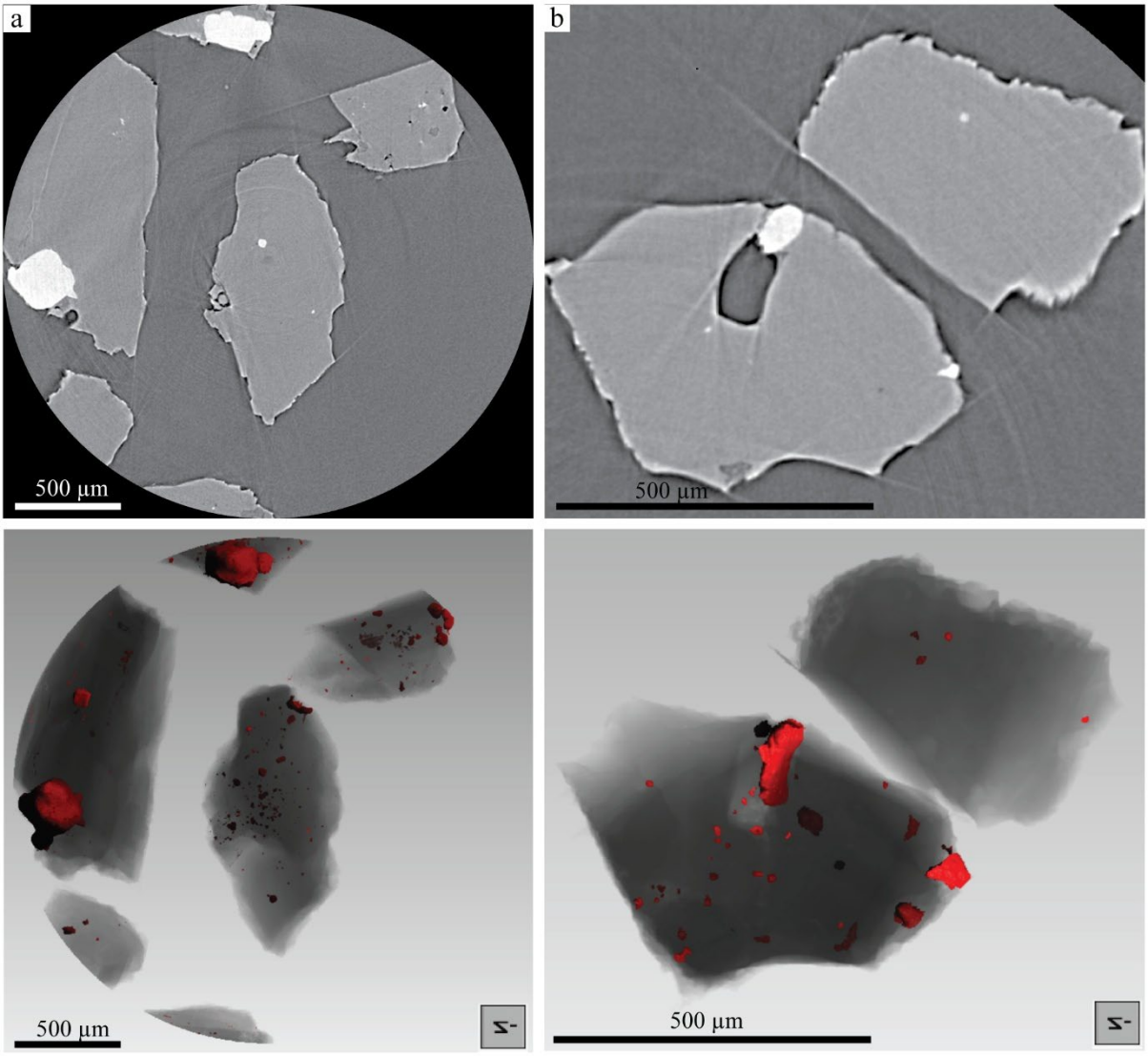

Fig. 5.2. a) representative reconstructed slice of the 5 clinopyroxenes seed before the heating process (top), and volume rendering of representative VOI (bottom left) of the same Cpx seeds in the experimental samples ETB-SeedCPX-1100drop (VOI size: 2532x2532x598 µm); b) representative reconstructed slice of the 2 Olivine seed before the heating process (top), and volume rendering of representative VOI (bottom left) of the same Olivine seeds in the experimental samples ETB-SeedOL-dyno (VOI size: 1128x960x598 µm); in the reconstructed slices the crystal phase with whiter gray scales is represented by Spl grains, while the light grey crystal phase is represented by the Cpx and Ol grains respectively.

Sample ETB_Seed$_{CPX}$_1100$_{drop}$ after 2 minutes:

After 2 minutes of crystallization remnants of partially or totally melted Cpx seeds cannot be recognized or found just from the visual inspection of the slices because of the nucleation and growth of 500 µm long Cpx dendrites (Fig.5.3a). These newly formed Cpx grains seem to radiate from centres of nucleation that closely follow the position of the Cpx seeds before the

heating process (from the comparison of Fig 5.3 and Fig 5.2), which make me think that the Cpx seeds do not completely melt. This hypothesis will be confirmed if I later find Cpx cores with different composition during chemical analysis through EPMA or SEM imaging.
The longer dendrites are mostly directed upward and occupy the portion of the sample with the higher amount of melt and free from other crystals or capsule walls. We notice the presence of a bubble, that did not migrate upward during the heating process and got stuck in the bottom of the sample. It is also possible to notice few big Spl grains which survived the heating process without major morphological changes (Fig.5.3a). Other than these few big Spl grains, no other newly formed Spl bigger than 2 um in size can be observed in the scans.

Sample ETB_Seed$_{CPX}$_1100$_{drop}$ from 22 to 62 minutes:

In the following hour of experiments Cpx dendrites continue to grow but slower than in the first 2-8 minutes of crystallization. Small morphological changes can also be observed, where the Cpx tips seem to become slightly bulkier (Fig.5.3 b-d middle row).
Spl grains start to appear mostly in the melt between the Cpx grains from 42 minutes on, and in minor abundance in the central to higher portions of the sample (Fig.5.3 b-d bottom row).
The main crystal phases forming in the sample (not yet analysed and 3D rendered) are elongated Plg grains which nucleate and grow from the melt meniscus at the top of the crucible in contact with air, and in a downwards direction (Plg not yet analysed).

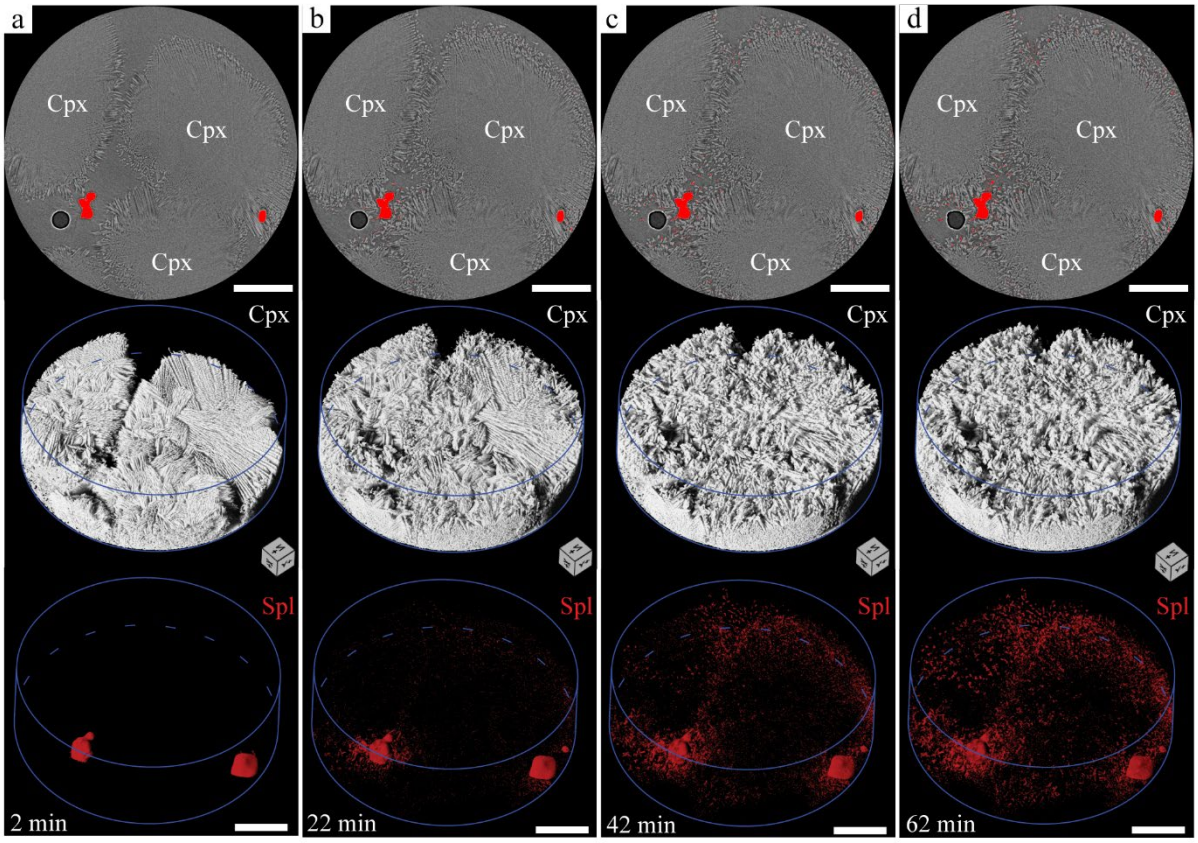

Fig.5.3. Sample ETB_SeedCPX_1100drop at a) 2 minutes, b) 22 minutes, c) 42 minutes and d) 62 minutes of crystallization. In the top row are the slices of the sample at fixed high in the Z axis. In the middle row there are the rendered volumes with only the Cpx grains segmented, while in the bottom row there are the volumes with only the Spl grains segmented. The VOI cylinders are 2532µm in diameter and 598 µm in hight. The bar scale is 500 µm long in each slice and volume,

Sample ETB_SeedOL_dyno at 1210 °C after 2 minutes:

The Ol seeds partially melted and assumed a more rounded morphology. The Spl grains closer to the edges got free and completely melted. Only the biggest Spl grains with size > than 100 µm survived the superheating process. Some newly crystallized Spl grains formed already after 2 minutes near the Olivine seeds (Fig.5.4a). Another explanation is that some of the smaller grains were able to not melt completely and stayed close to the Ol seed they were previously entrapped. Future chemical and COR analysis on the clustered phases could reveal if the Spl grains are formed through heterogeneous nucleation (CORs between the phases) or homogeneously before incorporation into olivine.

Other probably newly formed Spl grains crystallize at the bottom of the crucible. There is no evidence for other crystal phases, since Plg still did not crystallize at this temperature.

Sample ETB SeedOL dyno at 1210 °C after 180 minutes (3 hours);

All the Ol seeds slightly increase in size with the formation of sharper and straighter faces in the form of small skeletal fringes (Fig.5.4b). These skeletal newly formed portions of the silicate show different grey scale compared to the round cores, which could be caused by a different chemistry of the crystal. If we exclude the Ol seeds and the newly formed fringes, no other Ol grain formed in the sample after 3h. The Spl grains continue to crystallize near or from the Olivine seed and from the bottom of the sample at the contact with the Al_2O_3 crucible. The oxides are found just in the first 500 μm close to the bottom of the sample. Interestingly we recorded the movement of the large "bean shaped" Spl grain (also present in the sample pre-heating treatment in Fig.5.2b), which settled and moved near the Olivin seed. During the 3h of the experiment we record a massive crystallization of Plg grains with elongated shape (very high aspect ratio) which possibly compose more than 30 % of the sample volume.

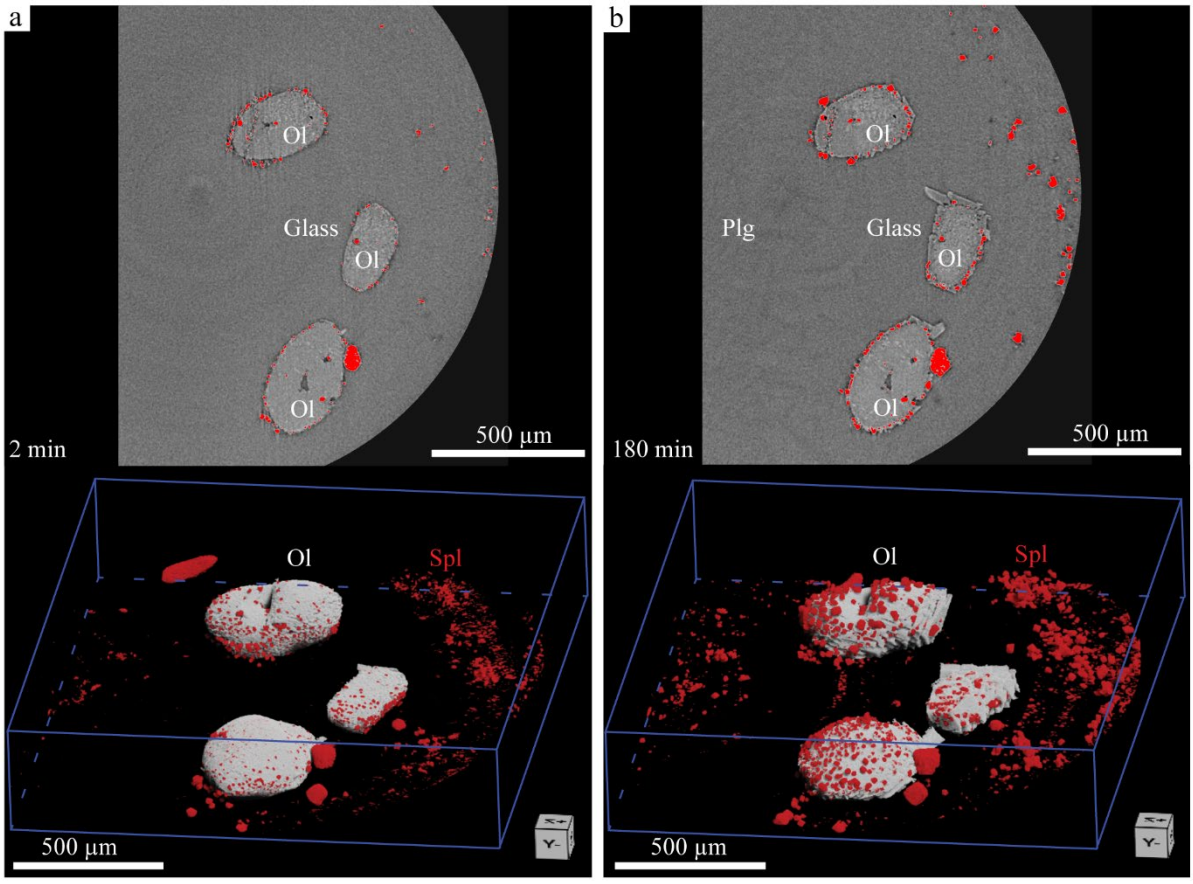

Fig. 5.4. a) reconstructed slice sample ETB-SeedOL-dyno after 2 minutes of crystallization at 1210 °C (top) and volume rendering of representative VOI (bottom left) of the same same sample (VOI size: 1128x960x364 µm); b) reconstructed slice sample ETB-SeedOL-dyno after 180 minutes of crystallization at 1150 °C (top) and volume rendering of representative VOI (bottom left) of the same same sample (VOI size: 1128x960x364 µm); in the reconstructed slices and the rendered volumes in red are segmented the Spl grains, while in light grey is segmented the Ol grains.

5.4 Scientific questions and future steps

The preliminary results presented in the previous sections represent only a small portion of the data we have already collected and planned to collect in the future. A potential scientific project aimed at studying the rheology of trachybasaltic magma during crystallization could be developed based on observations just introduced. The project would be based on the comparison between a full and comprehensive experimental set and the natural counterpart, which have been already sampled and partially examined and published on by many research groups in the last decade.

The first step in designing this research project is to analyse both the synthetic samples

already produced and selected natural samples using EPMA and EBSD techniques, with the following scientific questions in mind:

From a chemical point of view:

1. Do the seeds chemically interact with the melt?
2. If so, how does the chemistry of the cores and newly formed phases (e.g., rims or dendrites) differ from their natural counterparts (based on literature data)?
3. What are the chemical differences between the crystalline phases formed in seeded versus non-seeded experiments?

From a microstructural point of view:

4. Is heterogeneous nucleation the dominant nucleation mechanism?
5. What is the clustering mechanism between Spl and Ol, or Spl and Cpx?
6. What is the amount and nature of CORs (Crystallographic Orientation Relationship) between clustered phases (including Plg)?
7. Under which experimental conditions are CORs more abundant?
8. Are CORs observed between clustered phases in natural samples?
9. If present, in what quantities?
10. Are there experimental samples that show similar microstructures?
11. How does the heterogeneous nucleation of new rims and/or dendrites on the seeds (as seen in sample ETB_SeedCPX_1100drop, Fig. 5.3) influence the rheology of the magmatic system simulated?
12. What are the growing rate of all the crystal phases and how can this influence the rheology of the magmatic system simulated?

The second step is to complete the in situ 4D experimental series with a few additional samples. The most important experimental series to be carried out include:

- Drop experiments using only glass as the starting material, performed every 25 °C from 1175 °C to 1075 °C.
- Three sets of drop experiments using glass seeded with Ol, Cpx, and Plg, respectively, at the same temperature steps as in (a).
- Dynamic cooling experiments following the protocol used for sample ETB_SeedOL_dyno, one using only glass and three using glass seeded with Ol, Cpx, and Plg.

From these experimental series, the following are still to be created: all experiments seeded with Plg grains; all drop experiments at 1175 °C, 1125 °C, and 1075 °C; and the dynamic experiment seeded with Cpx.

The third step involves analysing all the old and newly created samples, focusing on the same scientific questions outlined in Step 1.

5.5 References

Arzilli F, Polacci M, La Spina G, Le Gall N, Llewellin EW, Brooker RA, Torres-Orozco R, Di Genova D, Neave DA, Hartley ME, Mader HM, Giornado D, Awwood R, Lee PD, Heidelbach F, Burton MR (2022). Dendritic crystallization in hydrous basaltic magmas controls magma mobility within the Earth's crust. Nat Commun 13, 3354. Doi: 10.1038/s41467-022-30890-8

Brun, F., Pacile., S., Accardo., A., Kourousias, G., Dreossi, D., Mancini, L., Tromba, G., Pugliese, R., (2015). Enhanced and Flexible Software Tools for X-ray Computed Tomography at the Italian Synchrotron Radiation Facility Elettra. Fundam. Inform. 141, 233–243.

Branca, S., Ferrara, V. (2013). The morphostructural setting of Mount Etna sedimentary basement (Italy): Implications for the geometry and volume of the volcano and its flank instability. Tectonophysics 586, 46–64.

La Spina, G., Burton, M., Vitturi, M. D. M., Arzilli, F (2016). Role of syn-eruptive plagioclase disequilibrium crystallisation in basaltic magma ascent dynamics. Nat. Commun. 7, 13402

Lanzafame, G., Giacomoni, P.P., Casetta, F., Mancini, L., Iezzi, G., Coltorti, M., Ferlito, C. (2022), Degassing, Crystallization and Rheology of Hawaiitic Lava Flows: the Case of the 1669 AD Eruption of Mount Etna (Italy), *Journal of Petrology*, 63 12 egac115, https://doi.org/10.1093/petrology/egac115

Kudrna Prasek, M., Pistone, M., Baker D.B., Sodini, N., Marinoni, N., Lanzafame, G., Mancini, L. (2018) Journal of Synchrotron Radiation 25. 1172-1181.

Marsh, B.D. (1998) On the Interpretation of Crystal Size Distributions in Magmatic Systems, *Journal of Petrology*, Volume 39, 4, 553-599, https://doi.org/10.1093/petroj/39.4.553

Polacci, M., Mancini, L., Baker, D.R. (2010). The contribution of synchrotron X-ray computed microtomography to understanding volcanic processes. J. Synchrotron Radiat. 17, 215–221.

Polacci M., Arzilli F., La Spina G., Le Gall N., Cai B., Di Hartley M.E., Genova D., Vo N.T., Nonni S., Atwood R.C., Llewellin E.W., Lee P.D., Burton M.R. (2018). Crystallisation in basaltic magmas revealed via in situ 4D synchrotron X-ray microtomography. Sci Rep 8:8377

6. GENERAL CONCLUSIONS

The results presented in this thesis contribute significantly to our understanding of the microstructures that form during the crystallization of magmas undergoing undercooling events. The study of experimental samples helped to consistently replicate the conditions necessary for controlled cooling and crystallization.

The second chapter of this thesis, titled "*Identifying crystal nucleation mechanisms in a synthetic trachybasalt: a multimodal approach*" (*Peres et al., 2024*) represents my first scientific paper as first author on this specific subject, and it was published in August 2024 on Contribution to Mineralogy and Petrology (doi.org/10.1007/s00410-024-02161-w). Using a combination of high-resolution 3D synchrotron radiation micro-CT (SR-µCT), EPMA, and EBSD mapping, we determined the nucleation mechanisms and order of crystal phases forming in our samples particularly titanomagnetite (Tmt) and clinopyroxene (Cpx), through detailed microstructural analysis.

One key finding from this study is the identification of three distinct populations of Tmt, discerned primarily through SR-µCT, which differ in morphology, size, and spatial relationships with other phases. These populations formed in a trachybasaltic melt cooled from superliquidus conditions under varying degrees of undercooling along a temperature gradient, following a single cooling ramp. A second major outcome is the recognition that a high number of crystallographic orientation relationships (CORs) shared between phases offers the most reliable 2D microstructural evidence for heterogeneous nucleation. Without this combined 2D and 3D microstructural approach, the encounter of different populations of the same phase in a natural rock could easily lead to misinterpretation, potentially suggesting multiple, discrete magmatic events where there were none.

The third chapter, titled “The effect of heterogeneous nuclei availability on rock microstructure: a new perspective from EBSD investigation of synthetic trachybasaltic magmas”, is the draft of my second first-author paper, which I plan to submit soon to Journal of Petrology. In this study, I explored the crystallization behavior of both undoped and Cr_2O_3-doped magmas, focusing on the microstructural effects of promoting the early crystallization of Cr-rich spinel (Spl), which acts as a nucleus for heterogeneous nucleation of Cpx. Our results indicate that in highly undercooled trachybasaltic magmas, the nucleation of Spl facilitates rapid and widespread heterogeneous nucleation of Cpx. Consequently, sample crystallinity exceeded 50% within just 5 to 30 minutes. Another important finding is that, in anhydrous samples from both series, the morphology of Cpx and the final sample textures are influenced more by the availability of heterogeneous nuclei than by the degree of undercooling. A high density of nuclei (Spl grains) leads to a high number of skeletal Cpx grains, whereas low nuclei density results in fewer, but longer and more dendritic Cpx crystals. A related insight is that the presence and spatial distribution of early-forming phases can directly influence the length and thus growth rate of later phases, especially when the latter form via heterogeneous nucleation.

Across both studies, it is important to highlight the potential role of heterogeneous nucleation and nuclei availability in modifying magma viscosity during crystallization. Specifically, the rapid growth of dendritic Cpx on pre-existing Tmt grains may significantly increase the viscosity of a magma, potentially leading to fragmentation (*Moitra et al., 2018*) and even explosive basaltic eruptions (*Arzilli et al., 2019*) if the crystallinity remains below 30%. In scenarios where the crystallinity is higher, the erupting magma may instead freeze within dykes or lock up as crystal mushes (*Arzilli et al., 2022*).

My collaborations built during the PhD extended the range of compositions and conditions studied. In particular, the study by *Colle et al., (2023)* based on experiments using

undercooled Stromboli-like basaltic melts, once again revealed clustering between Cpx and Tmt. I contributed to the 3D analysis of these samples, which showed strikingly similar microstructures to those in my own experiments. We concluded that Tmt likely nucleated heterogeneously on the edges and tips of Cpx crystals. Another key observation was a rosette-like Cpx microstructure, composed of skeletal to dendritic crystals radiating from a central point occupied by a Tmt grain. A similar microstructure is also present in my own undoped, anhydrous samples, supporting the hypothesis of Cpx nucleating heterogeneously on Tmt.

An ongoing collaboration with Lanzafame et al., (under review). enabled us to model the growth time and rates of Na-rich plagioclase (Plg) rims in the groundmass of a lava crust. Using high-resolution EPMA chemical mapping and chemical modelling, we estimated that the crystallization of the Na-rich rims occurred within 0.2 to 10 seconds (corresponding to growth rates in the range between 1.5×10^{-4} cm s^{-1} and 2×10^{-5} cm s^{-1}), likely representing the final rapid cooling event, possibly due to quenching at the lava-air interface.
The Plg microliths investigated in this collaboration are possibly formed at high degrees of undercooling, and consequently crystallized at high growth rate, which allowed the formation of a chemical boundary layer (CBL). Almost all the experimental samples we carried out at medium to high undercooling and anhydrous conditions are also characterized by high growth rate of the crystallized phases. The high crystallinity, the size of the Cpx grains (>300 μm in diameter), and the high degrees of crystallographic bending (Fig. 3.2)) after just 5 minutes of dwell time at experimental temperature, are all microstructure features confirming this hypothesis. Even if it was not possible to prove the presence of a CBL near the Cpx and Spl grains in these samples through post experiment analysis, it is likely that this was present during the early stages of crystallization. The supposed presence of a CBL could also be a factor responsible for the supersaturation of chemical components near the first crystal phase to form and consequently facilitating the heterogenous nucleation of phases enriched in the

components present in the CBL itself. Future comparisons between the growth rate of the phases formed in the experimental samples (both normal crystallization experiments (Chapter 2 and 3) and the 4D experiments (Chapter 5)) and the growth rate calculated through the study of the CBL (Chapter 4.2) have the potential to give precious insight into the crystallization kinetics at different undercooling conditions.

Looking ahead, I believe one of the most promising avenues for experimental petrology of undercooled magmas lies in the integration of 4D (3D + time) in situ crystallization experiments with seeded basaltic or trachybasaltic compositions. When combined with precise 2D EBSD and EPMA mapping, this approach can offer real-time insights into processes like clustering through heterogeneous nucleation. The results presented in Chapter 5 are promising even if preliminary and incomplete. Figure 5.4 shows Spl grains clustering around rounded olivine (Ol) grains, possibly because of heterogeneous nucleation, similar to the heterogeneous nucleation of Spl on Cpx and vice versa, already extensively documented in all my experimental samples, and discussed in chapter 2 and 3. Additionally, the drop experiment at 1100 °C using glass seeded with Cpx grains recorded immediate crystallization of dendritic Cpx within two minutes, highlighting the significant role of seed crystals (phenocrysts or xenocrysts) in determining final rock microstructure and their consequent impact on magma viscosity during cooling and crystallization. Both samples preliminarily analysed already confirm qualitatively most of the results discussed in chapter 2 and 3, i.e. that 1) heterogenous nucleation is the main nucleation and clustering mechanism occurring between silicate and oxides; 2) the presence of seeds, with particular regard for the Cpx ones, has the potential to deeply impact the microstructure of the system in the first few minutes of crystallization (between 0 and 5 minutes) after the onset of an undercooling event. These points are totally concordant with the results discussed mostly in chapter 3, where the anhydrous experimental samples reach high crystallinity in less than 5 minutes, and show

dendritic microstructures up to 300 µm long. Therefore, 4D in situ µCT seeding experiments clearly have the potential to further clarify the delay of nucleation on undercooling experiments or isothermal experiments. Finally, these new experiments extend these observations to atmospheric pressure and highly oxidized and evolved trachybasaltic compositions, typical of any Etnean superficial/shallow/lavaflow system.

References

Arzilli F, La Spina G, Burton MR, Polacci M, Le Gall N, Hartley ME, Di Genova D, Cai B, Vo NT, Bamber EC, Nonni S, Atwood R, Llewellin EW, Brooker RA, Mader HM, Lee PD (2019) Magma fragmentation in highly explosive basaltic eruptions induced by rapid crystallization. Nature Geoscience 12, 509 1023-1028. doi: 10.1038/s41561-019-0468-6

Arzilli F, Polacci M, La Spina G, Le Gall N, Llewellin EW, Brooker RA, Torres-Orozco R, Di Genova D, Neave DA, Hartley ME, Mader HM, Giornado D, Awwood R, Lee PD, Heidelbach F, Burton MR (2022). Dendritic crystallization in hydrous basaltic magmas controls magma mobility within the Earth's crust. Nat Commun 13, 3354. Doi: 10.1038/s41467-022-30890-8

Colle F, Masotta M, Costa S, Mollo S, Landi P, Pontesilli A, Peres S, Mancini L (2023). Effect of undercooling on clinopyroxene crystallization in a high K basalt: Implications for magma dynamics at Stromboli volcano. Lithos, Volumes 456–457. 107327. Doi: 10.1016/j.lithos.2023.107327

Moitra P, Gonnermann HM, Houghton BF, Tiwary CS (2018) Fragmentation and Plinian eruption of crystallizing basaltic magma. Earth and Planetary Science Letters, v 500, 97-104, https://doi.org/10.1016/j.epsl.2018.08.003.

7. SUPPLEMENTARY FIGURES AND TABLES

Chapter 7.1 – Supplementary Figures for Chapter 2 (from *Peres et al., 2024*, Supplementary Materials 1) corresponds, as the title suggests, to Supplementary Material 1 of Peres et al., 2024. Chapter 2 is, in fact, the scientific paper itself (*Peres et al., 2024*).

Chapter 7.2 – Supplementary Figures for Chapter 3 contains additional figures of the same samples, highlighting distinctive microstructural domains, specific EBSD maps, and details relevant for understanding Chapter 3. Both Chapter 3 and Chapter 7.2 are intended as a draft for my future scientific publication.

In Chapter 7.3 – Tables and Supplementary Materials, the following items are presented:

- (Page 178): Table 1, which corresponds to "Table 1. Chemical compositions of clinopyroxenes in samples 1100w-30min and 1100w-8h" from Peres et al., 2024.
- (Pages 179–180): Tables 2 and 3, which summarize key data relevant to Chapter 3.
- (Pages 181–224): Supplementary Materials 2 from *Peres et al., (2024)*. These materials (available online at https://link.springer.com/article/10.1007/s00410-024-02161-w) contain raw data and calculations that allow full replication of the graphs and results presented in Chapter 2 (and thus in Peres et al., 2024). The sheet titled "Authors and Affiliations", which appears as the first sheet in Supplementary Materials 1 of Peres et al., 2024, has been omitted to comply with the thesis submission guidelines. However, it is available at the link provided above.
- (Pages 225–245): Supplementary data and calculations necessary to fully replicate the graphs and results presented in Chapter 3.
- (Pages 246–247): Supplementary data supporting the graphs shown in Chapter 5.

7.4 References

Peres S, Griffiths TA, Colle F, Iannini Lelarge S, Masotta M, Pontesilli A, Mancini L, Abart R (2024) Identifying crystal nucleation mechanisms in a synthetic trachybasalt: a multimodal approach. *Contrib Mineral Petrol* **179**, 84 (2024). https://doi.org/10.1007/s00410-024-02161-w

7.1 Supplementary Figures for Chapter 2 (from Peres et al., 2024 Supplementary Materials 1)

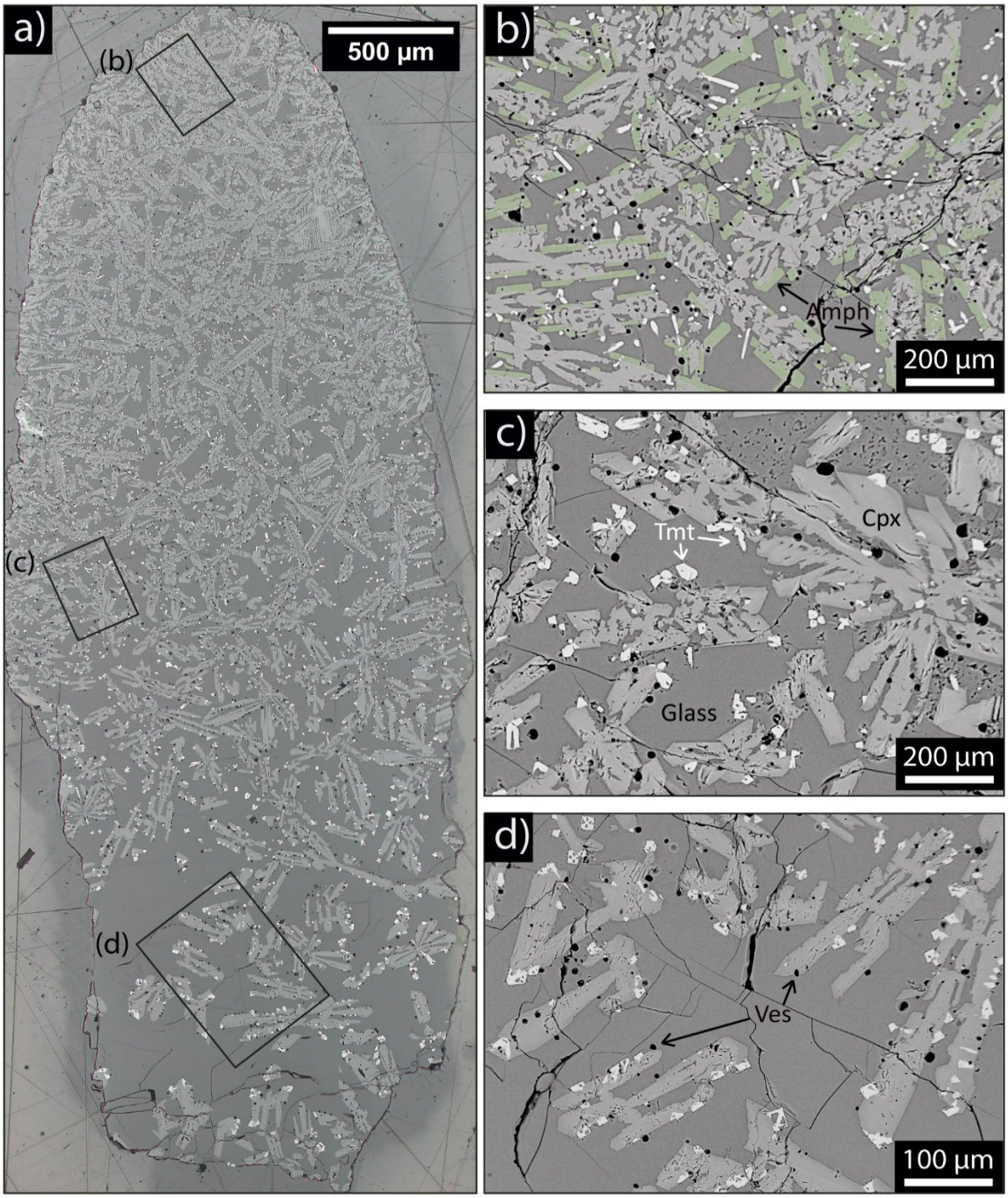

S1. Fig.1 Reflected light microscope image showing sample 1100w-30min; Cpx grains are grey; Tmt grains are light grey; Bubbles are black; glass is in darker grey, only in fig.1b, Amphibole is in translucent green. Figs. 1b is from the colder portion of the experiment; and c) is from the middle portion of the sample, and d) is from the hotter portion of the sample. (from Peres et al., 2024 supplementary Materials 1)

EMPA maps calibration

In order to calibrate the EMPA chemical map we acquired single point measurements, which locations are shown in Fig.2

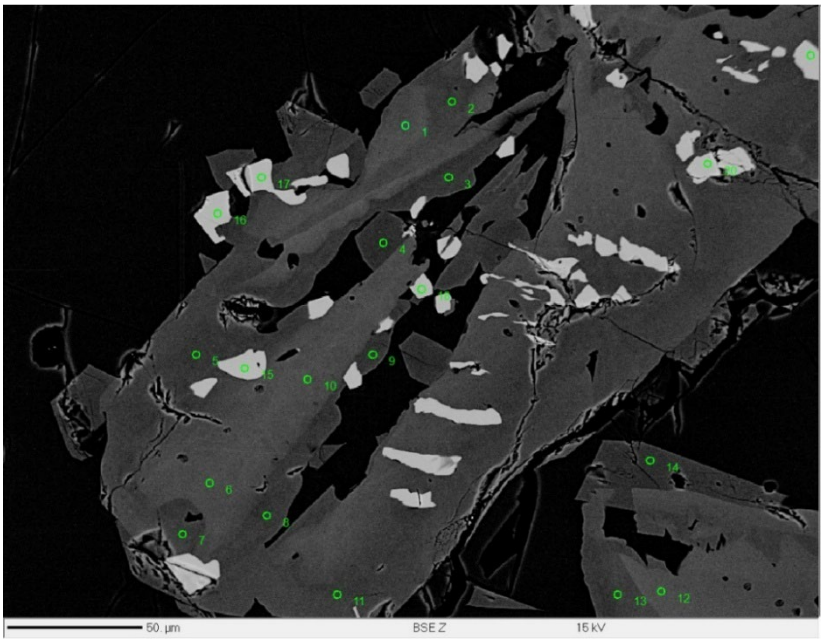

S2. Fig.2 BSE images showing the single spot analysis locations acquired (from Peres et al., 2024 supplementary Materials 1)

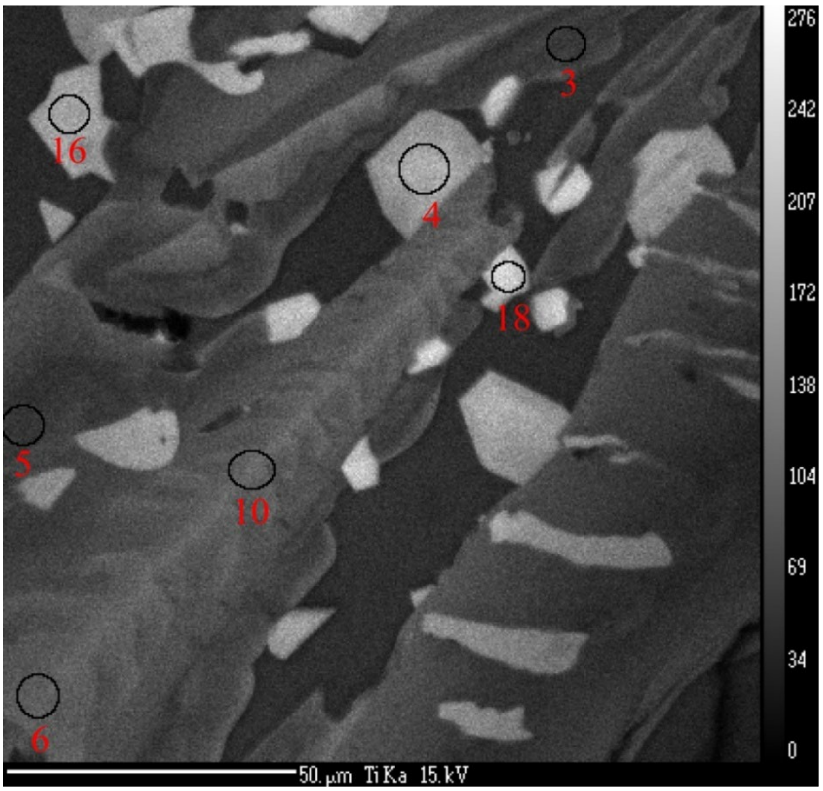

S3.Fig.3 Ti chemical acquired through EMPA. The grey values correspond to the amount of Ti present in the map. The black circles represent the spots where the single spots analysis were performed (from Peres et al., 2024 supplementary Materials 1).

The median of the grey value inside the black circles in Fig.4 have been correlated to amount of TiO_2 analysed during the single spot analysis as shown in the following table and Fig.4

sample 1100w-8h	element TiO2	grey value median	phase
point3	1.2133	59	Cpx
point 4	3.6533	170	Amph
point 5	1.2483	54	Cpx
point 6	1.9165	93	Cpx
point10	2.0463	99	Cpx
point16	3.8696	163	Tmt
point18	3.6533	205	Tmt

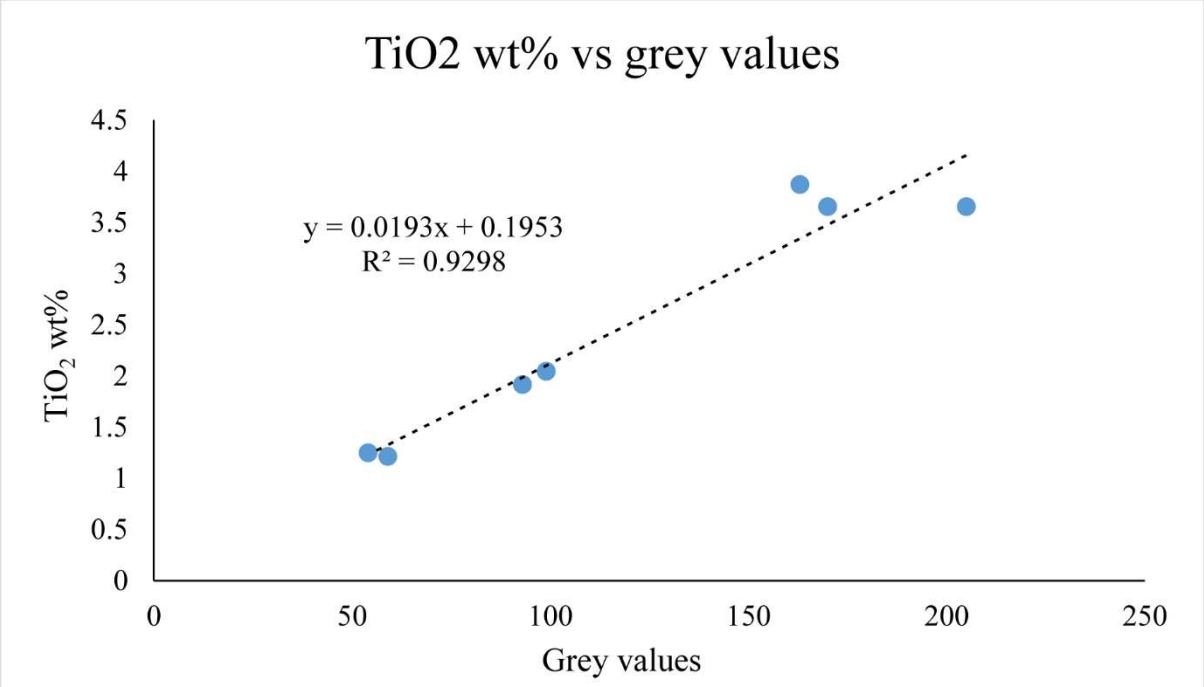

S4. Fig.4 graph correlating the grey values (in abscissa axis) and the relative TiO2 amount (in ordinate axis) measured in the EBSD chemical map relative to Ti composition, and the single spot analysis respectively (from Peres et al., 2024 supplementary Materials 1).

The ImageJ plugin "Calibrate…" has been used to calibrate the EBSD map relative to Ti content and the TiO_2 profile, shown as the black segmented line delimited between A and B (Fig.5) has been measured (Fig.6).

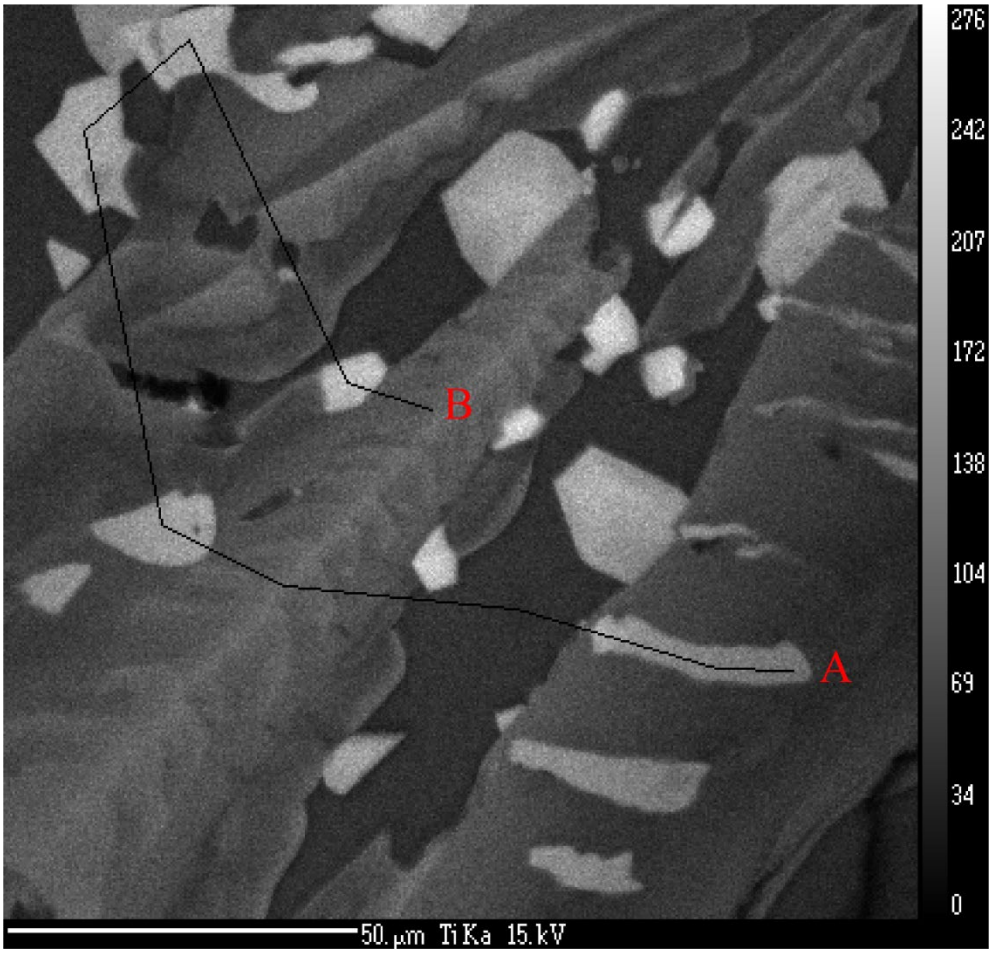

S5. Fig.5 Calibrated EMPA chemical showing the trace of the TiO2 chemical profile investigated (from Peres et al., 2024 supplementary Materials 1)

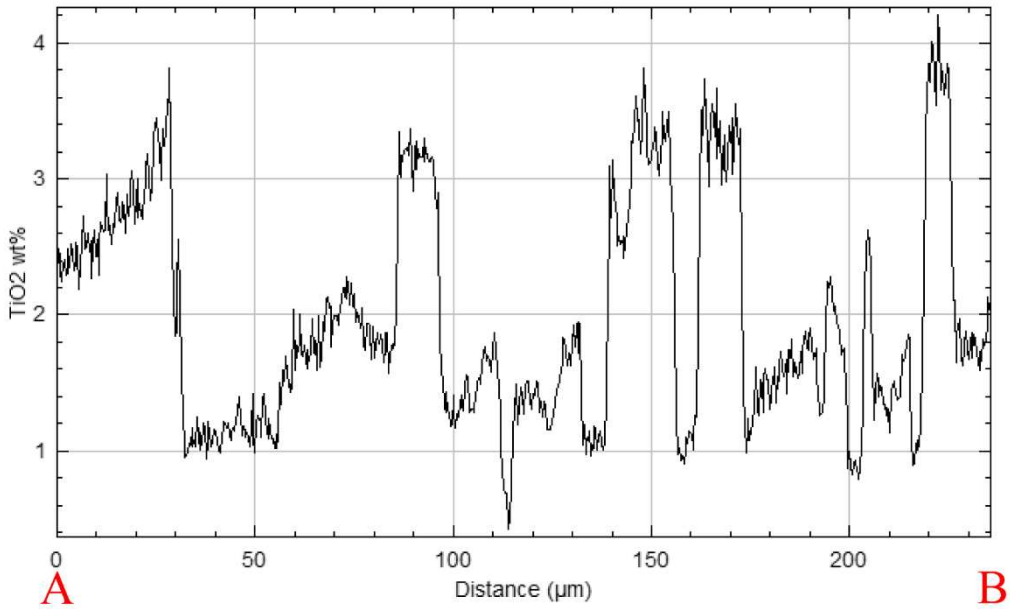

S6. Fig.6 graph showing the TiO2 content of the profile investigated. It is important to notice the increase in TiO2 content in the Pop3 Tmt crystal at the beginning of the profile (see text chapter 2.3.3 for more detailed information [from Peres et al., 2024 supplementary Materials 1]).

7.2 Supplementary Figures for Chapter 3

S7. Fig.7. Reflected light microscope image of Sample 1150d-Cr-doped-5min. To note the size gradient inside the sample and the lack of Cpx grains (<5% of the area) in the hottest portion of the sample, probably at T > 1170°C.

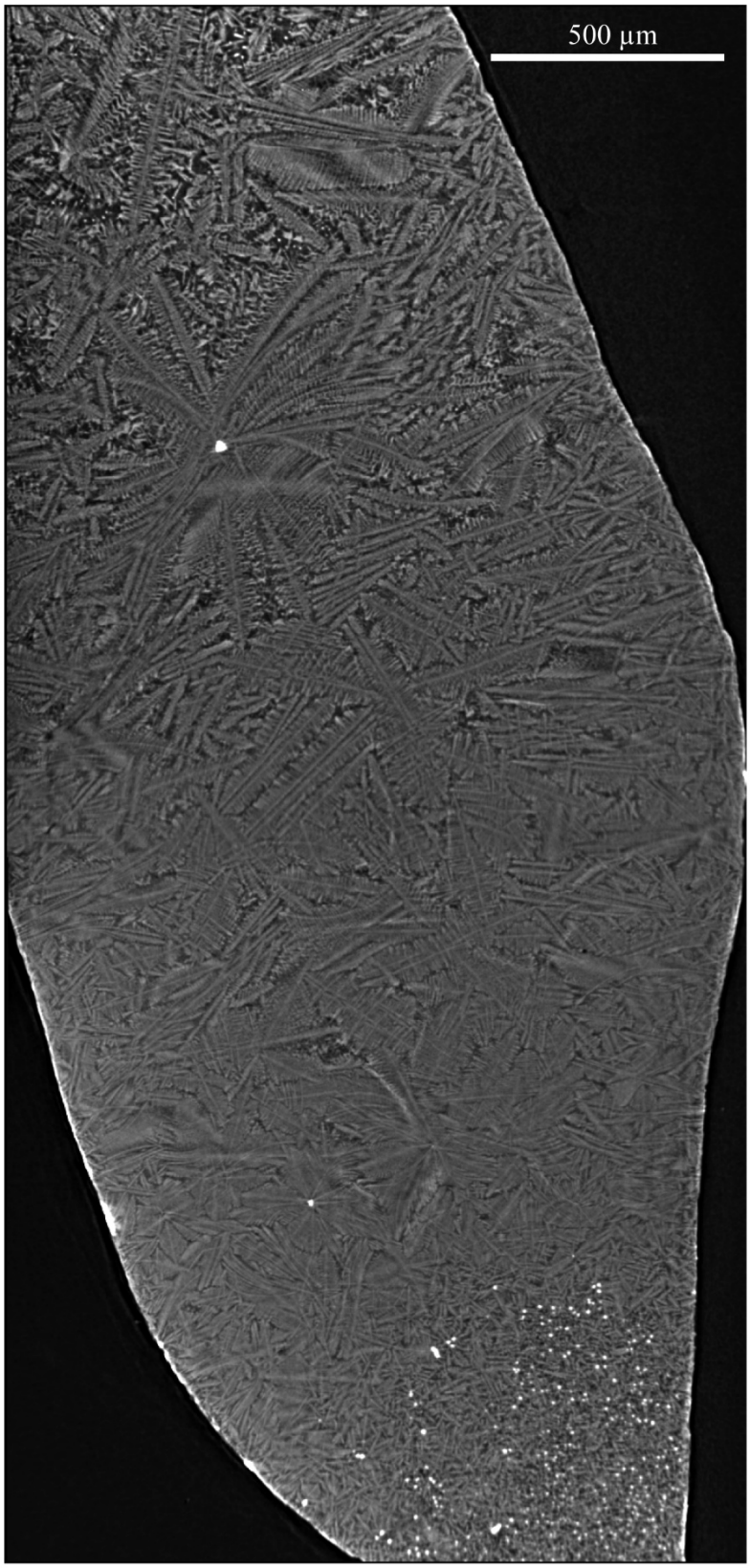

S8. Fig.8. Orthogonal slices (SR µCT) of the ZX-view of the sample 1150d_Undoped-30min. In white are the Spl grains, while in light grey are the Cp crystals. Important microstructural features to note are: 1) the two distinct microstructural zones, the skeletal Cpx domain on the left and the dendritic Cpx domain in the center to right portion of the sample; 2) the high number density of Spl grains in the skeletal Cpx domain; 3) some of the Cpx feather-like grains in the dendritic Cpx domain radiate from a central Spl grain/aggregate; 4) the dendritic Cpx grains perpendicularly arranged to the sample walls.

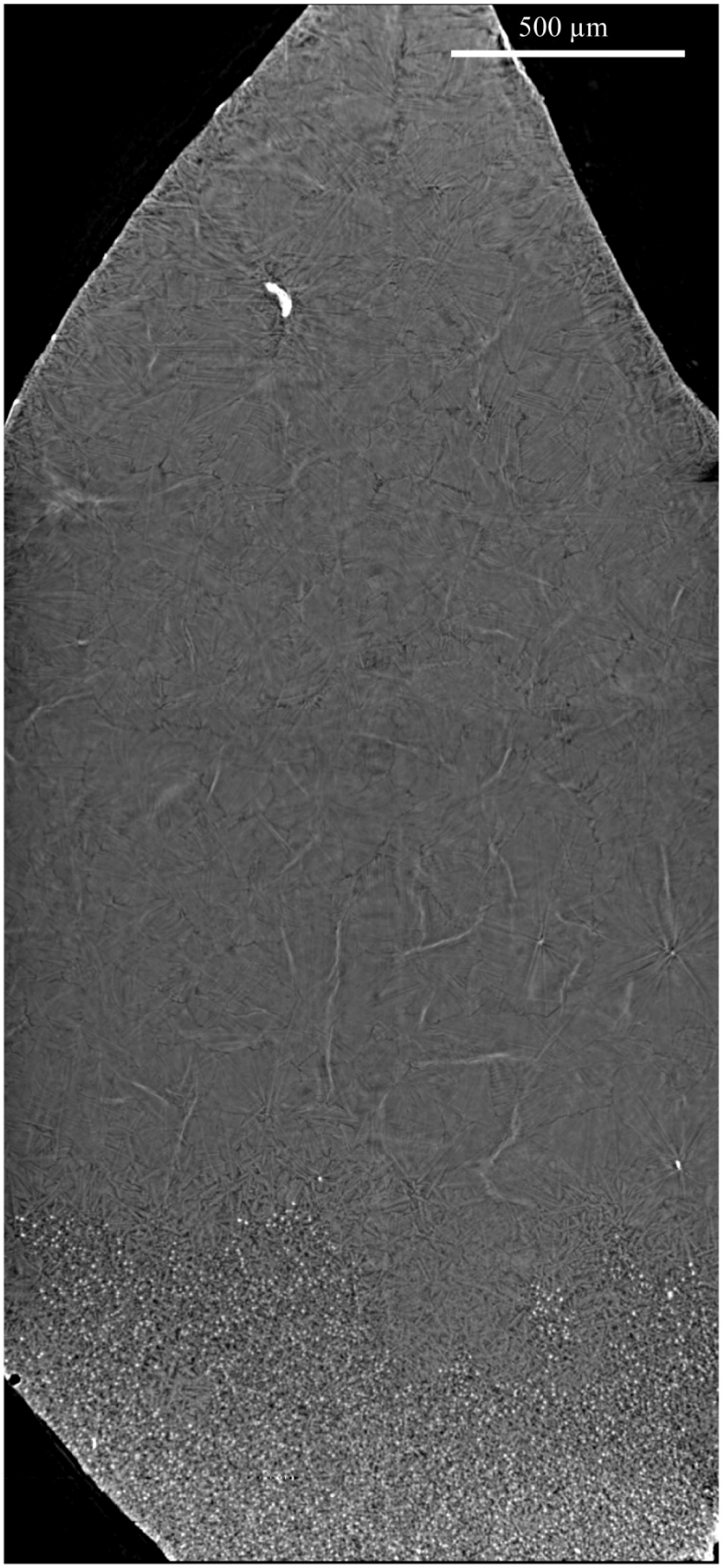

S9. Fig.9. Orthogonal slices (SR µCT) of the ZX-view of the sample 1100d_Undoped-30min. In white are the Spl grains, while in light grey are the Cp crystals. All the microstructural features that are recognizable in Supplementary Figure 2 are also present here, with the only differences represented by the smaller size and an higher number density of the grains.

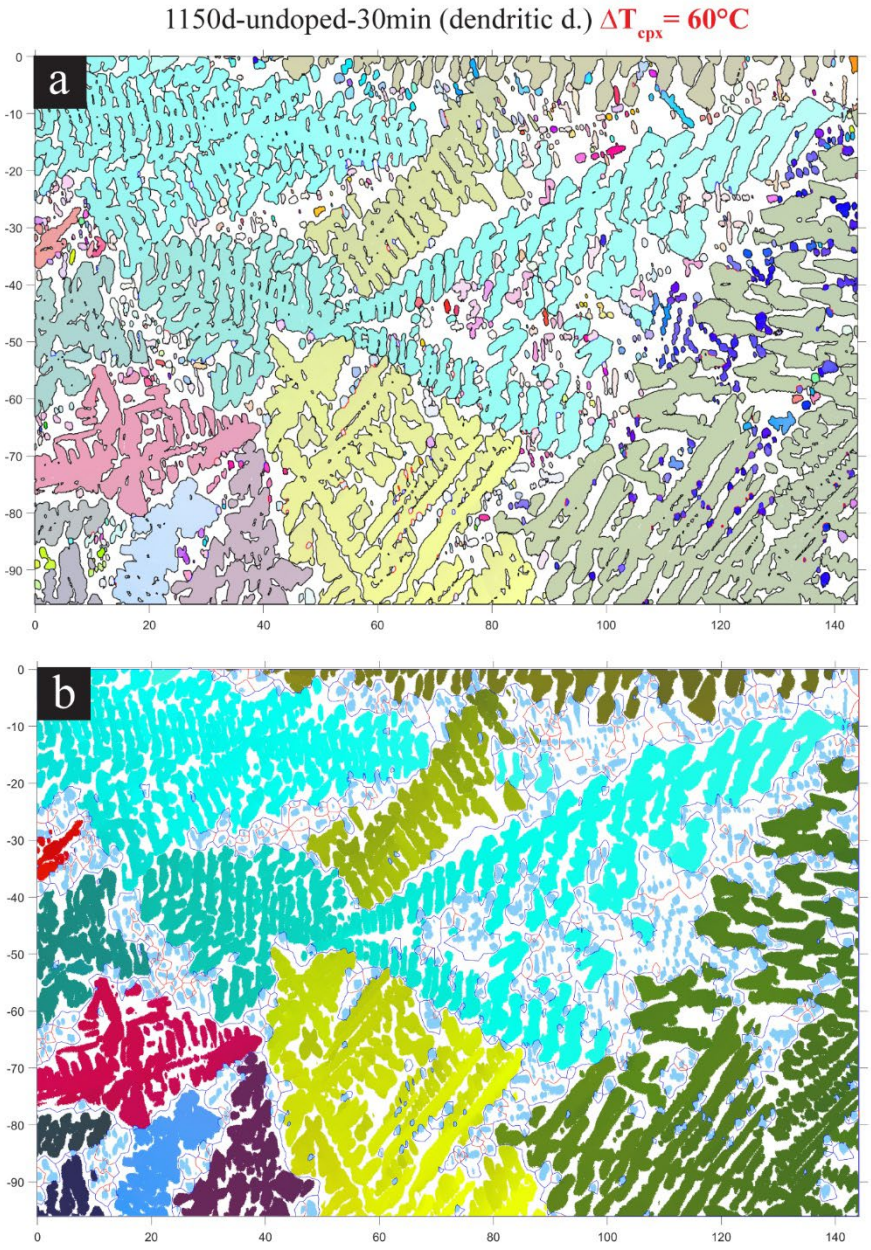

S10. Fig.10. Inverse pole figure (IPF) map of sample 1150d-undoped-30min in the left and an example of the same map without non-indexed points in the right. This kind of map allows to more precisely assess the number of grains present in the scanned area, The maps allow to avoid miscalculation caused by 2D cutting effects of grains characterized by complex 3D morphology, especially skeletal or dendritic.

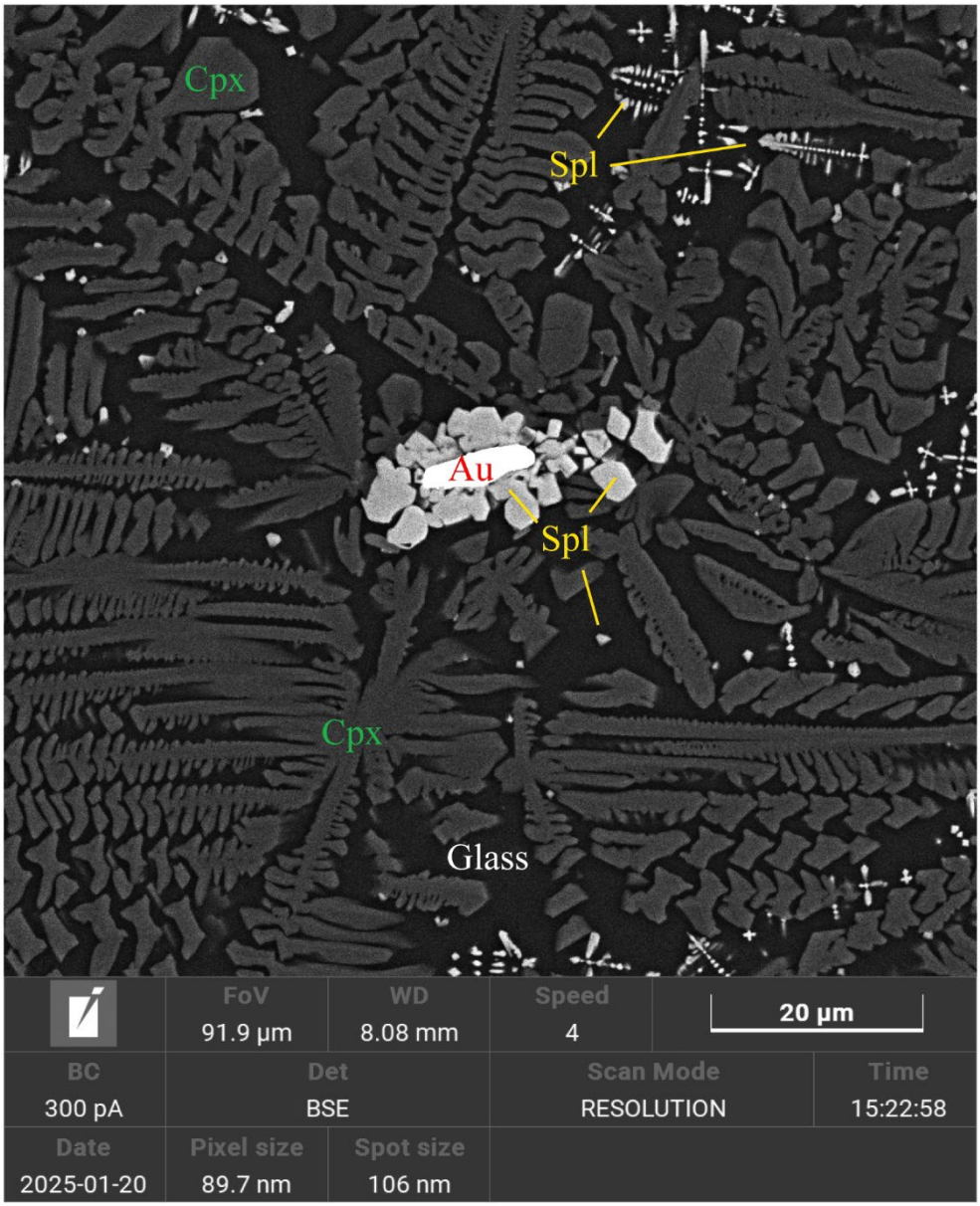

S11. Fig11. Detail BSE image of sample 1150d_Undoped-5min. In the dendritic zone of the sample, we found a Gold (Au, whiter grains, with red label) particle surrounded by Spl grains (whitish grains, with yellow label). The gold particle is an artifact caused by the contamination of the starting material during the process of welding of the capsule. The welding tip probably was contaminated by a previously welded gold capsule. Noteworthy is the easiness at witch any particle which escaped the superliquidus homogenization process can function as a surface for heterogenous nucleation of other phases. In light grey are the dendritic Cpx grains (green labels) while in blackish is the glass (white label).

7.3 Tables and supplementary materials

Table 1 of Peres et al., (2024), here Chapter 2.

Table 1

	1100w-30min		1100w-30min		1100w-30min	
	Average (13)	±1σ	Al+Ti sect (11)	±1σ	Si+Mg sect (2)	±1σ
SiO_2	41.58	0.98	41.25	0.64	43.43	0.09
TiO_2	1.85	0.24	1.91	0.2	1.51	0.08
Al_2O_3	10.08	0.85	10.31	0.71	8.81	0.13
FeO_{tot}	11.76	0.56	11.85	0.51	11.26	0.54
MgO	11.53	0.68	11.29	0.4	12.84	0.38
CaO	20.33	0.66	20.41	0.53	19.91	1.04
Na_2O	0.49	0.06	0.51	0.06	0.41	0.03
K_2O	0.02	0.01	0.02	0.01	0.02	0.01
Total	97.91		98.34		98.34	
Cations per formula unit according to Lindsley and Anderson (1982)						
Si	1.63	0.03	1.62	0.02	1.68	0
Ti	0.05	0.01	0.06	0.01	0.04	0
Al	0.47	0.04	0.48	0.03	0.4	0.01
Fe^{3+}	0.2	0.02	0.21	0.02	0.18	0
Fe^{2+}	0.18	0.01	0.18	0.01	0.18	0.02
Mg	0.67	0.04	0.66	0.02	0.74	0.02
Ca	0.85	0.03	0.86	0.02	0.83	0.04
Na	0.04	0.01	0.04	0	0.03	0
DiHd	0.18	0.03	0.17	0.02	0.2	0.04
EnFs	0.7	0.04	0.7	0.04	0.7	0.05
∑-Ts	0.15	0.02	0.15	0.02	0.13	0
	1100w-8h		1100w-8h		1100w-8h	
	Average (42)	±1σ	Al+Ti sect (17)	±1σ	Si+Mg sect (25)	±1σ
SiO_2	44.67	0.92	41.98	0.92	46.51	0.81
TiO_2	1.59	0.16	1.82	0.16	1.43	0.2
Al_2O_3	8.03	0.66	9.6	0.66	6.97	0.72
FeO_{tot}	8.8	0.68	11.24	0.68	7.15	0.49
MgO	12.79	0.58	11.41	0.58	13.73	0.46
CaO	21.97	0.22	21.28	0.22	22.45	0.35
Na_2O	0.44	0.02	0.45	0.02	0.42	0.02
K_2O	0.01	0.01	0.01	0.01	0.01	0.01
Total	98.3		97.79		98.67	
Cations per formula unit according to Lindsley and Anderson (1982)						
Si	1.71	0.06	1.64	0.03	1.76	0.02
Ti	0.05	0.01	0.05	0	0.04	0.01
Al	0.36	0.07	0.44	0.03	0.31	0.03
Fe^{3+}	0.15	0.04	0.2	0.02	0.12	0.01
Fe^{2+}	0.13	0.03	0.17	0.01	0.11	0.01
Mg	0.73	0.06	0.67	0.03	0.78	0.02
Ca	0.9	0.01	0.89	0.01	0.91	0.01
Na	0.03	0	0.03	0	0.03	0
DiHd	0.12	0.02	0.14	0.01	0.1	0.01
EnFs	0.78	0.03	0.75	0.01	0.8	0.02
∑-Ts	0.12	0.02	0.14	0.01	0.11	0.02

Table 2. Experimental conditions of samples used in Chapter 3.

Table 2

Sample	Pressure [MPa]	fO2	Cooling rate [°C/min]	H_2O wt%	Dwell time	D - UD
Cr-doped samples						
1150d-Cr-doped-5min	400	NNO+2	80	0	5	D
1150w-Cr-doped-5min	400	NNO+2	80	2	5	D
1100d-Cr-doped-5min	400	NNO+2	80	0	5	D
1100w-Cr-doped-5min	400	NNO+2	80	2	5	D
1050d-Cr-doped-5min	400	NNO+2	80	0	5	D
1050w-Cr-doped-5min	400	NNO+2	80	2	5	D
[BIS]1150d-Cr-doped-5min	400	NNO+2	80	0	5	D
[BIS]1100d-Cr-doped-5min	400	NNO+2	80	0	5	D
Undoped samples						
1150d-Undoped-30min	400	NNO+2	80	0	30	UD
1100d-Undoped-30min	400	NNO+2	80	0	30	UD
1050d-Undoped-30min	400	NNO+2	80	0	30	UD
1100w-Undoped-30min	400	NNO+2	80	2	30	UD
1150d-Undoped-5min	400	NNO+2	80	0	5	UD
1100d-Undoped-5min	400	NNO+2	80	0	5	UD
1100d-Undoped-0min	400	NNO+2	80	0	0	UD

Sample	T investigated [°C]	Bottom T°C	ΔT_{Cpx}	Centre T°C	ΔT_{Cpx}	Top T°C	ΔT_{Cpx}
Cr-doped samples							
1150d-Cr-doped-5min	1150	1170	40	1150	60	1130	80
1150w-Cr-doped-5min	1150	1170	-10	1150	10	1130	30
1100d-Cr-doped-5min	1100	1120	90	1100	110	1080	130
1100w-Cr-doped-5min	1100	1120	40	1100	60	1080	80
1050d-Cr-doped-5min	1050	1070	140	1050	160	1030	180
1050w-Cr-doped-5min	1050	1070	90	1050	110	1030	130
[BIS]1150d-Cr-doped-5min	1150	1150	60	1150	60	1140	70
[BIS]1100d-Cr-doped-5min	1100	1100	110	1100	110	1090	120
Undoped samples			ΔT_{liq}		ΔT_{liq}		ΔT_{liq}
1150d-Undoped-30min	1150	1150	60	1130	80	1110	100
1100d-Undoped-30min	1100	1100	110	1080	130	1060	150
1050d-Undoped-30min	1050	1050	160	1030	180	1010	200
1100w-Undoped-30min	1100	1100	60	1080	80	1060	100
1150d-Undoped-5min	1150	1150	60	1150	60	1140	70
1100d-Undoped-5min	1100	1100	110	1100	110	1090	120
1100d-Undoped-0min	1100	1100	110	1080	130	1060	150

Table 3. Cpx and Spl grains counting, number density, filtered and unfiltered from EBSD analysis, used in Chapter 3.3.2.1

Table 3

Sample	ΔT_{Cpx}	Area	Cpx grains Number (unfiltered)	Cpx grains Number (Filtered)	Cpx N_density (Unfiltered)	Cpx N_density (Filtered)
Cr-doped samples						
1150d-Cr-doped-5min	60	9.95	1092	**859**	10.97	**8.63**
1100d-Cr-doped-5min	110	8.81	261	**156**	2.96	**1.77**
1050d-Cr-doped-5min	160	7.96	1737	**1427**	21.82	**17.93**
Weighted (area) mean average Cr-doped anhydrous	60-160	26.72	3090	**2442**	11.56	**9.14**
1050w-Cr-doped-5min (colder)	130	0.95	230	**7**	24.22	**0.74**
Undoped samples	ΔT_{cpx}					
1150d-Undoped-30min	60	1.38	142	**14 - 17**	10.81	**1.01 – 1.23**
1100d-Undoped-30min	110	2.41	1896	**464 - 1174**	78.65	**19.25 - 48.70**
1050d-Undoped-30min	160	1.16	592	**185 - 328**	51.12	**15.98 - 28.41**
Feather-like Cpx domain		3.02	712	**89 - 110**	23.56	**2.9 - 3.64**
Sowflake-like Cpx domain		1.29	1140	**830**	88.39	**64.36**
Skletal Cpx domain		0.55	251	192	45.3	34.65
1100w-Undoped-30min (hotter)	60	15.11	35	**19**	0.23	**0.13**
1100w-Undoped-30min (centre)	80	63.29	348	**166**	0.55	**0.26**
1100w-Undoped-30min (colder)	100	23.5	286	**144**	1.22	**0.61**

Sample	ΔT_{Cpx}	Area	Cpx grains Number (unfiltered)	Cpx grains Number (Filtered)	Cpx N_density (Unfiltered)	Cpx N_density (Filtered)
Cr-doped samples						
1150d-Cr-doped-5min	60	9.95	5578	**5465**	56.06	**54.92**
1100d-Cr-doped-5min	110	8.81	3265	**3190**	37.39	**36.19**
1050d-Cr-doped-5min	160	7.96	5106	**5045**	64.14	**63.38**
Weighted (area) mean average Cr-doped anhydrous	60-160	26.72	13949	**13700**	52.19	**51.26**
1050w-Cr-doped-5min (colder)	130	0.95	351	**348**	36.97	**36.65**
Undoped samples	ΔT_{cpx}					
1150d-Undoped-30min	60	1.38	748	360	**54.11**	**26.04**
1100d-Undoped-30min	110	2.41	3481	2774	**144.39**	**115.1**
1050d-Undoped-30min	160	1.16	1255	1041	108.38	**89.9**
Feather-like Cpx domain		3.02	2556	1810	84.56	59.88
Sowflake-like Cpx domain		1.29	1430	**1153**	110.88	**89.4**
Skletal Cpx domain		0.55	258	**189**	46.56	**34.11**
1100w-Undoped-30min (hotter)	60	15.11	116	**89**	0.77	**0.59**
1100w-Undoped-30min (centre)	80	63.29	1047	**806**	1.65	**1.27**
1100w-Undoped-30min (colder)	100	23.5	900	**688**	3.83	**2.93**

note: values of Areas are expressed in $x10^{-2}mm^2$; values for the N_densities are expressed in $x10^3\ mm^{-2}$

Sheet "Raw EMPA analysis" of Peres et al., (2024) suplementary material 2

Raw microprobe single spot analyses on Glass, Cpx, Tmt, Amph and Spl of sample 1100w-30min and 1100w-8h

Sample name	Point	Phase	SiO2	MgO	Na2O	Al2O3	CaO	FeO	K2O	TiO2	Total
1100w-30min	13 / 1 .	Glass	54.03	2.43	4.55	20.08	5.87	4.03	2.44	0.83	94.25
1100w-30min	14 / 1 .	Glass	54.37	2.42	4.71	20.04	5.98	4.00	2.60	0.86	95.00
1100w-30min	15 / 1 .	Glass	54.77	2.27	4.69	20.07	5.95	3.78	2.44	0.86	94.84
1100w-30min	16 / 1 .	Glass	54.23	2.41	4.71	20.06	6.21	3.90	2.44	0.90	94.85
1100w-30min	17 / 1 .	Glass	54.35	2.17	4.51	20.13	6.29	3.86	2.33	0.88	94.52
1100w-30min	28 / 1 .	Amph	39.91	15.23	2.51	12.80	11.11	10.17	0.73	2.81	95.28
1100w-30min	32 / 1 .	Amph	39.95	16.14	2.59	13.49	11.05	8.61	0.72	2.87	95.42
1100w-30min	33 / 1 .	Amph	38.83	15.33	2.53	12.96	10.18	12.00	0.71	2.99	95.54
1100w-30min	34 / 1 .	Amph	38.89	14.93	2.51	13.18	10.68	11.31	0.74	3.67	95.90
1100w-30min	29 / 1 .	Cpx	40.86	11.07	0.55	11.49	20.08	11.64		1.72	97.42
1100w-30min	30 / 1 .	Cpx	41.12	11.05	0.61	11.44	19.65	11.86		1.75	97.48
1100w-30min	31 / 1 .	Cpx	40.65	11.26	0.47	11.10	19.99	11.94		2.00	97.42
1100w-30min	35 / 1 .	Spl	1.36	8.00		8.18		69.67		3.26	90.46
1100w-30min	36 / 1 .	Spl	0.86	7.97		8.24		70.60		3.27	90.94
1100w-30min	37 / 1 .	Spl	0.30	7.91		8.23		71.41		3.38	91.24
1100w-30min	18 / 1 .	Glass	51.48	4.51	4.36	19.05	6.66	5.02	1.92	1.39	94.39
1100w-30min	19 / 1 .	Glass	51.05	4.66	4.28	19.08	6.88	4.90	2.20	1.47	94.51
1100w-30min	20 / 1 .	Glass	51.71	4.64	4.28	19.32	6.79	5.02	2.05	1.44	95.26
1100w-30min	21 / 1 .	Glass	51.45	4.82	4.27	18.91	6.99	5.04	2.14	1.43	95.05
1100w-30min	38 / 1 .	Cpx	41.36	11.29	0.54	10.32	20.43	11.58		1.74	97.27
1100w-30min	39 / 1 .	Cpx	41.85	11.56	0.50	9.65	20.41	11.97		1.80	97.75
1100w-30min	40 / 1 .	Cpx	40.93	10.83	0.51	10.28	20.57	12.67		2.10	97.89
1100w-30min	41 / 1 .	Cpx	43.33	13.22	0.41	8.95	18.87	11.80		1.59	98.18
1100w-30min	42 / 1 .	Cpx	41.94	12.22	0.46	9.76	19.89	12.27		1.81	98.35
1100w-30min	52 / 1 .	Spl	0.25	10.98		9.98		66.32		4.39	91.93
1100w-30min	53 / 1 .	Spl	0.22	11.37		11.07		65.84		4.14	92.63
1100w-30min	54 / 1 .	Spl	0.22	11.56		11.44		64.50		4.21	91.92
1100w-30min	22 / 1 .	Glass	50.20	5.23	4.01	18.35	7.64	5.83	1.96	1.50	94.71
1100w-30min	23 / 1 .	Glass	49.97	5.49	4.04	18.11	7.70	6.17	1.97	1.59	95.04
1100w-30min	24 / 1 .	Glass	49.56	5.51	4.02	18.21	7.78	6.09	1.89	1.46	94.51
1100w-30min	25 / 1 .	Glass	48.58	6.25	3.73	17.41	8.40	7.26	1.72	1.65	95.01
1100w-30min	26 / 1 .	Glass	49.85	5.60	3.96	18.32	7.67	6.21	1.95	1.49	95.06
1100w-30min	43 / 1 .	Cpx	40.09	11.12	0.59	10.10	20.11	12.31	0.05	1.76	96.13
1100w-30min	44 / 1 .	Cpx	42.50	11.81	0.45	9.20	21.20	10.59		2.05	97.79
1100w-30min	45 / 1 .	Cpx	41.50	10.91	0.42	10.03	21.45	11.62		1.86	97.77
1100w-30min	46 / 1 .	Cpx	43.52	12.47	0.41	8.68	20.95	10.72		1.43	98.16
1100w-30min	47 / 1 .	Cpx	40.91	11.12	0.50	9.99	20.75	11.96		2.40	97.64
1100w-30min	48 / 1 .	Cpx	50.07	16.99	0.31	4.19	19.95	6.92		0.84	99.28
1100w-30min	49 / 1 .	Spl	0.15	10.43		9.01		69.26		3.47	92.32
1100w-30min	50 / 1 .	Spl	0.14	10.71		9.48		68.32		3.34	91.98
1100w-30min	51 / 1 .	Spl	0.14	10.71		9.84		67.56		3.49	91.74
1100w-8h	1 / 1 .	Cpx	42.28	11.59	0.48	9.85	21.17	10.60	0.01	1.80	97.79
1100w-8h	2 / 1 .	Cpx	47.29	14.25	0.41	6.25	22.25	6.83	0.02	1.18	98.49
1100w-8h	3 / 1 .	Cpx	47.48	14.46	0.40	6.14	22.10	6.74	0.02	1.21	98.55
1100w-8h	4 / 1 .	Amph	40.53	16.21	2.58	13.51	11.26	8.00	0.66	3.65	96.41
1100w-8h	5 / 1 .	Cpx	47.04	13.99	0.43	6.71	22.41	7.16	0.00	1.25	98.99
1100w-8h	6 / 1 .	Cpx	41.42	11.04	0.43	9.85	21.48	11.37	0.00	1.92	97.51
1100w-8h	7 / 1 .	Cpx	45.14	13.16	0.45	8.13	22.33	7.65	0.01	1.83	98.71
1100w-8h	8 / 1 .	Cpx	47.05	13.87	0.42	6.91	22.49	6.80	0.01	1.37	98.92
1100w-8h	9 / 1 .	Cpx	47.55	14.20	0.41	6.34	22.50	6.68	0.04	1.17	98.88
1100w-8h	10 / 1 .	Cpx	40.94	10.97	0.45	10.08	21.05	12.08	0.00	2.05	97.62
1100w-8h	11 / 1 .	Cpx	46.00	13.48	0.43	7.31	22.43	7.48	0.01	1.45	98.58
1100w-8h	12 / 1 .	Cpx	41.55	11.10	0.46	9.76	21.46	11.60	0.00	2.05	97.98
1100w-8h	13 / 1 .	Cpx	46.62	14.44	0.35	5.95	20.97	8.67	0.00	1.11	98.11
1100w-8h	14 / 1 .	Amph	38.20	14.68	2.50	15.68	11.55	8.58	0.82	3.64	95.66
1100w-8h	15 / 1 .	Spl	0.17	11.06		9.93	0.43	67.56		2.84	91.99
1100w-8h	16 / 1 .	Spl	0.16	10.76		12.16	0.23	65.36		3.87	92.55
1100w-8h	17 / 1 .	Spl	0.29	9.93		11.87	0.26	66.47		3.75	92.57
1100w-8h	18 / 1 .	Spl	0.20	9.41		12.42	0.30	66.62		3.65	92.60
1100w-8h	19 / 1 .	Spl	0.16	11.28		10.46	0.34	67.70		2.71	92.64
1100w-8h	20 / 1 .	Spl	0.13	11.34		9.80	0.31	68.32		2.75	92.64
1100w-8h	21 / 1 .	Cpx	41.77	11.26	0.43	10.08	21.51	11.06	0.00	1.64	97.74

Sample name	Point	Phase	SiO2	MgO	Na2O	Al2O3	CaO	FeO	K2O	TiO2	Total
1100w-8h	22 / 1 .	Cpx	47.48	14.02	0.41	6.83	22.61	6.48	0.00	1.45	99.28
1100w-8h	23 / 1 .	Cpx	44.78	13.12	0.43	7.90	21.55	9.01	0.00	1.50	98.31
1100w-8h	24 / 1 .	Amph	38.20	14.50	2.45	15.34	11.69	8.87	0.96	3.84	95.86
1100w-8h	25 / 1 .	Cpx	42.14	11.31	0.46	9.85	21.31	11.04	0.00	1.67	97.80
1100w-8h	26 / 1 .	Amph	38.72	14.93	2.37	14.91	11.90	8.81	0.77	3.73	96.15
1100w-8h	27 / 1 .	Cpx	42.39	11.47	0.46	9.47	21.36	10.95	0.01	1.70	97.81
1100w-8h	28 / 1 .	Cpx	46.33	13.59	0.41	7.17	22.74	7.32	0.01	1.41	98.98
1100w-8h	29 / 1 .	Cpx	43.23	11.96	0.47	8.34	20.86	11.38	0.01	1.75	98.00
1100w-8h	30 / 1 .	Cpx	47.58	13.95	0.42	6.49	22.76	6.91	0.01	1.27	99.40
1100w-8h	31 / 1 .	Cpx	41.47	10.99	0.47	9.68	21.31	11.75	0.03	1.97	97.68
1100w-8h	32 / 1 .	Cpx	47.11	13.99	0.43	6.77	22.68	6.79	0.01	1.40	99.17
1100w-8h	33 / 1 .	Cpx	45.57	13.35	0.44	7.71	22.50	7.02	0.02	1.65	98.25
1100w-8h	34 / 1 .	Cpx	42.43	12.03	0.40	9.46	21.17	10.98	0.00	1.64	98.12
1100w-8h	35 / 1 .	Cpx	47.14	14.07	0.39	6.08	22.54	6.57	0.01	1.38	98.18
1100w-8h	36 / 1 .	Spl	0.14	10.13		10.69	0.19	67.45		3.58	92.19
1100w-8h	37 / 1 .	Spl	0.14	10.42		10.70	0.22	67.83		3.43	92.73
1100w-8h	38 / 1 .	Spl	0.12	9.64		11.28	0.17	67.59		3.77	92.58
1100w-8h	39 / 1 .	Spl	0.09	9.75		11.25	0.13	67.70		3.41	92.33
1100w-8h	40 / 1 .	Spl	0.23	8.38		11.47	0.30	68.11		2.89	91.38
1100w-8h	41 / 1 .	Spl	0.15	9.60		11.32	0.14	68.27		3.38	92.85
1100w-8h	42 / 1 .	Spl	0.15	9.29		11.51	0.14	66.80		3.46	91.35
1100w-8h	43 / 1 .	Spl	0.16	9.74		11.33	0.29	67.62		3.49	92.62
1100w-8h	44 / 1 .	Spl	0.15	9.69		11.73	0.21	67.21		3.44	92.44
1100w-8h	45 / 1 .	cpx	44.84	12.69	0.46	8.25	22.45	7.66	0.02	1.77	98.14
1100w-8h	46 / 1 .	Cpx	40.91	10.80	0.49	10.68	21.29	11.62	0.01	1.84	97.65
1100w-8h	47 / 1 .	Cpx	47.17	14.25	0.43	5.96	22.46	6.46	0.01	1.34	98.08
1100w-8h	48 / 1 .	Cpx	41.73	11.25	0.48	9.55	21.04	11.76	0.01	1.75	97.57
1100w-8h	49 / 1 .	Cpx	45.72	13.37	0.44	7.86	22.31	7.22	0.02	1.82	98.75
1100w-8h	50 / 1 .	Cpx	40.86	10.57	0.46	10.49	21.35	11.81	0.01	1.99	97.53
1100w-8h	51 / 1 .	Cpx	46.38	13.49	0.44	6.77	22.74	7.41	0.01	1.57	98.81
1100w-8h	52 / 1 .	Cpx	41.56	11.13	0.47	9.64	21.30	11.68	0.01	1.97	97.76
1100w-8h	53 / 1 .	Cpx	46.35	13.67	0.45	6.42	22.62	7.00	0.02	1.37	97.91
1100w-8h	54 / 1 .	Cpx	42.03	11.79	0.43	9.18	20.90	11.34	0.01	1.68	97.37
1100w-8h	55 / 1 .	Cpx	45.33	13.06	0.45	8.13	22.57	7.32	0.02	1.62	98.51
1100w-8h	56 / 1 .	Cpx	47.01	13.89	0.44	6.70	22.42	6.56	0.01	1.57	98.61
1100w-8h	57 / 1 .	Cpx	45.49	13.08	0.44	7.95	22.27	7.57	0.00	1.49	98.29
1100w-8h	58 / 1 .	Cpx	42.16	11.61	0.45	9.29	21.64	10.97	0.00	1.96	98.09
1100w-8h	59 / 1 .	Cpx	45.71	13.20	0.43	7.82	22.41	7.64	0.00	1.55	98.77
1100w-8h	60 / 1 .	Cpx	46.33	13.69	0.43	7.06	22.73	7.50	0.00	1.28	99.01
1100w-8h	61 / 1 .	Cpx	46.97	14.02	0.41	6.54	22.89	7.24	0.01	1.23	99.31
1100w-8h	62 / 1 .	Amph	38.55	14.75	2.51	15.08	11.64	8.84	0.71	3.67	95.75
1100w-8h	63 / 1 .	Spl	0.16	10.79		9.98	0.11	68.87		3.13	93.04
1100w-8h	64 / 1 .	Spl	0.15	10.51		11.00	0.17	67.17		3.55	92.55

	Point	phase	SiO2	MgO	Na2O	Al2O3	CaO	FeO	K2O	TiO2	Cr2O3
Int standards	65 / 1 .	std alm	38.86	8.76	0.00	21.49	1.99	26.78	0.00	0.03	0.03
Int standards	66 / 1 .	std wol	51.67	0.08	0.00	0.01	48.13	-0.01	0.02	-0.01	0.01

	Point	phase	MnO	NiO	Total
Int standards	65 / 1 .	std alm	2.07	-0.01	100.01
Int standards	66 / 1 .	std wol	-0.01	0.01	99.90

Sheet "Clinopyroxene-sectors" of Peres et al., (2024) suplementary material 2

Cpx composition calculted according to Lindsley&Anderson (1982)

Raw Clinopyroxene Compositions - in Weight Percent

Sample name	Region in the sample	Point	Cpx Sector analyzed	SiO2	TiO2	Al2O3	FeO	MgO	CaO	Na2O	K2O	Total
1100w-30min	top/cold	29 / 1 .	Al+Ti rich	40.86	1.72	11.49	11.64	11.07	20.08	0.55	0.02	97.43
1100w-30min	top/cold	30 / 1 .	Al+Ti rich	41.12	1.75	11.44	11.86	11.05	19.65	0.61	0.03	97.51
1100w-30min	top/cold	31 / 1 .	Al+Ti rich	40.65	2.00	11.10	11.94	11.26	19.99	0.47	0.01	97.43
1100w-30min	centre	38 / 1 .	Al+Ti rich	41.36	1.74	10.32	11.58	11.29	20.43	0.54	0.01	97.28
1100w-30min	centre	39 / 1 .	Al+Ti rich	41.85	1.80	9.65	11.97	11.56	20.41	0.50	0.03	97.78
1100w-30min	centre	40 / 1 .	Al+Ti rich	40.93	2.10	10.28	12.67	10.83	20.57	0.51	0.03	97.91
1100w-30min	centre	42 / 1 .	Al+Ti rich	41.94	1.81	9.76	12.27	12.22	19.89	0.46	0.01	98.36
1100w-30min	bottom/hot	43 / 1 .	Al+Ti rich	40.09	1.76	10.10	12.31	11.12	20.11	0.59	0.05	96.13
1100w-30min	bottom/hot	44 / 1 .	Al+Ti rich	42.50	2.05	9.20	10.59	11.81	21.20	0.45	0.00	97.79
1100w-30min	bottom/hot	45 / 1 .	Al+Ti rich	41.50	1.86	10.03	11.62	10.91	21.45	0.42	0.00	97.77
1100w-30min	bottom/hot	47 / 1 .	Al+Ti rich	40.91	2.40	9.99	11.96	11.12	20.75	0.50	0.01	97.65
1100w-30min	bottom/hot	41 / 1 .	Si+Mg rich	43.33	1.59	8.95	11.80	13.22	18.87	0.41	0.03	98.21
1100w-30min	bottom/hot	46 / 1 .	Si+Mg rich	43.52	1.43	8.68	10.72	12.47	20.95	0.41	0.00	98.17
1100w-30min	bottom/hot	48 / 1 .	Si+Mg rich	50.07	0.84	4.19	6.92	16.99	19.95	0.31	0.02	99.30
1100w-8h	top/cold	46 / 1 .	Al+Ti rich	40.91	1.84	10.68	11.62	10.80	21.29	0.49	0.01	97.65
1100w-8h	top/cold	48 / 1 .	Al+Ti rich	41.73	1.75	9.55	11.76	11.25	21.04	0.48	0.01	97.57
1100w-8h	top/cold	50 / 1 .	Al+Ti rich	40.86	1.99	10.49	11.81	10.57	21.35	0.46	0.01	97.53
1100w-8h	top/cold	52 / 1 .	Al+Ti rich	41.56	1.97	9.64	11.68	11.13	21.30	0.47	0.01	97.76
1100w-8h	top/cold	54 / 1 .	Al+Ti rich	42.03	1.68	9.18	11.34	11.79	20.90	0.43	0.01	97.37
1100w-8h	centre	21 / 1 .	Al+Ti rich	41.77	1.64	10.08	11.06	11.26	21.51	0.43	0.00	97.74
1100w-8h	centre	23 / 1 .	Al+Ti rich	44.78	1.50	7.90	9.01	13.12	21.55	0.43	0.00	98.31
1100w-8h	centre	25 / 1 .	Al+Ti rich	42.14	1.67	9.85	11.04	11.31	21.31	0.46	0.00	97.80
1100w-8h	centre	27 / 1 .	Al+Ti rich	42.39	1.70	9.47	10.95	11.47	21.36	0.46	0.01	97.81
1100w-8h	centre	29 / 1 .	Al+Ti rich	43.23	1.75	8.34	11.38	11.96	20.86	0.47	0.01	98.00
1100w-8h	centre	31 / 1 .	Al+Ti rich	41.47	1.97	9.68	11.75	10.99	21.31	0.47	0.03	97.68
1100w-8h	centre	34 / 1 .	Al+Ti rich	42.43	1.64	9.46	10.98	12.03	21.17	0.40	0.00	98.12
1100w-8h	bottom/hot	1 / 1 .	Al+Ti rich	42.28	1.80	9.85	10.60	11.59	21.17	0.48	0.01	97.79
1100w-8h	bottom/hot	6 / 1 .	Al+Ti rich	41.42	1.92	9.85	11.37	11.04	21.48	0.43	0.00	97.51
1100w-8h	bottom/hot	10 / 1 .	Al+Ti rich	40.94	2.05	10.08	12.08	10.97	21.05	0.45	0.00	97.62
1100w-8h	bottom/hot	12 / 1 .	Al+Ti rich	41.55	2.05	9.76	11.60	11.10	21.46	0.46	0.00	97.98
1100w-8h	bottom/hot	58 / 1 .	Al+Ti rich	42.16	1.96	9.29	10.97	11.61	21.64	0.45	0.00	98.09
1100w-8h	top/cold	45 / 1 .	Si+Mg rich	44.84	1.77	8.25	7.66	12.69	22.45	0.46	0.02	98.14
1100w-8h	top/cold	47 / 1 .	Si+Mg rich	47.17	1.34	5.96	6.46	14.25	22.46	0.43	0.01	98.08
1100w-8h	top/cold	49 / 1 .	Si+Mg rich	45.72	1.82	7.86	7.22	13.37	22.31	0.44	0.02	98.75
1100w-8h	top/cold	51 / 1 .	Si+Mg rich	46.38	1.57	6.77	7.41	13.49	22.74	0.44	0.01	98.81
1100w-8h	top/cold	53 / 1 .	Si+Mg rich	46.35	1.37	6.42	7.00	13.67	22.62	0.45	0.02	97.91
1100w-8h	top/cold	55 / 1 .	Si+Mg rich	45.33	1.62	8.13	7.32	13.06	22.57	0.45	0.02	98.51
1100w-8h	top/cold	56 / 1 .	Si+Mg rich	47.01	1.57	6.70	6.56	13.89	22.42	0.44	0.01	98.61
1100w-8h	centre	22 / 1 .	Si+Mg rich	47.48	1.45	6.83	6.48	14.02	22.61	0.41	0.00	99.28
1100w-8h	centre	28 / 1 .	Si+Mg rich	46.33	1.41	7.17	7.32	13.59	22.74	0.41	0.01	98.98
1100w-8h	centre	30 / 1 .	Si+Mg rich	47.58	1.27	6.49	6.91	13.95	22.76	0.42	0.01	99.40
1100w-8h	centre	32 / 1 .	Si+Mg rich	47.11	1.40	6.77	6.79	13.99	22.68	0.43	0.01	99.17
1100w-8h	centre	33 / 1 .	Si+Mg rich	45.57	1.65	7.71	7.02	13.35	22.50	0.44	0.02	98.25
1100w-8h	centre	35 / 1 .	Si+Mg rich	47.14	1.38	6.08	6.57	14.07	22.54	0.39	0.01	98.18
1100w-8h	bottom/hot	2 / 1 .	Si+Mg rich	47.29	1.18	6.25	6.83	14.25	22.25	0.41	0.02	98.49
1100w-8h	bottom/hot	3 / 1 .	Si+Mg rich	47.48	1.21	6.14	6.74	14.46	22.10	0.40	0.02	98.55
1100w-8h	bottom/hot	5 / 1 .	Si+Mg rich	47.04	1.25	6.71	7.16	13.99	22.41	0.43	0.00	98.99
1100w-8h	bottom/hot	7 / 1 .	Si+Mg rich	45.14	1.83	8.13	7.65	13.16	22.33	0.45	0.01	98.71
1100w-8h	bottom/hot	8 / 1 .	Si+Mg rich	47.05	1.37	6.91	6.80	13.87	22.49	0.42	0.01	98.92
1100w-8h	bottom/hot	9 / 1 .	Si+Mg rich	47.55	1.17	6.34	6.68	14.20	22.50	0.41	0.04	98.88
1100w-8h	bottom/hot	11 / 1 .	Si+Mg rich	46.00	1.45	7.31	7.48	13.48	22.43	0.43	0.01	98.58
1100w-8h	bottom/hot	13 / 1 .	Si+Mg rich	46.62	1.11	5.95	8.67	14.44	20.97	0.35	0.00	98.11
1100w-8h	bottom/hot	57 / 1 .	Si+Mg rich	45.49	1.49	7.95	7.57	13.08	22.27	0.44	0.00	98.29
1100w-8h	bottom/hot	59 / 1 .	Si+Mg rich	45.71	1.55	7.82	7.64	13.20	22.41	0.43	0.00	98.77
1100w-8h	bottom/hot	60 / 1 .	Si+Mg rich	46.33	1.28	7.06	7.50	13.69	22.73	0.43	0.00	99.01
1100w-8h	bottom/hot	61 / 1 .	Si+Mg rich	46.97	1.23	6.54	7.24	14.02	22.89	0.41	0.01	99.31

Sample name	Region in the sample	Point	Cpx Sector analyzed	Atoms Si	Ti	Al	Fe	Mg	Ca	Na	K	Total
1100w-30min	top/cold	29 / 1 .	Al+Ti rich	0.68	0.02	0.11	0.16	0.27	0.36	0.01	0.00	1.62
1100w-30min	top/cold	30 / 1 .	Al+Ti rich	0.68	0.02	0.11	0.17	0.27	0.35	0.01	0.00	1.62
1100w-30min	top/cold	31 / 1 .	Al+Ti rich	0.68	0.02	0.11	0.17	0.28	0.36	0.01	0.00	1.62
1100w-30min	centre	38 / 1 .	Al+Ti rich	0.69	0.02	0.10	0.16	0.28	0.36	0.01	0.00	1.63
1100w-30min	centre	39 / 1 .	Al+Ti rich	0.70	0.02	0.09	0.17	0.29	0.36	0.01	0.00	1.64
1100w-30min	centre	40 / 1 .	Al+Ti rich	0.68	0.03	0.10	0.18	0.27	0.37	0.01	0.00	1.63
1100w-30min	centre	42 / 1 .	Al+Ti rich	0.70	0.02	0.10	0.17	0.30	0.35	0.01	0.00	1.65
1100w-30min	bottom/hot	43 / 1 .	Al+Ti rich	0.67	0.02	0.10	0.17	0.28	0.36	0.01	0.00	1.60
1100w-30min	bottom/hot	44 / 1 .	Al+Ti rich	0.71	0.03	0.09	0.15	0.29	0.38	0.01	0.00	1.65
1100w-30min	bottom/hot	45 / 1 .	Al+Ti rich	0.69	0.02	0.10	0.16	0.27	0.38	0.01	0.00	1.63
1100w-30min	bottom/hot	47 / 1 .	Al+Ti rich	0.68	0.03	0.10	0.17	0.28	0.37	0.01	0.00	1.63
1100w-30min	bottom/hot	41 / 1 .	Si+Mg rich	0.72	0.02	0.09	0.16	0.33	0.34	0.01	0.00	1.66
1100w-30min	bottom/hot	46 / 1 .	Si+Mg rich	0.72	0.02	0.09	0.15	0.31	0.37	0.01	0.00	1.67
1100w-30min	bottom/hot	48 / 1 .	Si+Mg rich	0.83	0.01	0.04	0.10	0.42	0.36	0.01	0.00	1.76
1100w-8h	top/cold	46 / 1 .	Al+Ti rich	0.68	0.02	0.10	0.16	0.27	0.38	0.01	0.00	1.63
1100w-8h	top/cold	48 / 1 .	Al+Ti rich	0.69	0.02	0.09	0.16	0.28	0.38	0.01	0.00	1.64
1100w-8h	top/cold	50 / 1 .	Al+Ti rich	0.68	0.02	0.10	0.16	0.26	0.38	0.01	0.00	1.62
1100w-8h	top/cold	52 / 1 .	Al+Ti rich	0.69	0.02	0.09	0.16	0.28	0.38	0.01	0.00	1.64
1100w-8h	top/cold	54 / 1 .	Al+Ti rich	0.70	0.02	0.09	0.16	0.29	0.37	0.01	0.00	1.64
1100w-8h	centre	21 / 1 .	Al+Ti rich	0.70	0.02	0.10	0.15	0.28	0.38	0.01	0.00	1.64
1100w-8h	centre	23 / 1 .	Al+Ti rich	0.75	0.02	0.08	0.13	0.33	0.38	0.01	0.00	1.68
1100w-8h	centre	25 / 1 .	Al+Ti rich	0.70	0.02	0.10	0.15	0.28	0.38	0.01	0.00	1.64
1100w-8h	centre	27 / 1 .	Al+Ti rich	0.71	0.02	0.09	0.15	0.28	0.38	0.01	0.00	1.65
1100w-8h	centre	29 / 1 .	Al+Ti rich	0.72	0.02	0.08	0.16	0.30	0.37	0.01	0.00	1.66
1100w-8h	centre	31 / 1 .	Al+Ti rich	0.69	0.02	0.10	0.16	0.27	0.38	0.01	0.00	1.63
1100w-8h	centre	34 / 1 .	Al+Ti rich	0.71	0.02	0.09	0.15	0.30	0.38	0.01	0.00	1.65
1100w-8h	bottom/hot	1 / 1 .	Al+Ti rich	0.70	0.02	0.10	0.15	0.29	0.38	0.01	0.00	1.64
1100w-8h	bottom/hot	6 / 1 .	Al+Ti rich	0.69	0.02	0.10	0.16	0.27	0.38	0.01	0.00	1.63
1100w-8h	bottom/hot	10 / 1 .	Al+Ti rich	0.68	0.03	0.10	0.17	0.27	0.38	0.01	0.00	1.63
1100w-8h	bottom/hot	12 / 1 .	Al+Ti rich	0.69	0.03	0.10	0.16	0.28	0.38	0.01	0.00	1.64
1100w-8h	bottom/hot	58 / 1 .	Al+Ti rich	0.70	0.02	0.09	0.15	0.29	0.39	0.01	0.00	1.65
1100w-8h	top/cold	45 / 1 .	Si+Mg rich	0.75	0.02	0.08	0.11	0.31	0.40	0.01	0.00	1.68
1100w-8h	top/cold	47 / 1 .	Si+Mg rich	0.79	0.02	0.06	0.09	0.35	0.40	0.01	0.00	1.71
1100w-8h	top/cold	49 / 1 .	Si+Mg rich	0.76	0.02	0.08	0.10	0.33	0.40	0.01	0.00	1.70
1100w-8h	top/cold	51 / 1 .	Si+Mg rich	0.77	0.02	0.07	0.10	0.33	0.41	0.01	0.00	1.71
1100w-8h	top/cold	53 / 1 .	Si+Mg rich	0.77	0.02	0.06	0.10	0.34	0.40	0.01	0.00	1.70
1100w-8h	top/cold	55 / 1 .	Si+Mg rich	0.75	0.02	0.08	0.10	0.32	0.40	0.01	0.00	1.69
1100w-8h	top/cold	56 / 1 .	Si+Mg rich	0.78	0.02	0.07	0.09	0.34	0.40	0.01	0.00	1.71
1100w-8h	centre	22 / 1 .	Si+Mg rich	0.79	0.02	0.07	0.09	0.35	0.40	0.01	0.00	1.72
1100w-8h	centre	28 / 1 .	Si+Mg rich	0.77	0.02	0.07	0.10	0.34	0.41	0.01	0.00	1.71
1100w-8h	centre	30 / 1 .	Si+Mg rich	0.79	0.02	0.06	0.10	0.35	0.41	0.01	0.00	1.73
1100w-8h	centre	32 / 1 .	Si+Mg rich	0.78	0.02	0.07	0.09	0.35	0.40	0.01	0.00	1.72
1100w-8h	centre	33 / 1 .	Si+Mg rich	0.76	0.02	0.08	0.10	0.33	0.40	0.01	0.00	1.69
1100w-8h	centre	35 / 1 .	Si+Mg rich	0.78	0.02	0.06	0.09	0.35	0.40	0.01	0.00	1.71
1100w-8h	bottom/hot	2 / 1 .	Si+Mg rich	0.79	0.01	0.06	0.10	0.35	0.40	0.01	0.00	1.72
1100w-8h	bottom/hot	3 / 1 .	Si+Mg rich	0.79	0.02	0.06	0.09	0.36	0.39	0.01	0.00	1.72
1100w-8h	bottom/hot	5 / 1 .	Si+Mg rich	0.78	0.02	0.07	0.10	0.35	0.40	0.01	0.00	1.72
1100w-8h	bottom/hot	7 / 1 .	Si+Mg rich	0.75	0.02	0.08	0.11	0.33	0.40	0.01	0.00	1.69
1100w-8h	bottom/hot	8 / 1 .	Si+Mg rich	0.78	0.02	0.07	0.09	0.34	0.40	0.01	0.00	1.71
1100w-8h	bottom/hot	9 / 1 .	Si+Mg rich	0.79	0.01	0.06	0.09	0.35	0.40	0.01	0.00	1.72
1100w-8h	bottom/hot	11 / 1 .	Si+Mg rich	0.77	0.02	0.07	0.10	0.33	0.40	0.01	0.00	1.70
1100w-8h	bottom/hot	13 / 1 .	Si+Mg rich	0.78	0.01	0.06	0.12	0.36	0.37	0.01	0.00	1.71
1100w-8h	bottom/hot	57 / 1 .	Si+Mg rich	0.76	0.02	0.08	0.11	0.32	0.40	0.01	0.00	1.69
1100w-8h	bottom/hot	59 / 1 .	Si+Mg rich	0.76	0.02	0.08	0.11	0.33	0.40	0.01	0.00	1.70
1100w-8h	bottom/hot	60 / 1 .	Si+Mg rich	0.77	0.02	0.07	0.10	0.34	0.41	0.01	0.00	1.71
1100w-8h	bottom/hot	61 / 1 .	Si+Mg rich	0.78	0.02	0.06	0.10	0.35	0.41	0.01	0.00	1.72

				Charges									
Sample name	Region in the sample	Point	Cpx Sector analyzed	Si	Ti	Al	Fe	Mg	Ca	Na	K	Total	OMEGA
1100w-30min	top/cold	29 / 1 .	Al+Ti rich	2.72	0.09	0.68	0.32	0.55	0.72	0.02	0.00	5.09	2.36
1100w-30min	top/cold	30 / 1 .	Al+Ti rich	2.74	0.09	0.67	0.33	0.55	0.70	0.02	0.00	5.10	2.35
1100w-30min	top/cold	31 / 1 .	Al+Ti rich	2.71	0.10	0.65	0.33	0.56	0.71	0.02	0.00	5.08	2.36
1100w-30min	centre	38 / 1 .	Al+Ti rich	2.75	0.09	0.61	0.32	0.56	0.73	0.02	0.00	5.08	2.36
1100w-30min	centre	39 / 1 .	Al+Ti rich	2.79	0.09	0.57	0.33	0.57	0.73	0.02	0.00	5.10	2.35
1100w-30min	centre	40 / 1 .	Al+Ti rich	2.72	0.11	0.60	0.35	0.54	0.73	0.02	0.00	5.08	2.36
1100w-30min	centre	42 / 1 .	Al+Ti rich	2.79	0.09	0.57	0.34	0.61	0.71	0.01	0.00	5.13	2.34
1100w-30min	bottom/hot	43 / 1 .	Al+Ti rich	2.67	0.09	0.59	0.34	0.55	0.72	0.02	0.00	4.98	2.41
1100w-30min	bottom/hot	44 / 1 .	Al+Ti rich	2.83	0.10	0.54	0.29	0.59	0.76	0.01	0.00	5.12	2.34
1100w-30min	bottom/hot	45 / 1 .	Al+Ti rich	2.76	0.09	0.59	0.32	0.54	0.76	0.01	0.00	5.09	2.36
1100w-30min	bottom/hot	47 / 1 .	Al+Ti rich	2.72	0.12	0.59	0.33	0.55	0.74	0.02	0.00	5.07	2.37
1100w-30min	bottom/hot	41 / 1 .	Si+Mg rich	2.88	0.08	0.53	0.33	0.66	0.67	0.01	0.00	5.16	2.32
1100w-30min	bottom/hot	46 / 1 .	Si+Mg rich	2.90	0.07	0.51	0.30	0.62	0.75	0.01	0.00	5.16	2.33
1100w-30min	bottom/hot	48 / 1 .	Si+Mg rich	3.33	0.04	0.25	0.19	0.84	0.71	0.01	0.00	5.38	2.23
1100w-8h	top/cold	46 / 1 .	Al+Ti rich	2.72	0.09	0.63	0.32	0.54	0.76	0.02	0.00	5.08	2.36
1100w-8h	top/cold	48 / 1 .	Al+Ti rich	2.78	0.09	0.56	0.33	0.56	0.75	0.02	0.00	5.08	2.36
1100w-8h	top/cold	50 / 1 .	Al+Ti rich	2.72	0.10	0.62	0.33	0.52	0.76	0.01	0.00	5.07	2.37
1100w-8h	top/cold	52 / 1 .	Al+Ti rich	2.77	0.10	0.57	0.33	0.55	0.76	0.02	0.00	5.09	2.36
1100w-8h	top/cold	54 / 1 .	Al+Ti rich	2.80	0.08	0.54	0.32	0.59	0.75	0.01	0.00	5.08	2.36
1100w-8h	centre	21 / 1 .	Al+Ti rich	2.78	0.08	0.59	0.31	0.56	0.77	0.01	0.00	5.10	2.35
1100w-8h	centre	23 / 1 .	Al+Ti rich	2.98	0.08	0.47	0.25	0.65	0.77	0.01	0.00	5.21	2.30
1100w-8h	centre	25 / 1 .	Al+Ti rich	2.81	0.08	0.58	0.31	0.56	0.76	0.01	0.00	5.11	2.35
1100w-8h	centre	27 / 1 .	Al+Ti rich	2.82	0.09	0.56	0.30	0.57	0.76	0.01	0.00	5.12	2.35
1100w-8h	centre	29 / 1 .	Al+Ti rich	2.88	0.09	0.49	0.32	0.59	0.74	0.02	0.00	5.13	2.34
1100w-8h	centre	31 / 1 .	Al+Ti rich	2.76	0.10	0.57	0.33	0.55	0.76	0.02	0.00	5.08	2.36
1100w-8h	centre	34 / 1 .	Al+Ti rich	2.83	0.08	0.56	0.31	0.60	0.76	0.01	0.00	5.13	2.34
1100w-8h	bottom/hot	1 / 1 .	Al+Ti rich	2.81	0.09	0.58	0.30	0.58	0.76	0.02	0.00	5.13	2.34
1100w-8h	bottom/hot	6 / 1 .	Al+Ti rich	2.76	0.10	0.58	0.32	0.55	0.77	0.01	0.00	5.08	2.36
1100w-8h	bottom/hot	10 / 1 .	Al+Ti rich	2.73	0.10	0.59	0.34	0.54	0.75	0.01	0.00	5.07	2.37
1100w-8h	bottom/hot	12 / 1 .	Al+Ti rich	2.77	0.10	0.57	0.32	0.55	0.77	0.01	0.00	5.10	2.35
1100w-8h	bottom/hot	58 / 1 .	Al+Ti rich	2.81	0.10	0.55	0.31	0.58	0.77	0.01	0.00	5.12	2.34
1100w-8h	top/cold	45 / 1 .	Si+Mg rich	2.99	0.09	0.49	0.21	0.63	0.80	0.01	0.00	5.22	2.30
1100w-8h	top/cold	47 / 1 .	Si+Mg rich	3.14	0.07	0.35	0.18	0.71	0.80	0.01	0.00	5.26	2.28
1100w-8h	top/cold	49 / 1 .	Si+Mg rich	3.04	0.09	0.46	0.20	0.66	0.80	0.01	0.00	5.27	2.28
1100w-8h	top/cold	51 / 1 .	Si+Mg rich	3.09	0.08	0.40	0.21	0.67	0.81	0.01	0.00	5.27	2.28
1100w-8h	top/cold	53 / 1 .	Si+Mg rich	3.09	0.07	0.38	0.19	0.68	0.81	0.01	0.00	5.23	2.30
1100w-8h	top/cold	55 / 1 .	Si+Mg rich	3.02	0.08	0.48	0.20	0.65	0.80	0.01	0.00	5.25	2.29
1100w-8h	top/cold	56 / 1 .	Si+Mg rich	3.13	0.08	0.39	0.18	0.69	0.80	0.01	0.00	5.29	2.27
1100w-8h	centre	22 / 1 .	Si+Mg rich	3.16	0.07	0.40	0.18	0.70	0.81	0.01	0.00	5.33	2.25
1100w-8h	centre	28 / 1 .	Si+Mg rich	3.08	0.07	0.42	0.20	0.67	0.81	0.01	0.00	5.28	2.27
1100w-8h	centre	30 / 1 .	Si+Mg rich	3.17	0.06	0.38	0.19	0.69	0.81	0.01	0.00	5.32	2.25
1100w-8h	centre	32 / 1 .	Si+Mg rich	3.14	0.07	0.40	0.19	0.69	0.81	0.01	0.00	5.31	2.26
1100w-8h	centre	33 / 1 .	Si+Mg rich	3.03	0.08	0.45	0.20	0.66	0.80	0.01	0.00	5.25	2.29
1100w-8h	centre	35 / 1 .	Si+Mg rich	3.14	0.07	0.36	0.18	0.70	0.80	0.01	0.00	5.26	2.28
1100w-8h	bottom/hot	2 / 1 .	Si+Mg rich	3.15	0.06	0.37	0.19	0.71	0.79	0.01	0.00	5.28	2.27
1100w-8h	bottom/hot	3 / 1 .	Si+Mg rich	3.16	0.06	0.36	0.19	0.72	0.79	0.01	0.00	5.29	2.27
1100w-8h	bottom/hot	5 / 1 .	Si+Mg rich	3.13	0.06	0.39	0.20	0.69	0.80	0.01	0.00	5.30	2.27
1100w-8h	bottom/hot	7 / 1 .	Si+Mg rich	3.01	0.09	0.48	0.21	0.65	0.80	0.01	0.00	5.25	2.28
1100w-8h	bottom/hot	8 / 1 .	Si+Mg rich	3.13	0.07	0.41	0.19	0.69	0.80	0.01	0.00	5.30	2.26
1100w-8h	bottom/hot	9 / 1 .	Si+Mg rich	3.17	0.06	0.37	0.19	0.70	0.80	0.01	0.00	5.30	2.26
1100w-8h	bottom/hot	11 / 1 .	Si+Mg rich	3.06	0.07	0.43	0.21	0.67	0.80	0.01	0.00	5.26	2.28
1100w-8h	bottom/hot	13 / 1 .	Si+Mg rich	3.10	0.06	0.35	0.24	0.72	0.75	0.01	0.00	5.23	2.30
1100w-8h	bottom/hot	57 / 1 .	Si+Mg rich	3.03	0.07	0.47	0.21	0.65	0.79	0.01	0.00	5.24	2.29
1100w-8h	bottom/hot	59 / 1 .	Si+Mg rich	3.04	0.08	0.46	0.21	0.66	0.80	0.01	0.00	5.26	2.28
1100w-8h	bottom/hot	60 / 1 .	Si+Mg rich	3.08	0.06	0.42	0.21	0.68	0.81	0.01	0.00	5.28	2.27
1100w-8h	bottom/hot	61 / 1 .	Si+Mg rich	3.13	0.06	0.39	0.20	0.70	0.82	0.01	0.00	5.30	2.26

				Cations (all Fe2+)											
Sample name	Region in the sample	Point	Cpx Sector analyzed	Si	Ti	Al	Fe	Mg	Ca	Na	K	Total	Al4	Al6	Fe3+ (Lindsley)
1100w-30min	top/cold	29 / 1 .	Al+Ti rich	1.60	0.05	0.53	0.38	0.65	0.84	0.04	0.00	4.10	0.40	0.13	0.20
1100w-30min	top/cold	30 / 1 .	Al+Ti rich	1.61	0.05	0.53	0.39	0.65	0.82	0.05	0.00	4.10	0.39	0.14	0.19
1100w-30min	top/cold	31 / 1 .	Al+Ti rich	1.60	0.06	0.51	0.39	0.66	0.84	0.04	0.00	4.10	0.40	0.11	0.21
1100w-30min	centre	38 / 1 .	Al+Ti rich	1.63	0.05	0.48	0.38	0.66	0.86	0.04	0.00	4.10	0.37	0.11	0.21
1100w-30min	centre	39 / 1 .	Al+Ti rich	1.64	0.05	0.45	0.39	0.68	0.86	0.04	0.00	4.10	0.36	0.09	0.21
1100w-30min	centre	40 / 1 .	Al+Ti rich	1.61	0.06	0.48	0.42	0.63	0.87	0.04	0.00	4.11	0.39	0.09	0.22
1100w-30min	centre	42 / 1 .	Al+Ti rich	1.63	0.05	0.45	0.40	0.71	0.83	0.03	0.00	4.11	0.37	0.08	0.21
1100w-30min	bottom/hot	43 / 1 .	Al+Ti rich	1.61	0.05	0.48	0.41	0.66	0.86	0.05	0.00	4.13	0.39	0.08	0.25
1100w-30min	bottom/hot	44 / 1 .	Al+Ti rich	1.66	0.06	0.42	0.35	0.69	0.89	0.03	0.00	4.09	0.34	0.08	0.18
1100w-30min	bottom/hot	45 / 1 .	Al+Ti rich	1.63	0.05	0.46	0.38	0.64	0.90	0.03	0.00	4.10	0.37	0.09	0.20
1100w-30min	bottom/hot	47 / 1 .	Al+Ti rich	1.61	0.07	0.46	0.39	0.65	0.88	0.04	0.00	4.11	0.39	0.07	0.21
1100w-30min	bottom/hot	41 / 1 .	Si+Mg rich	1.68	0.05	0.41	0.38	0.76	0.78	0.03	0.00	4.09	0.32	0.08	0.18
1100w-30min	bottom/hot	46 / 1 .	Si+Mg rich	1.69	0.04	0.40	0.35	0.72	0.87	0.03	0.00	4.09	0.31	0.08	0.18
1100w-30min	bottom/hot	48 / 1 .	Si+Mg rich	1.86	0.02	0.18	0.21	0.94	0.79	0.02	0.00	4.04	0.14	0.04	0.08
1100w-8h	top/cold	46 / 1 .	Al+Ti rich	1.61	0.05	0.50	0.38	0.63	0.90	0.04	0.00	4.11	0.39	0.10	0.22
1100w-8h	top/cold	48 / 1 .	Al+Ti rich	1.64	0.05	0.44	0.39	0.66	0.89	0.04	0.00	4.10	0.36	0.08	0.21
1100w-8h	top/cold	50 / 1 .	Al+Ti rich	1.61	0.06	0.49	0.39	0.62	0.90	0.03	0.00	4.10	0.39	0.10	0.21
1100w-8h	top/cold	52 / 1 .	Al+Ti rich	1.63	0.06	0.45	0.38	0.65	0.90	0.04	0.00	4.10	0.37	0.08	0.21
1100w-8h	top/cold	54 / 1 .	Al+Ti rich	1.65	0.05	0.42	0.37	0.69	0.88	0.03	0.00	4.10	0.35	0.08	0.21
1100w-8h	centre	21 / 1 .	Al+Ti rich	1.63	0.05	0.46	0.36	0.66	0.90	0.03	0.00	4.10	0.37	0.10	0.20
1100w-8h	centre	23 / 1 .	Al+Ti rich	1.72	0.04	0.36	0.29	0.75	0.89	0.03	0.00	4.08	0.28	0.08	0.15
1100w-8h	centre	25 / 1 .	Al+Ti rich	1.65	0.05	0.45	0.36	0.66	0.89	0.03	0.00	4.10	0.35	0.10	0.19
1100w-8h	centre	27 / 1 .	Al+Ti rich	1.66	0.05	0.44	0.36	0.67	0.89	0.03	0.00	4.09	0.34	0.09	0.19
1100w-8h	centre	29 / 1 .	Al+Ti rich	1.68	0.05	0.38	0.37	0.69	0.87	0.04	0.00	4.09	0.32	0.07	0.18
1100w-8h	centre	31 / 1 .	Al+Ti rich	1.63	0.06	0.45	0.39	0.64	0.90	0.04	0.00	4.10	0.37	0.08	0.21
1100w-8h	centre	34 / 1 .	Al+Ti rich	1.65	0.05	0.43	0.36	0.70	0.88	0.03	0.00	4.10	0.35	0.08	0.20
1100w-8h	bottom/hot	1 / 1 .	Al+Ti rich	1.65	0.05	0.45	0.35	0.67	0.88	0.04	0.00	4.09	0.35	0.10	0.18
1100w-8h	bottom/hot	6 / 1 .	Al+Ti rich	1.63	0.06	0.46	0.37	0.65	0.91	0.03	0.00	4.10	0.37	0.09	0.20
1100w-8h	bottom/hot	10 / 1 .	Al+Ti rich	1.61	0.06	0.47	0.40	0.64	0.89	0.03	0.00	4.11	0.39	0.08	0.22
1100w-8h	bottom/hot	12 / 1 .	Al+Ti rich	1.63	0.06	0.45	0.38	0.65	0.90	0.03	0.00	4.10	0.37	0.08	0.21
1100w-8h	bottom/hot	58 / 1 .	Al+Ti rich	1.64	0.06	0.43	0.36	0.68	0.90	0.03	0.00	4.10	0.36	0.07	0.20
1100w-8h	top/cold	45 / 1 .	Si+Mg rich	1.72	0.05	0.37	0.25	0.72	0.92	0.03	0.00	4.06	0.28	0.09	0.13
1100w-8h	top/cold	47 / 1 .	Si+Mg rich	1.79	0.04	0.27	0.21	0.81	0.91	0.03	0.00	4.05	0.21	0.06	0.11
1100w-8h	top/cold	49 / 1 .	Si+Mg rich	1.73	0.05	0.35	0.23	0.75	0.91	0.03	0.00	4.06	0.27	0.08	0.11
1100w-8h	top/cold	51 / 1 .	Si+Mg rich	1.76	0.04	0.30	0.23	0.76	0.92	0.03	0.00	4.06	0.24	0.06	0.12
1100w-8h	top/cold	53 / 1 .	Si+Mg rich	1.77	0.04	0.29	0.22	0.78	0.93	0.03	0.00	4.06	0.23	0.06	0.12
1100w-8h	top/cold	55 / 1 .	Si+Mg rich	1.72	0.05	0.36	0.23	0.74	0.92	0.03	0.00	4.06	0.28	0.09	0.13
1100w-8h	top/cold	56 / 1 .	Si+Mg rich	1.78	0.04	0.30	0.21	0.78	0.91	0.03	0.00	4.05	0.22	0.07	0.09
1100w-8h	centre	22 / 1 .	Si+Mg rich	1.78	0.04	0.30	0.20	0.78	0.91	0.03	0.00	4.04	0.22	0.08	0.09
1100w-8h	centre	28 / 1 .	Si+Mg rich	1.75	0.04	0.32	0.23	0.77	0.92	0.03	0.00	4.06	0.25	0.07	0.12
1100w-8h	centre	30 / 1 .	Si+Mg rich	1.79	0.04	0.29	0.22	0.78	0.91	0.03	0.00	4.05	0.21	0.07	0.10
1100w-8h	centre	32 / 1 .	Si+Mg rich	1.77	0.04	0.30	0.21	0.78	0.91	0.03	0.00	4.05	0.23	0.07	0.11
1100w-8h	centre	33 / 1 .	Si+Mg rich	1.74	0.05	0.35	0.22	0.76	0.92	0.03	0.00	4.06	0.26	0.08	0.12
1100w-8h	centre	35 / 1 .	Si+Mg rich	1.79	0.04	0.27	0.21	0.80	0.92	0.03	0.00	4.05	0.21	0.06	0.10
1100w-8h	bottom/hot	2 / 1 .	Si+Mg rich	1.79	0.03	0.28	0.22	0.80	0.90	0.03	0.00	4.05	0.21	0.07	0.11
1100w-8h	bottom/hot	3 / 1 .	Si+Mg rich	1.79	0.03	0.27	0.21	0.81	0.89	0.03	0.00	4.05	0.21	0.07	0.10
1100w-8h	bottom/hot	5 / 1 .	Si+Mg rich	1.77	0.04	0.30	0.23	0.79	0.91	0.03	0.00	4.06	0.23	0.07	0.11
1100w-8h	bottom/hot	7 / 1 .	Si+Mg rich	1.72	0.05	0.36	0.24	0.75	0.91	0.03	0.00	4.07	0.28	0.08	0.13
1100w-8h	bottom/hot	8 / 1 .	Si+Mg rich	1.77	0.04	0.31	0.21	0.78	0.91	0.03	0.00	4.05	0.23	0.08	0.10
1100w-8h	bottom/hot	9 / 1 .	Si+Mg rich	1.79	0.03	0.28	0.21	0.80	0.91	0.03	0.00	4.05	0.21	0.07	0.10
1100w-8h	bottom/hot	11 / 1 .	Si+Mg rich	1.75	0.04	0.33	0.24	0.76	0.91	0.03	0.00	4.06	0.25	0.08	0.13
1100w-8h	bottom/hot	13 / 1 .	Si+Mg rich	1.78	0.03	0.27	0.28	0.82	0.86	0.03	0.00	4.07	0.22	0.05	0.13
1100w-8h	bottom/hot	57 / 1 .	Si+Mg rich	1.73	0.04	0.36	0.24	0.74	0.91	0.03	0.00	4.06	0.27	0.09	0.12
1100w-8h	bottom/hot	59 / 1 .	Si+Mg rich	1.73	0.04	0.35	0.24	0.75	0.91	0.03	0.00	4.06	0.27	0.08	0.12
1100w-8h	bottom/hot	60 / 1 .	Si+Mg rich	1.75	0.04	0.31	0.24	0.77	0.92	0.03	0.00	4.07	0.25	0.07	0.14
1100w-8h	bottom/hot	61 / 1 .	Si+Mg rich	1.77	0.03	0.29	0.23	0.79	0.92	0.03	0.00	4.07	0.23	0.06	0.13

				Cations (according to L&A Fe3+)									
Sample name	Region in the sample	Point	Cpx Sector analyzed	Si	Ti	Al	Fe3+	Fe2+	Mg	Ca	Na	K	Total
1100w-30min	top/cold	29 / 1 .	Al+Ti rich	1.60	0.05	0.53	0.20	0.18	0.65	0.84	0.04	0.00	4.10
1100w-30min	top/cold	30 / 1 .	Al+Ti rich	1.61	0.05	0.53	0.19	0.19	0.65	0.82	0.05	0.00	4.10
1100w-30min	top/cold	31 / 1 .	Al+Ti rich	1.60	0.06	0.51	0.21	0.19	0.66	0.84	0.04	0.00	4.10
1100w-30min	centre	38 / 1 .	Al+Ti rich	1.63	0.05	0.48	0.21	0.18	0.66	0.86	0.04	0.00	4.10
1100w-30min	centre	39 / 1 .	Al+Ti rich	1.64	0.05	0.45	0.21	0.19	0.68	0.86	0.04	0.00	4.10
1100w-30min	centre	40 / 1 .	Al+Ti rich	1.61	0.06	0.48	0.22	0.20	0.63	0.87	0.04	0.00	4.11
1100w-30min	centre	42 / 1 .	Al+Ti rich	1.63	0.05	0.45	0.21	0.18	0.71	0.83	0.03	0.00	4.11
1100w-30min	bottom/hot	43 / 1 .	Al+Ti rich	1.61	0.05	0.48	0.25	0.16	0.66	0.86	0.05	0.00	4.13
1100w-30min	bottom/hot	44 / 1 .	Al+Ti rich	1.66	0.06	0.42	0.18	0.17	0.69	0.89	0.03	0.00	4.09
1100w-30min	bottom/hot	45 / 1 .	Al+Ti rich	1.63	0.05	0.46	0.20	0.18	0.64	0.90	0.03	0.00	4.10
1100w-30min	bottom/hot	47 / 1 .	Al+Ti rich	1.61	0.07	0.46	0.21	0.18	0.65	0.88	0.04	0.00	4.11
1100w-30min	bottom/hot	41 / 1 .	Si+Mg rich	1.68	0.05	0.41	0.18	0.20	0.76	0.78	0.03	0.00	4.09
1100w-30min	bottom/hot	46 / 1 .	Si+Mg rich	1.69	0.04	0.40	0.18	0.17	0.72	0.87	0.03	0.00	4.09
1100w-30min	bottom/hot	48 / 1 .	Si+Mg rich	1.86	0.02	0.18	0.08	0.14	0.94	0.79	0.02	0.00	4.04
1100w-8h	top/cold	46 / 1 .	Al+Ti rich	1.61	0.05	0.50	0.22	0.17	0.63	0.90	0.04	0.00	4.11
1100w-8h	top/cold	48 / 1 .	Al+Ti rich	1.64	0.05	0.44	0.21	0.18	0.66	0.89	0.04	0.00	4.10
1100w-8h	top/cold	50 / 1 .	Al+Ti rich	1.61	0.06	0.49	0.21	0.18	0.62	0.90	0.03	0.00	4.10
1100w-8h	top/cold	52 / 1 .	Al+Ti rich	1.63	0.06	0.45	0.21	0.17	0.65	0.90	0.04	0.00	4.10
1100w-8h	top/cold	54 / 1 .	Al+Ti rich	1.65	0.05	0.42	0.21	0.17	0.69	0.88	0.03	0.00	4.10
1100w-8h	centre	21 / 1 .	Al+Ti rich	1.63	0.05	0.46	0.20	0.16	0.66	0.90	0.03	0.00	4.10
1100w-8h	centre	23 / 1 .	Al+Ti rich	1.72	0.04	0.36	0.15	0.14	0.75	0.89	0.03	0.00	4.08
1100w-8h	centre	25 / 1 .	Al+Ti rich	1.65	0.05	0.45	0.19	0.17	0.66	0.89	0.03	0.00	4.10
1100w-8h	centre	27 / 1 .	Al+Ti rich	1.66	0.05	0.44	0.19	0.17	0.67	0.89	0.03	0.00	4.09
1100w-8h	centre	29 / 1 .	Al+Ti rich	1.68	0.05	0.38	0.18	0.19	0.69	0.87	0.04	0.00	4.09
1100w-8h	centre	31 / 1 .	Al+Ti rich	1.63	0.06	0.45	0.21	0.18	0.64	0.90	0.04	0.00	4.10
1100w-8h	centre	34 / 1 .	Al+Ti rich	1.65	0.05	0.43	0.20	0.16	0.70	0.88	0.03	0.00	4.10
1100w-8h	bottom/hot	1 / 1 .	Al+Ti rich	1.65	0.05	0.45	0.18	0.16	0.67	0.88	0.04	0.00	4.09
1100w-8h	bottom/hot	6 / 1 .	Al+Ti rich	1.63	0.06	0.46	0.20	0.17	0.65	0.91	0.03	0.00	4.10
1100w-8h	bottom/hot	10 / 1 .	Al+Ti rich	1.61	0.06	0.47	0.22	0.18	0.64	0.89	0.03	0.00	4.11
1100w-8h	bottom/hot	12 / 1 .	Al+Ti rich	1.63	0.06	0.45	0.21	0.17	0.65	0.90	0.03	0.00	4.10
1100w-8h	bottom/hot	58 / 1 .	Al+Ti rich	1.64	0.06	0.43	0.20	0.16	0.68	0.90	0.03	0.00	4.10
1100w-8h	top/cold	45 / 1 .	Si+Mg rich	1.72	0.05	0.37	0.13	0.12	0.72	0.92	0.03	0.00	4.06
1100w-8h	top/cold	47 / 1 .	Si+Mg rich	1.79	0.04	0.27	0.11	0.10	0.81	0.91	0.03	0.00	4.05
1100w-8h	top/cold	49 / 1 .	Si+Mg rich	1.73	0.05	0.35	0.11	0.11	0.75	0.91	0.03	0.00	4.06
1100w-8h	top/cold	51 / 1 .	Si+Mg rich	1.76	0.04	0.30	0.12	0.11	0.76	0.92	0.03	0.00	4.06
1100w-8h	top/cold	53 / 1 .	Si+Mg rich	1.77	0.04	0.29	0.12	0.10	0.78	0.93	0.03	0.00	4.06
1100w-8h	top/cold	55 / 1 .	Si+Mg rich	1.72	0.05	0.36	0.13	0.11	0.74	0.92	0.03	0.00	4.06
1100w-8h	top/cold	56 / 1 .	Si+Mg rich	1.78	0.04	0.30	0.09	0.11	0.78	0.91	0.03	0.00	4.05
1100w-8h	centre	22 / 1 .	Si+Mg rich	1.78	0.04	0.30	0.09	0.11	0.78	0.91	0.03	0.00	4.04
1100w-8h	centre	28 / 1 .	Si+Mg rich	1.75	0.04	0.32	0.12	0.11	0.77	0.92	0.03	0.00	4.06
1100w-8h	centre	30 / 1 .	Si+Mg rich	1.79	0.04	0.29	0.10	0.11	0.78	0.91	0.03	0.00	4.05
1100w-8h	centre	32 / 1 .	Si+Mg rich	1.77	0.04	0.30	0.11	0.10	0.78	0.91	0.03	0.00	4.05
1100w-8h	centre	33 / 1 .	Si+Mg rich	1.74	0.05	0.35	0.12	0.10	0.76	0.92	0.03	0.00	4.06
1100w-8h	centre	35 / 1 .	Si+Mg rich	1.79	0.04	0.27	0.10	0.11	0.80	0.92	0.03	0.00	4.05
1100w-8h	bottom/hot	2 / 1 .	Si+Mg rich	1.79	0.03	0.28	0.11	0.11	0.80	0.90	0.03	0.00	4.05
1100w-8h	bottom/hot	3 / 1 .	Si+Mg rich	1.79	0.03	0.27	0.10	0.11	0.81	0.89	0.03	0.00	4.05
1100w-8h	bottom/hot	5 / 1 .	Si+Mg rich	1.77	0.04	0.30	0.11	0.11	0.79	0.91	0.03	0.00	4.06
1100w-8h	bottom/hot	7 / 1 .	Si+Mg rich	1.72	0.05	0.36	0.13	0.11	0.75	0.91	0.03	0.00	4.07
1100w-8h	bottom/hot	8 / 1 .	Si+Mg rich	1.77	0.04	0.31	0.10	0.11	0.78	0.91	0.03	0.00	4.05
1100w-8h	bottom/hot	9 / 1 .	Si+Mg rich	1.79	0.03	0.28	0.10	0.11	0.80	0.91	0.03	0.00	4.05
1100w-8h	bottom/hot	11 / 1 .	Si+Mg rich	1.75	0.04	0.33	0.13	0.11	0.76	0.91	0.03	0.00	4.06
1100w-8h	bottom/hot	13 / 1 .	Si+Mg rich	1.78	0.03	0.27	0.13	0.15	0.82	0.86	0.03	0.00	4.07
1100w-8h	bottom/hot	57 / 1 .	Si+Mg rich	1.73	0.04	0.36	0.12	0.12	0.74	0.91	0.03	0.00	4.06
1100w-8h	bottom/hot	59 / 1 .	Si+Mg rich	1.73	0.04	0.35	0.12	0.12	0.75	0.91	0.03	0.00	4.06
1100w-8h	bottom/hot	60 / 1 .	Si+Mg rich	1.75	0.04	0.31	0.14	0.10	0.77	0.92	0.03	0.00	4.07
1100w-8h	bottom/hot	61 / 1 .	Si+Mg rich	1.77	0.03	0.29	0.13	0.10	0.79	0.92	0.03	0.00	4.07

				Wt.% Recalculated									
Sample name	Region in the sample	Point	Cpx Sector analyzed	SiO2	TiO2	Al2O3	Fe2O3	FeO	MgO	CaO	NaO	K2O	Total
1100w-30min	top/cold	29 / 1 .	Al+Ti rich	40.86	1.72	11.49	6.88	5.44	11.07	20.08	0.55	0.02	98.12
1100w-30min	top/cold	30 / 1 .	Al+Ti rich	41.12	1.75	11.44	6.58	5.93	11.05	19.65	0.61	0.03	98.17
1100w-30min	top/cold	31 / 1 .	Al+Ti rich	40.65	2.00	11.10	7.00	5.64	11.26	19.99	0.47	0.01	98.13
1100w-30min	centre	38 / 1 .	Al+Ti rich	41.36	1.74	10.32	6.96	5.32	11.29	20.43	0.54	0.01	97.98
1100w-30min	centre	39 / 1 .	Al+Ti rich	41.85	1.80	9.65	7.01	5.66	11.56	20.41	0.50	0.03	98.48
1100w-30min	centre	40 / 1 .	Al+Ti rich	40.93	2.10	10.28	7.35	6.05	10.83	20.57	0.51	0.03	98.65
1100w-30min	centre	42 / 1 .	Al+Ti rich	41.94	1.81	9.76	7.34	5.66	12.22	19.89	0.46	0.01	99.09
1100w-30min	bottom/hot	43 / 1 .	Al+Ti rich	40.09	1.76	10.10	8.33	4.81	11.12	20.11	0.59	0.05	96.97
1100w-30min	bottom/hot	44 / 1 .	Al+Ti rich	42.50	2.05	9.20	6.07	5.13	11.81	21.20	0.45	0.00	98.40
1100w-30min	bottom/hot	45 / 1 .	Al+Ti rich	41.50	1.86	10.03	6.80	5.50	10.91	21.45	0.42	0.00	98.45
1100w-30min	bottom/hot	47 / 1 .	Al+Ti rich	40.91	2.40	9.99	7.12	5.55	11.12	20.75	0.50	0.01	98.36
1100w-30min	bottom/hot	41 / 1 .	Si+Mg rich	43.33	1.59	8.95	6.14	6.27	13.22	18.87	0.41	0.03	98.82
1100w-30min	bottom/hot	46 / 1 .	Si+Mg rich	43.52	1.43	8.68	6.18	5.16	12.47	20.95	0.41	0.00	98.79
1100w-30min	bottom/hot	48 / 1 .	Si+Mg rich	50.07	0.84	4.19	2.70	4.49	16.99	19.95	0.31	0.02	99.57
1100w-8h	top/cold	46 / 1 .	Al+Ti rich	40.91	1.84	10.68	7.32	5.04	10.80	21.29	0.49	0.01	98.38
1100w-8h	top/cold	48 / 1 .	Al+Ti rich	41.73	1.75	9.55	7.06	5.41	11.25	21.04	0.48	0.01	98.28
1100w-8h	top/cold	50 / 1 .	Al+Ti rich	40.86	1.99	10.49	7.03	5.48	10.57	21.35	0.46	0.01	98.24
1100w-8h	top/cold	52 / 1 .	Al+Ti rich	41.56	1.97	9.64	7.07	5.32	11.13	21.30	0.47	0.01	98.46
1100w-8h	top/cold	54 / 1 .	Al+Ti rich	42.03	1.68	9.18	6.96	5.08	11.79	20.90	0.43	0.01	98.07
1100w-8h	centre	21 / 1 .	Al+Ti rich	41.77	1.64	10.08	6.84	4.90	11.26	21.51	0.43	0.00	98.43
1100w-8h	centre	23 / 1 .	Al+Ti rich	44.78	1.50	7.90	5.28	4.27	13.12	21.55	0.43	0.00	98.83
1100w-8h	centre	25 / 1 .	Al+Ti rich	42.14	1.67	9.85	6.48	5.21	11.31	21.31	0.46	0.00	98.44
1100w-8h	centre	27 / 1 .	Al+Ti rich	42.39	1.70	9.47	6.43	5.16	11.47	21.36	0.46	0.01	98.45
1100w-8h	centre	29 / 1 .	Al+Ti rich	43.23	1.75	8.34	6.17	5.82	11.96	20.86	0.47	0.01	98.62
1100w-8h	centre	31 / 1 .	Al+Ti rich	41.47	1.97	9.68	7.08	5.38	10.99	21.31	0.47	0.03	98.39
1100w-8h	centre	34 / 1 .	Al+Ti rich	42.43	1.64	9.46	6.81	4.85	12.03	21.17	0.40	0.00	98.80
1100w-8h	bottom/hot	1 / 1 .	Al+Ti rich	42.28	1.80	9.85	6.26	4.97	11.59	21.17	0.48	0.01	98.42
1100w-8h	bottom/hot	6 / 1 .	Al+Ti rich	41.42	1.92	9.85	6.91	5.15	11.04	21.48	0.43	0.00	98.20
1100w-8h	bottom/hot	10 / 1 .	Al+Ti rich	40.94	2.05	10.08	7.33	5.49	10.97	21.05	0.45	0.00	98.36
1100w-8h	bottom/hot	12 / 1 .	Al+Ti rich	41.55	2.05	9.76	7.04	5.27	11.10	21.46	0.46	0.00	98.69
1100w-8h	bottom/hot	58 / 1 .	Al+Ti rich	42.16	1.96	9.29	6.90	4.76	11.61	21.64	0.45	0.00	98.78
1100w-8h	top/cold	45 / 1 .	Si+Mg rich	44.84	1.77	8.25	4.45	3.66	12.69	22.45	0.46	0.02	98.59
1100w-8h	top/cold	47 / 1 .	Si+Mg rich	47.17	1.34	5.96	3.73	3.10	14.25	22.46	0.43	0.01	98.45
1100w-8h	top/cold	49 / 1 .	Si+Mg rich	45.72	1.82	7.86	4.02	3.60	13.37	22.31	0.44	0.02	99.15
1100w-8h	top/cold	51 / 1 .	Si+Mg rich	46.38	1.57	6.77	4.29	3.54	13.49	22.74	0.44	0.01	99.24
1100w-8h	top/cold	53 / 1 .	Si+Mg rich	46.35	1.37	6.42	4.31	3.12	13.67	22.62	0.45	0.02	98.34
1100w-8h	top/cold	55 / 1 .	Si+Mg rich	45.33	1.62	8.13	4.45	3.31	13.06	22.57	0.45	0.02	98.95
1100w-8h	top/cold	56 / 1 .	Si+Mg rich	47.01	1.57	6.70	3.32	3.58	13.89	22.42	0.44	0.01	98.94
1100w-8h	centre	22 / 1 .	Si+Mg rich	47.48	1.45	6.83	3.16	3.64	14.02	22.61	0.41	0.00	99.59
1100w-8h	centre	28 / 1 .	Si+Mg rich	46.33	1.41	7.17	4.38	3.38	13.59	22.74	0.41	0.01	99.42
1100w-8h	centre	30 / 1 .	Si+Mg rich	47.58	1.27	6.49	3.62	3.65	13.95	22.76	0.42	0.01	99.76
1100w-8h	centre	32 / 1 .	Si+Mg rich	47.11	1.40	6.77	3.86	3.32	13.99	22.68	0.43	0.01	99.56
1100w-8h	centre	33 / 1 .	Si+Mg rich	45.57	1.65	7.71	4.26	3.18	13.35	22.50	0.44	0.02	98.68
1100w-8h	centre	35 / 1 .	Si+Mg rich	47.14	1.38	6.08	3.51	3.41	14.07	22.54	0.39	0.01	98.53
1100w-8h	bottom/hot	2 / 1 .	Si+Mg rich	47.29	1.18	6.25	3.77	3.44	14.25	22.25	0.41	0.02	98.86
1100w-8h	bottom/hot	3 / 1 .	Si+Mg rich	47.48	1.21	6.14	3.59	3.50	14.46	22.10	0.40	0.02	98.91
1100w-8h	bottom/hot	5 / 1 .	Si+Mg rich	47.04	1.25	6.71	4.04	3.53	13.99	22.41	0.43	0.00	99.39
1100w-8h	bottom/hot	7 / 1 .	Si+Mg rich	45.14	1.83	8.13	4.59	3.52	13.16	22.33	0.45	0.01	99.17
1100w-8h	bottom/hot	8 / 1 .	Si+Mg rich	47.05	1.37	6.91	3.55	3.61	13.87	22.49	0.42	0.01	99.27
1100w-8h	bottom/hot	9 / 1 .	Si+Mg rich	47.55	1.17	6.34	3.65	3.39	14.20	22.50	0.41	0.04	99.25
1100w-8h	bottom/hot	11 / 1 .	Si+Mg rich	46.00	1.45	7.31	4.38	3.53	13.48	22.43	0.43	0.01	99.02
1100w-8h	bottom/hot	13 / 1 .	Si+Mg rich	46.62	1.11	5.95	4.54	4.58	14.44	20.97	0.35	0.00	98.56
1100w-8h	bottom/hot	57 / 1 .	Si+Mg rich	45.49	1.49	7.95	4.22	3.77	13.08	22.27	0.44	0.00	98.71
1100w-8h	bottom/hot	59 / 1 .	Si+Mg rich	45.71	1.55	7.82	4.33	3.75	13.20	22.41	0.43	0.00	99.20
1100w-8h	bottom/hot	60 / 1 .	Si+Mg rich	46.33	1.28	7.06	4.78	3.20	13.69	22.73	0.43	0.00	99.49
1100w-8h	bottom/hot	61 / 1 .	Si+Mg rich	46.97	1.23	6.54	4.60	3.10	14.02	22.89	0.41	0.01	99.77

Sample name	Region in the sample	Point	Cpx Sector analyzed	xMg(Fetot)	Fe3+/Fe(tot)	Mg*number
1100w-30min	top/cold	29 / 1 .	Al+Ti rich	0.63	0.53	0.66
1100w-30min	top/cold	30 / 1 .	Al+Ti rich	0.62	0.50	0.65
1100w-30min	top/cold	31 / 1 .	Al+Ti rich	0.63	0.53	0.65
1100w-30min	centre	38 / 1 .	Al+Ti rich	0.63	0.54	0.66
1100w-30min	centre	39 / 1 .	Al+Ti rich	0.63	0.53	0.66
1100w-30min	centre	40 / 1 .	Al+Ti rich	0.60	0.52	0.63
1100w-30min	centre	42 / 1 .	Al+Ti rich	0.64	0.54	0.67
1100w-30min	bottom/hot	43 / 1 .	Al+Ti rich	0.62	0.61	0.65
1100w-30min	bottom/hot	44 / 1 .	Al+Ti rich	0.67	0.52	0.69
1100w-30min	bottom/hot	45 / 1 .	Al+Ti rich	0.63	0.53	0.65
1100w-30min	bottom/hot	47 / 1 .	Al+Ti rich	0.62	0.54	0.65
1100w-30min	bottom/hot	41 / 1 .	Si+Mg rich	0.67	0.47	0.69
1100w-30min	bottom/hot	46 / 1 .	Si+Mg rich	0.67	0.52	0.70
1100w-30min	bottom/hot	48 / 1 .	Si+Mg rich	0.81	0.35	0.83
1100w-8h	top/cold	46 / 1 .	Al+Ti rich	0.62	0.57	0.65
1100w-8h	top/cold	48 / 1 .	Al+Ti rich	0.63	0.54	0.66
1100w-8h	top/cold	50 / 1 .	Al+Ti rich	0.61	0.54	0.64
1100w-8h	top/cold	52 / 1 .	Al+Ti rich	0.63	0.54	0.66
1100w-8h	top/cold	54 / 1 .	Al+Ti rich	0.65	0.55	0.68
1100w-8h	centre	21 / 1 .	Al+Ti rich	0.64	0.56	0.67
1100w-8h	centre	23 / 1 .	Al+Ti rich	0.72	0.53	0.75
1100w-8h	centre	25 / 1 .	Al+Ti rich	0.65	0.53	0.67
1100w-8h	centre	27 / 1 .	Al+Ti rich	0.65	0.53	0.68
1100w-8h	centre	29 / 1 .	Al+Ti rich	0.65	0.49	0.68
1100w-8h	centre	31 / 1 .	Al+Ti rich	0.63	0.54	0.65
1100w-8h	centre	34 / 1 .	Al+Ti rich	0.66	0.56	0.69
1100w-8h	bottom/hot	1 / 1 .	Al+Ti rich	0.66	0.53	0.69
1100w-8h	bottom/hot	6 / 1 .	Al+Ti rich	0.63	0.55	0.66
1100w-8h	bottom/hot	10 / 1 .	Al+Ti rich	0.62	0.55	0.65
1100w-8h	bottom/hot	12 / 1 .	Al+Ti rich	0.63	0.55	0.66
1100w-8h	bottom/hot	58 / 1 .	Al+Ti rich	0.65	0.57	0.68
1100w-8h	top/cold	45 / 1 .	Si+Mg rich	0.75	0.52	0.77
1100w-8h	top/cold	47 / 1 .	Si+Mg rich	0.80	0.52	0.82
1100w-8h	top/cold	49 / 1 .	Si+Mg rich	0.77	0.50	0.79
1100w-8h	top/cold	51 / 1 .	Si+Mg rich	0.76	0.52	0.79
1100w-8h	top/cold	53 / 1 .	Si+Mg rich	0.78	0.55	0.80
1100w-8h	top/cold	55 / 1 .	Si+Mg rich	0.76	0.55	0.78
1100w-8h	top/cold	56 / 1 .	Si+Mg rich	0.79	0.45	0.81
1100w-8h	centre	22 / 1 .	Si+Mg rich	0.79	0.44	0.81
1100w-8h	centre	28 / 1 .	Si+Mg rich	0.77	0.54	0.79
1100w-8h	centre	30 / 1 .	Si+Mg rich	0.78	0.47	0.80
1100w-8h	centre	32 / 1 .	Si+Mg rich	0.79	0.51	0.81
1100w-8h	centre	33 / 1 .	Si+Mg rich	0.77	0.55	0.79
1100w-8h	centre	35 / 1 .	Si+Mg rich	0.79	0.48	0.81
1100w-8h	bottom/hot	2 / 1 .	Si+Mg rich	0.79	0.50	0.81
1100w-8h	bottom/hot	3 / 1 .	Si+Mg rich	0.79	0.48	0.81
1100w-8h	bottom/hot	5 / 1 .	Si+Mg rich	0.78	0.51	0.80
1100w-8h	bottom/hot	7 / 1 .	Si+Mg rich	0.75	0.54	0.78
1100w-8h	bottom/hot	8 / 1 .	Si+Mg rich	0.78	0.47	0.80
1100w-8h	bottom/hot	9 / 1 .	Si+Mg rich	0.79	0.49	0.81
1100w-8h	bottom/hot	11 / 1 .	Si+Mg rich	0.76	0.53	0.78
1100w-8h	bottom/hot	13 / 1 .	Si+Mg rich	0.75	0.47	0.77
1100w-8h	bottom/hot	57 / 1 .	Si+Mg rich	0.75	0.50	0.78
1100w-8h	bottom/hot	59 / 1 .	Si+Mg rich	0.75	0.51	0.78
1100w-8h	bottom/hot	60 / 1 .	Si+Mg rich	0.76	0.57	0.79
1100w-8h	bottom/hot	61 / 1 .	Si+Mg rich	0.78	0.57	0.80

Sample name	Region in the sample	Point	Cpx Sector analyzed	Endmembers NaFeSi2O6 (acm)	NaAlSi2O6 (jad)	CaTiAl2O6	CaCrAlSiO6	CaFeAlSiO6
1100w-30min	top/cold	29 / 1 .	Al+Ti rich	0.04	0.00	0.05	0.00	0.16
1100w-30min	top/cold	30 / 1 .	Al+Ti rich	0.05	0.00	0.05	0.00	0.15
1100w-30min	top/cold	31 / 1 .	Al+Ti rich	0.04	0.00	0.06	0.00	0.17
1100w-30min	centre	38 / 1 .	Al+Ti rich	0.04	0.00	0.05	0.00	0.16
1100w-30min	centre	39 / 1 .	Al+Ti rich	0.04	0.00	0.05	0.00	0.17
1100w-30min	centre	40 / 1 .	Al+Ti rich	0.04	0.00	0.06	0.00	0.18
1100w-30min	centre	42 / 1 .	Al+Ti rich	0.04	0.00	0.05	0.00	0.18
1100w-30min	bottom/hot	43 / 1 .	Al+Ti rich	0.05	0.00	0.05	0.00	0.20
1100w-30min	bottom/hot	44 / 1 .	Al+Ti rich	0.03	0.00	0.06	0.00	0.14
1100w-30min	bottom/hot	45 / 1 .	Al+Ti rich	0.03	0.00	0.05	0.00	0.17
1100w-30min	bottom/hot	47 / 1 .	Al+Ti rich	0.04	0.00	0.07	0.00	0.17
1100w-30min	bottom/hot	41 / 1 .	Si+Mg rich	0.03	0.00	0.05	0.00	0.15
1100w-30min	bottom/hot	46 / 1 .	Si+Mg rich	0.03	0.00	0.04	0.00	0.15
1100w-30min	bottom/hot	48 / 1 .	Si+Mg rich	0.02	0.00	0.02	0.00	0.05
1100w-8h	top/cold	46 / 1 .	Al+Ti rich	0.04	0.00	0.05	0.00	0.18
1100w-8h	top/cold	48 / 1 .	Al+Ti rich	0.04	0.00	0.05	0.00	0.17
1100w-8h	top/cold	50 / 1 .	Al+Ti rich	0.04	0.00	0.06	0.00	0.17
1100w-8h	top/cold	52 / 1 .	Al+Ti rich	0.04	0.00	0.06	0.00	0.17
1100w-8h	top/cold	54 / 1 .	Al+Ti rich	0.03	0.00	0.05	0.00	0.17
1100w-8h	centre	21 / 1 .	Al+Ti rich	0.03	0.00	0.05	0.00	0.17
1100w-8h	centre	23 / 1 .	Al+Ti rich	0.03	0.00	0.04	0.00	0.12
1100w-8h	centre	25 / 1 .	Al+Ti rich	0.04	0.00	0.05	0.00	0.16
1100w-8h	centre	27 / 1 .	Al+Ti rich	0.04	0.00	0.05	0.00	0.15
1100w-8h	centre	29 / 1 .	Al+Ti rich	0.04	0.00	0.05	0.00	0.15
1100w-8h	centre	31 / 1 .	Al+Ti rich	0.04	0.00	0.06	0.00	0.17
1100w-8h	centre	34 / 1 .	Al+Ti rich	0.03	0.00	0.05	0.00	0.17
1100w-8h	bottom/hot	1 / 1 .	Al+Ti rich	0.04	0.00	0.05	0.00	0.15
1100w-8h	bottom/hot	6 / 1 .	Al+Ti rich	0.03	0.00	0.06	0.00	0.17
1100w-8h	bottom/hot	10 / 1 .	Al+Ti rich	0.03	0.00	0.06	0.00	0.18
1100w-8h	bottom/hot	12 / 1 .	Al+Ti rich	0.04	0.00	0.06	0.00	0.17
1100w-8h	bottom/hot	58 / 1 .	Al+Ti rich	0.03	0.00	0.06	0.00	0.17
1100w-8h	top/cold	45 / 1 .	Si+Mg rich	0.03	0.00	0.05	0.00	0.09
1100w-8h	top/cold	47 / 1 .	Si+Mg rich	0.03	0.00	0.04	0.00	0.07
1100w-8h	top/cold	49 / 1 .	Si+Mg rich	0.03	0.00	0.05	0.00	0.08
1100w-8h	top/cold	51 / 1 .	Si+Mg rich	0.03	0.00	0.04	0.00	0.09
1100w-8h	top/cold	53 / 1 .	Si+Mg rich	0.03	0.00	0.04	0.00	0.09
1100w-8h	top/cold	55 / 1 .	Si+Mg rich	0.03	0.00	0.05	0.00	0.09
1100w-8h	top/cold	56 / 1 .	Si+Mg rich	0.03	0.00	0.04	0.00	0.06
1100w-8h	centre	22 / 1 .	Si+Mg rich	0.03	0.00	0.04	0.00	0.06
1100w-8h	centre	28 / 1 .	Si+Mg rich	0.03	0.00	0.04	0.00	0.09
1100w-8h	centre	30 / 1 .	Si+Mg rich	0.03	0.00	0.04	0.00	0.07
1100w-8h	centre	32 / 1 .	Si+Mg rich	0.03	0.00	0.04	0.00	0.08
1100w-8h	centre	33 / 1 .	Si+Mg rich	0.03	0.00	0.05	0.00	0.09
1100w-8h	centre	35 / 1 .	Si+Mg rich	0.03	0.00	0.04	0.00	0.07
1100w-8h	bottom/hot	2 / 1 .	Si+Mg rich	0.03	0.00	0.03	0.00	0.08
1100w-8h	bottom/hot	3 / 1 .	Si+Mg rich	0.03	0.00	0.03	0.00	0.07
1100w-8h	bottom/hot	5 / 1 .	Si+Mg rich	0.03	0.00	0.04	0.00	0.08
1100w-8h	bottom/hot	7 / 1 .	Si+Mg rich	0.03	0.00	0.05	0.00	0.10
1100w-8h	bottom/hot	8 / 1 .	Si+Mg rich	0.03	0.00	0.04	0.00	0.07
1100w-8h	bottom/hot	9 / 1 .	Si+Mg rich	0.03	0.00	0.03	0.00	0.07
1100w-8h	bottom/hot	11 / 1 .	Si+Mg rich	0.03	0.00	0.04	0.00	0.09
1100w-8h	bottom/hot	13 / 1 .	Si+Mg rich	0.03	0.00	0.03	0.00	0.10
1100w-8h	bottom/hot	57 / 1 .	Si+Mg rich	0.03	0.00	0.04	0.00	0.09
1100w-8h	bottom/hot	59 / 1 .	Si+Mg rich	0.03	0.00	0.04	0.00	0.09
1100w-8h	bottom/hot	60 / 1 .	Si+Mg rich	0.03	0.00	0.04	0.00	0.10
1100w-8h	bottom/hot	61 / 1 .	Si+Mg rich	0.03	0.00	0.03	0.00	0.10

Point	Cpx Sector analyzed	CaAl2SiO6 (CaTs)	Ca0.5AlSi2O6 (esc)	Mg2Si2O6 (enst)	Fe2Si2O6	Mn2Si2O6	Ca2Si2O6	Total Endmemembers
29 / 1 .	Al+Ti rich	0.13	0.00	0.32	0.09	0.00	0.25	1.05
30 / 1 .	Al+Ti rich	0.14	0.00	0.32	0.10	0.00	0.24	1.05
31 / 1 .	Al+Ti rich	0.11	0.00	0.33	0.09	0.00	0.25	1.05
38 / 1 .	Al+Ti rich	0.11	0.00	0.33	0.09	0.00	0.27	1.05
39 / 1 .	Al+Ti rich	0.09	0.00	0.34	0.09	0.00	0.28	1.05
40 / 1 .	Al+Ti rich	0.09	0.00	0.32	0.10	0.00	0.27	1.05
42 / 1 .	Al+Ti rich	0.08	0.00	0.35	0.09	0.00	0.26	1.05
43 / 1 .	Al+Ti rich	0.08	0.00	0.33	0.08	0.00	0.26	1.06
44 / 1 .	Al+Ti rich	0.08	0.00	0.34	0.08	0.00	0.30	1.04
45 / 1 .	Al+Ti rich	0.09	0.00	0.32	0.09	0.00	0.29	1.05
47 / 1 .	Al+Ti rich	0.07	0.00	0.33	0.09	0.00	0.28	1.05
41 / 1 .	Si+Mg rich	0.08	0.00	0.38	0.10	0.00	0.25	1.04
46 / 1 .	Si+Mg rich	0.08	0.00	0.36	0.08	0.00	0.30	1.05
48 / 1 .	Si+Mg rich	0.04	0.00	0.47	0.07	0.00	0.34	1.02
46 / 1 .	Al+Ti rich	0.10	0.00	0.32	0.08	0.00	0.28	1.05
48 / 1 .	Al+Ti rich	0.08	0.00	0.33	0.09	0.00	0.29	1.05
50 / 1 .	Al+Ti rich	0.10	0.00	0.31	0.09	0.00	0.29	1.05
52 / 1 .	Al+Ti rich	0.08	0.00	0.33	0.09	0.00	0.29	1.05
54 / 1 .	Al+Ti rich	0.08	0.00	0.35	0.08	0.00	0.29	1.05
21 / 1 .	Al+Ti rich	0.10	0.00	0.33	0.08	0.00	0.29	1.05
23 / 1 .	Al+Ti rich	0.08	0.00	0.38	0.07	0.00	0.32	1.04
25 / 1 .	Al+Ti rich	0.10	0.00	0.33	0.09	0.00	0.29	1.05
27 / 1 .	Al+Ti rich	0.09	0.00	0.33	0.08	0.00	0.30	1.05
29 / 1 .	Al+Ti rich	0.07	0.00	0.35	0.09	0.00	0.30	1.05
31 / 1 .	Al+Ti rich	0.08	0.00	0.32	0.09	0.00	0.29	1.05
34 / 1 .	Al+Ti rich	0.08	0.00	0.35	0.08	0.00	0.29	1.05
1 / 1 .	Al+Ti rich	0.10	0.00	0.34	0.08	0.00	0.29	1.05
6 / 1 .	Al+Ti rich	0.09	0.00	0.32	0.08	0.00	0.30	1.05
10 / 1 .	Al+Ti rich	0.08	0.00	0.32	0.09	0.00	0.28	1.05
12 / 1 .	Al+Ti rich	0.08	0.00	0.32	0.09	0.00	0.29	1.05
58 / 1 .	Al+Ti rich	0.07	0.00	0.34	0.08	0.00	0.30	1.05
45 / 1 .	Si+Mg rich	0.09	0.00	0.36	0.06	0.00	0.34	1.03
47 / 1 .	Si+Mg rich	0.06	0.00	0.40	0.05	0.00	0.37	1.03
49 / 1 .	Si+Mg rich	0.08	0.00	0.38	0.06	0.00	0.34	1.03
51 / 1 .	Si+Mg rich	0.06	0.00	0.38	0.06	0.00	0.36	1.03
53 / 1 .	Si+Mg rich	0.06	0.00	0.39	0.05	0.00	0.37	1.03
55 / 1 .	Si+Mg rich	0.09	0.00	0.37	0.05	0.00	0.35	1.03
56 / 1 .	Si+Mg rich	0.07	0.00	0.39	0.06	0.00	0.36	1.02
22 / 1 .	Si+Mg rich	0.08	0.00	0.39	0.06	0.00	0.36	1.02
28 / 1 .	Si+Mg rich	0.07	0.00	0.38	0.05	0.00	0.36	1.03
30 / 1 .	Si+Mg rich	0.07	0.00	0.39	0.06	0.00	0.37	1.03
32 / 1 .	Si+Mg rich	0.07	0.00	0.39	0.05	0.00	0.36	1.03
33 / 1 .	Si+Mg rich	0.08	0.00	0.38	0.05	0.00	0.35	1.03
35 / 1 .	Si+Mg rich	0.06	0.00	0.40	0.05	0.00	0.37	1.03
2 / 1 .	Si+Mg rich	0.07	0.00	0.40	0.05	0.00	0.36	1.03
3 / 1 .	Si+Mg rich	0.07	0.00	0.41	0.06	0.00	0.36	1.03
5 / 1 .	Si+Mg rich	0.07	0.00	0.39	0.06	0.00	0.36	1.03
7 / 1 .	Si+Mg rich	0.08	0.00	0.37	0.06	0.00	0.34	1.03
8 / 1 .	Si+Mg rich	0.08	0.00	0.39	0.06	0.00	0.36	1.03
9 / 1 .	Si+Mg rich	0.07	0.00	0.40	0.05	0.00	0.37	1.03
11 / 1 .	Si+Mg rich	0.08	0.00	0.38	0.06	0.00	0.35	1.03
13 / 1 .	Si+Mg rich	0.05	0.00	0.41	0.07	0.00	0.34	1.03
57 / 1 .	Si+Mg rich	0.09	0.00	0.37	0.06	0.00	0.34	1.03
59 / 1 .	Si+Mg rich	0.08	0.00	0.37	0.06	0.00	0.35	1.03
60 / 1 .	Si+Mg rich	0.07	0.00	0.39	0.05	0.00	0.36	1.03
61 / 1 .	Si+Mg rich	0.06	0.00	0.39	0.05	0.00	0.36	1.03

									Using same formula used in Colle et al., 2023			
Point	Cpx Sector analyzed	En	Fs	EnFs	Di	Hd	DiHd	∑-Ts	CaTs	CaTi	DiHd	EnFs
29 / 1 .	Al+Ti rich	0.12	0.07	0.19	0.41	0.24	0.66	0.19	0.09	0.02	0.73	0.15
30 / 1 .	Al+Ti rich	0.12	0.08	0.20	0.40	0.24	0.63	0.19	0.09	0.02	0.71	0.16
31 / 1 .	Al+Ti rich	0.12	0.07	0.19	0.42	0.25	0.67	0.17	0.08	0.02	0.75	0.15
38 / 1 .	Al+Ti rich	0.11	0.06	0.17	0.45	0.26	0.70	0.16	0.06	0.02	0.78	0.13
39 / 1 .	Al+Ti rich	0.11	0.06	0.17	0.45	0.26	0.72	0.14	0.05	0.02	0.79	0.14
40 / 1 .	Al+Ti rich	0.10	0.07	0.17	0.43	0.28	0.72	0.15	0.05	0.02	0.80	0.13
42 / 1 .	Al+Ti rich	0.13	0.07	0.21	0.44	0.25	0.70	0.13	0.05	0.02	0.77	0.17
43 / 1 .	Al+Ti rich	0.11	0.07	0.18	0.45	0.28	0.73	0.14	0.04	0.02	0.80	0.14
44 / 1 .	Al+Ti rich	0.09	0.05	0.14	0.50	0.25	0.75	0.14	0.05	0.02	0.82	0.10
45 / 1 .	Al+Ti rich	0.08	0.05	0.13	0.47	0.28	0.75	0.15	0.06	0.02	0.83	0.10
47 / 1 .	Al+Ti rich	0.10	0.06	0.16	0.46	0.27	0.73	0.15	0.04	0.02	0.82	0.11
41 / 1 .	Si+Mg rich	0.16	0.08	0.25	0.43	0.22	0.65	0.13	0.05	0.02	0.71	0.22
46 / 1 .	Si+Mg rich	0.11	0.05	0.16	0.50	0.24	0.75	0.12	0.05	0.02	0.80	0.13
48 / 1 .	Si+Mg rich	0.17	0.04	0.21	0.59	0.14	0.73	0.07	0.02	0.01	0.76	0.20
46 / 1 .	Al+Ti rich	0.09	0.05	0.14	0.46	0.28	0.74	0.16	0.07	0.02	0.81	0.10
48 / 1 .	Al+Ti rich	0.09	0.05	0.15	0.47	0.28	0.75	0.14	0.05	0.02	0.82	0.11
50 / 1 .	Al+Ti rich	0.08	0.05	0.13	0.46	0.29	0.74	0.16	0.06	0.02	0.82	0.09
52 / 1 .	Al+Ti rich	0.09	0.05	0.14	0.48	0.28	0.76	0.14	0.04	0.02	0.84	0.10
54 / 1 .	Al+Ti rich	0.10	0.05	0.15	0.49	0.26	0.75	0.13	0.04	0.02	0.82	0.12
21 / 1 .	Al+Ti rich	0.09	0.05	0.13	0.49	0.27	0.75	0.15	0.07	0.02	0.82	0.10
23 / 1 .	Al+Ti rich	0.10	0.04	0.14	0.55	0.21	0.77	0.12	0.04	0.02	0.83	0.11
25 / 1 .	Al+Ti rich	0.09	0.05	0.14	0.48	0.26	0.74	0.15	0.07	0.02	0.81	0.10
27 / 1 .	Al+Ti rich	0.09	0.05	0.14	0.49	0.26	0.75	0.14	0.06	0.02	0.82	0.10
29 / 1 .	Al+Ti rich	0.10	0.05	0.16	0.49	0.26	0.75	0.12	0.03	0.02	0.82	0.12
31 / 1 .	Al+Ti rich	0.08	0.05	0.14	0.47	0.28	0.76	0.14	0.04	0.02	0.84	0.10
34 / 1 .	Al+Ti rich	0.10	0.05	0.15	0.50	0.25	0.75	0.13	0.05	0.02	0.81	0.12
1 / 1 .	Al+Ti rich	0.10	0.05	0.14	0.48	0.25	0.73	0.15	0.06	0.02	0.80	0.11
6 / 1 .	Al+Ti rich	0.08	0.05	0.13	0.48	0.28	0.76	0.14	0.05	0.02	0.84	0.09
10 / 1 .	Al+Ti rich	0.09	0.06	0.15	0.46	0.28	0.75	0.14	0.05	0.02	0.82	0.11
12 / 1 .	Al+Ti rich	0.08	0.05	0.13	0.48	0.28	0.76	0.14	0.04	0.02	0.84	0.09
58 / 1 .	Al+Ti rich	0.08	0.04	0.13	0.51	0.27	0.78	0.13	0.04	0.02	0.85	0.09
45 / 1 .	Si+Mg rich	0.07	0.02	0.09	0.58	0.20	0.78	0.14	0.05	0.02	0.85	0.06
47 / 1 .	Si+Mg rich	0.08	0.02	0.10	0.65	0.17	0.82	0.10	0.03	0.02	0.87	0.07
49 / 1 .	Si+Mg rich	0.08	0.02	0.11	0.59	0.18	0.77	0.13	0.05	0.02	0.84	0.07
51 / 1 .	Si+Mg rich	0.07	0.02	0.09	0.63	0.19	0.82	0.11	0.03	0.02	0.88	0.06
53 / 1 .	Si+Mg rich	0.07	0.02	0.09	0.64	0.18	0.83	0.10	0.03	0.02	0.88	0.06
55 / 1 .	Si+Mg rich	0.07	0.02	0.09	0.60	0.19	0.78	0.14	0.06	0.02	0.85	0.06
56 / 1 .	Si+Mg rich	0.08	0.02	0.10	0.62	0.17	0.79	0.12	0.04	0.02	0.85	0.07
22 / 1 .	Si+Mg rich	0.08	0.02	0.10	0.62	0.16	0.79	0.12	0.05	0.01	0.84	0.07
28 / 1 .	Si+Mg rich	0.07	0.02	0.09	0.62	0.19	0.81	0.11	0.04	0.01	0.86	0.07
30 / 1 .	Si+Mg rich	0.07	0.02	0.10	0.63	0.18	0.81	0.11	0.04	0.02	0.86	0.07
32 / 1 .	Si+Mg rich	0.08	0.02	0.10	0.63	0.17	0.80	0.11	0.04	0.02	0.86	0.07
33 / 1 .	Si+Mg rich	0.07	0.02	0.10	0.61	0.18	0.79	0.13	0.05	0.02	0.85	0.06
35 / 1 .	Si+Mg rich	0.07	0.02	0.09	0.65	0.17	0.82	0.10	0.03	0.01	0.87	0.07
2 / 1 .	Si+Mg rich	0.09	0.02	0.11	0.63	0.17	0.80	0.10	0.04	0.01	0.85	0.09
3 / 1 .	Si+Mg rich	0.09	0.02	0.12	0.63	0.16	0.79	0.10	0.04	0.01	0.84	0.09
5 / 1 .	Si+Mg rich	0.08	0.02	0.11	0.62	0.18	0.80	0.11	0.04	0.02	0.85	0.08
7 / 1 .	Si+Mg rich	0.08	0.03	0.11	0.59	0.19	0.78	0.13	0.05	0.02	0.85	0.07
8 / 1 .	Si+Mg rich	0.08	0.02	0.10	0.62	0.17	0.79	0.12	0.05	0.02	0.84	0.07
9 / 1 .	Si+Mg rich	0.08	0.02	0.10	0.64	0.17	0.80	0.10	0.04	0.02	0.85	0.08
11 / 1 .	Si+Mg rich	0.08	0.02	0.10	0.61	0.19	0.80	0.12	0.04	0.02	0.85	0.07
13 / 1 .	Si+Mg rich	0.12	0.04	0.16	0.58	0.20	0.78	0.08	0.02	0.01	0.82	0.14
57 / 1 .	Si+Mg rich	0.08	0.03	0.10	0.59	0.19	0.78	0.13	0.06	0.02	0.83	0.07
59 / 1 .	Si+Mg rich	0.08	0.03	0.10	0.59	0.19	0.78	0.13	0.05	0.02	0.84	0.07
60 / 1 .	Si+Mg rich	0.07	0.02	0.10	0.62	0.19	0.82	0.10	0.04	0.02	0.87	0.07
61 / 1 .	Si+Mg rich	0.07	0.02	0.09	0.64	0.19	0.83	0.10	0.03	0.01	0.88	0.07

Sheet "Titanomagnetites" of Peres et al., (2024) suplementary material 2

Raw analyses and recalculated endmembers using EndMemberGenerator (EMG 8.0[Ferracutti et al., 2015])

Sample name	Region in the sample	Point	Phase	SiO2	MgO	Al2O3	CaO	FeO	TiO2	Total	Populations
1100w-30min	cold/top	35 / 1 .	Tmt	1.36	8.00	8.18		69.67	3.26	90.46	**unclassified**
1100w-30min	cold/top	36 / 1 .	Tmt	0.86	7.97	8.24		70.60	3.27	90.94	**unclassified**
1100w-30min	cold/top	37 / 1 .	Tmt	0.30	7.91	8.23		71.41	3.38	91.24	**unclassified**
1100w-30min	centre	52 / 1 .	Tmt	0.25	10.98	9.98		66.32	4.39	91.93	**1**
1100w-30min	centre	53 / 1 .	Tmt	0.22	11.37	11.07		65.84	4.14	92.63	**2**
1100w-30min	centre	54 / 1 .	Tmt	0.22	11.56	11.44		64.50	4.21	91.92	**1**
1100w-30min	bottom/hot	49 / 1 .	Tmt	0.15	10.43	9.01		69.26	3.47	92.32	**2**
1100w-30min	bottom/hot	50 / 1 .	Tmt	0.14	10.71	9.48		68.32	3.34	91.98	**2**
1100w-30min	bottom/hot	51 / 1 .	Tmt	0.14	10.71	9.84		67.56	3.49	91.74	**2**

Sample name	Region in the sample	Point	Phase	SiO2	MgO	Al2O3	CaO	FeO	TiO2	Total	Populations
1100w-8h	top/cold	39 / 1 .	Tmt	0.09	9.75	11.25	0.13	67.70	3.41	92.33	**2**
1100w-8h	top/cold	40 / 1 .	Tmt	0.23	8.38	11.47	0.30	68.11	2.89	91.38	**2**
1100w-8h	top/cold	41 / 1 .	Tmt	0.15	9.60	11.32	0.14	68.27	3.38	92.85	**2**
1100w-8h	top/cold	42 / 1 .	Tmt	0.15	9.29	11.51	0.14	66.80	3.46	91.35	**1**
1100w-8h	top/cold	43 / 1 .	Tmt	0.16	9.74	11.33	0.29	67.62	3.49	92.62	**2**
1100w-8h	top/cold	44 / 1 .	Tmt	0.15	9.69	11.73	0.21	67.21	3.44	92.44	**2**
1100w-8h	centre	36 / 1 .	Tmt	0.14	10.13	10.69	0.19	67.45	3.58	92.19	**2**
1100w-8h	centre	37 / 1 .	Tmt	0.14	10.42	10.70	0.22	67.83	3.43	92.73	**2**
1100w-8h	centre	38 / 1 .	Tmt	0.12	9.64	11.28	0.17	67.59	3.77	92.58	**2**
1100w-8h	bottom/hot	15 / 1 .	Tmt	0.17	11.06	9.93	0.43	67.56	2.84	91.99	**2**
1100w-8h	bottom/hot	16 / 1 .	Tmt	0.16	10.76	12.16	0.23	65.36	3.87	92.55	**2**
1100w-8h	bottom/hot	17 / 1 .	Tmt	0.29	9.93	11.87	0.26	66.47	3.75	92.57	**2**
1100w-8h	bottom/hot	18 / 1 .	Tmt	0.20	9.41	12.42	0.30	66.62	3.65	92.60	**2**
1100w-8h	bottom/hot	19 / 1 .	Tmt	0.16	11.28	10.46	0.34	67.70	2.71	92.64	**2**
1100w-8h	bottom/hot	20 / 1 .	Tmt	0.13	11.34	9.80	0.31	68.32	2.75	92.64	**2**
1100w-8h	bottom/hot	63 / 1 .	Tmt	0.16	10.79	9.98	0.11	68.87	3.13	93.04	**1**
1100w-8h	bottom/hot	64 / 1 .	Tmt	0.15	10.51	11.00	0.17	67.17	3.55	92.55	**1**

Sample name	Region in the sample	Point	Phase	Si	Ti	Al	Fe3+	Fe2+	Mg	Populations
1100w-30min	cold/top	35 / 1 .	Tmt	0.049	0.088	0.346	1.381	0.707	0.428	**unclassified**
1100w-30min	cold/top	36 / 1 .	Tmt	0.031	0.088	0.347	1.416	0.692	0.424	**unclassified**
1100w-30min	cold/top	37 / 1 .	Tmt	0.011	0.091	0.346	1.451	0.678	0.421	**unclassified**
1100w-30min	centre	52 / 1 .	Tmt	0.009	0.114	0.405	1.351	0.557	0.563	1
1100w-30min	centre	53 / 1 .	Tmt	0.007	0.106	0.443	1.331	0.537	0.575	2
1100w-30min	centre	54 / 1 .	Tmt	0.007	0.108	0.459	1.31	0.527	0.587	1
1100w-30min	bottom/hot	49 / 1 .	Tmt	0.005	0.09	0.367	1.443	0.557	0.537	2
1100w-30min	bottom/hot	50 / 1 .	Tmt	0.005	0.087	0.385	1.432	0.539	0.551	2
1100w-30min	bottom/hot	51 / 1 .	Tmt	0.005	0.091	0.401	1.409	0.542	0.551	2

Sample name	Region in the sample	Point	Phase	Si	Ti	Al	Fe3+	Fe2+	Mg	Populations
1100w-8h	top/cold	39 / 1 .	Tmt	0.003	0.088	0.456	1.362	0.585	0.5	2
1100w-8h	top/cold	40 / 1 .	Tmt	0.008	0.076	0.472	1.359	0.632	0.437	2
1100w-8h	top/cold	41 / 1 .	Tmt	0.005	0.087	0.456	1.359	0.595	0.49	2
1100w-8h	top/cold	42 / 1 .	Tmt	0.005	0.09	0.472	1.337	0.606	0.482	1
1100w-8h	top/cold	43 / 1 .	Tmt	0.005	0.09	0.457	1.352	0.585	0.498	2
1100w-8h	top/cold	44 / 1 .	Tmt	0.005	0.089	0.474	1.338	0.588	0.495	2
1100w-8h	centre	36 / 1 .	Tmt	0.005	0.093	0.433	1.372	0.568	0.519	2
1100w-8h	centre	37 / 1 .	Tmt	0.005	0.088	0.43	1.384	0.552	0.53	2
1100w-8h	centre	38 / 1 .	Tmt	0.004	0.097	0.457	1.34	0.6	0.493	2
1100w-8h	bottom/hot	15 / 1 .	Tmt	0.006	0.073	0.401	1.441	0.495	0.565	2
1100w-8h	bottom/hot	16 / 1 .	Tmt	0.006	0.099	0.487	1.305	0.55	0.544	2
1100w-8h	bottom/hot	17 / 1 .	Tmt	0.01	0.096	0.478	1.31	0.588	0.505	2
1100w-8h	bottom/hot	18 / 1 .	Tmt	0.007	0.094	0.5	1.298	0.607	0.48	2
1100w-8h	bottom/hot	19 / 1 .	Tmt	0.005	0.069	0.418	1.433	0.489	0.571	2
1100w-8h	bottom/hot	20 / 1 .	Tmt	0.004	0.07	0.393	1.458	0.486	0.575	2
1100w-8h	bottom/hot	63 / 1 .	Tmt	0.005	0.08	0.4	1.429	0.532	0.548	1
1100w-8h	bottom/hot	64 / 1 .	Tmt	0.005	0.091	0.443	1.365	0.553	0.535	1

Sample name	Region in the sample	Point	Phase	Spinel	Ercinite	Mg-Ferrite	Magnetite	Qandilite	Ulvospinel	Populations
1100w-30min	cold/top	35 / 1 .	Tmt	0.573	0.948	2.291	3.789	0.146	0.241	**unclassified**
1100w-30min	cold/top	36 / 1 .	Tmt	0.568	0.927	2.321	3.787	0.144	0.235	**unclassified**
1100w-30min	cold/top	37 / 1 .	Tmt	0.560	0.902	2.349	3.787	0.146	0.236	**unclassified**
1100w-30min	centre	52 / 1 .	Tmt	0.869	0.859	2.903	2.868	0.244	0.241	**1**
1100w-30min	centre	53 / 1 .	Tmt	0.973	0.908	2.928	2.732	0.232	0.217	**2**
1100w-30min	centre	54 / 1 .	Tmt	1.030	0.926	2.939	2.641	0.242	0.217	**1**
1100w-30min	bottom/hot	49 / 1 .	Tmt	0.757	0.785	2.979	3.089	0.186	0.193	**2**
1100w-30min	bottom/hot	50 / 1 .	Tmt	0.817	0.799	3.037	2.970	0.184	0.180	**2**
1100w-30min	bottom/hot	51 / 1 .	Tmt	0.849	0.835	2.985	2.937	0.192	0.189	**2**

Sample name	Region in the sample	Point	Phase	Spinel	Ercinite	Mg-Ferrite	Magnetite	Qandilite	Ulvospinel	Populations
1100w-8h	top/cold	39 / 1 .	Tmt	0.881	1.031	2.629	3.078	0.170	0.199	**2**
1100w-8h	top/cold	40 / 1 .	Tmt	0.807	1.167	2.322	3.359	0.130	0.188	**2**
1100w-8h	top/cold	41 / 1 .	Tmt	0.864	1.050	2.575	3.126	0.165	0.200	**2**
1100w-8h	top/cold	42 / 1 .	Tmt	0.878	1.104	2.487	3.129	0.168	0.212	**1**
1100w-8h	top/cold	43 / 1 .	Tmt	0.884	1.039	2.613	3.072	0.174	0.204	**2**
1100w-8h	top/cold	44 / 1 .	Tmt	0.910	1.081	2.568	3.051	0.170	0.202	**2**
1100w-8h	centre	36 / 1 .	Tmt	0.870	0.952	2.755	3.015	0.186	0.203	**2**
1100w-8h	centre	37 / 1 .	Tmt	0.885	0.922	2.845	2.964	0.181	0.189	**2**
1100w-8h	centre	38 / 1 .	Tmt	0.869	1.057	2.550	3.102	0.185	0.225	**2**
1100w-8h	bottom/hot	15 / 1 .	Tmt	0.891	0.780	3.201	2.804	0.162	0.142	**2**
1100w-8h	bottom/hot	16 / 1 .	Tmt	1.023	1.034	2.743	2.774	0.208	0.210	**2**
1100w-8h	bottom/hot	17 / 1 .	Tmt	0.935	1.088	2.564	2.983	0.188	0.219	**2**
1100w-8h	bottom/hot	18 / 1 .	Tmt	0.931	1.179	2.416	3.059	0.175	0.221	**2**
1100w-8h	bottom/hot	19 / 1 .	Tmt	0.937	0.803	3.210	2.751	0.155	0.133	**2**
1100w-8h	bottom/hot	20 / 1 .	Tmt	0.885	0.748	3.283	2.776	0.158	0.134	**2**
1100w-8h	bottom/hot	63 / 1 .	Tmt	0.849	0.825	3.032	2.945	0.170	0.165	**1**
1100w-8h	bottom/hot	64 / 1 .	Tmt	0.916	0.947	2.822	2.919	0.189	0.195	**1**

Sample name	Region in the sample	Spinel mol %	Ercinite mol%	Mg-Ferrite mol%	Magnetite mol%	Qandilite mol%	Ulvospinel mol%	Ulvo-Qandilite-series	Ulvo-Qandilite-series mol%
1100w-30min	cold/top	7.17	11.87	28.68	47.43	1.83	3.02	0.39	4.84
1100w-30min	cold/top	7.12	11.61	29.08	47.44	1.80	2.94	0.38	4.75
1100w-30min	cold/top	7.02	11.30	29.44	47.46	1.83	2.96	0.38	4.79
1100w-30min	centre	10.88	10.76	36.36	35.92	3.06	3.02	0.49	6.07
1100w-30min	centre	12.18	11.36	36.65	34.19	2.90	2.72	0.45	5.62
1100w-30min	centre	12.88	11.58	36.76	33.03	3.03	2.71	0.46	5.74
1100w-30min	bottom/hot	9.48	9.83	37.29	38.67	2.33	2.42	0.38	4.74
1100w-30min	bottom/hot	10.23	10.00	38.02	37.19	2.30	2.25	0.36	4.56
1100w-30min	bottom/hot	10.63	10.45	37.37	36.77	2.40	2.37	0.38	4.77

Sample name	Region in the sample	Spinel mol %	Ercinite mol%	Mg-Ferrite mol%	Magnetite mol%	Qandilite mol%	Ulvospinel mol%	Ulvo-Qandilite-series	Ulvo-Qandilite-series mol%
1100w-8h	top/cold	11.03	12.91	32.91	38.53	2.13	2.49	0.37	4.62
1100w-8h	top/cold	10.12	14.64	29.12	42.13	1.63	2.36	0.32	3.99
1100w-8h	top/cold	10.83	13.16	32.27	39.17	2.07	2.51	0.37	4.57
1100w-8h	top/cold	11.01	13.84	31.17	39.22	2.11	2.66	0.38	4.76
1100w-8h	top/cold	11.07	13.01	32.72	38.47	2.18	2.55	0.38	4.73
1100w-8h	top/cold	11.40	13.54	32.17	38.22	2.13	2.53	0.37	4.66
1100w-8h	centre	10.90	11.93	34.52	37.78	2.33	2.54	0.39	4.87
1100w-8h	centre	11.08	11.55	35.62	37.11	2.27	2.37	0.37	4.63
1100w-8h	centre	10.88	13.23	31.92	38.83	2.32	2.82	0.41	5.13
1100w-8h	bottom/hot	11.17	9.77	40.11	35.14	2.03	1.78	0.30	3.81
1100w-8h	bottom/hot	12.80	12.94	34.32	34.71	2.60	2.63	0.42	5.23
1100w-8h	bottom/hot	11.72	13.64	32.14	37.40	2.36	2.75	0.41	5.10
1100w-8h	bottom/hot	11.67	14.77	30.27	38.33	2.19	2.77	0.40	4.96
1100w-8h	bottom/hot	11.73	10.05	40.18	34.43	1.94	1.66	0.29	3.60
1100w-8h	bottom/hot	11.08	9.37	41.12	34.77	1.98	1.68	0.29	3.66
1100w-8h	bottom/hot	10.63	10.33	37.97	36.88	2.13	2.07	0.34	4.19
1100w-8h	bottom/hot	11.47	11.86	35.33	36.54	2.37	2.44	0.38	4.81

Sheet "EBSD_parameters_legenda" of Peres et al., (2024) suplementary material 2

EBSD parameters Legenda

CORs	Crystallographic Orientation Relationships	Parameters formulas	Parameters Formulas
N_MtGrains	Number of Tmt	1	EBSD result
Nunique_MtGrains_incontact	Number of Tmt in contact with a Cpx	2	EBSD result
Nunique_MtGrains_anyOR	Number of Tmt in contact with a Cpx and showing any COR	3	EBSD result
Nunique_MtGrains_OR1and2	Number of Tmt in contact with a Cpx and shearing specific COR 1 or 2	4	EBSD result
Nunique_MtGrains_id3	Number of Tmt in contact with a Cpx and shearing a COR near 1 and/or 2	5	EBSD result
Nunique_MtGrains_OR1	Number of Tmt in contact with a Cpx and shearing specific COR 1	6	EBSD result
Nunique_MtGrains_OR2	Number of Tmt in contact with a Cpx and shearing specific COR 2	7	EBSD result
frac_mt_incontact	Fraction of Tmt in contact to Cpx compared to the total of Tmt crystals	8	2/1
frac_incontact_mt_anyOR	Fraction of Tmt in contact to Cpx compared to the total of Tmt crystals shearing any COR with the Cpx in contact	9	3/2
frac_incontact_mt_OR1	Fraction of Tmt in contact to Cpx compared to the total of Tmt crystals shearing COR 1 with the Cpx in contact	10	6/3
frac_incontact_mt_OR2	Fraction of Tmt in contact to Cpx compared to the total of Tmt crystals shearing COR 2 with the Cpx in contact	11	7/3
GBLength_Di_Mt [µm]	Total grain boundary lenght shared between Cpx and Tmt	12	EBSD result
GBLength_Mt [µm]	Total Tmt grain boundary lenght	13	EBSD result
GBLength_Di [µm]	Total Cpx grain boundary lenght	14	EBSD result
GBLength_OR1 [µm]	Total grain boundary lenght shared between Cpx and Tmt characterized by COR1	15	EBSD result
GBLength_OR2 [µm]	Total grain boundary lenght shared between Cpx and Tmt characterized by COR2	16	EBSD result
GBLength_id3 [µm]	Total grain boundary lenght shared between Cpx and Tmt characterized by an COR near 1 and/or 2	17	EBSD result
GBLength_anyOR [µm]	Total grain boundary lenght shared between Cpx and Tmt characterized by any CORs	18	EBSD result
Lfrac_mt_incontact	Boundary lenght fraction of Tmt in contact with a Cpx	19	12/13
Lfrac_di_incontact	Boundary lenght fraction of Cpx in contact with a Tmt	20	12/14
BLF_{anyCOR}	Grain Boundary lenght fraction shared between Tmt and Cpx and characterized by any COR	21	18/12
BLF_{COR1}	Grain Boundary lenght fraction shared between Tmt and Cpx and characterized by COR1	22	15/12
BLF_{COR2}	Grain Boundary lenght fraction shared between Tmt and Cpx and characterized by COR2	23	16/12
$BLF_{nearCOR}$	Grain Boundary lenght fraction shared between Tmt and Cpx and characterized a COR near COR1 and/or 2	24	17/12
BLF_{noCORs}	Grain Boundary lenght fraction shared between Tmt and Cpx and characterized by no COR	25	(12-18)/12
BLF_{tot}	Total of Grain Boundary lenght fraction shared between Tmt and Cpx	26	22+23+24+25

Sheet "Raw_CORs" of Peres et al., (2024) suplementary material 2
Raw results of all the EBSD maps acquired in samples 1100w-30min and 1100w-8h

Area EBSD Map um^2	116620	252000	252000	235000	1419	181.25	563.75	600.25
Position in sample	**Bottom/Hot**	**Centre**		**Top/cold**	**Bottom/Hot**			
1100w-30min	scan 01	scan 02	scan 03	scan 04	scan 05	scan 06	scan 07	scan 08
N_MtGrains	85	395	452	900	2	1	4	6
Nunique_MtGrains_incontact	73	312	365	468	2	1	4	2
Nunique_MtGrains_anyOR	71	274	329	388	2	1	4	2
Nunique_MtGrains_OR1and2	69	255	308	332	2	1	3	2
Nunique_MtGrains_id3	27	155	185	203	2	1	1	1
Nunique_MtGrains_OR1	8	136	154	176	1	0	0	1
Nunique_MtGrains_OR2	63	162	200	186	2	1	3	2
frac_mt_incontact	0.859	0.790	0.808	0.520	1.000	1.000	1.000	0.333
frac_incontact_mt_anyOR	0.973	0.878	0.901	0.829	1.000	1.000	1.000	1.000
frac_incontact_mt_OR1	0.110	0.436	0.422	0.376	0.500	0.000	0.000	0.500
frac_incontact_mt_OR2	0.863	0.519	0.548	0.397	1.000	1.000	0.750	1.000
GBLength_Di_Mt	1565.381	2251.291	2677.649	1797.362	140.812	9.631	29.821	10.101
GBLength_Mt	3213.076	7572.856	8486.440	11081.859	234.667	41.441	63.599	157.556
GBLength_Di	8376.222	27132.806	27672.567	33386.892	259.612	41.896	181.125	30.005
GBLength_OR1	57.302	612.967	738.341	481.461	1.364	0.000	0.000	0.196
GBLength_OR2	1409.012	880.730	1071.276	612.059	10.064	9.254	29.613	2.667
GBLength_id3	92.265	489.334	601.990	429.310	66.873	0.378	0.208	0.404
GBLength_anyOR	1558.580	1983.032	2411.606	1522.830	78.302	9.631	29.821	3.267
BLF_{anyCOR}	**0.996**	**0.881**	**0.901**	**0.847**	**0.556**	**1.000**	**1.000**	**0.323**
BLF_{COR1}	**0.037**	**0.272**	**0.276**	**0.268**	**0.010**	**0.000**	**0.000**	**0.019**
BLF_{COR2}	**0.900**	**0.391**	**0.400**	**0.341**	**0.071**	**0.961**	**0.993**	**0.264**
$BLF_{nearCOR}$	**0.059**	**0.217**	**0.225**	**0.239**	**0.475**	**0.039**	**0.007**	**0.040**
BLF_{noCORs}	**0.004**	**0.119**	**0.099**	**0.153**	**0.444**	**0.000**	**0.000**	**0.677**

Area EBSD Map um^2	187	462	930	14107.5	1193.5	1326	232	130910	
				Bottom/Hot				**Centre**	
1100w-30min	scan09	scan10	scan11	scan12	scan13	scan14	scan15	scan16	**sum**
N_MtGrains	1	3	5	31	4	1	1	199	**2090**
Nunique_MtGrains_incontact	1	2	5	26	4	1	1	147	**1414**
Nunique_MtGrains_anyOR	1	2	5	24	4	1	1	144	**1253**
Nunique_MtGrains_OR1and2	1	2	5	24	4	1	1	142	**1152**
Nunique_MtGrains_id3	1	2	3	12	3	1	1	61	**659**
Nunique_MtGrains_OR1	0	2	0	8	0	1	0	47	**534**
Nunique_MtGrains_OR2	1	2	5	21	4	1	1	113	**767**
frac_mt_incontact	1.000	0.667	1.000	0.839	1.000	1.000	1.000	0.739	**0.677**
frac_incontact_mt_anyOR	1.000	1.000	1.000	0.923	1.000	1.000	1.000	0.980	**0.886**
frac_incontact_mt_OR1	0.000	1.000	0.000	0.308	0.000	1.000	0.000	0.320	**0.378**
frac_incontact_mt_OR2	1.000	1.000	1.000	0.808	1.000	1.000	1.000	0.769	**0.542**
GBLength_Di_Mt	26.421	57.743	76.262	244.897	131.042	119.845	31.301	1172.728	**10342.288**
GBLength_Mt	63.051	146.210	123.627	574.672	294.061	202.092	63.943	4224.614	**36543.765**
GBLength_Di	54.588	119.763	268.295	1492.353	225.945	259.365	64.175	15221.757	**114787.367**
GBLength_OR1	0.000	35.095	0.000	43.411	0.000	0.815	0.000	139.669	**2110.621**
GBLength_OR2	10.066	7.089	41.230	160.866	126.134	118.117	30.951	834.322	**5353.450**
GBLength_id3	2.927	8.630	35.033	21.771	4.908	0.913	0.350	191.849	**1947.145**
GBLength_anyOR	12.993	50.814	76.262	226.048	131.042	119.845	31.301	1165.840	**9411.215**
BLF_{anyCOR}	**0.492**	**0.880**	**1.000**	**0.923**	**1.000**	**1.000**	**1.000**	**0.994**	**0.910**
BLF_{COR1}	**0.000**	**0.608**	**0.000**	**0.177**	**0.000**	**0.007**	**0.000**	**0.119**	**0.204**
BLF_{COR2}	**0.381**	**0.123**	**0.541**	**0.657**	**0.963**	**0.986**	**0.989**	**0.711**	**0.518**
$BLF_{nearCOR}$	**0.111**	**0.149**	**0.459**	**0.089**	**0.037**	**0.008**	**0.011**	**0.164**	**0.188**
BLF_{noCORs}	**0.508**	**0.120**	**0.000**	**0.077**	**0.000**	**0.000**	**0.000**	**0.006**	**0.090**

Area EBSD Map um^2	137822.25	634910	235000

Position in sample

1100w-30min	**Bottom/Hot**	**Centre**	**Top/Cool**
N_MtGrains	**144**	**1046**	**900**
Nunique_MtGrains_incontact	**122**	**824**	**468**
Nunique_MtGrains_anyOR	**118**	**747**	**388**
Nunique_MtGrains_OR1and2	**115**	**705**	**332**
Nunique_MtGrains_id3	**55**	**401**	**203**
Nunique_MtGrains_OR1	**21**	**337**	**176**
Nunique_MtGrains_OR2	**106**	**475**	**186**
frac_mt_incontact	**0.847**	**0.788**	**0.520**
frac_incontact_mt_anyOR	**0.967**	**0.907**	**0.829**
frac_incontact_mt_OR1	**0.172**	**0.409**	**0.376**
frac_incontact_mt_OR2	**0.869**	**0.576**	**0.397**
GBLength_Di_Mt	**2443.3**	**6101.7**	**1797.4**
GBLength_Mt	**5178.0**	**20283.9**	**11081.9**
GBLength_Di	**11373.3**	**70027.1**	**33386.9**
GBLength_OR1	**138.2**	**1491.0**	**481.5**
GBLength_OR2	**1955.1**	**2786.3**	**612.1**
GBLength_id3	**234.7**	**1283.2**	**429.3**
GBLength_anyOR	**2327.9**	**5560.5**	**1522.8**
BLF_{anyCOR}	**0.953**	**0.911**	**0.847**
BLF_{COR1}	**0.057**	**0.244**	**0.268**
BLF_{COR2}	**0.800**	**0.457**	**0.341**
$BLF_{nearCOR}$	**0.096**	**0.210**	**0.239**
BLF_{noCORs}	**0.047**	**0.089**	**0.153**

Area EBSD Map um^2	10150	27500	24050	21450	20625	191250
Position in sample		**Bottom/Hot**			**Centre**	
1100w-30min	scan01a	scan01b	scan01c	scan02a	scan02b	scan03
N_MtGrains	14	34	37	27	32	129
Nunique_MtGrains_incontact	13	30	33	24	29	98
Nunique_MtGrains_anyOR	13	30	33	24	29	81
Nunique_MtGrains_OR1and2	13	30	33	24	29	73
Nunique_MtGrains_id3	6	16	11	7	10	47
Nunique_MtGrains_OR1	3	12	7	1	1	45
Nunique_MtGrains_OR2	13	29	32	23	29	44
frac_mt_incontact	0.929	0.882	0.892	0.889	0.906	0.760
frac_incontact_mt_anyOR	1.000	1.000	1.000	1.000	1.000	0.827
frac_incontact_mt_OR1	0.231	0.400	0.212	0.042	0.034	0.459
frac_incontact_mt_OR2	1.000	0.967	0.970	0.958	1.000	0.449
GBLength_Di_Mt	280.5	667.8	724.1	533.0	389.5	1080.0
GBLength_Mt	378.6	1026.9	950.8	784.3	757.6	3592.5
GBLength_Di	1018.7	2466.7	2873.1	1545.1	1930.7	13697.5
GBLength_OR1	0.6	25.0	7.5	2.9	0.6	283.2
GBLength_OR2	269.9	604.4	675.2	509.0	368.7	393.5
GBLength_id3	10.0	35.1	18.0	20.2	19.9	246.5
GBLength_anyOR	280.5	664.5	700.7	532.1	389.2	923.3
BLF_{anyCOR}	**1.000**	**0.995**	**0.968**	**0.998**	**0.999**	**0.855**
BLF_{COR1}	**0.002**	**0.037**	**0.010**	**0.006**	**0.002**	**0.262**
BLF_{COR2}	**0.962**	**0.905**	**0.932**	**0.955**	**0.946**	**0.364**
$BLF_{nearCOR}$	**0.036**	**0.053**	**0.025**	**0.038**	**0.051**	**0.228**
BLF_{noCORs}	**0.000**	**0.005**	**0.032**	**0.002**	**0.001**	**0.145**

Area EBSD Map um^2	1400	2064	2160	1350	1575	13600	20500
Position in sample			Top/cold				
1100w-30min	scan04	scan05	scan06	scan07a	scan07b	scan08a	scan08b
N_MtGrains	1	5	4	6	8	13	31
Nunique_MtGrains_incontact	1	4	3	6	5	13	22
Nunique_MtGrains_anyOR	1	4	3	5	4	12	17
Nunique_MtGrains_OR1and2	1	4	3	4	4	12	17
Nunique_MtGrains_id3	1	3	2	5	3	7	12
Nunique_MtGrains_OR1	1	1	3	2	0	1	7
Nunique_MtGrains_OR2	1	3	1	4	4	11	14
frac_mt_incontact	1.000	0.800	0.750	1.000	0.625	1.000	0.710
frac_incontact_mt_anyOR	1.000	1.000	1.000	0.833	0.800	0.923	0.773
frac_incontact_mt_OR1	1.000	0.250	1.000	0.333	0.000	0.077	0.318
frac_incontact_mt_OR2	1.000	0.750	0.333	0.667	0.800	0.846	0.636
GBLength_Di_Mt	66.8	49.7	78.1	65.4	67.9	138.5	300.7
GBLength_Mt	234.9	188.5	286.0	119.7	194.7	312.4	926.9
GBLength_Di	175.2	248.2	241.1	294.9	273.1	1031.1	1850.0
GBLength_OR1	0.2	8.5	22.6	9.4	0.0	23.5	46.9
GBLength_OR2	45.1	38.9	6.1	37.5	62.3	105.4	156.4
GBLength_id3	21.6	2.2	49.1	15.3	2.7	8.4	36.8
GBLength_anyOR	66.8	49.7	77.8	62.2	64.9	137.3	240.1
BLF_{anyCOR}	**1.000**	**1.000**	**0.996**	**0.952**	**0.956**	**0.991**	**0.799**
BLF_{COR1}	**0.003**	**0.172**	**0.289**	**0.144**	**0.000**	**0.169**	**0.156**
BLF_{COR2}	**0.674**	**0.784**	**0.078**	**0.573**	**0.916**	**0.761**	**0.520**
$BLF_{nearCOR}$	**0.323**	**0.044**	**0.628**	**0.234**	**0.039**	**0.061**	**0.122**
BLF_{noCORs}	**0.000**	**0.000**	**0.004**	**0.048**	**0.044**	**0.009**	**0.201**

Area EBSD Map um^2	95875	101250	1530	832	874	1872	13775
Position in sample	Centre		Bottom/Hot				
1100w-30min	scan09a	scan09b	scan10	scan11	scan12	scan13	scan14
N_MtGrains	58	92	5	3	2	2	11
Nunique_MtGrains_incontact	56	71	4	1	2	2	9
Nunique_MtGrains_anyOR	51	60	2	1	2	1	6
Nunique_MtGrains_OR1and2	50	56	2	0	2	1	5
Nunique_MtGrains_id3	24	28	1	1	2	1	6
Nunique_MtGrains_OR1	5	8	1	0	2	0	0
Nunique_MtGrains_OR2	47	51	1	0	2	1	5
frac_mt_incontact	0.966	0.772	0.800	0.333	1.000	1.000	0.818
frac_incontact_mt_anyOR	0.911	0.845	0.500	1.000	1.000	0.500	0.667
frac_incontact_mt_OR1	0.089	0.113	0.250	0.000	1.000	0.000	0.000
frac_incontact_mt_OR2	0.839	0.718	0.250	0.000	1.000	0.500	0.556
GBLength_Di_Mt	1183.2	905.9	54.7	18.5	64.6	96.3	259.5
GBLength_Mt	2442.1	2590.0	272.2	117.0	148.7	188.7	717.1
GBLength_Di	6210.8	6689.3	169.2	89.4	133.0	212.9	1049.0
GBLength_OR1	25.6	33.9	0.5	0.0	3.2	0.0	0.0
GBLength_OR2	962.0	646.2	7.8	0.0	11.1	3.5	67.0
GBLength_id3	88.7	121.4	22.6	0.9	50.3	49.6	46.2
GBLength_anyOR	1076.3	801.4	30.9	0.9	64.6	53.1	113.2
BLF_{anyCOR}	**0.910**	**0.885**	**0.564**	**0.047**	**1.000**	**0.552**	**0.436**
BLF_{COR1}	**0.022**	**0.037**	**0.008**	**0.000**	**0.049**	**0.000**	**0.000**
BLF_{COR2}	**0.813**	**0.713**	**0.142**	**0.000**	**0.172**	**0.036**	**0.258**
$BLF_{nearCOR}$	**0.075**	**0.134**	**0.414**	**0.047**	**0.779**	**0.516**	**0.178**
BLF_{noCORs}	**0.090**	**0.115**	**0.436**	**0.953**	**0.000**	**0.448**	**0.564**

Area EBSD Map um^2	5320	20604		106507	430450	42649

Position in sample

1100w-30min	scan15	scan16	**sum**	**Bottom/Hot**	**Centre**	**Top/Cool**
N_MtGrains	18	22	**554**	**148**	**338**	**68**
Nunique_MtGrains_incontact	17	21	**464**	**132**	**278**	**54**
Nunique_MtGrains_anyOR	17	20	**416**	**125**	**245**	**46**
Nunique_MtGrains_OR1and2	16	19	**398**	**121**	**232**	**45**
Nunique_MtGrains_id3	12	7	**212**	**63**	**116**	**33**
Nunique_MtGrains_OR1	0	1	**101**	**26**	**60**	**15**
Nunique_MtGrains_OR2	16	19	**350**	**118**	**194**	**38**
frac_mt_incontact	0.944	0.955	**0.838**	**0.892**	**0.822**	**0.794**
frac_incontact_mt_anyOR	1.000	0.952	**0.897**	**0.947**	**0.881**	**0.852**
frac_incontact_mt_OR1	0.000	0.048	**0.218**	**0.197**	**0.216**	**0.278**
frac_incontact_mt_OR2	0.941	0.905	**0.754**	**0.894**	**0.698**	**0.704**
GBLength_Di_Mt	473.3	566.3	**8064.3**	**3205.5**	**4091.6**	**767.1**
GBLength_Mt	570.3	838.4	**17638.4**	**5208.8**	**10166.5**	**2263.1**
GBLength_Di	912.8	1727.3	**44839.2**	**10652.2**	**30073.4**	**4113.6**
GBLength_OR1	0.0	0.4	**494.6**	**37.2**	**346.3**	**111.1**
GBLength_OR2	306.5	534.7	**5810.9**	**2479.9**	**2879.3**	**451.7**
GBLength_id3	166.8	10.2	**1042.6**	**409.8**	**496.7**	**136.0**
GBLength_anyOR	473.3	545.3	**7348.1**	**2926.9**	**3722.3**	**698.8**
BLF_{anyCOR}	**1.000**	**0.963**	**0.911**	**0.913**	**0.910**	**0.911**
BLF_{COR1}	**0.000**	**0.001**	**0.061**	**0.012**	**0.085**	**0.145**
BLF_{COR2}	**0.647**	**0.944**	**0.721**	**0.774**	**0.704**	**0.589**
$BLF_{nearCOR}$	**0.353**	**0.018**	**0.129**	**0.128**	**0.121**	**0.177**
BLF_{noCORs}	**0.000**	**0.037**	**0.089**	**0.087**	**0.090**	**0.089**

Sheet "CORs_for_Tmt_Pop" of Peres et al., (2024) suplementary material 2

EBSD results sorted by Tmt populations in samples 1100w-30min and 1100w-8h

Tmt population 1 CORs statistics

1100w-30min	scan05	scan06	scan08	scan09	scan10	scan13	scan14	Tot-pop1
N_MtGrains	2	1	6	1	2	4	1	17
Nunique_MtGrains_incontact	**2**	**1**	**1**	**1**	**2**	**4**	**1**	**12**
Nunique_MtGrains_anyOR	2	1	1	1	2	4	1	12
Nunique_MtGrains_OR1and2	2	1	1	1	2	4	1	12
Nunique_MtGrains_id3	2	1	0	1	2	2	0	8
Nunique_MtGrains_OR1	2	0	1	0	1	0	1	5
Nunique_MtGrains_OR2	2	1	1	1	2	4	1	12
frac_mt_incontact	1	1	0.17	1	1	1	1	1
frac_incontact_mt_anyOR	1	1	1	1	1	1	1	1.00
frac_incontact_mt_OR1	1	0	1	0	0.5	0	1	0.42
frac_incontact_mt_OR2	1	1	1	1	1	1	1	1.00
GBLength_Di_Mt	140.456	9.117	8.194	25.529	49.720	124.683	118.771	476.469
GBLength_Mt	234.462	41.811	157.911	63.501	145.992	294.821	202.473	1140.970
GBLength_Di	259.407	42.272	30.004	54.956	120.307	226.314	259.746	993.006
GBLength_OR1	3.439	0.000	0.231	0.000	34.960	0.000	0.425	39.055
GBLength_OR2	6.268	8.687	1.129	9.228	4.901	120.334	118.346	268.892
GBLength_id3	69.242	0.430	0.000	4.593	4.494	4.350	0.000	83.109
GBLength_anyOR	78.949	9.117	1.360	13.821	44.354	124.683	118.771	391.056
Lfrac_mt_incontact	0.599	0.218	0.052	0.402	0.341	0.423	0.587	0.418
Lfrac_di_incontact	0.541	0.216	0.273	0.465	0.413	0.551	0.457	0.480
BLF_{anyCOR}	**0.562**	**1.000**	**0.166**	**0.541**	**0.892**	**1.000**	**1.000**	**0.821**
BLF_{COR1}	**0.024**	**0.000**	**0.028**	**0.000**	**0.703**	**0.000**	**0.004**	**0.082**
BLF_{COR2}	**0.045**	**0.953**	**0.138**	**0.361**	**0.099**	**0.965**	**0.996**	**0.564**
$BLF_{nearCOR}$	**0.493**	**0.047**	**0.000**	**0.180**	**0.090**	**0.035**	**0.000**	**0.174**
BLF_{noCORs}	**0.438**	**0.000**	**0.834**	**0.459**	**0.108**	**0.000**	**0.000**	**0.179**
BLF_{tot}	1.000	1.000	1.000	1.000	1.000	1.000	1.000	1.000

Tmt population 1 CORs statistics

1100w-8h	scan04	scan06	scan10	scan11	scan12	scan13	scan14	Tot-pop1
N_MtGrains	1	4	5	3	2	2	11	28
Nunique_MtGrains_incontact	**1**	**3**	**4**	**1**	**2**	**2**	**9**	**22**
Nunique_MtGrains_anyOR	1	3	2	1	2	1	6	16
Nunique_MtGrains_OR1and2	1	3	2	0	2	1	5	14
Nunique_MtGrains_id3	1	2	1	1	2	1	4	12
Nunique_MtGrains_OR1	1	3	1	0	2	0	0	7
Nunique_MtGrains_OR2	1	1	1	0	2	1	5	11
frac_mt_incontact	1.000	0.750	0.800	0.333	1.000	1.000	0.818	0.786
frac_incontact_mt_anyOR	1.000	1.000	0.500	1.000	1.000	0.500	0.667	0.727
frac_incontact_mt_OR1	1.000	1.000	0.250	0.000	1.000	0.000	0.000	0.318
frac_incontact_mt_OR2	1.000	0.333	0.250	0.000	1.000	0.500	0.556	0.500
GBLength_Di_Mt	62.242	76.825	54.914	18.444	64.397	97.866	251.164	625.852
GBLength_Mt	235.549	286.763	272.218	117.152	149.418	189.832	718.104	1969.036
GBLength_Di	175.828	241.769	169.289	89.471	133.346	214.410	1050.049	2074.161
GBLength_OR1	0.698	29.062	0.459	0.000	6.534	0.000	0.000	36.754
GBLength_OR2	34.623	6.772	7.755	0.000	9.383	1.158	85.248	144.938
GBLength_id3	26.922	40.991	22.639	1.530	48.480	65.101	26.198	231.861
GBLength_anyOR	62.242	76.825	30.853	1.530	64.397	66.259	111.446	413.553
Lfrac_mt_incontact	0.264	0.268	0.202	0.157	0.431	0.516	0.350	0.318
Lfrac_di_incontact	0.354	0.318	0.324	0.206	0.483	0.456	0.239	0.302
BLF_{anyCOR}	1.000	1.000	0.562	0.083	1.000	0.677	0.444	0.661
BLF_{COR1}	**0.011**	**0.378**	**0.008**	**0.000**	**0.101**	**0.000**	**0.000**	**0.059**
BLF_{COR2}	**0.556**	**0.088**	**0.141**	**0.000**	**0.146**	**0.012**	**0.339**	**0.232**
$BLF_{nearCOR}$	**0.433**	**0.534**	**0.412**	**0.083**	**0.753**	**0.665**	**0.104**	**0.370**
BLF_{noCORs}	**0.000**	**0.000**	**0.438**	**0.917**	**0.000**	**0.323**	**0.556**	**0.339**
BLF_{tot}	1.000	1.000	1.000	1.000	1.000	1.000	1.000	1.000

Tmt population 2 CORs statistics

1100w-30min	scan01	scan02	scan03	scan04	scan07
N_MtGrains	65	395	452	900	4
Nunique_MtGrains_incontact	**65**	**312**	**359**	**455**	**3**
Nunique_MtGrains_anyOR	64	273	325	380	3
Nunique_MtGrains_OR1and2	63	249	299	324	3
Nunique_MtGrains_id3	20	142	177	175	0
Nunique_MtGrains_OR1	8	134	156	181	0
Nunique_MtGrains_OR2	56	147	175	169	3
frac_mt_incontact	1.00	0.79	0.79	0.51	0.75
frac_incontact_mt_anyOR	0.98	0.88	0.91	0.84	1.00
frac_incontact_mt_OR1	0.12	0.43	0.43	0.40	0.00
frac_incontact_mt_OR2	0.86	0.47	0.49	0.37	1.00
GBLength_Di_Mt	1224.78	2072.40	2471.94	1635.35	29.25
GBLength_Mt	2760.11	7577.36	8492.89	11088.15	63.94
GBLength_Di	8378.43	27137.10	27678.96	33400.52	181.74
GBLength_OR1	38.82	616.82	756.53	484.28	0.00
GBLength_OR2	1121.63	794.83	949.10	541.70	29.25
GBLength_id3	63.34	421.12	520.32	370.83	0.00
GBLength_anyOR	1223.80	1832.77	2225.95	1396.81	29.25
Lfrac_mt_incontact	0.44	0.27	0.29	0.15	0.46
Lfrac_di_incontact	0.15	0.08	0.09	0.05	0.16
BLF_{anyCOR}	**0.999**	**0.884**	**0.900**	**0.854**	**1.000**
BLF_{COR1}	**0.032**	**0.298**	**0.306**	**0.296**	**0.000**
BLF_{COR2}	**0.916**	**0.384**	**0.384**	**0.331**	**1.000**
$BLF_{nearCOR}$	**0.052**	**0.203**	**0.210**	**0.227**	**0.000**
BLF_{noCORs}	**0.001**	**0.116**	**0.100**	**0.146**	**0.000**
BLF_{tot}	1.00	1.00	1.00	1.00	1.00

Tmt population 2 CORs statistics

1100w-8h	scan01a	scan01b	scan01c	scan02a	scan02b
N_MtGrains	9	13	17	8	22
Nunique_MtGrains_incontact	**9**	**13**	**17**	**8**	**22**
Nunique_MtGrains_anyOR	9	13	17	8	22
Nunique_MtGrains_OR1and2	9	13	17	8	22
Nunique_MtGrains_id3	2	5	5	2	8
Nunique_MtGrains_OR1	0	1	1	0	0
Nunique_MtGrains_OR2	9	13	17	8	22
frac_mt_incontact	1.000	1.000	1.000	1.000	1.000
frac_incontact_mt_anyOR	1.000	1.000	1.000	1.000	1.000
frac_incontact_mt_OR1	0.000	0.077	0.059	0.000	0.000
frac_incontact_mt_OR2	1.000	1.000	1.000	1.000	1.000
GBLength_Di_Mt	135.969	141.347	255.953	103.371	255.811
GBLength_Mt	212.308	310.872	396.834	222.510	517.378
GBLength_Di	1018.352	2327.783	2874.096	1545.735	1931.372
GBLength_OR1	0.000	7.299	2.059	0.000	0.000
GBLength_OR2	131.020	126.118	234.219	102.426	247.157
GBLength_id3	4.949	7.929	9.404	0.945	8.331
GBLength_anyOR	135.969	141.347	245.683	103.371	255.488
Lfrac_mt_incontact	0.640	0.455	0.645	0.465	0.494
Lfrac_di_incontact	0.134	0.061	0.089	0.067	0.132
BLF_{anyCOR}	**1.000**	**1.000**	**0.960**	**1.000**	**0.999**
BLF_{COR1}	**0.000**	**0.052**	**0.008**	**0.000**	**0.000**
BLF_{COR2}	**0.964**	**0.892**	**0.915**	**0.991**	**0.966**
$BLF_{nearCOR}$	**0.036**	**0.056**	**0.037**	**0.009**	**0.033**
BLF_{noCORs}	**0.000**	**0.000**	**0.040**	**0.000**	**0.001**
BLF_{tot}	1.000	1.000	1.000	1.000	1.000

	Tmt population 2 CORs statistics				
1100w-30min	**scan11**	**scan12**	**scan15**	**scan16**	**Tot-pop2**
N_MtGrains	5	31	1	199	2052
Nunique_MtGrains_incontact	**5**	**26**	**1**	**145**	**1371**
Nunique_MtGrains_anyOR	5	24	1	142	1217
Nunique_MtGrains_OR1and2	5	24	1	139	1107
Nunique_MtGrains_id3	3	10	1	56	584
Nunique_MtGrains_OR1	0	10	0	45	534
Nunique_MtGrains_OR2	5	21	1	109	686
frac_mt_incontact	1.00	0.84	1.00	0.73	66.81
frac_incontact_mt_anyOR	1.00	0.92	1.00	0.98	0.89
frac_incontact_mt_OR1	0.00	0.38	0.00	0.31	0.39
frac_incontact_mt_OR2	1.00	0.81	1.00	0.75	0.50
GBLength_Di_Mt	75.31	238.61	30.83	1121.41	8899.88
GBLength_Mt	123.79	575.38	63.96	4226.28	34971.86
GBLength_Di	268.46	1494.07	64.17	15228.72	113832.18
GBLength_OR1	0.00	46.89	0.00	144.17	2087.50
GBLength_OR2	40.00	150.76	30.65	786.55	4444.48
GBLength_id3	35.31	22.96	0.17	184.71	1618.76
GBLength_anyOR	75.31	220.61	30.83	1115.43	8150.74
Lfrac_mt_incontact	0.61	0.41	0.48	0.27	0.25
Lfrac_di_incontact	0.28	0.16	0.48	0.07	0.08
BLF_{anyCOR}	**1.000**	**0.925**	**1.000**	**0.995**	**0.916**
BLF_{COR1}	**0.000**	**0.197**	**0.000**	**0.129**	**0.235**
BLF_{COR2}	**0.531**	**0.632**	**0.994**	**0.701**	**0.499**
$BLF_{nearCOR}$	**0.469**	**0.096**	**0.006**	**0.165**	**0.182**
BLF_{noCORs}	**0.000**	**0.075**	**0.000**	**0.005**	**0.084**
BLF_{tot}	1.00	1.00	1.00	1.00	1.00

	Tmt population 2 CORs statistics				
1100w-8h	**scan03**	**scan05**	**scan07a**	**scan07b**	**scan08a**
N_MtGrains	129	5	6	8	7
Nunique_MtGrains_incontact	**97**	**4**	**5**	**5**	**7**
Nunique_MtGrains_anyOR	82	4	4	4	7
Nunique_MtGrains_OR1and2	73	4	2	4	6
Nunique_MtGrains_id3	44	2	4	2	5
Nunique_MtGrains_OR1	44	1	1	0	1
Nunique_MtGrains_OR2	42	3	2	4	5
frac_mt_incontact	0.752	0.800	0.833	0.625	1.000
frac_incontact_mt_anyOR	0.845	1.000	0.800	0.800	1.000
frac_incontact_mt_OR1	0.454	0.250	0.200	0.000	0.143
frac_incontact_mt_OR2	0.433	0.750	0.400	0.800	0.714
GBLength_Di_Mt	1030.375	49.078	62.617	66.294	96.162
GBLength_Mt	3596.393	188.588	119.890	195.039	238.299
GBLength_Di	13701.956	248.333	295.190	273.323	1031.317
GBLength_OR1	289.684	8.507	10.691	0.000	21.149
GBLength_OR2	365.572	38.278	33.628	62.345	72.015
GBLength_id3	230.995	2.292	15.535	1.024	2.998
GBLength_anyOR	886.251	49.078	59.853	63.369	96.162
Lfrac_mt_incontact	0.287	0.260	0.522	0.340	0.404
Lfrac_di_incontact	0.075	0.198	0.212	0.243	0.093
BLF_{anyCOR}	**0.860**	**1.000**	**0.956**	**0.956**	**1.000**
BLF_{COR1}	**0.281**	**0.173**	**0.171**	**0.000**	**0.220**
BLF_{COR2}	**0.355**	**0.780**	**0.537**	**0.940**	**0.749**
$BLF_{nearCOR}$	**0.224**	**0.047**	**0.248**	**0.015**	**0.031**
BLF_{noCORs}	**0.140**	**0.000**	**0.044**	**0.044**	**0.000**
BLF_{tot}	1.000	1.000	1.000	1.000	1.000

Tmt population 3 CORs statistics

1100w-30min	Tot-pop3
N_MtGrains	9
Nunique_MtGrains_incontact	**9**
Nunique_MtGrains_anyOR	8
Nunique_MtGrains_OR1and2	8
Nunique_MtGrains_id3	1
Nunique_MtGrains_OR1	1
Nunique_MtGrains_OR2	8
frac_mt_incontact	1
frac_incontact_mt_anyOR	0.89
frac_incontact_mt_OR1	0.11
frac_incontact_mt_OR2	0.89
GBLength_Di_Mt	232.32
GBLength_Mt	308.32
GBLength_Di	8378.43
GBLength_OR1	21.73
GBLength_OR2	199.45
GBLength_id3	7.48
GBLength_anyOR	228.67
Lfrac_mt_incontact	0.75
Lfrac_di_incontact	0.03
BLF_{anyCOR}	**0.984**
BLF_{COR1}	**0.094**
BLF_{COR2}	**0.859**
$BLF_{nearCOR}$	**0.032**
BLF_{noCORs}	**0.016**
BLF_{tot}	1.000

Tmt population 2 CORs statistics

1100w-8h	scan08b	scan09a	scan09b	scan16	Tot-pop2
N_MtGrains	8	58	60	11	361
Nunique_MtGrains_incontact	**5**	**56**	**60**	**11**	**319**
Nunique_MtGrains_anyOR	4	51	48	10	283
Nunique_MtGrains_OR1and2	4	49	46	9	266
Nunique_MtGrains_id3	2	19	20	3	123
Nunique_MtGrains_OR1	0	6	7	0	62
Nunique_MtGrains_OR2	4	46	42	9	226
frac_mt_incontact	0.625	0.966	1.000	1.000	0.884
frac_incontact_mt_anyOR	0.800	0.911	0.800	0.909	0.887
frac_incontact_mt_OR1	0.000	0.107	0.117	0.000	0.194
frac_incontact_mt_OR2	0.800	0.821	0.700	0.818	0.708
GBLength_Di_Mt	66.294	1161.765	667.607	164.368	4257.010
GBLength_Mt	195.039	2444.766	1878.687	334.433	10851.037
GBLength_Di	273.323	6213.174	6691.661	1729.566	40155.181
GBLength_OR1	0.000	29.397	27.748	0.000	396.533
GBLength_OR2	62.345	950.521	470.430	136.100	3032.176
GBLength_id3	1.024	77.569	100.245	8.737	471.978
GBLength_anyOR	63.369	1057.487	598.423	144.837	3900.687
Lfrac_mt_incontact	0.340	0.475	0.355	0.491	0.392
Lfrac_di_incontact	0.243	0.187	0.100	0.095	0.106
BLF_{anyCOR}	**0.956**	**0.910**	**0.896**	**0.881**	**0.916**
BLF_{COR1}	**0.000**	**0.025**	**0.042**	**0.000**	**0.093**
BLF_{COR2}	**0.940**	**0.818**	**0.705**	**0.828**	**0.712**
$BLF_{nearCOR}$	**0.015**	**0.067**	**0.150**	**0.053**	**0.111**
BLF_{noCORs}	**0.044**	**0.090**	**0.104**	**0.119**	**0.084**
BLF_{tot}	1.000	1.000	1.000	1.000	1.000

Tmt population 3 CORs statistics

1100w-8h	scan01a	scan01b	scan01c	scan02a	scan02b	scan08a
N_MtGrains	5	18	17	16	8	6
Nunique_MtGrains_incontact	**5**	**18**	**17**	**16**	**8**	**6**
Nunique_MtGrains_anyOR	5	18	17	16	8	5
Nunique_MtGrains_OR1and2	5	18	17	16	8	5
Nunique_MtGrains_id3	3	11	4	4	2	2
Nunique_MtGrains_OR1	1	9	3	1	1	0
Nunique_MtGrains_OR2	5	17	16	15	8	5
frac_mt_incontact	1	1	1	1	1	1
frac_incontact_mt_anyOR	1.000	1.000	1.000	1.000	1.000	0.833
frac_incontact_mt_OR1	0.200	0.500	0.176	0.063	0.125	0.000
frac_incontact_mt_OR2	1.000	0.944	0.941	0.938	1.000	0.833
GBLength_Di_Mt	122.421	442.706	398.830	397.378	93.457	29.671
GBLength_Mt	167.464	585.623	546.980	514.406	190.167	78.750
GBLength_Di	1018.352	2327.783	2874.096	1545.735	1931.372	1031.317
GBLength_OR1	1.842	19.843	5.085	4.116	0.818	0.000
GBLength_OR2	116.284	397.055	372.901	376.050	84.949	25.686
GBLength_id3	4.295	24.550	14.387	16.714	7.690	2.819
GBLength_anyOR	122.421	441.448	392.373	396.880	93.457	28.505
Lfrac_mt_incontact	0.731	0.756	0.729	0.772	0.491	0.377
Lfrac_di_incontact	0.120	0.190	0.139	0.257	0.048	0.029
BLF_{anyCOR}	**1.000**	**0.997**	**0.984**	**0.999**	**1.000**	**0.961**
BLF_{COR1}	**0.015**	**0.045**	**0.013**	**0.010**	**0.009**	**0.000**
BLF_{COR2}	**0.950**	**0.897**	**0.935**	**0.946**	**0.909**	**0.866**
$BLF_{nearCOR}$	**0.035**	**0.055**	**0.036**	**0.042**	**0.082**	**0.095**
BLF_{noCORs}	**0.000**	**0.003**	**0.016**	**0.001**	**0.000**	**0.039**
BLF_{tot}	1.000	1.000	1.000	1.000	1.000	1.000

Tmt population 3 CORs statistics

1100w-8h	scan09b	scan16	Tot-pop3
N_MtGrains	13	10	70
Nunique_MtGrains_incontact	**13**	**10**	**70**
Nunique_MtGrains_anyOR	13	10	69
Nunique_MtGrains_OR1and2	11	10	69
Nunique_MtGrains_id3	4	1	26
Nunique_MtGrains_OR1	2	0	15
Nunique_MtGrains_OR2	9	10	66
frac_mt_incontact	1	1	1
frac_incontact_mt_anyOR	1.000	1.000	0.986
frac_incontact_mt_OR1	0.154	0.000	0.214
frac_incontact_mt_OR2	0.692	1.000	0.943
GBLength_Di_Mt	137.505	353.674	1484.463
GBLength_Mt	283.790	495.169	2083.390
GBLength_Di	6691.661	1729.566	10728.656
GBLength_OR1	8.943	0.000	31.705
GBLength_OR2	113.571	353.198	1372.925
GBLength_id3	8.207	0.476	70.455
GBLength_anyOR	130.720	353.674	1475.084
Lfrac_mt_incontact	0.485	0.714	0.713
Lfrac_di_incontact	0.021	0.204	0.138
BLF_{anyCOR}	**0.951**	**1.000**	**0.994**
BLF_{COR1}	**0.065**	**0.000**	**0.021**
BLF_{COR2}	**0.826**	**0.999**	**0.925**
$BLF_{nearCOR}$	**0.060**	**0.001**	**0.047**
BLF_{noCORs}	**0.049**	**0.000**	**0.006**
BLF_{tot}	1.000	1.000	1.000

Sheet "Pcf" of Peres et al., (2024) suplementary material 2

pcf function calculated using translation ("trans") and Ripley isotropic edge correction ("iso") for the different Tmt populations in sample 1150w-30min

Sample 1150w-30min Tmt Population1 VOI in hot (ΔT≈10°) portion of the sample 500-1-POP1			Sample 1150w-30min Tmt Population1 VOI in the central (ΔT≈30°) portion of the sample 500-2-POP1			Sample 1150w-30min Tmt Population1 VOI in the colder (ΔT≈60°) portion of the sample 500-3-POP1		
r [µm]	**trans**	**iso**	**r [µm]**	**trans**	**iso**	**r [µm]**	**trans**	**iso**
0.000	0.000	0.000	0.000	0.122	0.146	0.000	4.253	4.521
3.416	0.039	0.036	2.732	0.159	0.187	3.421	4.400	4.671
6.833	0.068	0.063	5.464	0.229	0.257	6.842	4.385	4.650
10.249	0.111	0.112	8.197	0.301	0.326	10.263	4.323	4.574
13.665	0.141	0.147	10.929	0.374	0.393	13.684	4.229	4.465
17.082	0.171	0.184	13.661	0.428	0.443	17.105	4.097	4.315
20.498	0.208	0.232	16.393	0.479	0.494	20.525	3.944	4.138
23.915	0.260	0.292	19.125	0.529	0.544	23.946	3.740	3.910
27.331	0.335	0.373	21.857	0.589	0.603	27.367	3.508	3.649
30.747	0.407	0.451	24.590	0.652	0.665	30.788	3.157	3.265
34.164	0.486	0.533	27.322	0.715	0.729	34.209	2.663	2.732
37.580	0.568	0.615	30.054	0.764	0.778	37.630	2.029	2.051
40.996	0.653	0.695	32.786	0.807	0.822	41.051	1.490	1.473
44.413	0.745	0.782	35.518	0.839	0.855	44.472	1.267	1.236
47.829	0.823	0.856	38.251	0.860	0.874	47.893	1.087	1.044
51.246	0.899	0.924	40.983	0.884	0.899	51.314	0.981	0.939
54.662	0.971	0.985	43.715	0.896	0.914	54.735	0.905	0.865
58.078	1.033	1.035	46.447	0.887	0.909	58.156	0.814	0.775
61.495	1.084	1.072	49.179	0.902	0.926	61.576	0.756	0.720
64.911	1.121	1.092	51.912	0.917	0.942	64.997	0.732	0.698
68.327	1.152	1.106	54.644	0.955	0.976	68.418	0.721	0.690
71.744	1.176	1.116	57.376	0.989	1.002	71.839	0.745	0.713
75.160	1.190	1.119	60.108	1.011	1.017	75.260	0.762	0.728
78.576	1.190	1.110	62.840	1.018	1.019	78.681	0.784	0.746
81.993	1.172	1.084	65.572	1.019	1.013	82.102	0.814	0.771
85.409	1.154	1.065	68.305	1.013	1.001	85.523	0.840	0.793
88.826	1.126	1.038	71.037	1.011	0.994	88.944	0.869	0.820
92.242	1.120	1.034	73.769	1.007	0.994	92.365	0.907	0.859
95.658	1.113	1.029	76.501	1.002	0.992	95.786	0.939	0.896
99.075	1.108	1.027	79.233	0.999	0.994	99.207	0.966	0.931
102.491	1.096	1.018	81.966	0.990	0.988	102.627	0.986	0.960
105.907	1.097	1.016	84.698	0.984	0.982	106.048	1.006	0.993
109.324	1.117	1.030	87.430	0.969	0.966	109.469	1.022	1.020
112.740	1.140	1.050	90.162	0.956	0.954	112.890	1.038	1.048
116.157	1.162	1.070	92.894	0.945	0.942	116.311	1.049	1.071
119.573	1.186	1.092	95.627	0.931	0.930	119.732	1.052	1.085
122.989	1.205	1.110	98.359	0.921	0.923	123.153	1.053	1.095
126.406	1.211	1.114	101.091	0.928	0.928	126.574	1.048	1.095
129.822	1.221	1.118	103.823	0.937	0.936	129.995	1.039	1.084
133.238	1.225	1.118	106.555	0.951	0.949	133.416	1.017	1.060
136.655	1.220	1.115	109.287	0.962	0.960	136.837	0.998	1.034
140.071	1.206	1.104	112.020	0.969	0.965	140.258	0.973	1.001
143.487	1.185	1.086	114.752	0.978	0.972	143.678	0.965	0.984
146.904	1.153	1.057	117.484	0.983	0.979	147.099	0.967	0.980
150.320	1.120	1.028	120.216	0.986	0.988	150.520	0.973	0.983
153.737	1.093	1.007	122.948	0.992	1.000	153.941	0.981	0.986
157.153	1.063	0.982	125.681	0.994	1.006	157.362	0.985	0.986
160.569	1.029	0.953	128.413	0.991	1.006	160.783	0.994	0.991
163.986	1.005	0.936	131.145	0.988	1.005	164.204	1.008	1.003
167.402	0.979	0.917	133.877	0.986	1.001	167.625	1.029	1.025
170.818	0.957	0.899	136.609	0.986	1.001	171.046	1.051	1.048

Sample 1150w-30min Tmt Population1 VOI in hot (ΔT≈10°) portion of the sample 500-1-POP1			Sample 1150w-30min Tmt Population1 VOI in the central (ΔT≈30°) portion of the sample 500-2-POP1			Sample 1150w-30min Tmt Population1 VOI in the colder (ΔT≈60°) portion of the sample 500-3-POP1		
174.235	0.952	0.898	139.342	0.985	0.998	174.467	1.076	1.073
177.651	0.958	0.908	142.074	0.978	0.988	177.888	1.097	1.095
181.068	0.973	0.925	144.806	0.969	0.977	181.309	1.120	1.118
184.484	1.003	0.957	147.538	0.966	0.970	184.729	1.140	1.137
187.900	1.036	0.992	150.270	0.969	0.971	188.150	1.151	1.149
191.317	1.062	1.019	153.002	0.975	0.975	191.571	1.153	1.152
194.733	1.085	1.042	155.735	0.987	0.987	194.992	1.146	1.146
198.149	1.104	1.060	158.467	1.006	1.004	198.413	1.137	1.139
201.566	1.119	1.075	161.199	1.022	1.019	201.834	1.125	1.131
204.982	1.126	1.083	163.931	1.031	1.024	205.255	1.112	1.120
208.398	1.135	1.093	166.663	1.039	1.031	208.676	1.093	1.102
211.815	1.144	1.102	169.396	1.048	1.037	212.097	1.069	1.075
215.231	1.153	1.111	172.128	1.055	1.042	215.518	1.039	1.044
218.648	1.165	1.124	174.860	1.057	1.041	218.939	1.013	1.018
222.064	1.181	1.139	177.592	1.058	1.039	222.360	0.993	0.996
225.480	1.193	1.149	180.324	1.059	1.038	225.780	0.975	0.975
228.897	1.196	1.153	183.057	1.061	1.038	229.201	0.960	0.956
232.313	1.201	1.159	185.789	1.060	1.034	232.622	0.951	0.945
235.729	1.207	1.164	188.521	1.053	1.024	236.043	0.953	0.945
239.146	1.209	1.166	191.253	1.047	1.016	239.464	0.960	0.949
242.562	1.217	1.176	193.985	1.041	1.010	242.885	0.967	0.953
245.978	1.213	1.176	196.717	1.034	1.006	246.306	0.975	0.959
249.395	1.215	1.183	199.450	1.029	1.005	249.727	0.983	0.966
252.811	1.221	1.192	202.182	1.028	1.008	253.148	0.995	0.976
256.228	1.223	1.197	204.914	1.028	1.011	256.569	1.008	0.986
259.644	1.226	1.201	207.646	1.026	1.014	259.990	1.021	0.997
263.060	1.221	1.196	210.378	1.031	1.021	263.410	1.034	1.009
266.477	1.210	1.183	213.111	1.037	1.030	266.831	1.048	1.024
269.893	1.190	1.163	215.843	1.050	1.046	270.252	1.058	1.035
273.309	1.163	1.137	218.575	1.058	1.058	273.673	1.070	1.047
276.726	1.137	1.112	221.307	1.064	1.067	277.094	1.078	1.055
280.142	1.113	1.090	224.039	1.068	1.073	280.515	1.077	1.054
283.559	1.096	1.075	226.772	1.068	1.075	283.936	1.076	1.055
286.975	1.080	1.061	229.504	1.072	1.079	287.357	1.071	1.051
290.391	1.063	1.045	232.236	1.074	1.080	290.778	1.062	1.045
293.808	1.042	1.024	234.968	1.074	1.078	294.199	1.051	1.038
297.224	1.015	0.998	237.700	1.075	1.076	297.620	1.039	1.030
300.640	0.991	0.975	240.432	1.072	1.073	301.041	1.030	1.023
304.057	0.968	0.953	243.165	1.067	1.067	304.461	1.025	1.021
307.473	0.946	0.930	245.897	1.058	1.057	307.882	1.018	1.016
310.889	0.926	0.911	248.629	1.045	1.042	311.303	1.011	1.012
314.306	0.917	0.903	251.361	1.030	1.028	314.724	1.006	1.008
317.722	0.905	0.893	254.093	1.022	1.019	318.145	1.009	1.012
321.139	0.899	0.889	256.826	1.012	1.009	321.566	1.017	1.023
324.555	0.894	0.884	259.558	1.000	0.998	324.987	1.023	1.030
327.971	0.894	0.884	262.290	0.992	0.991	328.408	1.030	1.037
331.388	0.897	0.886	265.022	0.988	0.990	331.829	1.037	1.045
334.804	0.898	0.887	267.754	0.984	0.990	335.250	1.045	1.052
338.220	0.899	0.888	270.487	0.983	0.991	338.671	1.051	1.057
341.637	0.904	0.894	273.219	0.984	0.995	342.092	1.051	1.057
345.053	0.909	0.899	275.951	0.983	0.994	345.512	1.050	1.056
348.470	0.918	0.908	278.683	0.983	0.997	348.933	1.051	1.057
351.886	0.930	0.922	281.415	0.986	1.001	352.354	1.050	1.055
355.302	0.939	0.931	284.147	0.988	1.006	355.775	1.048	1.052
358.719	0.946	0.939	286.880	0.990	1.008	359.196	1.042	1.046
362.135	0.944	0.938	289.612	0.993	1.010	362.617	1.034	1.039

Sample 1150w-30min Tmt Population1 VOI in hot (ΔT≈10°) portion of the sample 500-1-POP1			Sample 1150w-30min Tmt Population1 VOI in the central (ΔT≈30°) portion of the sample 500-2-POP1			Sample 1150w-30min Tmt Population1 VOI in the colder (ΔT≈60°) portion of the sample 500-3-POP1		
365.551	0.942	0.937	292.344	0.991	1.008	366.038	1.028	1.033
368.968	0.939	0.934	295.076	0.988	1.006	369.459	1.021	1.027
372.384	0.936	0.931	297.808	0.990	1.009	372.880	1.019	1.026
375.800	0.934	0.929	300.541	0.989	1.009	376.301	1.018	1.029
379.217	0.935	0.931	303.273	0.979	1.001	379.722	1.013	1.026
382.633	0.937	0.934	306.005	0.969	0.991	383.143	1.007	1.021
386.050	0.938	0.934	308.737	0.960	0.983	386.563	1.002	1.018
389.466	0.938	0.937	311.469	0.955	0.979	389.984	0.995	1.012
392.882	0.939	0.941	314.202	0.951	0.975	393.405	0.989	1.008
396.299	0.936	0.941	316.934	0.947	0.970	396.826	0.979	1.002
399.715	0.929	0.939	319.666	0.946	0.969	400.247	0.971	0.997
403.131	0.919	0.933	322.398	0.945	0.967	403.668	0.966	0.994
406.548	0.911	0.928	325.130	0.946	0.966	407.089	0.956	0.983
409.964	0.909	0.928	327.862	0.943	0.961	410.510	0.943	0.972
413.381	0.910	0.928	330.595	0.941	0.956	413.931	0.931	0.961
416.797	0.916	0.931	333.327	0.941	0.953	417.352	0.922	0.953
420.213	0.921	0.931	336.059	0.939	0.950	420.773	0.911	0.941
423.630	0.923	0.928	338.791	0.938	0.946	424.194	0.899	0.929
427.046	0.918	0.918	341.523	0.938	0.942	427.614	0.891	0.923
430.462	0.906	0.902	344.256	0.938	0.939	431.035	0.884	0.915
433.879	0.896	0.888	346.988	0.934	0.930	434.456	0.880	0.910

Sample 1150w-30min Tmt Population2 VOI in hot (ΔT≈10°) portion of the sample 500-1-POP2			Sample 1150w-30min Tmt Population2 VOI in the central (ΔT≈30°) portion of the sample 500-2-POP2			Sample 1150w-30min Tmt Population2 VOI in the colder (ΔT≈60°) portion of the sample 500-3-POP2		
r [µm]	**trans**	**iso**	**r [µm]**	**trans**	**iso**	**r [µm]**	**trans**	**iso**
0.000	0.700	0.703	0.000	0.042	0.043	0.000	0.022	0.024
3.416	1.167	1.200	2.732	0.146	0.159	3.421	0.107	0.111
6.833	1.659	1.731	5.464	0.309	0.336	6.842	0.295	0.305
10.249	2.138	2.252	8.197	0.545	0.588	10.263	0.586	0.604
13.665	2.655	2.814	10.929	0.865	0.926	13.684	0.865	0.891
17.082	3.137	3.336	13.661	1.163	1.238	17.105	1.026	1.058
20.498	3.391	3.615	16.393	1.363	1.441	20.525	1.081	1.112
23.915	3.412	3.648	19.125	1.454	1.532	23.946	1.079	1.106
27.331	3.282	3.516	21.857	1.468	1.546	27.367	1.071	1.096
30.747	3.118	3.344	24.590	1.434	1.510	30.788	1.065	1.089
34.164	2.977	3.202	27.322	1.406	1.483	34.209	1.061	1.086
37.580	2.835	3.060	30.054	1.398	1.482	37.630	1.058	1.084
40.996	2.723	2.948	32.786	1.386	1.475	41.051	1.054	1.080
44.413	2.656	2.875	35.518	1.363	1.456	44.472	1.046	1.070
47.829	2.599	2.806	38.251	1.341	1.437	47.893	1.033	1.054
51.246	2.532	2.729	40.983	1.314	1.412	51.314	1.022	1.042
54.662	2.462	2.652	43.715	1.284	1.382	54.735	1.016	1.035
58.078	2.390	2.573	46.447	1.262	1.360	58.156	1.012	1.030
61.495	2.330	2.511	49.179	1.236	1.333	61.576	1.007	1.024
64.911	2.267	2.443	51.912	1.207	1.302	64.997	1.003	1.020
68.327	2.213	2.383	54.644	1.185	1.279	68.418	1.000	1.016
71.744	2.167	2.336	57.376	1.167	1.263	71.839	0.998	1.012
75.160	2.126	2.293	60.108	1.153	1.251	75.260	0.994	1.006
78.576	2.085	2.252	62.840	1.140	1.241	78.681	0.991	1.003
81.993	2.042	2.208	65.572	1.127	1.230	82.102	0.992	1.004
85.409	1.995	2.165	68.305	1.113	1.218	85.523	0.992	1.004
88.826	1.945	2.117	71.037	1.100	1.206	88.944	0.992	1.004

Sample 1150w-30min Tmt Population2 VOI in hot (ΔT≈10°) portion of the sample 500-1-POP2			Sample 1150w-30min Tmt Population2 VOI in the central (ΔT≈30°) portion of the sample 500-2-POP2			Sample 1150w-30min Tmt Population2 VOI in the colder (ΔT≈60°) portion of the sample 500-3-POP2		
92.242	1.899	2.071	73.769	1.085	1.190	92.365	0.991	1.002
95.658	1.859	2.027	76.501	1.069	1.175	95.786	0.991	1.001
99.075	1.827	1.991	79.233	1.056	1.160	99.207	0.992	0.999
102.491	1.800	1.961	81.966	1.045	1.148	102.627	0.992	0.999
105.907	1.775	1.933	84.698	1.036	1.140	106.048	0.994	1.000
109.324	1.748	1.903	87.430	1.031	1.137	109.469	0.996	1.003
112.740	1.720	1.874	90.162	1.021	1.128	112.890	0.998	1.005
116.157	1.688	1.841	92.894	1.009	1.116	116.311	1.000	1.006
119.573	1.655	1.810	95.627	0.999	1.107	119.732	1.001	1.007
122.989	1.626	1.786	98.359	0.992	1.102	123.153	1.000	1.005
126.406	1.599	1.763	101.091	0.987	1.097	126.574	1.001	1.004
129.822	1.576	1.746	103.823	0.983	1.093	129.995	1.000	1.003
133.238	1.557	1.731	106.555	0.979	1.089	133.416	1.000	1.003
136.655	1.541	1.718	109.287	0.974	1.084	136.837	0.999	1.002
140.071	1.526	1.704	112.020	0.971	1.082	140.258	1.000	1.002
143.487	1.509	1.686	114.752	0.967	1.080	143.678	1.001	1.002
146.904	1.490	1.665	117.484	0.963	1.077	147.099	1.002	1.002
150.320	1.472	1.646	120.216	0.958	1.072	150.520	1.002	1.002
153.737	1.452	1.625	122.948	0.952	1.065	153.941	1.002	1.002
157.153	1.430	1.602	125.681	0.947	1.059	157.362	1.002	1.002
160.569	1.410	1.581	128.413	0.942	1.053	160.783	1.004	1.004
163.986	1.392	1.562	131.145	0.936	1.046	164.204	1.005	1.005
167.402	1.371	1.540	133.877	0.932	1.043	167.625	1.006	1.006
170.818	1.351	1.520	136.609	0.929	1.040	171.046	1.005	1.005
174.235	1.328	1.497	139.342	0.929	1.041	174.467	1.005	1.004
177.651	1.302	1.468	142.074	0.930	1.041	177.888	1.006	1.004
181.068	1.277	1.439	144.806	0.929	1.041	181.309	1.007	1.005
184.484	1.253	1.410	147.538	0.927	1.038	184.729	1.007	1.005
187.900	1.236	1.390	150.270	0.921	1.031	188.150	1.007	1.006
191.317	1.224	1.375	153.002	0.914	1.022	191.571	1.008	1.007
194.733	1.212	1.358	155.735	0.911	1.017	194.992	1.009	1.008
198.149	1.199	1.342	158.467	0.912	1.016	198.413	1.008	1.007
201.566	1.184	1.326	161.199	0.913	1.016	201.834	1.008	1.007
204.982	1.168	1.306	163.931	0.914	1.016	205.255	1.008	1.006
208.398	1.150	1.284	166.663	0.912	1.012	208.676	1.009	1.008
211.815	1.131	1.261	169.396	0.906	1.004	212.097	1.010	1.009
215.231	1.116	1.243	172.128	0.900	0.996	215.518	1.011	1.011
218.648	1.103	1.226	174.860	0.899	0.991	218.939	1.010	1.010
222.064	1.090	1.210	177.592	0.899	0.990	222.360	1.011	1.010
225.480	1.078	1.196	180.324	0.898	0.988	225.780	1.009	1.009
228.897	1.070	1.186	183.057	0.895	0.983	229.201	1.010	1.010
232.313	1.062	1.177	185.789	0.890	0.976	232.622	1.009	1.009
235.729	1.054	1.167	188.521	0.887	0.971	236.043	1.009	1.010
239.146	1.043	1.154	191.253	0.887	0.968	239.464	1.009	1.009
242.562	1.034	1.143	193.985	0.888	0.967	242.885	1.009	1.009
245.978	1.024	1.130	196.717	0.889	0.967	246.306	1.009	1.009
249.395	1.010	1.112	199.450	0.891	0.968	249.727	1.009	1.009
252.811	0.995	1.094	202.182	0.890	0.965	253.148	1.009	1.008
256.228	0.984	1.080	204.914	0.890	0.964	256.569	1.008	1.008
259.644	0.976	1.070	207.646	0.891	0.964	259.990	1.006	1.006
263.060	0.970	1.061	210.378	0.893	0.964	263.410	1.006	1.006
266.477	0.962	1.052	213.111	0.893	0.961	266.831	1.006	1.006
269.893	0.955	1.043	215.843	0.894	0.961	270.252	1.006	1.007
273.309	0.951	1.037	218.575	0.895	0.959	273.673	1.008	1.009
276.726	0.944	1.029	221.307	0.894	0.955	277.094	1.008	1.010
280.142	0.937	1.020	224.039	0.891	0.950	280.515	1.008	1.009

Sample 1150w-30min Tmt Population2 VOI in hot (ΔT≈10°) portion of the sample 500-1-POP2			Sample 1150w-30min Tmt Population2 VOI in the central (ΔT≈30°) portion of the sample 500-2-POP2			Sample 1150w-30min Tmt Population2 VOI in the colder (ΔT≈60°) portion of the sample 500-3-POP2		
283.559	0.932	1.014	226.772	0.891	0.948	283.936	1.006	1.008
286.975	0.929	1.010	229.504	0.894	0.948	287.357	1.006	1.008
290.391	0.928	1.008	232.236	0.896	0.949	290.778	1.006	1.009
293.808	0.927	1.005	234.968	0.899	0.949	294.199	1.006	1.008
297.224	0.923	0.998	237.700	0.904	0.952	297.620	1.006	1.008
300.640	0.919	0.991	240.432	0.906	0.953	301.041	1.004	1.007
304.057	0.916	0.986	243.165	0.907	0.952	304.461	1.003	1.006
307.473	0.913	0.981	245.897	0.907	0.949	307.882	1.002	1.005
310.889	0.908	0.975	248.629	0.906	0.946	311.303	1.001	1.005
314.306	0.904	0.968	251.361	0.905	0.942	314.724	1.000	1.004
317.722	0.901	0.963	254.093	0.906	0.940	318.145	0.998	1.003
321.139	0.899	0.960	256.826	0.910	0.942	321.566	0.997	1.002
324.555	0.895	0.953	259.558	0.913	0.943	324.987	0.997	1.002
327.971	0.892	0.947	262.290	0.916	0.944	328.408	0.995	1.001
331.388	0.890	0.942	265.022	0.920	0.946	331.829	0.995	1.001
334.804	0.887	0.936	267.754	0.923	0.946	335.250	0.994	1.000
338.220	0.884	0.931	270.487	0.925	0.946	338.671	0.993	1.000
341.637	0.882	0.927	273.219	0.932	0.950	342.092	0.991	0.998
345.053	0.879	0.922	275.951	0.938	0.954	345.512	0.989	0.996
348.470	0.877	0.918	278.683	0.942	0.956	348.933	0.987	0.995
351.886	0.873	0.912	281.415	0.945	0.957	352.354	0.985	0.993
355.302	0.869	0.906	284.147	0.949	0.958	355.775	0.985	0.994
358.719	0.866	0.902	286.880	0.950	0.957	359.196	0.985	0.994
362.135	0.860	0.896	289.612	0.953	0.958	362.617	0.983	0.993
365.551	0.856	0.890	292.344	0.958	0.961	366.038	0.982	0.992
368.968	0.850	0.884	295.076	0.964	0.965	369.459	0.981	0.992
372.384	0.846	0.878	297.808	0.971	0.969	372.880	0.981	0.993
375.800	0.842	0.874	300.541	0.977	0.972	376.301	0.981	0.993
379.217	0.838	0.868	303.273	0.983	0.976	379.722	0.980	0.992
382.633	0.833	0.863	306.005	0.991	0.980	383.143	0.978	0.991
386.050	0.832	0.862	308.737	0.997	0.984	386.563	0.975	0.989
389.466	0.830	0.860	311.469	1.002	0.986	389.984	0.974	0.988
392.882	0.830	0.860	314.202	1.005	0.987	393.405	0.975	0.990
396.299	0.827	0.858	316.934	1.007	0.986	396.826	0.976	0.992
399.715	0.823	0.856	319.666	1.010	0.987	400.247	0.977	0.994
403.131	0.822	0.856	322.398	1.015	0.990	403.668	0.976	0.994
406.548	0.821	0.854	325.130	1.023	0.995	407.089	0.974	0.992
409.964	0.818	0.851	327.862	1.030	0.999	410.510	0.972	0.992
413.381	0.819	0.852	330.595	1.037	1.004	413.931	0.972	0.993
416.797	0.820	0.852	333.327	1.043	1.007	417.352	0.973	0.996
420.213	0.823	0.854	336.059	1.048	1.010	420.773	0.973	0.998
423.630	0.823	0.853	338.791	1.054	1.013	424.194	0.972	0.998
427.046	0.821	0.853	341.523	1.058	1.015	427.614	0.972	0.998
430.462	0.819	0.853	344.256	1.062	1.017	431.035	0.971	0.999
433.879	0.817	0.851	346.988	1.069	1.021	434.456	0.972	1.001

Sample 1100w-8h Tmt Population1 VOI in hoter (ΔT≈60°) portion of the sample 600-1-POP1			Sample 1100w-8h Tmt Population1 VOI in the hot-central (ΔT≈70°) portion of the sample 600-2-POP1			Sample 1100w-8h Tmt Population1 VOI in the colder-central (ΔT≈90°) portion of the sample 600-3-POP1		
r [µm]	**trans**	**iso**	**r [µm]**	**trans**	**iso**	**r [µm]**	**trans**	**iso**
0.000	0.406	0.384	0.000	0.024	0.022	0.000	0.060	0.058
4.091	0.409	0.386	4.098	0.066	0.060	4.094	0.164	0.157
8.183	0.400	0.378	8.197	0.111	0.101	8.187	0.246	0.236
12.274	0.390	0.368	12.295	0.164	0.149	12.281	0.332	0.318
16.366	0.404	0.385	16.393	0.228	0.206	16.375	0.425	0.411
20.457	0.445	0.427	20.491	0.301	0.274	20.469	0.520	0.506
24.549	0.513	0.492	24.590	0.381	0.349	24.562	0.636	0.618
28.640	0.592	0.572	28.688	0.479	0.445	28.656	0.757	0.735
32.732	0.669	0.650	32.786	0.584	0.545	32.750	0.877	0.847
36.823	0.753	0.735	36.884	0.708	0.663	36.844	0.997	0.959
40.915	0.832	0.817	40.983	0.826	0.775	40.937	1.109	1.061
45.006	0.896	0.883	45.081	0.940	0.882	45.031	1.195	1.140
49.098	0.949	0.942	49.179	1.042	0.979	49.125	1.254	1.193
53.189	0.992	0.991	53.278	1.136	1.071	53.219	1.292	1.228
57.280	1.021	1.027	57.376	1.215	1.153	57.312	1.305	1.238
61.372	1.066	1.075	61.474	1.272	1.215	61.406	1.297	1.227
65.463	1.129	1.140	65.572	1.305	1.253	65.500	1.294	1.220
69.555	1.186	1.197	69.671	1.302	1.256	69.593	1.300	1.222
73.646	1.226	1.239	73.769	1.285	1.245	73.687	1.285	1.205
77.738	1.247	1.260	77.867	1.253	1.220	77.781	1.262	1.182
81.829	1.248	1.260	81.966	1.208	1.184	81.875	1.247	1.170
85.921	1.225	1.234	86.064	1.174	1.159	85.968	1.236	1.162
90.012	1.182	1.187	90.162	1.136	1.129	90.062	1.244	1.172
94.104	1.147	1.153	94.260	1.104	1.105	94.156	1.249	1.178
98.195	1.132	1.138	98.359	1.071	1.084	98.250	1.246	1.177
102.286	1.135	1.140	102.457	1.055	1.080	102.343	1.244	1.177
106.378	1.136	1.145	106.555	1.048	1.079	106.437	1.244	1.180
110.469	1.134	1.145	110.653	1.060	1.095	110.531	1.236	1.178
114.561	1.134	1.154	114.752	1.061	1.096	114.625	1.220	1.168
118.652	1.127	1.155	118.850	1.066	1.099	118.718	1.205	1.163
122.744	1.112	1.147	122.948	1.065	1.096	122.812	1.196	1.163
126.835	1.104	1.148	127.047	1.069	1.098	126.906	1.190	1.163
130.927	1.100	1.154	131.145	1.075	1.102	130.999	1.181	1.160
135.018	1.084	1.149	135.243	1.078	1.101	135.093	1.178	1.161
139.110	1.065	1.137	139.341	1.075	1.094	139.187	1.177	1.167
143.201	1.059	1.136	143.440	1.061	1.077	143.281	1.174	1.168
147.293	1.050	1.131	147.538	1.038	1.052	147.374	1.172	1.170
151.384	1.038	1.121	151.636	1.012	1.027	151.468	1.172	1.171
155.475	1.034	1.116	155.735	0.991	1.007	155.562	1.171	1.168
159.567	1.030	1.107	159.833	0.974	0.994	159.656	1.160	1.158
163.658	1.021	1.092	163.931	0.952	0.974	163.749	1.151	1.148
167.750	1.006	1.073	168.029	0.929	0.953	167.843	1.144	1.141
171.841	0.992	1.055	172.128	0.914	0.941	171.937	1.132	1.130
175.933	0.975	1.034	176.226	0.898	0.928	176.031	1.120	1.119
180.024	0.957	1.013	180.324	0.890	0.921	180.124	1.110	1.110
184.116	0.939	0.995	184.422	0.890	0.922	184.218	1.106	1.106
188.207	0.920	0.978	188.521	0.885	0.918	188.312	1.106	1.105
192.299	0.912	0.973	192.619	0.881	0.916	192.405	1.096	1.094
196.390	0.899	0.962	196.717	0.877	0.914	196.499	1.086	1.084
200.481	0.893	0.959	200.816	0.872	0.908	200.593	1.080	1.077
204.573	0.890	0.958	204.914	0.873	0.907	204.687	1.077	1.073

Sample 1100w-8h Tmt Population1 VOI in hoter (ΔT≈60°) portion of the sample 600-1-POP1			Sample 1100w-8h Tmt Population1 VOI in the hot-central (ΔT≈70°) portion of the sample 600-2-POP1			Sample 1100w-8h Tmt Population1 VOI in the colder-central (ΔT≈90°) portion of the sample 600-3-POP1		
208.664	0.893	0.960	209.012	0.876	0.906	208.780	1.078	1.072
212.756	0.895	0.963	213.110	0.880	0.907	212.874	1.080	1.073
216.847	0.892	0.960	217.209	0.886	0.911	216.968	1.073	1.064
220.939	0.893	0.960	221.307	0.891	0.915	221.062	1.063	1.052
225.030	0.890	0.955	225.405	0.902	0.925	225.155	1.046	1.034
229.122	0.890	0.952	229.504	0.913	0.938	229.249	1.035	1.024
233.213	0.892	0.949	233.602	0.921	0.947	233.343	1.027	1.018
237.305	0.898	0.952	237.700	0.924	0.950	237.437	1.013	1.005
241.396	0.905	0.956	241.798	0.925	0.949	241.530	0.998	0.990
245.488	0.908	0.956	245.897	0.932	0.954	245.624	0.983	0.976
249.579	0.907	0.951	249.995	0.935	0.955	249.718	0.972	0.966
253.670	0.900	0.941	254.093	0.932	0.951	253.811	0.960	0.957
257.762	0.891	0.932	258.191	0.929	0.948	257.905	0.950	0.950
261.853	0.881	0.924	262.290	0.927	0.947	261.999	0.947	0.949
265.945	0.876	0.920	266.388	0.924	0.946	266.093	0.944	0.948
270.036	0.873	0.919	270.486	0.918	0.941	270.186	0.938	0.945
274.128	0.879	0.927	274.585	0.907	0.930	274.280	0.932	0.941
278.219	0.880	0.929	278.683	0.898	0.923	278.374	0.932	0.944
282.311	0.884	0.931	282.781	0.889	0.916	282.468	0.932	0.945
286.402	0.889	0.934	286.879	0.886	0.915	286.561	0.936	0.951
290.494	0.893	0.934	290.978	0.884	0.913	290.655	0.938	0.954
294.585	0.900	0.936	295.076	0.885	0.916	294.749	0.947	0.964
298.676	0.906	0.939	299.174	0.889	0.922	298.843	0.954	0.971
302.768	0.912	0.941	303.273	0.893	0.926	302.936	0.957	0.972
306.859	0.917	0.942	307.371	0.897	0.929	307.030	0.962	0.975
310.951	0.925	0.947	311.469	0.902	0.932	311.124	0.969	0.979
315.042	0.934	0.956	315.567	0.904	0.932	315.217	0.974	0.981
319.134	0.940	0.964	319.666	0.907	0.933	319.311	0.976	0.982
323.225	0.943	0.967	323.764	0.907	0.931	323.405	0.980	0.983
327.317	0.943	0.966	327.862	0.912	0.936	327.499	0.985	0.986
331.408	0.945	0.969	331.960	0.923	0.946	331.592	0.984	0.983
335.500	0.945	0.968	336.059	0.938	0.958	335.686	0.978	0.975
339.591	0.940	0.964	340.157	0.949	0.967	339.780	0.971	0.965
343.683	0.933	0.958	344.255	0.960	0.975	343.874	0.964	0.956
347.774	0.929	0.954	348.354	0.966	0.978	347.967	0.953	0.944
351.865	0.926	0.952	352.452	0.963	0.973	352.061	0.947	0.937
355.957	0.923	0.949	356.550	0.962	0.970	356.155	0.942	0.933
360.048	0.915	0.941	360.648	0.960	0.966	360.248	0.941	0.932
364.140	0.907	0.932	364.747	0.956	0.961	364.342	0.935	0.927
368.231	0.899	0.923	368.845	0.952	0.956	368.436	0.924	0.916
372.323	0.890	0.911	372.943	0.945	0.949	372.530	0.916	0.908
376.414	0.883	0.902	377.042	0.944	0.947	376.623	0.912	0.904
380.506	0.879	0.894	381.140	0.945	0.948	380.717	0.911	0.904
384.597	0.876	0.887	385.238	0.951	0.954	384.811	0.910	0.902
388.689	0.875	0.885	389.336	0.953	0.957	388.905	0.909	0.901
392.780	0.878	0.888	393.435	0.956	0.960	392.998	0.914	0.906
396.871	0.883	0.893	397.533	0.956	0.961	397.092	0.919	0.908
400.963	0.885	0.896	401.631	0.967	0.973	401.186	0.921	0.910
405.054	0.899	0.910	405.729	0.982	0.988	405.280	0.928	0.915
409.146	0.918	0.929	409.828	0.999	1.004	409.373	0.938	0.923
413.237	0.932	0.941	413.926	1.012	1.016	413.467	0.945	0.928
417.329	0.942	0.950	418.024	1.028	1.030	417.561	0.953	0.936
421.420	0.953	0.959	422.123	1.037	1.039	421.654	0.964	0.945
425.512	0.965	0.969	426.221	1.043	1.043	425.748	0.973	0.953
429.603	0.980	0.981	430.319	1.052	1.050	429.842	0.985	0.964
433.695	0.997	0.997	434.417	1.057	1.054	433.936	0.995	0.972

Sample 1100w-8h Tmt Population1			Sample 1100w-8h Tmt Population1			Sample 1100w-8h Tmt Population1		
VOI in hoter (ΔT≈60°) portion of the sample			VOI in the hot-central (ΔT≈70°) portion of the sample			VOI in the colder-central (ΔT≈90°) portion of the sample		
600-1-POP1			600-2-POP1			600-3-POP1		
437.786	1.016	1.014	438.516	1.055	1.052	438.029	1.007	0.983
441.878	1.031	1.027	442.614	1.043	1.038	442.123	1.016	0.992
445.969	1.037	1.032	446.712	1.020	1.013	446.217	1.026	1.002
450.060	1.040	1.033	450.811	1.003	0.996	450.311	1.030	1.006
454.152	1.041	1.032	454.909	0.989	0.982	454.404	1.034	1.011
458.243	1.042	1.030	459.007	0.974	0.968	458.498	1.035	1.013
462.335	1.043	1.031	463.105	0.959	0.953	462.592	1.035	1.015
466.426	1.037	1.025	467.204	0.945	0.939	466.686	1.029	1.010
470.518	1.027	1.014	471.302	0.932	0.925	470.779	1.021	1.002
474.609	1.017	1.002	475.400	0.926	0.918	474.873	1.015	0.997
478.701	1.016	0.999	479.498	0.928	0.919	478.967	1.010	0.991
482.792	1.022	1.002	483.597	0.940	0.929	483.060	1.001	0.982
486.884	1.024	1.000	487.695	0.949	0.936	487.154	0.990	0.970
490.975	1.030	1.003	491.793	0.960	0.946	491.248	0.981	0.960
495.066	1.045	1.014	495.892	0.972	0.955	495.342	0.975	0.954
499.158	1.058	1.025	499.990	0.986	0.964	499.435	0.967	0.946
503.249	1.067	1.029	504.088	1.003	0.975	503.529	0.961	0.940
507.341	1.073	1.032	508.186	1.025	0.990	507.623	0.959	0.940
511.432	1.085	1.040	512.285	1.042	0.998	511.717	0.955	0.939
515.524	1.101	1.053	516.383	1.050	1.000	515.810	0.952	0.937
519.615	1.110	1.058	520.481	1.053	0.997	519.904	0.955	0.943

Sample 1100w-8h Tmt Population1			Sample 1100w-8h Tmt Population1			Sample 1100w-8h Tmt Population1		
VOI in hoter (ΔT≈60°) portion of the sample			VOI in the hot-central (ΔT≈70°) portion of the sample			VOI in the colder-central (ΔT≈90°) portion of the sample		
600-1-POP2			600-2-POP2			600-3-POP2		
r [µm]	**trans**	**iso**	**r [µm]**	**trans**	**iso**	**r [µm]**	**trans**	**iso**
0.000	0.027	0.028	0.000	0.016	0.018	0.000	0.026	0.026
4.091	0.218	0.228	4.098	0.117	0.123	4.094	0.203	0.208
8.183	0.573	0.596	8.197	0.364	0.379	8.187	0.563	0.577
12.274	1.064	1.104	12.295	0.771	0.799	12.281	1.076	1.099
16.366	1.522	1.575	16.393	1.145	1.189	16.375	1.508	1.536
20.457	1.768	1.823	20.491	1.338	1.392	20.469	1.687	1.720
24.549	1.824	1.878	24.590	1.373	1.432	24.562	1.674	1.710
28.640	1.804	1.852	28.688	1.358	1.417	28.656	1.613	1.650
32.732	1.760	1.802	32.786	1.326	1.384	32.750	1.547	1.581
36.823	1.703	1.743	36.884	1.281	1.341	36.844	1.499	1.528
40.915	1.638	1.674	40.983	1.237	1.298	40.937	1.454	1.480
45.006	1.583	1.617	45.081	1.196	1.258	45.031	1.409	1.433
49.098	1.525	1.557	49.179	1.162	1.223	49.125	1.374	1.398
53.189	1.476	1.504	53.278	1.129	1.190	53.219	1.341	1.366
57.280	1.429	1.454	57.376	1.102	1.164	57.312	1.302	1.325
61.372	1.386	1.407	61.474	1.076	1.139	61.406	1.264	1.286
65.463	1.350	1.368	65.572	1.050	1.111	65.500	1.235	1.257
69.555	1.314	1.329	69.671	1.026	1.085	69.593	1.209	1.231
73.646	1.284	1.299	73.769	1.007	1.064	73.687	1.190	1.211
77.738	1.259	1.272	77.867	0.992	1.048	77.781	1.169	1.189
81.829	1.235	1.245	81.966	0.979	1.036	81.875	1.156	1.174
85.921	1.218	1.224	86.064	0.969	1.028	85.968	1.143	1.161
90.012	1.201	1.203	90.162	0.960	1.020	90.062	1.133	1.151
94.104	1.182	1.182	94.260	0.953	1.012	94.156	1.126	1.144
98.195	1.167	1.164	98.359	0.947	1.005	98.250	1.118	1.134
102.286	1.153	1.147	102.457	0.943	1.001	102.343	1.110	1.125
106.378	1.142	1.134	106.555	0.938	0.998	106.437	1.101	1.114

Sample 1100w-8h Tmt Population1 VOI in hoter (ΔT≈60°) portion of the sample 600-1-POP2			Sample 1100w-8h Tmt Population1 VOI in the hot-central (ΔT≈70°) portion of the sample 600-2-POP2			Sample 1100w-8h Tmt Population1 VOI in the colder-central (ΔT≈90°) portion of the sample 600-3-POP2		
110.469	1.133	1.124	110.653	0.932	0.992	110.531	1.094	1.105
114.561	1.128	1.116	114.752	0.926	0.985	114.625	1.088	1.098
118.652	1.123	1.109	118.850	0.925	0.983	118.718	1.083	1.093
122.744	1.117	1.102	122.948	0.925	0.984	122.812	1.079	1.088
126.835	1.111	1.093	127.047	0.925	0.983	126.906	1.076	1.085
130.927	1.104	1.085	131.145	0.925	0.983	130.999	1.074	1.081
135.018	1.101	1.079	135.243	0.926	0.983	135.093	1.070	1.077
139.110	1.095	1.072	139.341	0.926	0.984	139.187	1.067	1.072
143.201	1.087	1.064	143.440	0.925	0.982	143.281	1.062	1.066
147.293	1.081	1.059	147.538	0.923	0.980	147.374	1.058	1.062
151.384	1.079	1.057	151.636	0.923	0.980	151.468	1.052	1.057
155.475	1.081	1.059	155.735	0.926	0.983	155.562	1.047	1.052
159.567	1.079	1.056	159.833	0.927	0.984	159.656	1.043	1.048
163.658	1.073	1.050	163.931	0.928	0.983	163.749	1.039	1.044
167.750	1.068	1.045	168.029	0.928	0.981	167.843	1.037	1.042
171.841	1.066	1.043	172.128	0.927	0.979	171.937	1.033	1.038
175.933	1.067	1.043	176.226	0.926	0.979	176.031	1.029	1.032
180.024	1.067	1.043	180.324	0.927	0.978	180.124	1.025	1.028
184.116	1.067	1.042	184.422	0.927	0.978	184.218	1.022	1.025
188.207	1.068	1.042	188.521	0.927	0.976	188.312	1.021	1.024
192.299	1.067	1.041	192.619	0.927	0.975	192.405	1.018	1.022
196.390	1.067	1.040	196.717	0.929	0.977	196.499	1.016	1.021
200.481	1.065	1.038	200.816	0.931	0.979	200.593	1.015	1.019
204.573	1.064	1.037	204.914	0.932	0.980	204.687	1.012	1.016
208.664	1.065	1.039	209.012	0.933	0.980	208.780	1.011	1.015
212.756	1.066	1.041	213.110	0.934	0.980	212.874	1.012	1.016
216.847	1.068	1.043	217.209	0.935	0.980	216.968	1.014	1.017
220.939	1.068	1.043	221.307	0.933	0.977	221.062	1.015	1.018
225.030	1.068	1.043	225.405	0.930	0.973	225.155	1.017	1.019
229.122	1.069	1.044	229.504	0.929	0.971	229.249	1.017	1.020
233.213	1.069	1.044	233.602	0.930	0.971	233.343	1.019	1.021
237.305	1.068	1.042	237.700	0.932	0.972	237.437	1.019	1.022
241.396	1.065	1.041	241.798	0.932	0.973	241.530	1.019	1.022
245.488	1.064	1.040	245.897	0.932	0.972	245.624	1.020	1.023
249.579	1.062	1.039	249.995	0.931	0.970	249.718	1.022	1.026
253.670	1.059	1.037	254.093	0.931	0.969	253.811	1.026	1.029
257.762	1.058	1.036	258.191	0.931	0.968	257.905	1.028	1.031
261.853	1.057	1.036	262.290	0.931	0.967	261.999	1.028	1.031
265.945	1.059	1.038	266.388	0.932	0.968	266.093	1.026	1.029
270.036	1.059	1.039	270.486	0.933	0.968	270.186	1.025	1.028
274.128	1.058	1.039	274.585	0.934	0.969	274.280	1.025	1.028
278.219	1.057	1.039	278.683	0.935	0.970	278.374	1.026	1.028
282.311	1.055	1.037	282.781	0.935	0.969	282.468	1.027	1.028
286.402	1.053	1.036	286.879	0.935	0.968	286.561	1.025	1.026
290.494	1.051	1.035	290.978	0.934	0.966	290.655	1.023	1.023
294.585	1.050	1.035	295.076	0.933	0.965	294.749	1.019	1.020
298.676	1.050	1.036	299.174	0.933	0.963	298.843	1.018	1.019
302.768	1.049	1.035	303.273	0.933	0.962	302.936	1.018	1.017
306.859	1.047	1.033	307.371	0.933	0.962	307.030	1.016	1.015
310.951	1.046	1.033	311.469	0.935	0.963	311.124	1.013	1.013
315.042	1.046	1.032	315.567	0.937	0.965	315.217	1.011	1.012
319.134	1.045	1.032	319.666	0.938	0.965	319.311	1.011	1.011
323.225	1.043	1.031	323.764	0.938	0.964	323.405	1.009	1.010
327.317	1.041	1.030	327.862	0.938	0.962	327.499	1.005	1.005
331.408	1.040	1.030	331.960	0.939	0.963	331.592	1.003	1.002
335.500	1.041	1.030	336.059	0.940	0.963	335.686	1.000	1.000

Sample 1100w-8h Tmt Population1			Sample 1100w-8h Tmt Population1			Sample 1100w-8h Tmt Population1		
VOI in hoter (ΔT≈60°) portion of the sample			VOI in the hot-central (ΔT≈70°) portion of the sample			VOI in the colder-central (ΔT≈90°) portion of the sample		
600-1-POP2			600-2-POP2			600-3-POP2		
339.591	1.040	1.030	340.157	0.941	0.963	339.780	0.998	0.998
343.683	1.040	1.031	344.255	0.942	0.964	343.874	0.995	0.996
347.774	1.039	1.031	348.354	0.944	0.965	347.967	0.994	0.995
351.865	1.037	1.029	352.452	0.947	0.967	352.061	0.993	0.994
355.957	1.037	1.030	356.550	0.948	0.968	356.155	0.992	0.993
360.048	1.039	1.033	360.648	0.950	0.970	360.248	0.992	0.993
364.140	1.040	1.035	364.747	0.953	0.971	364.342	0.991	0.994
368.231	1.041	1.036	368.845	0.954	0.973	368.436	0.990	0.993
372.323	1.039	1.035	372.943	0.955	0.973	372.530	0.985	0.989
376.414	1.037	1.034	377.042	0.957	0.975	376.623	0.982	0.986
380.506	1.037	1.035	381.140	0.960	0.977	380.717	0.981	0.986
384.597	1.037	1.036	385.238	0.962	0.978	384.811	0.980	0.986
388.689	1.037	1.037	389.336	0.963	0.979	388.905	0.977	0.984
392.780	1.037	1.038	393.435	0.964	0.980	392.998	0.973	0.980
396.871	1.037	1.038	397.533	0.968	0.983	397.092	0.969	0.976
400.963	1.036	1.038	401.631	0.970	0.985	401.186	0.966	0.974
405.054	1.033	1.037	405.729	0.972	0.986	405.280	0.963	0.973
409.146	1.030	1.035	409.828	0.974	0.988	409.373	0.960	0.970
413.237	1.026	1.032	413.926	0.975	0.989	413.467	0.957	0.968
417.329	1.022	1.030	418.024	0.977	0.990	417.561	0.955	0.967
421.420	1.018	1.027	422.123	0.977	0.990	421.654	0.954	0.966
425.512	1.013	1.025	426.221	0.978	0.991	425.748	0.952	0.965
429.603	1.009	1.022	430.319	0.979	0.991	429.842	0.950	0.964
433.695	1.005	1.020	434.417	0.979	0.992	433.936	0.949	0.963
437.786	1.000	1.017	438.516	0.981	0.993	438.029	0.948	0.962
441.878	0.996	1.015	442.614	0.984	0.996	442.123	0.947	0.962
445.969	0.992	1.013	446.712	0.986	0.998	446.217	0.946	0.961
450.060	0.988	1.011	450.811	0.987	0.999	450.311	0.946	0.961
454.152	0.982	1.008	454.909	0.986	0.998	454.404	0.946	0.961
458.243	0.976	1.003	459.007	0.987	0.999	458.498	0.946	0.962
462.335	0.971	1.000	463.105	0.990	1.002	462.592	0.946	0.962
466.426	0.966	0.997	467.204	0.994	1.005	466.686	0.946	0.963
470.518	0.961	0.996	471.302	0.996	1.008	470.779	0.947	0.963
474.609	0.957	0.994	475.400	0.998	1.009	474.873	0.947	0.963
478.701	0.951	0.991	479.498	1.000	1.012	478.967	0.950	0.966
482.792	0.947	0.989	483.597	1.002	1.014	483.060	0.951	0.968
486.884	0.941	0.986	487.695	1.005	1.015	487.154	0.952	0.970
490.975	0.934	0.982	491.793	1.006	1.017	491.248	0.951	0.970
495.066	0.927	0.979	495.892	1.008	1.018	495.342	0.952	0.971
499.158	0.922	0.977	499.990	1.010	1.021	499.435	0.953	0.973
503.249	0.917	0.975	504.088	1.013	1.024	503.529	0.954	0.973
507.341	0.913	0.973	508.186	1.016	1.027	507.623	0.954	0.973
511.432	0.908	0.971	512.285	1.019	1.029	511.717	0.955	0.974
515.524	0.903	0.969	516.383	1.022	1.032	515.810	0.958	0.979
519.615	0.899	0.968	520.481	1.025	1.036	519.904	0.961	0.984

Sample 1100w-8h Tmt Population1 VOI in the colder (ΔT≈100°) portion of the sample 600-4-POP1			Sample 1100w-8h Tmt Population3 VOI in hoter (ΔT≈60°) portion of the sample 600-1-POP3			Sample 1100w-8h Tmt Population3 VOI in the colder-central (ΔT≈90°) portion 600-3-POP3		
r [µm]	**trans**	**iso**	**r [µm]**	**trans**	**iso**	**r [µm]**	**trans**	**iso**
0.000	0.447	0.436	0.000	0.279	0.288	0.000	0.176	0.181
4.091	0.411	0.401	4.091	0.576	0.598	4.094	0.478	0.488
8.183	0.386	0.376	8.183	0.929	0.965	8.187	0.859	0.877
12.274	0.392	0.379	12.274	1.320	1.372	12.281	1.301	1.326
16.366	0.425	0.407	16.366	1.750	1.818	16.375	1.734	1.761
20.457	0.473	0.450	20.457	2.062	2.135	20.469	1.994	2.013
24.549	0.523	0.495	24.549	2.180	2.251	24.562	2.034	2.043
28.640	0.567	0.535	28.640	2.192	2.253	28.656	1.962	1.961
32.732	0.609	0.579	32.732	2.122	2.168	32.750	1.884	1.876
36.823	0.636	0.607	36.823	2.047	2.080	36.844	1.810	1.798
40.915	0.655	0.630	40.915	1.980	2.001	40.937	1.730	1.713
45.006	0.728	0.705	45.006	1.919	1.932	45.031	1.672	1.648
49.098	0.801	0.782	49.098	1.860	1.862	49.125	1.631	1.601
53.189	0.859	0.844	53.189	1.818	1.807	53.219	1.588	1.554
57.280	0.909	0.898	57.280	1.798	1.776	57.312	1.552	1.518
61.372	0.935	0.927	61.372	1.781	1.750	61.406	1.520	1.484
65.463	0.950	0.945	65.463	1.764	1.725	65.500	1.477	1.441
69.555	0.966	0.960	69.555	1.743	1.698	69.593	1.436	1.400
73.646	0.990	0.981	73.646	1.715	1.664	73.687	1.402	1.367
77.738	1.024	1.009	77.738	1.682	1.626	77.781	1.369	1.336
81.829	1.063	1.044	81.829	1.653	1.590	81.875	1.338	1.307
85.921	1.095	1.073	85.921	1.635	1.565	85.968	1.311	1.280
90.012	1.125	1.102	90.012	1.622	1.548	90.062	1.282	1.251
94.104	1.145	1.122	94.104	1.612	1.532	94.156	1.258	1.226
98.195	1.165	1.142	98.195	1.598	1.514	98.250	1.241	1.207
102.286	1.176	1.153	102.286	1.577	1.488	102.343	1.230	1.197
106.378	1.193	1.169	106.378	1.552	1.458	106.437	1.222	1.189
110.469	1.204	1.179	110.469	1.520	1.421	110.531	1.216	1.182
114.561	1.214	1.187	114.561	1.496	1.393	114.625	1.209	1.175
118.652	1.220	1.188	118.652	1.481	1.373	118.718	1.203	1.167
122.744	1.221	1.183	122.744	1.472	1.358	122.812	1.195	1.157
126.835	1.214	1.171	126.835	1.463	1.343	126.906	1.195	1.155
130.927	1.196	1.148	130.927	1.454	1.326	130.999	1.195	1.156
135.018	1.166	1.114	135.018	1.441	1.310	135.093	1.190	1.152
139.110	1.144	1.092	139.110	1.429	1.294	139.187	1.183	1.145
143.201	1.118	1.068	143.201	1.417	1.280	143.281	1.180	1.143
147.293	1.091	1.044	147.293	1.410	1.272	147.374	1.176	1.140
151.384	1.071	1.029	151.384	1.407	1.268	151.468	1.177	1.141
155.475	1.052	1.015	155.475	1.407	1.266	155.562	1.179	1.143
159.567	1.047	1.014	159.567	1.404	1.261	159.656	1.181	1.144
163.658	1.049	1.019	163.658	1.394	1.252	163.749	1.179	1.142
167.750	1.054	1.027	167.750	1.387	1.245	167.843	1.177	1.138
171.841	1.058	1.033	171.841	1.377	1.236	171.937	1.171	1.131
175.933	1.071	1.046	175.933	1.371	1.229	176.031	1.165	1.126
180.024	1.082	1.055	180.024	1.364	1.223	180.124	1.160	1.121
184.116	1.090	1.061	184.116	1.361	1.220	184.218	1.155	1.117
188.207	1.095	1.064	188.207	1.360	1.220	188.312	1.149	1.113
192.299	1.091	1.059	192.299	1.357	1.219	192.405	1.142	1.107
196.390	1.093	1.060	196.390	1.354	1.219	196.499	1.135	1.100
200.481	1.094	1.060	200.481	1.350	1.218	200.593	1.130	1.096
204.573	1.091	1.058	204.573	1.346	1.217	204.687	1.124	1.091

Sample 1100w-8h Tmt Population1 VOI in the colder (ΔT≈100°) portion of the sample 600-4-POP1			Sample 1100w-8h Tmt Population3 VOI in hoter (ΔT≈60°) portion of the sample 600-1-POP3			Sample 1100w-8h Tmt Population3 VOI in the colder-central (ΔT≈90°) portion 600-3-POP3		
208.664	1.093	1.061	208.664	1.340	1.214	208.780	1.119	1.087
212.756	1.094	1.062	212.756	1.336	1.213	212.874	1.114	1.083
216.847	1.097	1.065	216.847	1.331	1.212	216.968	1.110	1.081
220.939	1.103	1.072	220.939	1.327	1.211	221.062	1.109	1.081
225.030	1.103	1.074	225.030	1.322	1.210	225.155	1.110	1.084
229.122	1.096	1.070	229.122	1.317	1.209	229.249	1.111	1.086
233.213	1.094	1.072	233.213	1.313	1.208	233.343	1.110	1.087
237.305	1.096	1.076	237.305	1.307	1.206	237.437	1.107	1.084
241.396	1.099	1.082	241.396	1.302	1.204	241.530	1.101	1.079
245.488	1.102	1.088	245.488	1.295	1.201	245.624	1.096	1.073
249.579	1.097	1.085	249.579	1.287	1.197	249.718	1.090	1.068
253.670	1.084	1.074	253.670	1.279	1.192	253.811	1.085	1.066
257.762	1.072	1.064	257.762	1.273	1.190	257.905	1.081	1.064
261.853	1.056	1.051	261.853	1.269	1.189	261.999	1.078	1.063
265.945	1.047	1.044	265.945	1.262	1.187	266.093	1.074	1.060
270.036	1.039	1.039	270.036	1.255	1.184	270.186	1.071	1.057
274.128	1.031	1.031	274.128	1.246	1.178	274.280	1.065	1.052
278.219	1.029	1.027	278.219	1.237	1.171	278.374	1.059	1.047
282.311	1.027	1.024	282.311	1.226	1.164	282.468	1.054	1.043
286.402	1.019	1.017	286.402	1.219	1.160	286.561	1.049	1.039
290.494	1.012	1.010	290.494	1.214	1.158	290.655	1.044	1.035
294.585	1.010	1.008	294.585	1.210	1.157	294.749	1.041	1.033
298.676	1.015	1.013	298.676	1.204	1.156	298.843	1.038	1.030
302.768	1.026	1.024	302.768	1.196	1.151	302.936	1.033	1.025
306.859	1.033	1.030	306.859	1.185	1.142	307.030	1.028	1.020
310.951	1.034	1.031	310.951	1.174	1.134	311.124	1.022	1.015
315.042	1.033	1.031	315.042	1.163	1.126	315.217	1.019	1.011
319.134	1.030	1.030	319.134	1.154	1.119	319.311	1.018	1.010
323.225	1.031	1.033	323.225	1.145	1.112	323.405	1.017	1.009
327.317	1.032	1.035	327.317	1.137	1.105	327.499	1.015	1.007
331.408	1.034	1.038	331.408	1.126	1.096	331.592	1.013	1.005
335.500	1.040	1.043	335.500	1.112	1.084	335.686	1.011	1.003
339.591	1.045	1.047	339.591	1.098	1.072	339.780	1.009	1.001
343.683	1.043	1.045	343.683	1.084	1.061	343.874	1.009	1.001
347.774	1.037	1.038	347.774	1.075	1.054	347.967	1.009	1.001
351.865	1.028	1.028	351.865	1.067	1.048	352.061	1.006	0.997
355.957	1.019	1.018	355.957	1.061	1.043	356.155	1.000	0.992
360.048	1.012	1.010	360.048	1.054	1.037	360.248	0.996	0.988
364.140	1.004	1.001	364.140	1.045	1.030	364.342	0.993	0.985
368.231	0.995	0.990	368.231	1.037	1.023	368.436	0.991	0.984
372.323	0.985	0.979	372.323	1.028	1.016	372.530	0.992	0.985
376.414	0.978	0.971	376.414	1.022	1.012	376.623	0.990	0.983
380.506	0.973	0.967	380.506	1.015	1.008	380.717	0.986	0.979
384.597	0.969	0.964	384.597	1.008	1.003	384.811	0.982	0.976
388.689	0.971	0.966	388.689	0.999	0.996	388.905	0.979	0.974
392.780	0.978	0.973	392.780	0.987	0.986	392.998	0.977	0.972
396.871	0.986	0.982	396.871	0.976	0.977	397.092	0.975	0.972
400.963	0.989	0.985	400.963	0.966	0.969	401.186	0.971	0.968
405.054	0.993	0.989	405.054	0.957	0.963	405.280	0.964	0.961
409.146	0.994	0.991	409.146	0.951	0.958	409.373	0.959	0.957
413.237	0.992	0.989	413.237	0.942	0.952	413.467	0.955	0.954
417.329	0.986	0.984	417.329	0.932	0.944	417.561	0.952	0.952
421.420	0.981	0.980	421.420	0.920	0.934	421.654	0.950	0.950
425.512	0.975	0.975	425.512	0.909	0.925	425.748	0.948	0.949
429.603	0.972	0.972	429.603	0.898	0.917	429.842	0.944	0.946
433.695	0.968	0.969	433.695	0.888	0.908	433.936	0.941	0.943

Sample 1100w-8h Tmt Population1 VOI in the colder (ΔT≈100°) portion of the sample 600-4-POP1			Sample 1100w-8h Tmt Population3 VOI in hoter (ΔT≈60°) portion of the sample 600-1-POP3			Sample 1100w-8h Tmt Population3 VOI in the colder-central (ΔT≈90°) portion 600-3-POP3		
437.786	0.964	0.965	437.786	0.879	0.902	438.029	0.938	0.941
441.878	0.963	0.964	441.878	0.872	0.897	442.123	0.936	0.939
445.969	0.960	0.962	445.969	0.863	0.891	446.217	0.934	0.938
450.060	0.962	0.964	450.060	0.854	0.884	450.311	0.932	0.937
454.152	0.967	0.970	454.152	0.844	0.876	454.404	0.930	0.936
458.243	0.970	0.973	458.243	0.833	0.867	458.498	0.927	0.935
462.335	0.974	0.978	462.335	0.821	0.858	462.592	0.927	0.935
466.426	0.978	0.984	466.426	0.810	0.849	466.686	0.927	0.936
470.518	0.981	0.989	470.518	0.803	0.844	470.779	0.927	0.937
474.609	0.977	0.988	474.609	0.797	0.840	474.873	0.924	0.936
478.701	0.972	0.986	478.701	0.790	0.835	478.967	0.923	0.936
482.792	0.962	0.980	482.792	0.783	0.829	483.060	0.920	0.936
486.884	0.955	0.978	486.884	0.773	0.821	487.154	0.919	0.936
490.975	0.945	0.974	490.975	0.763	0.812	491.248	0.917	0.935
495.066	0.936	0.968	495.066	0.752	0.803	495.342	0.915	0.936
499.158	0.928	0.961	499.158	0.743	0.798	499.435	0.913	0.935
503.249	0.916	0.950	503.249	0.737	0.794	503.529	0.911	0.935
507.341	0.906	0.939	507.341	0.732	0.792	507.623	0.910	0.936
511.432	0.897	0.928	511.432	0.729	0.792	511.717	0.910	0.939
515.524	0.886	0.918	515.524	0.725	0.792	515.810	0.908	0.938
519.615	0.880	0.912	519.615	0.720	0.788	519.904	0.905	0.940

Sample 1100w-8h Tmt Population1 VOI in the colder (ΔT≈100°) portion of the sample 600-4-POP2

r [µm]	trans	iso
0.000	0.023	0.024
4.091	0.144	0.146
8.183	0.402	0.412
12.274	0.805	0.831
16.366	1.169	1.212
20.457	1.359	1.414
24.549	1.399	1.459
28.640	1.390	1.449
32.732	1.363	1.423
36.823	1.319	1.378
40.915	1.270	1.330
45.006	1.231	1.291
49.098	1.194	1.253
53.189	1.162	1.222
57.280	1.131	1.192
61.372	1.107	1.169
65.463	1.085	1.146
69.555	1.058	1.118
73.646	1.034	1.094
77.738	1.018	1.078
81.829	1.003	1.064
85.921	0.991	1.053
90.012	0.978	1.039
94.104	0.968	1.029
98.195	0.961	1.021
102.286	0.955	1.014
106.378	0.950	1.008

Sample 1100w-8h Tmt Population1 VOI in the colder (ΔT≈100°) portion of the sample 600-4-POP2		
110.469	0.945	1.003
114.561	0.939	0.997
118.652	0.935	0.993
122.744	0.931	0.988
126.835	0.930	0.985
130.927	0.930	0.985
135.018	0.929	0.984
139.110	0.928	0.982
143.201	0.925	0.978
147.293	0.923	0.975
151.384	0.922	0.974
155.475	0.922	0.973
159.567	0.921	0.972
163.658	0.922	0.972
167.750	0.923	0.973
171.841	0.921	0.971
175.933	0.922	0.971
180.024	0.923	0.971
184.116	0.924	0.971
188.207	0.925	0.972
192.299	0.924	0.972
196.390	0.926	0.972
200.481	0.926	0.971
204.573	0.929	0.973
208.664	0.932	0.976
212.756	0.935	0.980
216.847	0.937	0.982
220.939	0.939	0.982
225.030	0.941	0.983
229.122	0.944	0.984
233.213	0.946	0.986
237.305	0.949	0.988
241.396	0.953	0.991
245.488	0.956	0.992
249.579	0.957	0.993
253.670	0.957	0.993
257.762	0.958	0.993
261.853	0.959	0.993
265.945	0.960	0.993
270.036	0.963	0.995
274.128	0.966	0.996
278.219	0.967	0.996
282.311	0.968	0.997
286.402	0.968	0.996
290.494	0.967	0.994
294.585	0.966	0.993
298.676	0.965	0.992
302.768	0.965	0.991
306.859	0.966	0.990
310.951	0.965	0.989
315.042	0.966	0.988
319.134	0.965	0.987
323.225	0.964	0.987
327.317	0.965	0.987
331.408	0.966	0.987
335.500	0.966	0.987

Sample 1100w-8h Tmt Population1 VOI in the colder (ΔT≈100°) portion of the sample 600-4-POP2		
339.591	0.966	0.986
343.683	0.965	0.984
347.774	0.963	0.982
351.865	0.962	0.981
355.957	0.962	0.981
360.048	0.962	0.981
364.140	0.960	0.979
368.231	0.958	0.977
372.323	0.957	0.975
376.414	0.956	0.974
380.506	0.955	0.974
384.597	0.955	0.973
388.689	0.956	0.974
392.780	0.956	0.974
396.871	0.957	0.975
400.963	0.957	0.976
405.054	0.958	0.977
409.146	0.961	0.978
413.237	0.962	0.979
417.329	0.963	0.981
421.420	0.964	0.982
425.512	0.966	0.983
429.603	0.967	0.984
433.695	0.969	0.986
437.786	0.970	0.987
441.878	0.972	0.988
445.969	0.973	0.989
450.060	0.977	0.993
454.152	0.981	0.996
458.243	0.983	0.998
462.335	0.984	0.999
466.426	0.985	0.999
470.518	0.986	1.001
474.609	0.986	1.001
478.701	0.987	1.001
482.792	0.989	1.003
486.884	0.992	1.005
490.975	0.996	1.007
495.066	0.999	1.008
499.158	1.001	1.010
503.249	1.005	1.013
507.341	1.009	1.016
511.432	1.013	1.019
515.524	1.016	1.020
519.615	1.019	1.020

Modal analysis and diameters of the crystla phases in the experimental samples used in Chapter 3

Sample	H_2O wt%	Dwell time	D - UD	Temperture [°C]	Cpx area %		Spl area %
Cr-doped samples							
1150d-Cr-doped-5min	0	5	D	1150	25-40		< 5
1150w-Cr-doped-5min	2	5	D	1150	/		< 5
1100d-Cr-doped-5min	0	5	D	1100	30-40		< 5
1100w-Cr-doped-5min	2	5	D	1100	/		< 5
1050d-Cr-doped-5min	0	5	D	1050	45-50		5-6
1050w-Cr-doped-5min	2	5	D	1050	0-18		< 4
[BIS]1150d-Cr-doped-5min	0	5	D	1150	40-45		4-6
[BIS]1100d-Cr-doped-5min	0	5	D	1100	45		4-5
Undoped samples					**Cpx area % [skeletal d.]**	**Cpx area % [dendritic d.]**	**Spl area % [skeletal d.]**
1150d-Undoped-30min	0	30	UD	1150	**/**	**55-65**	**/**
1100d-Undoped-30min	0	30	UD	1100	**50**	**55-65**	**/**
1050d-Undoped-30min	0	30	UD	1050	**/**	**55-65**	**/**
1100w-Undoped-30min	2	30	UD	1100			
1150d-Undoped-5min	0	5	UD	1150	45-50	45	5
1100d-Undoped-5min	0	5	UD	1100	50	50	5-6
1100d-Undoped-0min	0	0	UD	1100	/	/	/

Sample	Cpx max diameter [µm]	Spl max diameter [µm]
Cr-doped samples		
1150d-Cr-doped-5min	< 120	< 3
1150w-Cr-doped-5min	/	< 5
1100d-Cr-doped-5min	< 120	< 3
1100w-Cr-doped-5min	/	< 5
1050d-Cr-doped-5min	< 50	< 3
1050w-Cr-doped-5min	< 500	< 4
[BIS]1150d-Cr-doped-5min	< 70	< 3
[BIS]1100d-Cr-doped-5min	< 70	< 3

Undoped samples	Spl area % [dendritic d.]	Cpx max diameter [skeletal d.] [µm]	Cpx max diameter [feather d.] [µm]	Spl max diameter [skeletal d.] [µm]	Spl max diameter [dendritic d.] [µm]
1150d-Undoped-30min	**2-3**	**/**	**< 300**	**/**	**< 30**
1100d-Undoped-30min	**2-3**		**< 250**		**< 10**
1050d-Undoped-30min	**2-3**	**/**	**< 250**	**/**	**< 10**
1100w-Undoped-30min					
1150d-Undoped-5min	2.5	< 50	< 200	< 5	< 50
1100d-Undoped-5min	2.5	< 50	< 200	< 6	< 30
1100d-Undoped-0min	/	/	/	/	/

Sheet "EBSD_parameters_legenda" for the supplementary data of Chapter 3 preliminary article draft

EBSD parameters Legenda		Legenda for the parameters formulas	Parameters Formulas
CORs	Crystallographic Orientation Relationships		
Tmt/Spl	Titanomagnetite or Spinel. It does **not** represent a fraction. Tmt is the most common composition of Spl grains in undoped samples. Spl (s.l) for the doped ones		
Area in µm^2	Area of the Sample scanned (in µm^2)	0	EBSD result
N_Tmt/Spl_Grains	Number of Tmt/Spl grains	1	EBSD result
N_Tmt/Spl_Filtered	Number of Tmt/Spl grains counted after removing non indexed pixel	2	EBSD result
N_CpxGrains	Number of Cpx grains	3	EBSD result
N_Cpx_Filtered	Number of Cpx grains counted after removing non indexed pixel	4	EBSD result
N_Cpx_Filtered[100]	Number of Cpx grains counted after removing non indexed pixel with size larger than 100 µm^2	5	EBSD result
N_Cpx_Filtered[200]	Number of Cpx grains counted after removing non indexed pixel with size larger than 200 µm^2	6	EBSD result
N_Cpx_Filtered[500]	Number of Cpx grains counted after removing non indexed pixel with size larger than 500 µm^2	7	EBSD result
N_Cpx_Filtered[1000]	Number of Cpx grains counted after removing non indexed pixel with size larger than 1000 µm^2	8	EBSD result
Mean_Spl/Tmt_misorientation	Mean Spl/Tmt misorientation of each EBSD pixel relative to the mean orientation of the grain to which it was assigned (mis2mean)	9	EBSD result
Mean_Cpx_misorientation	Mean Cpx misorientation of each EBSD pixel relative to the mean orientation of the grain to which it was assigned (mis2mean)	10	EBSD result
Nunique_MtGrains_incontact	Number of Tmt/Spl in contact with a Cpx	11	EBSD result
Nunique_MtGrains_anyOR	Number of Tmt/Spl in contact with a Cpx and showing any COR	12	EBSD result
Nunique_MtGrains_OR1and2	Number of Tmt/Spl in contact with a Cpx and shearing specific COR 1 or 2	13	EBSD result
Nunique_MtGrains_OR1	Number of Tmt/Spl in contact with a Cpx and shearing specific COR 1	14	EBSD result
Nunique_MtGrains_OR2	Number of Tmt/Spl in contact with a Cpx and shearing specific COR 2	15	EBSD result
Nunique_MtGrains_id3	Number of Tmt/Spl in contact with a Cpx and shearing a COR near 1 and/or 2	16	EBSD result
frac_mt_incontact	Fraction of Tmt/Spl in contact to Cpx compared to the total of Tmt/Spl crystals	17	11/1

EBSD parameters Legenda		Legenda for the parameters formulas	Parameters Formulas
frac_incontact_mt_anyOR	Fraction of Tmt/Spl in contact to Cpx compared to the total of Tmt/Spl crystals shearing any COR with the Cpx in contact	18	12/11
frac_incontact_mt_OR1	Fraction of Tmt/Spl in contact to Cpx compared to the total of Tmt/Spl crystals shearing COR 1 with the Cpx in contact	19	14/12
frac_incontact_mt_OR2	Fraction of Tmt/Spl in contact to Cpx compared to the total of Tmt/Spl crystals shearing COR 2 with the Cpx in contact	20	15/12
frac_incontact_mt_id3	Fraction of Tmt/Spl in contact to Cpx compared to the total of Tmt/Spl crystals shearing CORs near COR1 and/or 2 with the Cpx in contact	21	16/12
GBLength_Di_Tmt/Spl_[µm]	Total grain boundary lenght shared between Cpx and Tmt/Spl	22	EBSD result
GBLength_Tmt/Spl_[µm]	Total Tmt/Spl grain boundary lenght	23	EBSD result
GBLength_Di_[µm]	Total Cpx grain boundary lenght	24	EBSD result
GBLength_OR1_[µm]	Total grain boundary lenght shared between Cpx and Tmt/Spl characterized by COR1	25	EBSD result
GBLength_OR2_[µm]	Total grain boundary lenght shared between Cpx and Tmt/Spl characterized by COR2	26	EBSD result
GBLength_id3_[µm]	Total grain boundary lenght shared between Cpx and Tmt/Spl characterized by an COR near 1 and/or 2	27	EBSD result
GBLength_anyOR_[µm]	Total grain boundary lenght shared between Cpx and Tmt/Spl characterized by any CORs	28	EBSD result
BLFincontactTmt/Spl	Boundary lenght fraction of Tmt/Spl in contact with a Cpx	29	22/23
BLFincontactCpx	Boundary lenght fraction of Cpx in contact with a Tmt/Spl	30	22/24
BLF_{anyCOR}	Grain Boundary lenght fraction shared between Tmt/Spl and Cpx and characterized by any COR	31	28/22
BLF_{COR1}	Grain Boundary lenght fraction shared between Tmt/Spl and Cpx and characterized by COR1	32	25/22
BLF_{COR2}	Grain Boundary lenght fraction shared between Tmt/Spl and Cpx and characterized by COR2	33	26/22
$BLF_{nearCOR}$	Grain Boundary lenght fraction shared between Tmt/Spl and Cpx and characterized a COR near COR1 and/or 2	34	27/22
BLF_{noCORs}	Grain Boundary lenght fraction shared between Tmt/Spl and Cpx and characterized by no COR	35	(22-28)/22

Sheet "EBSD-raw_CORs-Cr-doped" for the supplementary data of Chapter 3 preliminary article draft

all the EBSD scans	1150d_5min_Cr_doped			1100d_5min_Cr_doped		
GB_and_CORs_stats	Scan_01	Scan_02	Scan_03	Scan_01	Scan_02	Scan_03
Area in µm2	19500	40000	40000	2680	46225	41925
				n.r		
N_Tmt/Spl_Grains	1457	2342	1779	631	1650	1615
N_Tmt/Spl_Filtered	**1440**	**2283**	**1742**	**620**	**1614**	**1576**
N_CpxGrains	483	318	291	56	137	124
N_Cpx_Filtered	**380**	**241**	**238**	**37**	**84**	**72**
N_Cpx_Filtered[100]	316	217	221	20	74	64
N_Cpx_Filtered[200]	281	202	211	16	71	63
N_Cpx_Filtered[500]	181	182	191	11	69	57
N_Cpx_Filtered[1000]	93	161	167	10	65	47
Mean_Spl_misorientation	0.512	0.618	0.614	1.007	0.662	0.636
Mean_Cpx_misorientation	0.718	0.738	0.588	1.016	0.899	0.859
Nunique_MtGrains_incontact	1032	1262	1051	270	793	735
Nunique_MtGrains_anyOR	29	19	23	3	8	4
Nunique_MtGrains_OR1and2	29	17	22	1	7	3
Nunique_MtGrains_OR1	1	3	1	0	1	1
Nunique_MtGrains_OR2	28	15	21	1	6	2
Nunique_MtGrains_id3	10	8	7	2	4	3
frac_mt_incontact	0.708	0.539	0.591	0.428	0.481	0.455
frac_incontact_mt_anyOR	0.028	0.015	0.022	0.011	0.010	0.005
frac_incontact_mt_OR1	0.001	0.002	0.001	0.000	0.001	0.001
frac_incontact_mt_OR2	0.027	0.012	0.020	0.004	0.008	0.003
frac_incontact_mt_id3	0.010	0.006	0.007	0.007	0.005	0.004
GBLength_Di_Tmt/Spl_[µm]	1591.847	2190.223	1907.286	286.029	1540.824	1391.422
GBLength_Tmt/Spl_[µm]	4797.430	8525.458	6542.271	1753.408	6388.839	6066.725
GBLength_Di_[µm]	11288.165	14770.919	13995.671	1265.334	10517.621	9360.988
GBLength_OR1_[µm]	0.571	6.451	0.544	0.000	1.634	0.410
GBLength_OR2_[µm]	66.667	44.139	63.958	4.117	22.674	3.917
GBLength_id3_[µm]	5.420	3.856	4.523	0.146	3.943	6.099
GBLength_anyOR_[µm]	72.658	54.446	69.025	4.263	28.250	10.426
BLFincontactTmt/Spl	0.332	0.257	0.292	0.163	0.241	0.229
BLFincontactCpx	0.141	0.148	0.136	0.226	0.146	0.149
BLF_{anyCOR}	**0.046**	**0.025**	**0.036**	**0.015**	**0.018**	**0.007**
BLF_{COR1}	**0.000**	**0.003**	**0.000**	**0.000**	**0.001**	**0.000**
BLF_{COR2}	**0.042**	**0.020**	**0.034**	**0.014**	**0.015**	**0.003**
$BLF_{nearCOR}$	**0.003**	**0.002**	**0.002**	**0.001**	**0.003**	**0.004**
BLF_{noCORs}	**0.954**	**0.975**	**0.964**	**0.985**	**0.982**	**0.993**

n.r.= not representative area scanned

all the EBSD scans	1050d_5min_Cr_doped		1050w_5min_Cr_doped		
GB_and_CORs_stats	Scan_01	Scan_02	Scan_01	Scan_02	Scan_03
Area in µm2	40000	39600	3025	3720	2750
N_Tmt/Spl_Grains	2495	2611	126	106	119
N_Tmt/Spl_Filtered	**2470**	**2575**	**126**	**106**	**116**
N_CpxGrains	903	834	119	47	64
N_Cpx_Filtered	**734**	**693**	**110**	**47**	**56**
N_Cpx_Filtered[100]	635	600	4	1	2
N_Cpx_Filtered[200]	561	523	1	1	2
N_Cpx_Filtered[500]	386	363	1	1	2
N_Cpx_Filtered[1000]	221	198	1	1	1
Mean_Spl_misorientation	0.505	0.490	0.420	0.327	0.607
Mean_Cpx_misorientation	0.710	0.779	0.950	0.501	0.518
Nunique_MtGrains_incontact	1761	1845	95	77	58
Nunique_MtGrains_anyOR	81	76	18	10	15
Nunique_MtGrains_OR1and2	74	74	18	10	15
Nunique_MtGrains_OR1	1	2	3	0	2
Nunique_MtGrains_OR2	73	73	17	10	13
Nunique_MtGrains_id3	26	12	3	2	0
frac_mt_incontact	0.706	0.707	0.754	0.726	0.487
frac_incontact_mt_anyOR	0.046	0.041	0.189	0.130	0.259
frac_incontact_mt_OR1	0.001	0.001	0.032	0.000	0.034
frac_incontact_mt_OR2	0.041	0.040	0.179	0.130	0.224
frac_incontact_mt_id3	0.015	0.007	0.032	0.026	0.000
GBLength_Di_Tmt/Spl_[µm]	2638.328	2723.817	189.320	179.330	111.831
GBLength_Tmt/Spl_[µm]	8114.817	8359.050	461.153	357.662	452.539
GBLength_Di_[µm]	22610.669	22197.208	1018.563	763.225	566.269
GBLength_OR1_[µm]	1.246	0.512	1.256	0.000	0.520
GBLength_OR2_[µm]	182.761	168.803	18.598	6.011	10.021
GBLength_id3_[µm]	17.201	8.714	0.456	0.600	0.000
GBLength_anyOR_[µm]	201.208	178.029	20.310	6.612	10.541
BLFincontactTmt/Spl	0.325	0.326	0.411	0.501	0.247
BLFincontactCpx	0.117	0.123	0.186	0.235	0.197
BLF_{anyCOR}	**0.076**	**0.065**	**0.107**	**0.037**	**0.094**
BLF_{COR1}	**0.000**	**0.000**	**0.007**	**0.000**	**0.005**
BLF_{COR2}	**0.069**	**0.062**	**0.098**	**0.034**	**0.090**
$BLF_{nearCOR}$	**0.007**	**0.003**	**0.002**	**0.003**	**0.000**
BLF_{noCORs}	**0.924**	**0.935**	**0.893**	**0.963**	**0.906**

n.r.= not representative area scanned

all the EBSD scans	Cr_doped_ total	Cr_doped_total_de nsity [mm^{-1}]
GB_and_CORs_stats Area in µm2	Area in µm2 267250	Area in mm2 0.26725
N_Tmt/Spl_Grains	**13949**	**52195**
N_Tmt/Spl_Filtered	**13700**	**51263**
N_CpxGrains	**3090**	**11562**
N_Cpx_Filtered	**2442**	**9138**
N_Cpx_Filtered[100]	2127	7959
N_Cpx_Filtered[200]	1912	7154
N_Cpx_Filtered[500]	1429	5347
N_Cpx_Filtered[1000]	**952**	3562
Mean_Spl_misorientation		
Mean_Cpx_misorientation		
Nunique_MtGrains_incontact	8479	31727
Nunique_MtGrains_anyOR	240	898
Nunique_MtGrains_OR1and2	226	846
Nunique_MtGrains_OR1	10	37
Nunique_MtGrains_OR2	218	816
Nunique_MtGrains_id3	70	262
frac_mt_incontact	**0.608**	
frac_incontact_mt_anyOR	0.028	
frac_incontact_mt_OR1	0.001	
frac_incontact_mt_OR2	0.026	
frac_incontact_mt_id3	0.008	
GBLength_Di_Tmt/Spl_[µm]	13984	52324.587
GBLength_Tmt/Spl_[µm]	48795	182580.316
GBLength_Di_[µm]	104741	391922.320
GBLength_OR1_[µm]	11	42.538
GBLength_OR2_[µm]	553	2068.918
GBLength_id3_[µm]	50	186.178
GBLength_anyOR_[µm]	614	**2297.633**
BLFincontactTmt/Spl	0.287	
BLFincontactCpx	0.134	
BLF_{anyCOR}	**0.044**	
BLF_{COR1}	**0.001**	
BLF_{COR2}	**0.040**	
$BLF_{nearCOR}$	**0.004**	
BLF_{noCORs}	**0.956**	

n.r.= not representative area scanned

results sample by sample	1150d_5min_Cr_doped	1150d_5min_Cr_doped_density [mm-1]	1100d_5min_Cr_doped	1100d_5min_Cr_doped_density [mm-1]
GB_and_CORs_stats	Area in µm2	Area in mm2	Area in µm2	Area in mm2
Area in µm2	99500	0.100	88150	0.08815
N_Tmt/Spl_Grains	5578	56060.302	3265	37039.138
N_Tmt/Spl_Filtered	**5465**	**54924.623**	**3190**	**36188.315**
N_CpxGrains	1092	10974.874	261	2960.862
N_Cpx_Filtered	**859**	**8633.166**	**156**	**1769.711**
N_Cpx_Filtered[100]	754	7577.889	138	1565.513
N_Cpx_Filtered[200]	694	6974.874	134	1520.136
N_Cpx_Filtered[500]	554	5567.839	126	1429.382
N_Cpx_Filtered[1000]	421	4231.156	112	1270.562
Mean_Spl_misorientation				
Mean_Cpx_misorientation				
Nunique_MtGrains_incontact	3345	33618.090	1798	20397.050
Nunique_MtGrains_anyOR	71	713.568	15	170.164
Nunique_MtGrains_OR1and2	68	683.417	11	124.787
Nunique_MtGrains_OR1	5	50.251	2	22.689
Nunique_MtGrains_OR2	64	643.216	9	102.099
Nunique_MtGrains_id3	25	251.256	9	102.099
frac_mt_incontact	**0.600**		**0.551**	
frac_incontact_mt_anyOR	0.021		0.008	
frac_incontact_mt_OR1	0.001		0.001	
frac_incontact_mt_OR2	0.019		0.005	
frac_incontact_mt_id3	**0.007**	0.075	**0.005**	0.057
GBLength_Di_Tmt/Spl_[µm]	5689.356	57179.453	3218.275	36509.074
GBLength_Tmt/Spl_[µm]	19865.159	199649.835	14208.972	161190.831
GBLength_Di_[µm]	40054.754	402560.345	21143.943	239863.216
GBLength_OR1_[µm]	7.566	76.044	2.044	23.182
GBLength_OR2_[µm]	174.764	1756.417	30.708	348.362
GBLength_id3_[µm]	13.799	138.679	10.188	115.572
GBLength_anyOR_[µm]	196.128	1971.140	42.939	487.116
BLFincontactTmt/Spl	0.286		0.226	
BLFincontactCpx	0.142		0.152	
BLF_{anyCOR}	**0.034**		**0.013**	
BLF_{COR1}	**0.001**		**0.001**	
BLF_{COR2}	**0.031**		**0.010**	
$BLF_{nearCOR}$	**0.002**		**0.003**	
BLF_{noCORs}	**0.966**		**0.987**	

n.r.= not representative area scanned

results sample by sample	1050d_5min_Cr_doped	1050d_5min_Cr_doped [mm-1]	1050w_5min_Cr_doped	1050w_5min_Cr_doped density [mm^{-1}]
GB_and_CORs_stats	Area in µm2	Area in mm2	Area in µm2	Area in mm2
Area in µm2	79600	0.0796	9495	0.009495
N_Tmt/Spl_Grains	5106	64145.729	351	36966.825
N_Tmt/Spl_Filtered	**5045**	**63379.397**	**348**	**36650.869**
N_CpxGrains	1737	21821.608	230	24223.275
N_Cpx_Filtered	**1427**	**17927.136**	213	22432.859
N_Cpx_Filtered[100]	1235	15515.075	**7**	**737.230**
N_Cpx_Filtered[200]	1084	13618.090	4	421.274
N_Cpx_Filtered[500]	749	9409.548	4	421.274
N_Cpx_Filtered[1000]	419	5263.819	3	315.956
Mean_Spl_misorientation				
Mean_Cpx_misorientation				
Nunique_MtGrains_incontact	3606	45301.508	230	24223.275
Nunique_MtGrains_anyOR	157	1972.362	43	4528.699
Nunique_MtGrains_OR1and2	148	1859.296	43	4528.699
Nunique_MtGrains_OR1	3	37.688	5	526.593
Nunique_MtGrains_OR2	146	1834.171	40	4212.744
Nunique_MtGrains_id3	38	477.387	5	526.593
frac_mt_incontact	**0.706**		**0.655**	
frac_incontact_mt_anyOR	0.044		0.187	
frac_incontact_mt_OR1	0.001		0.022	
frac_incontact_mt_OR2	0.040		0.174	
frac_incontact_mt_id3	**0.011**	0.132	**0.022**	2.290
GBLength_Di_Tmt/Spl_[µm]	5362.144	67363.622	480.481	50603.590
GBLength_Tmt/Spl_[µm]	16473.867	206958.127	1271.354	133897.205
GBLength_Di_[µm]	44807.877	562913.029	2348.057	247294.044
GBLength_OR1_[µm]	1.758	22.089	1.775	186.972
GBLength_OR2_[µm]	351.564	4416.628	34.631	3647.278
GBLength_id3_[µm]	25.916	325.572	1.057	111.311
GBLength_anyOR_[µm]	379.237	4764.289	37.463	3945.561
BLFincontactTmt/Spl	0.325		0.378	
BLFincontactCpx	0.120		0.205	
BLF_{anyCOR}	**0.071**		**0.078**	
BLF_{COR1}	**0.000**		**0.004**	
BLF_{COR2}	**0.066**		**0.072**	
$BLF_{nearCOR}$	**0.005**		**0.002**	
BLF_{noCORs}	**0.929**		**0.922**	

n.r.= not representative area scanned

Sheet "EBSD-raw_CORs-Undoped" for the supplementary data of Chapter 3 preliminary article draft

all the EBSD scans	1050d_30min		1100d_30min	
scan name (µstructural domain)	scan_01 (feather-like)	scan_02 (snowflake-like)	scan_01 (feather-like)	scan_02 (skeletal Cpx)
Area_in_µm2	2744	8836	1155	1764
notes				
GB_and_CORs_stats				
N_Tmt/Spl_Grains	**366**	**889**	**194**	**127**
N_Tmt/Spl_Filtered	306	735	165	106
N_CpxGrains	92	500	62	65
N_Cpx_Filtered	20	309	27	56
N_Cpx_Filtered[100]	15	254	18	43
N_Cpx_Filtered[200]	14	236	17	42
N_Cpx_Filtered[500]	11	212	15	39
N_Cpx_Filtered[1000]	8	177	11	34
Mean_Spl_misorientation	1.385	1.202	1.083	0.779
Mean_Cpx_misorientation	8.980	2.110	2.837	0.609
Nunique_MtGrains_incontact	319	708	151	89
Nunique_MtGrains_anyOR	267	486	82	74
Nunique_MtGrains_OR1and2	245	442	75	69
Nunique_MtGrains_OR1	164	261	51	37
Nunique_MtGrains_OR2	136	267	38	41
Nunique_MtGrains_id3	158	281	48	34
frac_mt_incontact	**0.872**	**0.796**	**0.778**	**0.701**
frac_incontact_mt_anyOR	**0.837**	**0.686**	**0.543**	**0.831**
frac_incontact_mt_OR1	0.514	0.369	0.338	0.416
frac_incontact_mt_OR2	0.426	0.377	0.252	0.461
frac_incontact_mt_id3	0.495	0.397	0.318	0.382
GBLength_Di_Tmt/Spl_[µm]	232.963	461.991	102.574	135.180
GBLength_Tmt/Spl_[µm]	687.433	2439.647	513.187	510.886
GBLength_Di_[µm]	4136.690	12471.932	1551.385	1230.202
GBLength_OR1_[µm]	88.697	125.369	31.671	29.633
GBLength_OR2_[µm]	73.479	135.183	13.769	67.994
GBLength_id3_[µm]	41.595	61.435	12.477	13.404
GBLength_anyOR_[µm]	203.770	321.987	57.918	111.031
BLFincontactTmt/Spl	0.339	0.189	0.200	0.265
BLFincontactCpx	0.056	0.037	0.066	0.110
BLF_{anyCOR}	**0.875**	**0.697**	**0.565**	**0.821**
BLF_{COR1}	**0.381**	**0.271**	**0.309**	**0.219**
BLF_{COR2}	**0.315**	**0.293**	**0.134**	**0.503**
$BLF_{nearCOR}$	**0.179**	**0.133**	**0.122**	**0.099**
BLF_{noCORs}	**0.125**	**0.303**	**0.435**	**0.179**

n.r.= not representative area scanned

all the EBSD scans	1100d_30min				
scan name (µstructural domain)	scan_03 (not representative)	scan_04 (both µ-structures)	scan_04 (snowflake-like)	scan_04 (feather-like)	scan_06 (both µ-structures)
Area_in_µm2	45.36	10098	2680	6570	2046
notes	top	both			both
GB_and_CORs_stats	n.r.				
N_Tmt/Spl_Grains	**8**	**1260**	**396**	**869**	**195**
N_Tmt/Spl_Filtered	6	991	292	706	173
N_CpxGrains	4	588	393	237	262
N_Cpx_Filtered	4	346	314	53	215
N_Cpx_Filtered[100]	4	255	236	29	175
N_Cpx_Filtered[200]	3	211	203	25	144
N_Cpx_Filtered[500]	3	140	131	17	83
N_Cpx_Filtered[1000]	1	72	69	11	50
Mean_Spl_misorientation	0.451	0.981	0.962	0.991	0.912
Mean_Cpx_misorientation	0.730	8.895	1.407	11.038	1.486
Nunique_MtGrains_incontact	6	937	285	652	144
Nunique_MtGrains_anyOR	5	465	154	309	70
Nunique_MtGrains_OR1and2	5	435	141	291	66
Nunique_MtGrains_OR1	4	239	60	177	32
Nunique_MtGrains_OR2	2	293	110	181	44
Nunique_MtGrains_id3	2	251	78	172	35
frac_mt_incontact	**0.750**	**0.744**	**0.720**	**0.750**	**0.738**
frac_incontact_mt_anyOR	**0.833**	**0.496**	**0.540**	**0.474**	**0.486**
frac_incontact_mt_OR1	0.667	0.255	0.211	0.271	0.222
frac_incontact_mt_OR2	0.333	0.313	0.386	0.278	0.306
frac_incontact_mt_id3	0.333	0.268	0.274	0.264	0.243
GBLength_Di_Tmt/Spl_[µm]	9.102	707.923	220.405	485.136	101.034
GBLength_Tmt/Spl_[µm]	44.856	4534.474	1841.569	2681.212	767.320
GBLength_Di_[µm]	38.957	11582.795	3350.833	8351.995	2882.795
GBLength_OR1_[µm]	3.407	132.462	24.687	107.625	13.253
GBLength_OR2_[µm]	5.028	176.864	73.528	102.516	29.943
GBLength_id3_[µm]	0.378	70.323	21.267	48.832	8.738
GBLength_anyOR_[µm]	8.813	379.649	119.483	258.973	51.934
BLFincontactTmt/Spl	0.203	0.156	0.120	0.181	0.132
BLFincontactCpx	0.234	0.061	0.066	0.058	0.035
BLF_{anyCOR}	**0.968**	**0.536**	**0.542**	**0.534**	**0.514**
BLF_{COR1}	**0.374**	**0.187**	**0.112**	**0.222**	**0.131**
BLF_{COR2}	**0.552**	**0.250**	**0.334**	**0.211**	**0.296**
$BLF_{nearCOR}$	**0.042**	**0.099**	**0.096**	**0.101**	**0.086**
BLF_{noCORs}	**0.032**	**0.464**	**0.458**	**0.466**	**0.486**

n.r.= not representative area scanned

all the EBSD scans	1100d_30min		1100d_30min_new		
scan name (µstructural domain)	scan_06 (snowflake-like)	scan_06 (feather-like)	scan_01 (skeletal Cpx)	scan_02 (skeletal Cpx)	scan_03_top (feahter-like)
Area_in_µm2	1381	665	1480	918	5268
notes					
GB_and_CORs_stats					
N_Tmt/Spl_Grains	**145**	**60**	**58**	36	**319**
N_Tmt/Spl_Filtered	126	58	36	21	215
N_CpxGrains	247	38	59	46	141
N_Cpx_Filtered	207	38	45	38	65
N_Cpx_Filtered[100]	168	17	40	35	55
N_Cpx_Filtered[200]	136	13	37	33	52
N_Cpx_Filtered[500]	76	9	28	28	44
N_Cpx_Filtered[1000]	44	7	22	20	38
Mean_Spl_misorientation	0.942	0.659	1.529	0.362	1.505
Mean_Cpx_misorientation	0.980	2.240	0.631	0.568	2.174
Nunique_MtGrains_incontact	100	46	31	18	202
Nunique_MtGrains_anyOR	48	23	27	17	145
Nunique_MtGrains_OR1and2	45	22	25	16	132
Nunique_MtGrains_OR1	18	14	6	4	63
Nunique_MtGrains_OR2	34	11	22	13	84
Nunique_MtGrains_id3	24	11	12	7	90
frac_mt_incontact	**0.690**	**0.767**	**0.534**	0.5	**0.633**
frac_incontact_mt_anyOR	**0.480**	**0.500**	**0.871**	0.944	**0.718**
frac_incontact_mt_OR1	0.180	0.304	0.194	0.222	0.312
frac_incontact_mt_OR2	0.340	0.239	0.710	0.722	0.416
frac_incontact_mt_id3	0.240	0.239	0.387	0.389	0.446
GBLength_Di_Tmt/Spl_[µm]	61.827	39.276	34.003	43.685	284.408
GBLength_Tmt/Spl_[µm]	584.348	191.738	242.119	204.845	1527.051
GBLength_Di_[µm]	2057.016	887.748	1073.168	787.401	4461.499
GBLength_OR1_[µm]	7.618	5.536	3.044	1.845	42.813
GBLength_OR2_[µm]	16.217	13.899	19.966	30.188	98.589
GBLength_id3_[µm]	4.412	4.422	3.315	2.352	39.996
GBLength_anyOR_[µm]	28.246	23.857	26.326	34.385	181.397
BLFincontactTmt/Spl	0.106	0.205	0.140	0.213	0.186
BLFincontactCpx	0.030	0.044	0.032	0.055	0.064
BLF_{anyCOR}	**0.457**	**0.607**	**0.774**	**0.787**	**0.638**
BLF_{COR1}	**0.123**	**0.141**	**0.090**	**0.042**	**0.151**
BLF_{COR2}	**0.262**	**0.354**	**0.587**	**0.691**	**0.347**
$BLF_{nearCOR}$	**0.071**	**0.113**	**0.097**	**0.054**	**0.141**
BLF_{noCORs}	**0.543**	**0.393**	**0.226**	**0.213**	**0.362**

n.r.= not representative area scanned

all the EBSD scans	1100d_30min_new	1150d_30min		
scan name (µstructural domain)	scan_03_bottom (skeletal cpx)	scan_02 (not representative)	scan_03 (not representative)	scan_04 (feather-like)
Area_in_µm2	1379	2120	1444	13824
notes		n.r.	n.r.	
GB_and_CORs_stats				
N_Tmt/Spl_Grains	**37**	71	41	**748**
N_Tmt/Spl_Filtered	26	21	9	360
N_CpxGrains	81	31	15	142
N_Cpx_Filtered	53	16	3	17
N_Cpx_Filtered[100]	49	13	3	16
N_Cpx_Filtered[200]	46	11	3	16
N_Cpx_Filtered[500]	38	9	3	14
N_Cpx_Filtered[1000]	32	6	3	14
Mean_Spl_misorientation	1.035	2.507	2.928	3.058
Mean_Cpx_misorientation	0.602	1.259	0.869	5.237
Nunique_MtGrains_incontact	28	29	16	350
Nunique_MtGrains_anyOR	19	14	14	259
Nunique_MtGrains_OR1and2	16	10	12	227
Nunique_MtGrains_OR1	3	2	6	126
Nunique_MtGrains_OR2	14	8	7	126
Nunique_MtGrains_id3	15	10	11	150
frac_mt_incontact	**0.757**	**0.408**	**0.390**	**0.468**
frac_incontact_mt_anyOR	**0.679**	**0.483**	**0.875**	**0.740**
frac_incontact_mt_OR1	0.107	0.069	0.375	0.360
frac_incontact_mt_OR2	0.500	0.276	0.438	0.360
frac_incontact_mt_id3	0.536	0.345	0.688	0.429
GBLength_Di_Tmt/Spl_[µm]	124.802	73.154	23.991	399.988
GBLength_Tmt/Spl_[µm]	377.238	766.171	431.712	3604.382
GBLength_Di_[µm]	1176.095	674.640	516.089	9260.599
GBLength_OR1_[µm]	6.291	3.541	5.204	113.441
GBLength_OR2_[µm]	64.678	12.837	8.140	115.012
GBLength_id3_[µm]	10.181	8.049	5.561	91.771
GBLength_anyOR_[µm]	81.149	24.427	18.904	320.223
BLFincontactTmt/Spl	0.331	0.095	0.056	0.111
BLFincontactCpx	0.106	0.108	0.046	0.043
BLF_{anyCOR}	**0.650**	**0.334**	**0.788**	**0.801**
BLF_{COR1}	**0.050**	**0.048**	**0.217**	**0.284**
BLF_{COR2}	**0.518**	**0.175**	**0.339**	**0.288**
$BLF_{nearCOR}$	**0.082**	**0.110**	**0.232**	**0.229**
BLF_{noCORs}	**0.350**	0.666	0.212	**0.199**

n.r.= not representative area scanned

all the EBSD scans	Undoped_dry_30min	
scan name (µstructural domain)	Area in µm2	Area in mm2
Area_in_µm2	52273	0.05227336
notes		
GB_and_CORs_stats		
N_Tmt/Spl_Grains	**4349**	**83197**
N_Tmt/Spl_Filtered	**3170**	**60643**
N_CpxGrains	**2088**	**39944**
N_Cpx_Filtered	**1214**	**23224**
N_Cpx_Filtered[100]	975	18652
N_Cpx_Filtered[200]	865	16548
N_Cpx_Filtered[500]	667	12760
N_Cpx_Filtered[1000]	488	9336
Mean_Spl_misorientation		
Mean_Cpx_misorientation		
Nunique_MtGrains_incontact	3028	57926
Nunique_MtGrains_anyOR	1944	37189
Nunique_MtGrains_OR1and2	1775	33956
Nunique_MtGrains_OR1	998	19092
Nunique_MtGrains_OR2	1095	20948
Nunique_MtGrains_id3	1104	21120
frac_mt_incontact	**0.696**	
frac_incontact_mt_anyOR	**0.642**	
frac_incontact_mt_OR1	0.330	
frac_incontact_mt_OR2	0.362	
frac_incontact_mt_id3	0.365	
GBLength_Di_Tmt/Spl_[µm]	2735	52317.235
GBLength_Tmt/Spl_[µm]	16651	318543.150
GBLength_Di_[µm]	51844	991790.975
GBLength_OR1_[µm]	601	11490.931
GBLength_OR2_[µm]	852	16292.606
GBLength_id3_[µm]	370	7070.035
GBLength_anyOR_[µm]	1822	**34853.571**
BLFincontactTmt/Spl	0.164	
BLFincontactCpx	0.053	
BLF_{anyCOR}	**0.666**	
BLF_{COR1}	**0.220**	
BLF_{COR2}	**0.311**	
$BLF_{nearCOR}$	**0.135**	
BLF_{noCORs}	**0.334**	

n.r.= not representative area scanned

Results microstructurally based	1050d_30min	1100d_30min		
	scan_01 (feather-like)	scan_01 (feather-like)	scan_04 (feather-like)	scan_06 (feather-like)
Area_in_µm2	2744	1155	6570	665
notes				
GB_and_CORs_stats				
N_Tmt/Spl_Grains	**366**	**194**	**869**	**60**
N_Tmt/Spl_Filtered	306	165	706	58
N_CpxGrains	92	62	237	38
N_Cpx_Filtered	20	27	53	38
N_Cpx_Filtered[100]	15	18	29	17
N_Cpx_Filtered[200]	14	17	25	13
N_Cpx_Filtered[500]	11	15	17	9
N_Cpx_Filtered[1000]	8	11	11	7
Mean_Spl_misorientation	**1.385**	**1.083**	**0.991**	**0.659**
Mean_Cpx_misorientation	**8.980**	**2.837**	**11.038**	**2.240**
Nunique_MtGrains_incontact	319	151	652	46
Nunique_MtGrains_anyOR	267	82	309	23
Nunique_MtGrains_OR1and2	245	75	291	22
Nunique_MtGrains_OR1	164	51	177	14
Nunique_MtGrains_OR2	136	38	181	11
Nunique_MtGrains_id3	158	48	172	11
frac_mt_incontact	**0.872**	**0.778**	**0.750**	**0.767**
frac_incontact_mt_anyOR	**0.837**	**0.543**	**0.474**	**0.500**
frac_incontact_mt_OR1	0.514	0.338	0.271	0.304
frac_incontact_mt_OR2	0.426	0.252	0.278	0.239
frac_incontact_mt_id3	0.495	0.318	0.264	0.239
GBLength_Di_Tmt/Spl_[µm]	232.963	102.574	485.136	39.276
GBLength_Tmt/Spl_[µm]	687.433	513.187	2681.212	191.738
GBLength_Di_[µm]	4136.690	1551.385	8351.995	887.748
GBLength_OR1_[µm]	88.697	31.671	107.625	5.536
GBLength_OR2_[µm]	73.479	13.769	102.516	13.899
GBLength_id3_[µm]	41.595	12.477	48.832	4.422
GBLength_anyOR_[µm]	203.770	57.918	258.973	23.857
BLFincontactTmt/Spl	0.339	0.200	0.181	0.205
BLFincontactCpx	0.056	0.066	0.058	0.044
BLF_{anyCOR}	**0.875**	**0.565**	**0.534**	**0.607**
BLF_{COR1}	**0.381**	**0.309**	**0.222**	**0.141**
BLF_{COR2}	**0.315**	**0.134**	**0.211**	**0.354**
$BLF_{nearCOR}$	**0.179**	**0.122**	**0.101**	**0.113**
BLF_{noCORs}	**0.125**	**0.435**	**0.466**	**0.393**

n.r.= not representative area scanned

Results microstructurally based	1100d_30min_new	1150d_30min	**feather-like Cpx domain**	
	scan_03_top (feather-like)	scan_04 (feather-like)	Area_in_µm2	Area_in_mm2
Area_in_µm2	5268	13824	30226	0.0302
notes				
GB_and_CORs_stats				
N_Tmt/Spl_Grains	**319**	**748**	**2556**	**84563**
N_Tmt/Spl_Filtered	215	360	1810	59882
N_CpxGrains	141	142	**712**	**23556**
N_Cpx_Filtered	65	17	220	7278
N_Cpx_Filtered[100]	55	16	150	4963
N_Cpx_Filtered[200]	52	16	137	4533
N_Cpx_Filtered[500]	44	14	**110**	**3639**
N_Cpx_Filtered[1000]	38	14	**89**	**2944**
Mean_Spl_misorientation	**1.505**	**3.058**		
Mean_Cpx_misorientation	**2.174**	**5.237**		
Nunique_MtGrains_incontact	202	350	1720	56905
Nunique_MtGrains_anyOR	145	259	1085	35896
Nunique_MtGrains_OR1and2	132	227	992	32819
Nunique_MtGrains_OR1	63	126	595	19685
Nunique_MtGrains_OR2	84	126	576	19056
Nunique_MtGrains_id3	90	150	629	20810
frac_mt_incontact	**0.633**	**0.468**	**0.673**	
frac_incontact_mt_anyOR	**0.718**	**0.740**	**0.631**	
frac_incontact_mt_OR1	0.312	0.360	0.346	
frac_incontact_mt_OR2	0.416	0.360	0.335	
frac_incontact_mt_id3	0.446	0.429	0.366	
GBLength_Di_Tmt/Spl_[µm]	284.408	399.988	1544	51093
GBLength_Tmt/Spl_[µm]	1527.051	3604.382	9205	304539
GBLength_Di_[µm]	4461.499	9260.599	28650	947855
GBLength_OR1_[µm]	42.813	113.441	390	12896
GBLength_OR2_[µm]	98.589	115.012	417	13805
GBLength_id3_[µm]	39.996	91.771	239	7910
GBLength_anyOR_[µm]	181.397	320.223	1046	**34610**
BLFincontactTmt/Spl	0.186	0.111	0.168	
BLFincontactCpx	0.064	0.043	0.054	
BLF_{anyCOR}	**0.638**	**0.801**	**0.677**	
BLF_{COR1}	**0.151**	**0.284**	**0.252**	
BLF_{COR2}	**0.347**	**0.288**	**0.270**	
$BLF_{nearCOR}$	**0.141**	**0.229**	**0.155**	
BLF_{noCORs}	**0.362**	**0.199**	**0.323**	

n.r.= not representative area scanned

Results microstructurally based	1050d_30min	1100d_30min		**snowflake-like Cpx domain**	
	scan_02 (snowflake-like)	scan_04 (snowflake-like)	scan_06 (snowflake-like)	Area_in_µm2	Area_in_mm2
Area_in_µm2	8836	2680	1381	12896.9425	0.012896943
notes					
GB_and_CORs_stats					
N_Tmt/Spl_Grains	**889**	**396**	**145**	**1430**	**110879**
N_Tmt/Spl_Filtered	735	292	126	1153	89401
N_CpxGrains	500	393	247	**1140**	**88393**
N_Cpx_Filtered	309	314	207	**830**	**64356**
N_Cpx_Filtered[100]	254	236	168	658	51020
N_Cpx_Filtered[200]	236	203	136	575	44584
N_Cpx_Filtered[500]	212	131	76	419	32488
N_Cpx_Filtered[1000]	177	69	44	290	22486
Mean_Spl_misorientation	1.202	0.962	0.942		
Mean_Cpx_misorientation	2.110	1.407	0.980		
Nunique_MtGrains_incontact	708	285	100	1093	84749
Nunique_MtGrains_anyOR	486	154	48	688	53346
Nunique_MtGrains_OR1and2	442	141	45	628	48694
Nunique_MtGrains_OR1	261	60	18	339	26285
Nunique_MtGrains_OR2	267	110	34	411	31868
Nunique_MtGrains_id3	281	78	24	383	29697
frac_mt_incontact	**0.796**	**0.720**	**0.690**	**0.764**	
frac_incontact_mt_anyOR	**0.686**	**0.540**	**0.480**	**0.629**	
frac_incontact_mt_OR1	0.369	0.211	0.180	0.310	
frac_incontact_mt_OR2	0.377	0.386	0.340	0.376	
frac_incontact_mt_id3	0.397	0.274	0.240	0.350	
GBLength_Di_Tmt/Spl_[µm]	461.991	220.405	61.827	744.222	57705
GBLength_Tmt/Spl_[µm]	2439.647	1841.569	584.348	4865.564	377265
GBLength_Di_[µm]	12471.932	3350.833	2057.016	17879.781	1386358
GBLength_OR1_[µm]	125.369	24.687	7.618	157.675	12226
GBLength_OR2_[µm]	135.183	73.528	16.217	224.928	17440
GBLength_id3_[µm]	61.435	21.267	4.412	87.114	6755
GBLength_anyOR_[µm]	321.987	119.483	28.246	469.716	**36421**
BLFincontactTmt/Spl	0.189	0.120	0.106	0.153	
BLFincontactCpx	0.037	0.066	0.030	0.042	
BLF_{anyCOR}	**0.697**	**0.542**	**0.457**	**0.631**	
BLF_{COR1}	**0.271**	**0.112**	**0.123**	**0.212**	
BLF_{COR2}	**0.293**	**0.334**	**0.262**	**0.302**	
$BLF_{nearCOR}$	**0.133**	**0.096**	**0.071**	**0.117**	
BLF_{noCORs}	**0.303**	**0.458**	**0.543**	**0.369**	

n.r.= not representative area scanned

Results microstructurally based	1100d_30min	1100d_30min_new		1100d_30min_new
	scan_02 (skeletal cpx)	scan01 (skeletal cpx)	scan02 (skeletal cpx)	scan_03 (skeletal cpx)
Area_in_µm2	1764	1480	918	1379
notes				top
GB_and_CORs_stats				
N_Tmt/Spl_Grains	**127**	**58**	**36**	**37**
N_Tmt/Spl_Filtered	106	36	21	26
N_CpxGrains	65	59	46	81
N_Cpx_Filtered	56	45	38	53
N_Cpx_Filtered[100]	43	40	35	49
N_Cpx_Filtered[200]	42	37	33	46
N_Cpx_Filtered[500]	39	28	28	38
N_Cpx_Filtered[1000]	34	22	20	32
Mean_Spl_misorientation	0.779	1.529	0.362	1.035
Mean_Cpx_misorientation	0.609	0.631	0.568	0.602
Nunique_MtGrains_incontact	89	31	18	28
Nunique_MtGrains_anyOR	74	27	17	19
Nunique_MtGrains_OR1and2	69	25	16	16
Nunique_MtGrains_OR1	37	6	4	3
Nunique_MtGrains_OR2	41	22	13	14
Nunique_MtGrains_id3	34	12	7	15
frac_mt_incontact	**0.701**	**0.534**	0.5	**0.757**
frac_incontact_mt_anyOR	**0.831**	**0.871**	0.944	**0.679**
frac_incontact_mt_OR1	0.416	0.194	0.222	0.107
frac_incontact_mt_OR2	0.461	0.710	0.722	0.500
frac_incontact_mt_id3	0.382	0.387	0.389	0.536
GBLength_Di_Tmt/Spl_[µm]	135.180	34.003	43.685	124.802
GBLength_Tmt/Spl_[µm]	510.886	242.119	204.845	377.238
GBLength_Di_[µm]	1230.202	1073.168	787.401	1176.095
GBLength_OR1_[µm]	29.633	3.044	1.845	6.291
GBLength_OR2_[µm]	67.994	19.966	30.188	64.678
GBLength_id3_[µm]	13.404	3.315	2.352	10.181
GBLength_anyOR_[µm]	111.031	26.326	34.385	81.149
BLFincontactTmt/Spl	0.265	0.140	0.213	0.331
BLFincontactCpx	0.110	0.032	0.055	0.106
BLF_{anyCOR}	**0.821**	**0.774**	**0.787**	**0.650**
BLF_{COR1}	**0.219**	**0.090**	**0.042**	**0.050**
BLF_{COR2}	**0.503**	**0.587**	**0.691**	**0.518**
$BLF_{nearCOR}$	**0.099**	**0.097**	**0.054**	**0.082**
BLF_{noCORs}	**0.179**	**0.226**	**0.213**	**0.350**

n.r.= not representative area scanned

Results microstructurally based	Skeletal Cpx domain	
	Area_in_µm2	Area_in_mm2
Area_in_µm2	5541	0.005541
notes		
GB_and_CORs_stats		
N_Tmt/Spl_Grains	**258**	**46562**
N_Tmt/Spl_Filtered	189	34109
N_CpxGrains	**251**	**45299**
N_Cpx_Filtered	**192**	**34651**
N_Cpx_Filtered[100]	167	30139
N_Cpx_Filtered[200]	158	28515
N_Cpx_Filtered[500]	133	24003
N_Cpx_Filtered[1000]	108	19491
Mean_Spl_misorientation		
Mean_Cpx_misorientation		
Nunique_MtGrains_incontact	166	12871
Nunique_MtGrains_anyOR	137	10623
Nunique_MtGrains_OR1and2	126	9770
Nunique_MtGrains_OR1	50	3877
Nunique_MtGrains_OR2	90	6978
Nunique_MtGrains_id3	68	5273
frac_mt_incontact	**0.643**	
frac_incontact_mt_anyOR	**0.825**	
frac_incontact_mt_OR1	0.301	
frac_incontact_mt_OR2	0.542	
frac_incontact_mt_id3	0.410	
GBLength_Di_Tmt/Spl_[µm]	337.6710245	26182
GBLength_Tmt/Spl_[µm]	1335.087616	103520
GBLength_Di_[µm]	4266.865216	330843
GBLength_OR1_[µm]	40.81264914	3165
GBLength_OR2_[µm]	182.8258287	14176
GBLength_id3_[µm]	29.25191166	2268
GBLength_anyOR_[µm]	252.8903895	**19609**
BLFincontactTmt/Spl	0.253	
BLFincontactCpx	0.079	
BLF_{anyCOR}	**0.749**	
BLF_{COR1}	**0.121**	
BLF_{COR2}	**0.541**	
$BLF_{nearCOR}$	**0.087**	
BLF_{noCORs}	**0.251**	

n.r.= not representative area scanned

Results sample based	1050d_30min	1050d_30min_tot_density [mm^{-1}]	1100d_30min	1100d_30min_tot_density [mm^{-1}]
	Area in µm2	Area in mm2	Area in µm2	Area in mm2
Area_in_µm2	11580	0.012	24108	0.024
notes				
GB_and_CORs_stats				
N_Tmt/Spl_Grains	**1255**	**108377**	**3481**	**144392**
N_Tmt/Spl_Filtered	**1041**	**89896**	**2774**	**115066**
N_CpxGrains	**592**	**51123**	**1896**	**78646**
N_Cpx_Filtered	**329**	**28411**	**1174**	**48698**
N_Cpx_Filtered[100]	269	23230	939	38950
N_Cpx_Filtered[200]	250	21589	832	34511
N_Cpx_Filtered[500]	223	19257	638	26464
N_Cpx_Filtered[1000]	**185**	**15976**	**464**	**19247**
Mean_Spl_misorientation				
Mean_Cpx_misorientation				
Nunique_MtGrains_incontact	1027	88687	2627	108968
Nunique_MtGrains_anyOR	753	65026	1652	68525
Nunique_MtGrains_OR1and2	687	59326	1521	63091
Nunique_MtGrains_OR1	425	36701	860	35673
Nunique_MtGrains_OR2	403	34801	952	39489
Nunique_MtGrains_id3	439	37910	931	38618
frac_mt_incontact	**0.818**		**0.755**	
frac_incontact_mt_anyOR	**0.733**		**0.629**	
frac_incontact_mt_OR1	0.414		0.327	
frac_incontact_mt_OR2	0.392		0.362	
frac_incontact_mt_id3	**0.427**		**0.354**	
GBLength_Di_Tmt/Spl_[µm]	694.954	60013.261	2229	92440.823
GBLength_Tmt/Spl_[µm]	3127.079	270041.397	11804	489638.254
GBLength_Di_[µm]	16608.622	1434250.577	41354	1715362.582
GBLength_OR1_[µm]	214.066	18485.837	475	19706.240
GBLength_OR2_[µm]	208.662	18019.165	711	29477.856
GBLength_id3_[µm]	**103.029**	**8897.192**	264	**10943.073**
GBLength_anyOR_[µm]	**525.757**	**45402.194**	1450	**60127.168**
BLFincontactTmt/Spl	0.222		0.189	
BLFincontactCpx	0.042		0.054	
BLF_{anyCOR}	**0.757**		**0.650**	
BLF_{COR1}	**0.308**		**0.213**	
BLF_{COR2}	**0.300**		**0.319**	
$BLF_{nearCOR}$	**0.148**		**0.118**	
BLF_{noCORs}	**0.243**		**0.350**	

n.r.= not representative area scanned

Results sample based	1150d_30min	1150d_30min_tot_density [mm^{-1}]
	Area in µm2	Area in mm2
Area_in_µm2	13824	0.013824
notes		
GB_and_CORs_stats		
N_Tmt/Spl_Grains	**748**	**54109**
N_Tmt/Spl_Filtered	**360**	**26042**
N_CpxGrains	**142**	**10272**
N_Cpx_Filtered	**17**	**1230**
N_Cpx_Filtered[100]	16	1157
N_Cpx_Filtered[200]	16	1157
N_Cpx_Filtered[500]	14	1013
N_Cpx_Filtered[1000]	**14**	**1013**
Mean_Spl_misorientation		
Mean_Cpx_misorientation		
Nunique_MtGrains_incontact	350	25318
Nunique_MtGrains_anyOR	259	18736
Nunique_MtGrains_OR1and2	227	16421
Nunique_MtGrains_OR1	126	9115
Nunique_MtGrains_OR2	126	9115
Nunique_MtGrains_id3	150	
frac_mt_incontact	**0.468**	
frac_incontact_mt_anyOR	**0.740**	
frac_incontact_mt_OR1	0.360	
frac_incontact_mt_OR2	0.360	
frac_incontact_mt_id3	**0.429**	**31.002**
GBLength_Di_Tmt/Spl_[µm]	400	28934.297
GBLength_Tmt/Spl_[µm]	3604	260733.685
GBLength_Di_[µm]	9261	669892.903
GBLength_OR1_[µm]	113	8206.061
GBLength_OR2_[µm]	115	8319.741
GBLength_id3_[µm]	**92**	**6638.511**
GBLength_anyOR_[µm]	**320**	**23164.313**
BLFincontactTmt/Spl	0.111	
BLFincontactCpx	0.043	
BLF_{anyCOR}	**0.801**	
BLF_{COR1}	**0.284**	
BLF_{COR2}	**0.288**	
$BLF_{nearCOR}$	**0.229**	
BLF_{noCORs}	**0.199**	

n.r.= not representative area scanned

Experimental strategy and scans timing in the experiment (Chapter 5.)

Dynamic experiment

T °C	t (s)	t (min)	Scan names
25	0	0.00	BH
1300	1275	21.25	
1300	3075	51.25	
1210	3165	52.75	
1210	3285	54.75	1210a
1210	3885	64.75	1210b
1210	4485	74.75	1210c
1210	5085	84.75	
1200	5095	84.92	
1200	5215	86.92	1200a
1200	5815	96.92	1200b
1200	6415	106.92	1200c
1200	7015	116.92	
1190	7025	117.08	
1190	7145	119.08	1190a
1190	7745	129.08	1190b
1190	8345	139.08	1190c
1190	8945	149.08	
1180	8955	149.25	
1180	9075	151.25	1180a
1180	9675	161.25	1180b
1180	10275	171.25	1180c
1180	10875	181.25	
1170	10885	181.42	
1170	11005	183.42	1170a
1170	11605	193.42	1170b
1170	12205	203.42	1170c
1170	12805	213.42	
1160	12815	213.58	
1160	12935	215.58	1160a
1160	13535	225.58	1160b
1160	14135	235.58	1160c
1160	14735	245.58	
1150	14745	245.75	
1150	14865	247.75	1150a
1150	15465	257.75	1150b
1150	16065	267.75	1150c
1150	16665	277.75	
25	17790	296.50	
25	18390	306.50	AH

Just scans T (°C) and time (min)

T °C	t (s)	t (min)	Scan names
25	0	0	BH
1210	3285	54.75	1210a
1210	3885	64.75	1210b
1210	4485	74.75	1210c
1200	5215	86.92	1200a
1200	5815	96.92	1200b
1200	6415	106.92	1200c
1190	7145	119.08	1190a
1190	7745	129.08	1190b
1190	8345	139.08	1190c
1180	9075	151.25	1180a
1180	9675	161.25	1180b
1180	10275	171.25	1180c
1170	11005	183.42	1170a
1170	11605	193.42	1170b
1170	12205	203.42	1170c
1160	12935	215.58	1160a
1160	13535	225.58	1160b
1160	14135	235.58	1160c
1150	14865	247.75	1150a
1150	15465	257.75	1150b
1150	16065	267.75	1150c
25	18390	306.50	AH

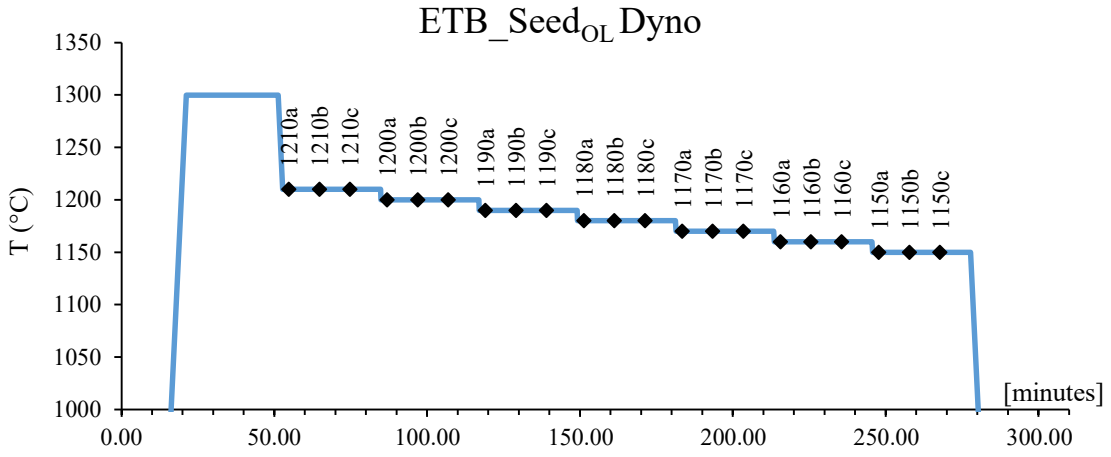

Experimental strategy and scans timing in the experiment (Chapter 5.)

Drop experiment

T °C	t (s)	t (min)	Scan names
25	0	0.00	BH
1300	1275	21.25	
1300	3075	51.25	
1100	3275	54.58	
1100	3395	56.58	1100_1
1100	3995	66.58	1100_2
1100	4595	76.58	1100_3
1100	5195	86.58	1100_4
1100	5795	96.58	1100_5
1100	6395	106.58	1100_6
1100	6995	116.58	1100_7
25	8070	134.50	
25	8670	144.50	AH

Just scans T (°C) and time (min)

T °C	t (s)	t (min)	Scan names
25	0	0.00	BH
1100	3395	56.58	1100_1
1100	3995	66.58	1100_2
1100	4595	76.58	1100_3
1100	5195	86.58	1100_4
1100	5795	96.58	1100_5
1100	6395	106.58	1100_6
1100	6995	116.58	1100_7
25	8670	144.50	AH